

*Editorial corner – a personal view*

## Should the passive voice be forced indiscriminately?

Attila Balaskó\*

Department of Polymer Engineering, Faculty of Mechanical Engineering, Budapest University of Technology and Economics, H-1111 Budapest, Műegyetem rkp. 3., Hungary

I am an electrical engineer, English teacher and linguist. I have been researching English grammar, pronunciation and style for over thirty years. I have written a book on English pronunciation and a three-volume English grammar book. For the past seven years, however, I have been focusing on the correct use of scientific and academic English and have proofread and corrected the English of a large number of manuscripts in polymer science.

Nowadays it is common practice that reviewers criticise the English of papers as well, as they are also asked by publishers. It is good because grammar and vocabulary mistakes make it difficult or impossible to understand the paper clearly, if at all. However, reviewers do not notice many actual grammar problems such as dangling modifiers or the incorrect use of articles. A far greater problem is that they often criticise perfectly correct sentences. For some unimaginable reason, many reviewers think that a scientific article should be written in the passive voice and not contain the words ‘I’, ‘we’, ‘my’ or ‘our’.

Nothing could be further from the truth. There is absolutely no such rule. Actually, many style guides and journals explicitly state that the passive voice should not be overused. Some examples:

Elsevier: [Writing Style Guidelines](#),

Springer: [Concise writing](#),

APA Style Guide 6<sup>th</sup> Edition: [APA Stylistics: Basics](#),

APA 7th Edition: [The 17 Most Notable Changes](#).

Also, a language does not work like that. One cannot make arbitrary rules in English. Could I say, for example, that from now on ‘medical language’ means everything in the past must be written in a future tense and everything happening in the future must

be written in a past tense? Because that is ‘medical language’? (It would not lead to misunderstanding, because the tenses would be used consistently.) No. English is always the same, there is no such thing as ‘scientific English’, ‘medical English’, or ‘legal English’ grammar. Obviously, each field has its own terminology but that is not grammar.

English is the same in different situations—grammar always works the same way. Let us see four examples:

- A reviewer requires that the passive is used in the Abstract in sentences like ‘A new composite has been developed’. instead of ‘We have developed a new composite’.
- A researcher gives a speech at a conference introducing his own research results and says ‘Good afternoon ladies and gentlemen. A new composite has been developed...’
- A child who has won a school contest goes home to tell their parents the good news: ‘I am so happy! The contest has been won!’
- A man confesses his love to a woman: ‘You are loved’.

The passive voice works the same way in all four examples. How acceptable or unacceptable is the passive voice in these examples? Equally unacceptable. The correct use of the passive and active voice is governed by intricate rules in English. An article written in correct English contains both the active voice and the passive voice in the right places.

It is quite surprising that many reviewers try to force authors who may be using both the active voice and the passive voice correctly in their paper to use incorrect English (only passive, without ‘I’ or ‘we’ or even ‘our’) in the paper and thus significantly reduce

\*Corresponding author, e-mail: [balaskoa@pt.bme.hu](mailto:balaskoa@pt.bme.hu)  
© BME-PT

the quality of the article. Well, it is not only surprising, it is harmful, and reviewers should immediately stop doing this. After all, reviewers of scientific articles are rarely linguists as well, and so they are by no means qualified to order authors to use the passive

incorrectly. Nobody is. Publishers also have a responsibility in educating reviewers (through Guides for authors). Express Polymer Letters also encourages authors and reviewers to use both the active voice and the passive voice correctly in manuscripts.



Attila Balaskó  
Member of Executive Editorial Board

Research article

# Microstructure and electrical properties of Li<sup>+</sup> ion conducting polymer blend electrolyte films

Rohan Nandeesh Sagar<sup>1,2</sup>, Ravindrachary Vasachar<sup>1\*</sup>, Shreedatta Hegde<sup>1</sup>

<sup>1</sup>Department of Physics, Mangalore University, 574199 Mangalagangothri, India

<sup>2</sup>Adichunchanagiri School of Natural Sciences, Adichunchanagiri University, 571418, India

Received 10 January 2023; accepted in revised form 9 May 2023

**Abstract.** Solid polymer electrolytes based on polyvinyl alcohol (PVA)–chitosan (CS) polymer blend and Li–salt doped blend electrolyte films are prepared using the solution cast technique. The Fourier transform infrared spectra showed that the absorption peaks shifted in Li–salt doped polymer blend composites compared to pure blend films: indicating the chemical modifications upon doping. From the UV–visible spectra, the spectral absorption response of Li<sup>+</sup> salt–doped polymer blend composites showed a red shift in the absorption band. The optical band gap of the pure polymer blend decreased upon doping. X–ray diffraction studies showed the dopant-dependent structural modification of pure polymer blend upon doping. SEM images also showed the change in the surface morphology of the pure polymer blend upon doping. The thermogravimetric analysis study revealed that the thermal stability of the pure polymer blend increases with Li<sub>2</sub>CO<sub>3</sub> concentration. The ionic conductivity of PVA–CS increases with Li–salt concentration, and the maximum conductivity of  $7.70 \cdot 10^{-5} \text{ S} \cdot \text{cm}^{-1}$  is observed for 15 wt% of Li<sub>2</sub>CO<sub>3</sub> salt concentration. The transport property study revealed that the ions are the majority conducting charge carriers in polymer blend composite.

**Keywords:** polymer blends and alloys, structural properties, electrical and transport properties

## 1. Introduction

Lithium–ion batteries have become a key source of choice not only in the application of portable electronic devices (mobile phones, power banks, and laptops) but also in hybrid electric vehicle applications. In the earlier days, liquid electrolytes were extensively used for battery applications, but these electrolytes are associated with some disadvantages or concerns like leakage and flammability leading to safety hazards. However, this obstacle can be evaded by replacing liquid electrolytes with solid polymer electrolytes (SPEs).

In addition, these SPE materials also provide beneficial properties such as high energy density, flexibility and tunability of the properties of the host as well as improved safety characteristics. Here it is observed that desired chemical and physical properties

of these SPEs can be obtained by doping/blending a polymer with a suitable dopant/polymer. It is known that the change in the property of a polymer composite for SPE depends on the chemical nature of the dopant/blend polymer, the type of polymer and the way in which the dopant interacts with the host polymer. As a result of these tunable properties, the polymer and its composite–based solid polymer electrolytes have become the most efficient and suitable materials for the fabrication of solid–state batteries. Owing to this, many researchers are focusing on polymeric blends and their composites for the fabrication of batteries due to their ease of fabrication and high performance, even at ambient temperatures. In particular, the polymers which are naturally occurring, biocompatible and possessing optimal properties, viz., mechanical, thermal, and high ionic conductivity

\*Corresponding author, e-mail: [rvavi2000@yahoo.com](mailto:rvavi2000@yahoo.com)

© BME-PT

properties (such as chitosan (CS) and methylcellulose, *etc.*) are considered to be interesting materials for blending [1, 2] and organic/inorganic fillers, plasticization, copolymerization are enforced to modulate the ionic conductivity in these polymers. The researchers also noticed that the polymer blending and its composites–based solid polymer blend electrolyte (SPBE) system possess great optical, mechanical, thermal, and high ionic conductivity properties compared to single polymer–based SPE system. To reach this objective, many researchers proposed various synthetic polymeric matrices, such as poly(acrylates), polyvinyl alcohol, elastomers, polythiophenes, and epoxy polymers, *etc.*, as host materials and naturally occurring polymers like chitosan, cellulose, and starch, *etc.* are suggested polymers for the preparing of solid polymer blend electrolyte films (SPBE) [3]. Among all the polymers, polyvinyl alcohol (PVA) and chitosan (CS) based polymer blends and their composites are proposed as the appreciable composite material for the preparation of blend electrolyte systems [4]. The polymer blends and their composites exhibit higher charge storage capacity and possess dopant dependant structural, thermal, and electrical properties. In general, the ionic conductivity within a polymer electrolyte system is strongly influenced by the dopant (LiCl, LiClO<sub>4</sub>, and Li<sub>2</sub>CO<sub>3</sub>, *etc.*) concentration and preparation methods. For example, Salman *et al.* [2] reported the highest electrical conductivity of  $3.74 \cdot 10^{-6} \text{ S} \cdot \text{cm}^{-1}$  in 40 wt% LiBF<sub>4</sub> doped chitosan–methylcellulose blend biopolymer electrolyte and Shukur *et al.* [3] observed the highest electrical conductivity of  $2.06 \pm 0.39 \cdot 10^{-3} \text{ S} \cdot \text{cm}^{-1}$  at room temperature for 11 wt% chitosan + 7 wt% PEO + 12 wt% NH<sub>4</sub>NO<sub>3</sub> sample with 70% ethylene carbonate (EC). Hence, the understanding effect of doping on polymer blend microstructure and modified physic–chemical changes is the topic of current research.

It is also known that the ionic conductivity in polymer/blend composites mainly depends on the presence of charge transfer (CT) complexes occurred due to inter/intra–molecular interaction between the dopant and the polymer. These charge complexes bridge the gap between the neighbouring sites for efficient charge transfer through the polymer backbone. Hence, the ionic conductivity in polymers depends on the chemical nature of the repeating units in the polymer chain, the electronic structure, and the segmental motion of the polymer backbone. Here the dopant

makes the polymer backbone more flexible, which helps to transfer mobile charge carriers from one conducting site to another. In other words, the dopant starts bridging between two localized sites of the polymer in the form of a CT complex, which leads to lowering the potential barrier between the two sites and facilitates more and more mobile charge carriers to transfer within the electrolyte systems. A polymer blend is a homogeneous mixture of two or more polymers, which can modulate the microstructure of the host material. The change in microstructural properties of polymer blends is depending on the characteristic features of each polymer and the blending concentrations. The main aim of polymer blending is to prepare the blend materials which conquer unique structural, good thermal and high electrical properties. When two or more suitable polymers are mixed with a suitable volume of solvent, inter/intramolecular interaction will take place, and these chemical interactions will affect the physical properties of the host or guest polymer. As a result, one can expect the enhancement of other properties in addition to electrical conductivity in the prepared polymer blend and its composites [4–6].

Polyvinyl alcohol (PVA) is a vinyl polymer possessing semicrystalline nature and also high  $T_g$  due to the existence of a solid pyrrolidone group which is familiar with forming distinctive complexes with various polymers and dopants. It has an excellent capacity of charge storage, and it exhibits dopant–dependent structural and electrical properties. The conductivity of PVA enhances due to the high rate of physical and chemical interactions through inter/ intramolecular interaction between functional groups of PVA and the dopant. These interactions form charge complexes and facilitate more and more ions transfer from one conductive site to another; hence conductivity enhances in the polymer composites [7, 8].

Unlike PVA polymer, chitosan is a naturally occurring polymer, and it comprises  $\beta$ –(1→4)–2–amino–2–deoxy–D–glucosamine, which is a derivative of chitin with a high degree of *N*–acetylation. Especially it is a copolymer of D–glucosamine and *N*–acetyl–D–glucosamine, and it is a naturally occurring mucopolysaccharide. Chitosan polymer exhibits a few eco–friendly properties such as nontoxicity, biodegradability, and excellent biocompatibility, and it also has adhesiveness properties, *etc.* which came from alkaline deacetylation of chitin [9–11]. Chitosan is a semicrystalline polymer, and its degree of

crystallinity is the function of the degree of deacetylation, and it can be degraded through enzymatic hydrolysis. Since chitosan is a biodegradable polymer, it drives it into technological applications such as tissue engineering, drug delivery, electrochromic devices, and membrane systems as a biomaterial, and its antigenicity behaviour avail it as a biomaterial in biomedical applications [10, 12–14]. Khair *et al.* [11] achieved the highest ionic conductivity of about  $8.91 \cdot 10^{-7} \text{ S} \cdot \text{cm}^{-1}$  was achieved in 50 wt% ammonium triflate ( $\text{NH}_4\text{CF}_3\text{SO}_3$ ) doped with chitosan-based polymer electrolyte system at room temperature. Hence PVA and chitosan are considered congenial polymers for the blending process. Since both the polymers are miscible to each other, the ionic complexation takes place between chitosan and PVA polymers through the hydroxyl groups of PVA and amine groups of chitosan polymer [4–6]. In this context, many researchers have paid great attention to chitosan polymer/polymer blend composite as a biological and technological active source [11, 15]. Hence in the present work, PVA and chitosan polymer blend are used as a host, and  $\text{Li}_2\text{CO}_3$  as a dopant for the preparation of blend composite and the modified optical, structural, morphological, thermal, electrical, and transport properties of solid polymer blend electrolyte (SPBE) system was intensively studied using various techniques.

## 2. Experimental methods

### 2.1. Materials

The polymers polyvinyl alcohol (PVA), chitosan (CS) and the dopant lithium carbonate ( $\text{Li}_2\text{CO}_3$ ) salt used in the present work are procured from M/s Sigma Aldrich, Bangalore, India. Pure PVA–CS polymer blend and  $\text{Li}_2\text{CO}_3$  doped blend polymer composite films are prepared using a standard solution casting method. Here 0.8 gm of chitosan was gently added to 40 ml of double distilled water containing 1% of acetic acid under stirring (16 hours) to make 2% (w/v) chitosan solution. 2 mg of PVA was dissolved separately in 40 ml of double distilled water and stirred for 1 hr at  $40^\circ\text{C}$ , after getting homogeneous solution the temperature is turned off again stirred for 16 hours to make 5% (w/v) PVA solution.

The prepared 5% PVA solution and 2% chitosan solution were mixed with a 50/50 ratio and again stirred for 12 hours to get a homogeneous solution. This homogeneous solution was poured into pure

Petri plates and left to dry at room temperature to get PVA–CS polymer blend film. Similarly,  $\text{Li}_2\text{CO}_3$  salt-doped PVA–CS polymer blend electrolyte films are prepared by dissolving different concentrations of  $\text{Li}_2\text{CO}_3$  (5, 10, and 15 wt%) separately in 10 ml double distilled water and stirred for 30 min. Finally, different concentration of the salt-dissolved solution is added to the 50/50 ratio of PVA–CS solution in separate beakers. The solution was again stirred for 6 h and gently poured into a dry petri dish. The samples are dried in a hot air oven for 24 h to get the free-standing films.

### 2.2. Characterization techniques

Fourier transform infrared (FTIR) spectra were recorded using an IR–Prestige 21FTIR spectrophotometer (Shimadzu, Kyoto, Japan) to identify the possible chemical modifications within the polymer composite in the range  $400\text{--}4000 \text{ cm}^{-1}$  with a resolution of  $4 \text{ cm}^{-1}$  to analyze for pure and Li-salt doped polymer composites (six samples). The optical absorption spectra of PVA-CS and Li-salt doped PVA-CS polymer composites were obtained using an Ultraviolet (UV)–visible 1800 spectrophotometer (Shimadzu, Kyoto, Japan) in the wavelength range 190–900 nm. X-ray diffraction (XRD) spectra were performed by using the Rigaku Miniflex–600 (Tokyo, Japan) benchtop X-ray diffractometer, where  $\text{Cu-K}_\alpha$  generates the X-rays with  $\lambda = 1.5406 \text{ \AA}$  with the glancing angle  $2\theta$  range from  $5\text{--}70^\circ$  with the step size of  $0.02^\circ$  and scanning rate 10 per min. The surface morphology of prepared electrolyte films is observed by Carl Zeiss scanning electron microscope (SEM) (Carl Zeiss AG, Jena, Germany). Thermal properties of the polymer blend electrolyte films are studied using a universal TA–SDT Q600 instrument (Bangalore, India) in the temperature range of  $25\text{--}600^\circ\text{C}$  with a scanning speed rate of  $10^\circ\text{C}/\text{min}$ . The electrical properties of the samples are measured using an Agilent 4294A precision impedance analyzer (Santa Clara, California) with a frequency range of 40 Hz–5 MHz using the two-probe method. Here the prepared electrolyte films were sandwiched between two silver (Ag) blocking electrodes (2.5 mm diameter) with constant pressure to maintain better interfacial contact between the electrode and electrolyte, and the conductivity of pure and Li-salt doped polymer blend electrolyte films were carried out at an ambient temperature. Also, the temperature-dependent conductivity

of the high-conducting solid polymer blend electrolyte film is studied for different temperatures using an Agilent 4294A precision impedance analyzer (Santa Clara, California).

### 3. Results and discussions

#### 3.1. FTIR

FTIR study is a powerful tool used to inspect the chemical complexation between polymers and the dopant. FTIR spectra of pure and salt-doped polymer blends are shown in Figure 1, and the corresponding band assignment is presented in Table 1. Pure PVA–CS polymer blend exhibiting a broad band at  $3290\text{ cm}^{-1}$  is assigned to (–OH) stretching vibrations related to PVA polymer. Another absorption band is observed at  $2923\text{ cm}^{-1}$  which is concerned with  $-\text{CH}_2$  asymmetric stretching of PVA polymer. Peak observed at  $1647\text{ cm}^{-1}$  related to amide I and III groups of  $\text{C}=\text{O}$  stretching vibrations of chitosan. The peak corresponding to the N–H (deformation) bending of the  $-\text{NH}_2$  group is located at  $1557\text{ cm}^{-1}$ . Nevertheless, two more peaks are observed at  $1417$  and  $1357\text{ cm}^{-1}$ , which is assigned to the existence of

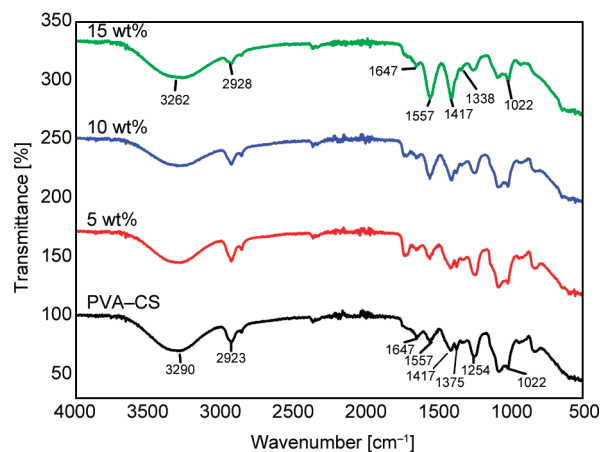


**Figure 1.** FTIR spectra of pure and  $\text{Li}_2\text{CO}_3$  (5, 10, and 15 wt%) doped PVA–CS polymer blend electrolyte films.

carboxylic acid and  $\text{CH}_2$  wagging. The peak located at  $1254\text{ cm}^{-1}$  is related to C–H vibrations within the polymer blend, and a weak absorption band is observed at  $1022\text{ cm}^{-1}$ , which is attributed to the (C–N) stretching peak of the PVA–CS polymer blend.

In a salt-doped polymer blend composite, the band corresponding to a hydroxyl group (–OH) located at  $3290\text{ cm}^{-1}$  is shifted to a lower wave number and becomes shallow upon doping. The second peak observed at  $2923\text{ cm}^{-1}$  is shifted to  $2928\text{ cm}^{-1}$  as well as a decrease in its intensity with an increase in salt concentration. In blend composite films, the peaks observed at  $1557$ ,  $1417$ ,  $1254$ , and  $1022\text{ cm}^{-1}$  exhibit the change in their intensities upon doping. The modification in the observed band is mainly due to inter/intra-molecular interaction between the dopant and the functional groups of the polymer blend [2]. The peak observed at  $1375\text{ cm}^{-1}$  for the pure polymer blend is shifted to  $1338\text{ cm}^{-1}$  in the composite. The changes in peak position and peak intensities in salt-doped blend composites are mainly due to the complexation of  $\text{Li}^+$  ions and the oxygen or nitrogen atoms of the hydroxyl or amine group of the polymer blend. Here, the chemical interaction takes place between the hydroxyl group of PVA polymer with  $\text{Li}^+$  ion of  $\text{Li}_2\text{CO}_3$  salt and also between amine groups of chitosan with  $\text{CO}_3^-$  of  $\text{Li}_2\text{CO}_3$  salt [15, 16].

#### 3.2. UV–visible studies

The UV–visible absorption spectrum is one of the simple and effective methods used to study the band structure and optical energy band gap ( $E_g$ ) in solid materials. The UV–visible absorption spectra of pure and Li–salt doped polymer blend electrolyte films are displayed in Figure 2. In the above plot, the pure polymer blend exhibits two absorption bands at 206 and 303 nm. The first peak observed at 206 nm is assigned to the  $n \rightarrow \pi^*$  transition formed due to the

**Table 1.** Peak positions and peak assignments of pure and Li–salt doped polymer blend composites.

Wavenumbers [cm <sup>-1</sup> ]		Peak assignments
PVA–CS	$\text{Li}_2\text{CO}_3$ (15 wt%)	
3290	3262	O–H stretching vibration
2923	2928	$-\text{CH}_2$ asymmetric stretching vibration
1647	–	Amide I and III groups of $\text{C}=\text{O}$ stretching vibrations
1557	Increase in intensity	N–H bending of $-\text{NH}_2$ group
1417	Increase in intensity	Carboxylic group
1375	1338	Wagging of $\text{CH}_2$ vibration
1254	Decrease in intensity	C–H vibrations
1022	Decrease in intensity	C–N stretching peak

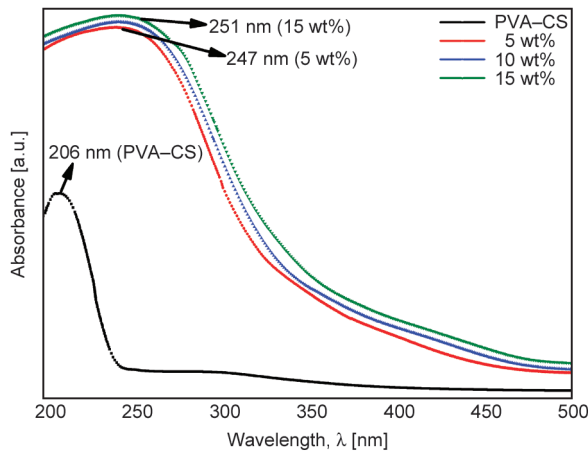


**Figure 2.** UV-Visible absorption spectra of pure and Li-salt doped blend composites.

unsaturated molecules within the polymer blend matrix. The second peak observed at 303 nm is assigned to  $\pi \rightarrow \pi^*$  transitions [5].

In blend composite films, the absorption bands and the band edges are shifted towards higher wavelengths with variant absorption intensities. Here the absorption band of the pure polymer blend observed at 206 nm suffered a slight shift towards a higher wavelength (red shift) that provides delocalization of charge carriers through polymer blend composite chains. The absorption band observed at 303 nm disappeared in the salt-doped blend composites. The shift and disappearance of the absorption band and enhancement in their intensities are attributed to the formation of localized occupied states in the band gap. These changes in peak position and intensities are due to inter/intra-molecular hydrogen bonding interactions between the functional groups of Li-salt and PVA-CS polymer blend and suggest the formation of charge transfer complexes (FTIR results). The observed modification in the absorption band and band edge also reflects the absorption of radiation is directly related to the number of absorbing molecules within the samples [17, 18]. These changes also affect the crystal structure of the blend, which will ultimately affect the band structure and optical energy band gap ( $E_g$ ).

The absorption of light by the optical medium is determined by its absorption coefficient ( $\alpha$ ), and is calculated using Equation (1):

$$\alpha = \frac{2.303A}{d} \quad (1)$$

where  $A$  is the absorbance and  $d$  is the thickness of pure and blend composite samples. It is well known

that the classical Tauc's assertion, which relates the absorption coefficient ( $\alpha$ ) and optical energy band gap ( $E_g$ ). Accordingly, the optical energy band gap ( $E_g$ ) is determined by converting the obtained UV-visible absorbance spectra into Tauc's plot by using a frequency-dependent absorption coefficient as represented by Mott and Devis equation [12] (Equation (2)):

$$\alpha(\nu) = \frac{\beta(h\nu - E_g)^r}{h\nu} \quad (2)$$

where  $\beta$  is a constant (band tail parameter) and exponent  $r$  is an empirical index that is equal to 2 for indirectly allowed transitions, and in a quantum mechanical sense, this is responsible for the optical absorption. Linear behaviour of the plotted graph of  $(\alpha h\nu)^{1/2}$  versus the photon energy ( $h\nu$ ) at room temperature signifies the indirectly allowed transitions. Further extrapolating the linear portion of the curve on photon energy ( $h\nu$ ) gives the optical energy band gap ( $E_g$ ) values (Figure 3a). Using this method  $E_g$  values for pure and doped blend composites are estimated, and the variation of  $E_g$  with dopant concentration is given in Figure 3b.

From the Figure 3b, it is observed that in blend composites, as the doping level increases, the  $E_g$  value decreases (*i.e.* from 4.82 to 2.85 eV). This decrease in  $E_g$  values is mainly due to the presence of complexes within the composite films, which arises due to the interaction of dopant with polymer and also due to the salt dissociation within the polymer blend.

Since the number of complexes within the blend composite increases with dopant concentration, it leads to a change in the microstructure of the PVA-CS polymer blend; as a result, a decrease in optical energy band gap ( $E_g$ ) is expected in blend composites. To understand the structural nature further, the optical activation energy of polymer blend composites is determined by using Urbach's energy ( $E_u$ ) Equation (3):

$$\alpha = \alpha_0 \exp\left(\frac{h\nu}{E_a}\right) \quad (3)$$

where  $\alpha_0$  is a constant and  $E_a$  is the activation energy (energy that causes a conduction mechanism within the system). The Urbach's rule conveys the exponential dependency of  $\alpha(\nu)$  on photon energy ( $h\nu$ ), also the Urbach's energy illustrates the disorder that occurred within the electrolyte system and is generally understood by the width of band tail of localized states in the forbidden gaps [18].

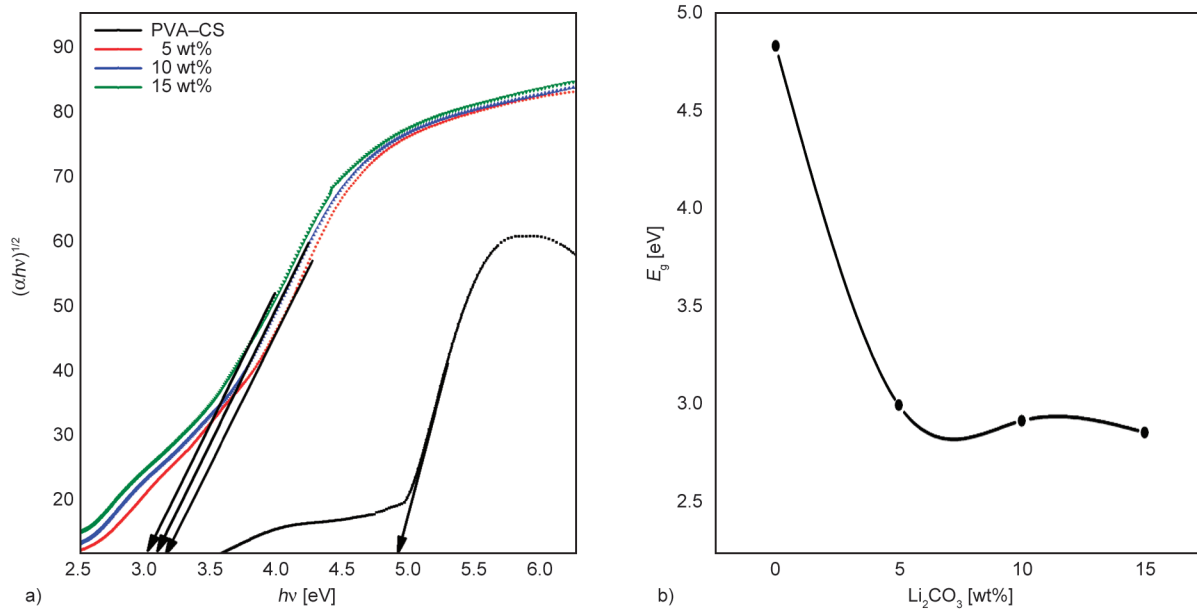


**Figure 3.** a) Variation of  $(\alpha h\nu)^{1/2}$  with  $h\nu$  (photon energy) for pure and doped PVA–CS blend composite films, b) optical energy band gap ( $E_g$ ) vs.  $\text{Li}_2\text{CO}_3$  doping concentrations.

The Urbach’s energy for pure blend composite is obtained by plotting the graph of the exponential of

$\alpha(\nu)$  versus photon energy (Figure 4a) and by a fitted curve of the linear region (Figure 4b). The estimated

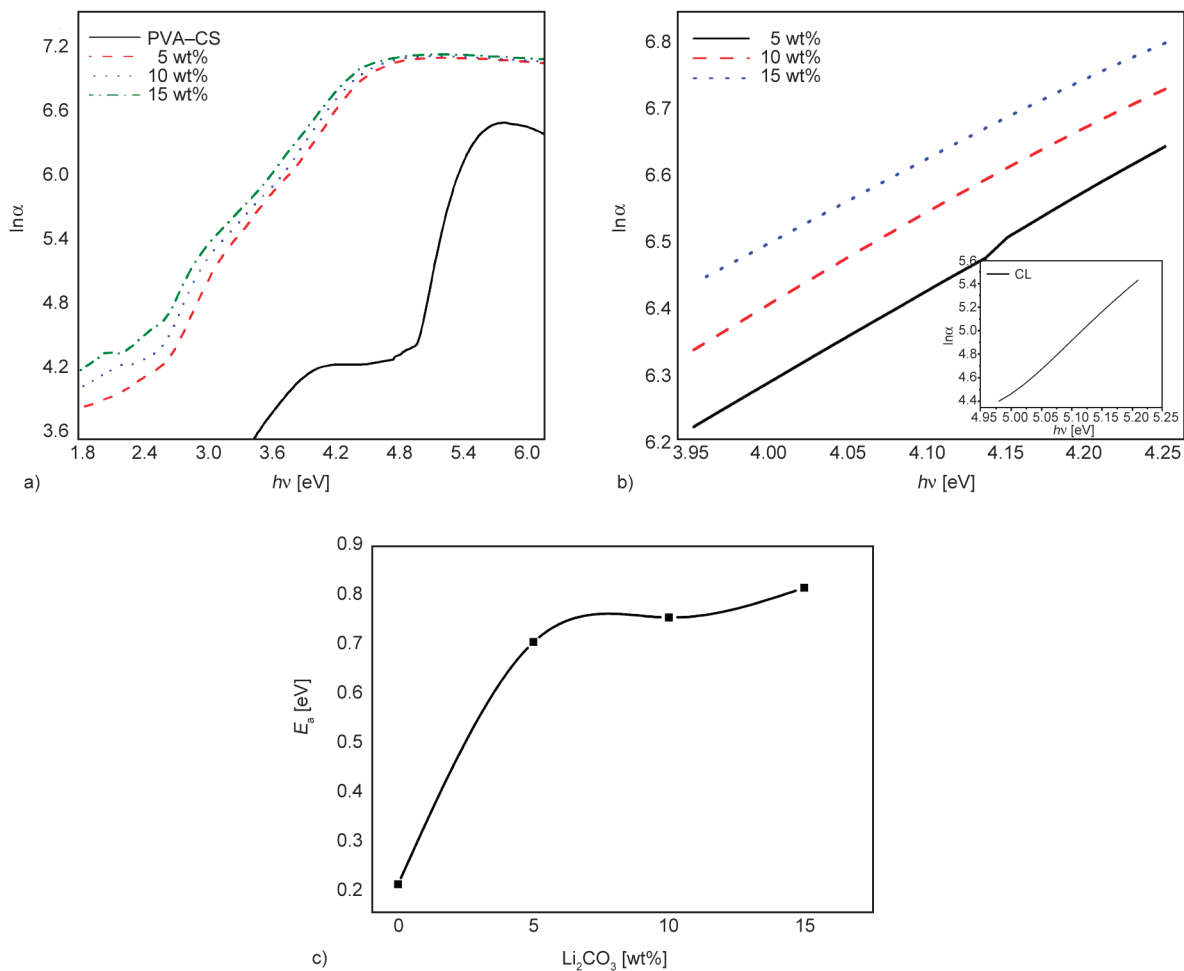


**Figure 4.** a) Variation of  $\ln\alpha$  with  $h\nu$  (photon energy), b) linear portion of  $\ln\alpha$  vs.  $h\nu$ , and c) activation energy ( $E_a$ ) vs.  $\text{Li}_2\text{CO}_3$  doping concentrations.

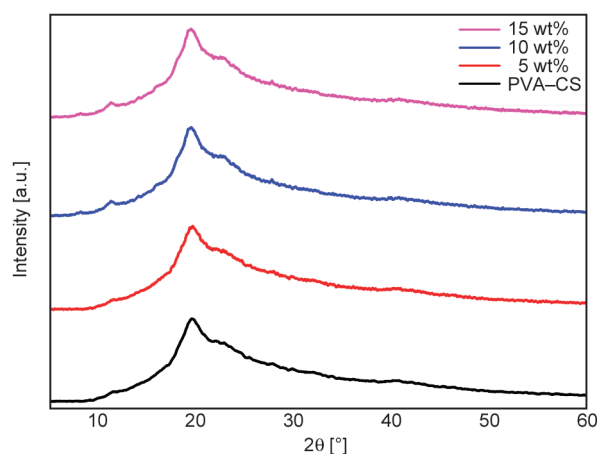
**Table 2.** UV–visible absorbance, optical energy band gap, and optical activation energy values of pure and salt–doped polymer blend composites.

Doping level, $M$ [wt%]	$\lambda_{\max 1}$ [nm]	$\lambda_{\max 2}$ [nm]	$\lambda_{\text{edge}1}$ [nm]	$\lambda_{\text{edge}2}$ [nm]	$E_g$ [eV]	$E_a$ [eV]
0	206	303	248	354	4.69	0.21
5	242	–	472	–	2.99	0.70
10	247	–	528	–	2.91	0.75
15	251	–	540	–	2.85	0.81

$E_a$  values for different dopant levels and their variations with salt concentrations are shown in Figure 4c and the same is tabulated in Table 2. From Figure 4c, it is observed that the  $E_a$  values increased with Li–salt doping concentration. Here, the ion mobility perception is responsible for the variation of Urbach’s energy values in the case of doped polymer blend composites. This dopant provides additional defect states and forms complexes within the polymer blend matrix; by increasing doping concentration increases the density of localized states, which creates more and more additional defects and extends the mobility gap. Hence, the increased defects and complex formation enhance the Urbach’s energy with an increase in salt concentration in the polymer matrix.

### 3.3. X–ray diffractometer studies (XRD)

The XRD instrument is a known tool to examine the crystal structure and yields appropriate information on the degree of crystallinity of the samples. The observed XRD pattern of pure and the salt-doped polymer blend composite are given in Figure 5, and the corresponding variations with salt concentration are in Table 3. From Figure 5, it is observed that, in the XRD pattern of pure PVA–CS polymer blend, a small

**Figure 5.** X–ray diffraction pattern of pure and Li–salt (5, 10, and 15 wt%) doped polymer blend composite.

peak is observed at  $11.52^\circ$  along with a broad peak spotted at  $19.62^\circ$ . Here the first peak centered at  $11.52^\circ$  is the corresponding characteristic peak of chitosan polymer, and another broad (highly intense) peak observed at  $19.62^\circ$  represents the semicrystalline nature of both PVA and chitosan polymers by comparing the diffraction peaks of pure and polymer blend composites in Figure 5. Figure 5 shows a modification and shifts in the characteristic peaks. For the Li–salt doped blend composites, it is observed that the intensity of the diffraction peak ( $2\theta = 11.52^\circ$ ) increases with salt concentration.

Besides this, the intensity of the peak observed at  $19.62^\circ$  for pure polymer blend increases with salt concentration along with a slight shift towards the lower  $2\theta$  value. This modification in peak position and a slight shift in its position suggests that salt dissociation in the polymer matrix, as well as structural modification, takes place in the blend composites. These structural modifications that take place within the doped blend composite mainly arise due to the hydrogen bonding interaction between PVA–CS and Li–salt (FTIR studies). These interactions lead to the complex formation within the blend matrix whose number increases with doping concentration, which leads to the change of microstructural (crystalline/amorphous) nature in blend composites [14, 19]. To understand these structural modifications in the blend composites with doping level further, the degree of crystallinity ( $X_c$ ) has been estimated for pure and doped blend composites using Hermans’ and Weidinger formula (Equation (4)), [7, 8]:

$$X_c = \frac{A_c}{A_c + A_a} \cdot 100 \quad [\%] \quad (4)$$

where  $A_c$  represents areas of sharp crystalline peaks,  $A_a$  is the area of amorphous halos. The observed variations with doping concentrations are given in Table 3. From the table, it is observed that the crystallinity increases with an increase in  $\text{Li}_2\text{CO}_3$  concentration in PVA–CS blend films; this is due to the formation of hydrogen bonding between  $\text{Li}_2\text{CO}_3$  and polymer blend. The increased crystalline phase in composites clearly shows the interaction between the dopant and the polymer blend; these results are consistent with FTIR results.

The average crystallite size of PVA–CS and PVA–CS– $\text{Li}_2\text{CO}_3$  composites is calculated using Scherer’s Equation (5):

**Table 3.** X-ray diffraction results of PVA–CS blend and PVA–CS–Li<sub>2</sub>CO<sub>3</sub> electrolytes.

Sample PVA–CS + Li <sub>2</sub> CO <sub>3</sub> [wt%]	2θ [°]	d-spacing [Å]	P [nm]	R <sub>s</sub> [Å]	Crystallinity, X <sub>c</sub> [%]
0	11.52	8.929	0.589	9.920	48
	19.62	6.278	0.591	7.847	
	40.45	5.151	0.593	6.439	
5	11.56	10.59	0.973	7.385	56
	19.60	6.742	0.918	4.984	
	40.50	4.077	1.234	3.941	
10	11.56	3.235	0.842	5.709	58
	19.57	4.453	0.689	4.837	
	40.50	3.117	0.661	3.896	
15	11.57	3.869	0.865	5.482	61
	19.50	3.955	0.647	4.944	
	40.56	2.140	0.654	3.918	

$$P = \frac{K\lambda}{\beta} \cos \theta \quad (5)$$

where  $K = 0.9$  is a constant, and it is related to the crystallite shape and miller indices of the reflecting crystallographic planes,  $\lambda$  – wavelength,  $\beta$  – FWHM (full width at half maximum) intensity of reflection in radians and  $\theta$  – Bragg's angle [20, 21].

The average inter-crystallite separation for pure and Li-salt doped polymer blend composites is calculated using equations in references [22–24], Equation (6):

$$R_s = \frac{5\lambda}{8 \sin \theta} \quad (6)$$

The estimated crystallite size and inter-crystallite separation are tabulated in Table 3; the calculated crystallite size values show that it is increased with salt concentration. The table shows that the average crystallite separation in composites increases with salt concentration. Hence from the XRD pattern, it is clear that the microstructure of the pure polymer blend is modified due to the addition of Li<sub>2</sub>CO<sub>3</sub>.

### 3.4. Scanning electron microscopy (SEM)

Scanning electron microscopy (SEM) is employed to determine the nature of dopant dispersion in the polymer matrix. The observed SEM images of the pure polymer blend and different Li<sub>2</sub>CO<sub>3</sub> concentrations (10 and 15 wt%) are presented in Figure 6. Figure 6a shows the smooth and homogenous surface attributed to the amorphous phase of the pure polymer blend, where the surface is clear, and there is no sign of any clusters on the surface of the polymer matrix. Figure 6b and Figure 6c shows the SEM images of Li-salt (10 and 15 wt%) doped polymer blend composites, here cluster formation on the

surface of the polymer matrix can be observed, and it increases with salt concentration which will be seen in Figure 6c [26].

This result indicates that the surface morphology of pure polymer blend is affected by the Li-salt doping and increases the surface roughness in doped polymer blend composites; this indicates the structural modification occurred due to salt doping (XRD results) [2, 22]. The increase in surface roughness with salt concentration is due to complexes formed through inter/intra-molecular interaction between functional groups of the polymer host and the dopant.

### 3.5. Thermogravimetric analysis (TGA)

The thermal property of pure and doped polymer composite films is studied using thermogravimetric analysis (TGA), where the mass loss percentage, phase transition, and decomposition temperature of pure and composite films are studied. Observed TGA graph of pure PVA–CS polymer blend and PVA–CS–Li<sub>2</sub>CO<sub>3</sub> (5, 10, and 15 wt%) composite films are shown in Figure 7, and the mass loss values for pure and salt-doped polymer blend composite for different temperatures are tabulated in Table 4. The TGA curves (Figure 7) of pure and Li-salt doped polymer blend composites exhibit three stages of weight loss from 60–500 °C. The first stage of small weight loss for PVA–CS polymer blend is in the range of 60 to 140 °C (mass loss percentage ≈ 15%) and is assigned to the elimination of moisture within the film. Here the water molecules are bonded mainly to the amine or hydroxyl groups present in the polymer blend, which will easily be detached in this temperature range.

The second stage of mass loss (rapid decrease in mass loss ≈ of 45%) is the degradation stage, which

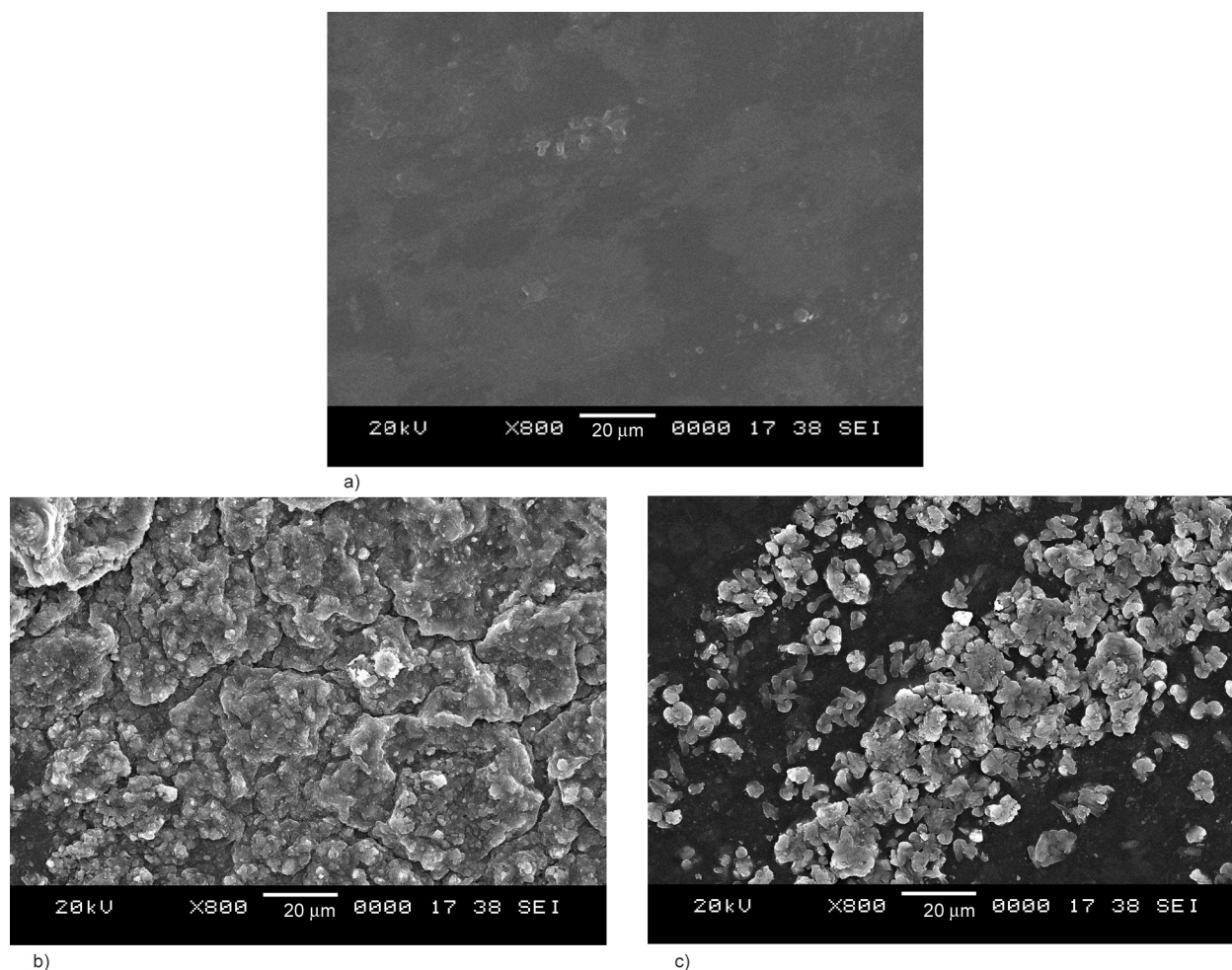


**Figure 6.** SEM images of a) PVA–CS polymer blend, b) PVA–CS–Li<sub>2</sub>CO<sub>3</sub> (10 wt%), and c) PVA–CS–Li<sub>2</sub>CO<sub>3</sub> (15 wt%).

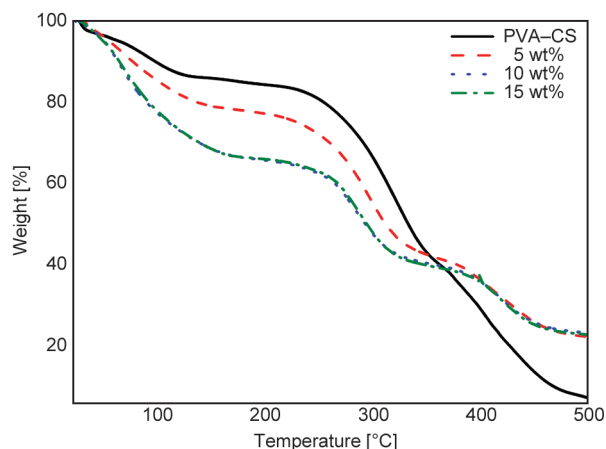


**Figure 7.** Thermogravimetric analysis of pure PVA–CS and PVA–CS–Li<sub>2</sub>CO<sub>3</sub> (5, 10 and 15 wt%) blend composites.

begins at 220 °C and ends at 350 °C, where the structural modification takes place due to the decomposition of the polymer backbone chain. These structural modifications affect the crystalline phase of the pure polymer blend (XRD results), and the final degradation stage is between 360–480 °C (mass loss ≈35%)

**Table 4.** The weight loss percentage in pure and Li–salt doped polymer blend composites.

Li <sub>2</sub> CO <sub>3</sub> [wt%]	Weight loss [%]					T <sub>0</sub> [°C]
	100 °C	200 °C	300 °C	400 °C	500 °C	
0	10.55	15.89	34.12	71.56	93.35	124
5	14.88	23.05	45.34	64.04	78.20	145
10	22.07	34.47	51.98	63.93	77.09	162
15	22.09	34.27	52.30	62.47	77.02	170

and is related to the decomposition of residues left within the pure blend [22, 23]. In blend composites, the first stage of mass loss (≈12%) is observed between 70–150 °C, which is due to the evaporation of moisture present in the composite films. The second stage (degradation) occurs between 260–390 °C (mass ≈25% for 15 wt%, Li<sub>2</sub>CO<sub>3</sub>), which is due to the chain scission of the polymer backbone and splitting of bonds between dopant and polymer backbone, and the final degradation stage occurs between 400–500 °C (mass loss ≈20%). Also, from the table, it is observed that the mass loss values of composite films decrease compared with the pure polymer blend film.

That is compared to the mass loss of pure blend, and in Li–salt (15 wt%) doped polymer blend composite, first stage mass loss decreases from 15 to 12%, for the second stage of mass loss varies from 40 to 25% and the final degradation stage decreased from 35% to 20%. These results show that the thermal stability of the polymer blend films increases with doping. This indicates the increase of thermal stability of the doped blend composite films due to the chemical degradation process via chain scission in the polymer backbone. Hence from the TGA graph, it is observed that the thermal stability of the PVA–CS polymer blend is increased after adding Li<sub>2</sub>CO<sub>3</sub> salt [24].

### 3.6. Impedance analysis studies

The impedance analysis is one of the familiar techniques used to study the charging and transport phenomenon in conducting and conjugated polymer composites. Figure 8a shows the observed Cole–Cole plot of the PVA–CS polymer blend and Li<sub>2</sub>CO<sub>3</sub> doped polymer blend electrolytes. The Cole–Cole plot of pure polymer blend and doped samples comprises a broad semi-circle or oblique region at the high-frequency window and a tail (linear region) at the low-frequency region. Here, the semi-circle corresponds to the bulk conductivity of the polymer electrolytes, and the linear region attributes to double-layer capacitance at the electrode/electrolyte interface. The semi-circle arises due to the parallel combination of bulk capacitance and bulk resistance of the electrolyte films [25, 26]. From the plot, it is observed that the semi-circle decreases with an increase in Li–salt concentration and the low-frequency linear region appeared as a spike which inclined at an angle less than 90° along the real axis. The variation in the plot indicates the decrease of resistance for charge

carriers in the electrolyte films, which is due to the ion migration through the free volume of the polymer electrolytes.

To understand the ionic conduction in the polymer electrolytes, the relaxation time ( $\tau$ ) of polymer blend electrolyte films is calculated using the relation (Equation (7)):

$$\tau = \frac{1}{\omega} \tag{7}$$

where  $\omega = 2\pi f_{\max}$ , here  $f_{\max}$  is relaxation frequency (maximum frequency of the imaginary part of impedance peak) displayed in Figure 8b. Here, no relaxation peaks are observed for the pure polymer blend. This is because the experiment was conducted in the frequency range 40 Hz–5 MHz, and the relaxation peaks of these samples lay below 40 Hz, which is due to the hindrance in mobile charge carriers within the matrix. For salt–doped polymer blend electrolytes, the relaxation peaks appear and shift towards a higher frequency region with an increase of dopant concentration up to 15 wt%. From Figure 9, one can clearly observe

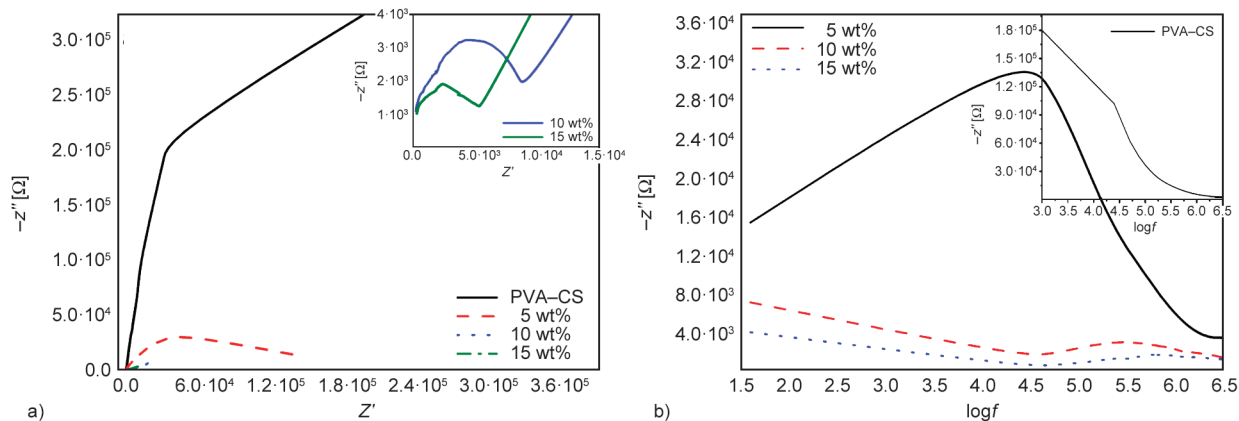


Figure 8. a) Cole–Cole plot, and b) imaginary part of impedance vs.  $\log f$ , of pure and Li–salt doped blend polymer electrolyte system.

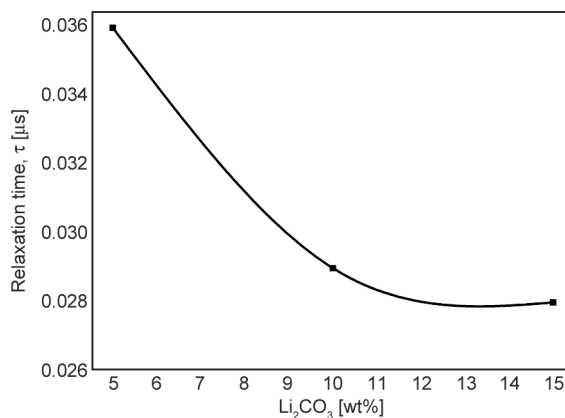
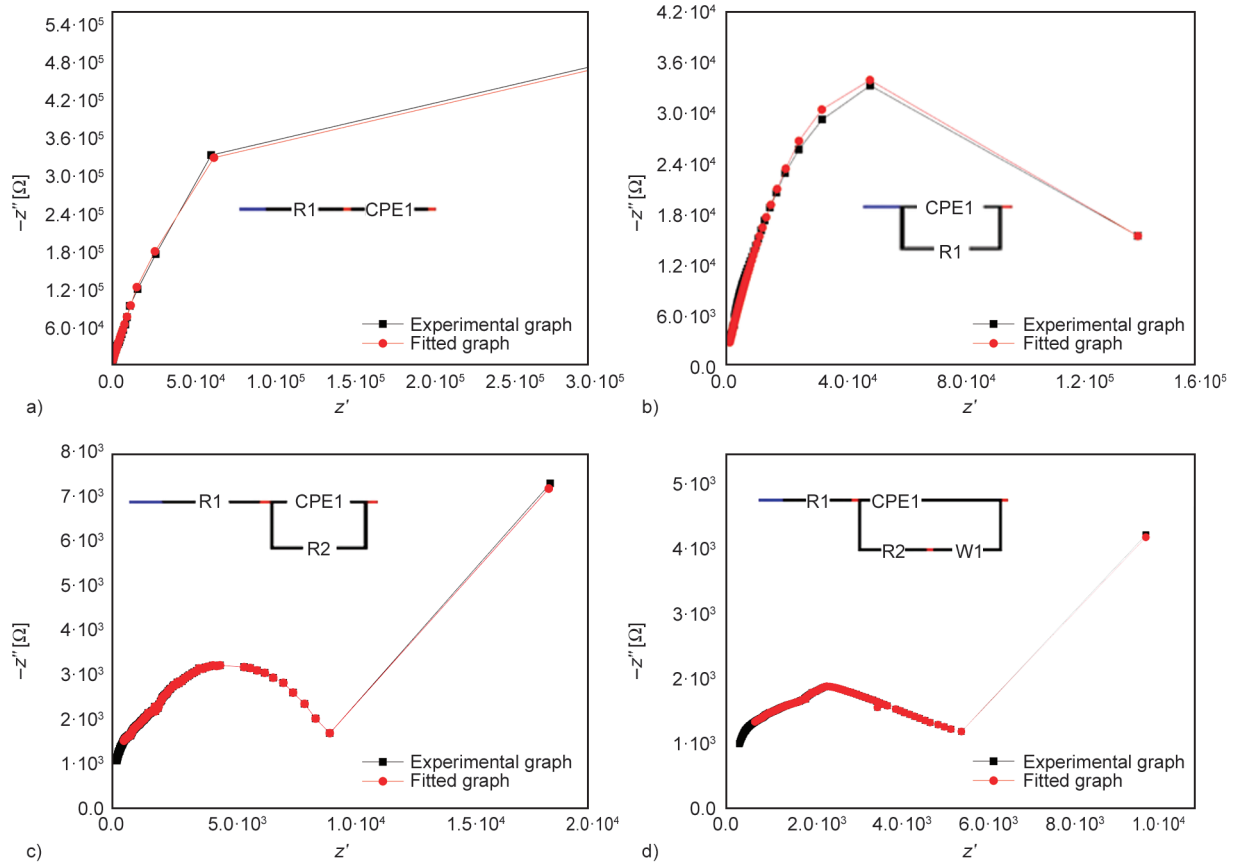


Figure 9. Variation of relaxation time of Li–salt doped PVA–CS polymer blend electrolyte.



**Figure 10.** Fitted graph of a) PVA–CS, b)  $\text{Li}_2\text{CO}_3$  (5 wt%), c)  $\text{Li}_2\text{CO}_3$  (10 wt%), and d)  $\text{Li}_2\text{CO}_3$  (15 wt%).

that the  $\tau$  value is decreased upon doping; as a result, surging of mobile charge carriers takes place within the electrolyte films. Hence such mobile charge carriers are responsible for the conduction mechanism within the doped polymer blend electrolytes [27].

Figure 10 shows the Cole–Cole plot of experimental data and equivalent circuit-fitted data using electrochemical impedance spectroscopy (EIS spectrum analyzer) for pure PVA–CS, and different concentrations of Li–salt (5, 10, and 15 wt%) doped polymer blend electrolytes. From Figure 10 it is observed that

the fitted impedance data is in good agreement with the experimental impedance data.

The Cole–Cole plot for a high–conducting polymer blend electrolyte ( $\text{Li}_2\text{CO}_3$ , 15 wt%) is studied for different temperatures (Figure 11a). From Figure 11 it is observed that there is a significant decrease in the size of the semi–circle with an increase in temperature. This shows the decrease in the resistive nature of the polymer blend electrolyte system. At higher temperatures, the semi-circle relatively disappeared; as a result, the ionic resistance of the polymer blend

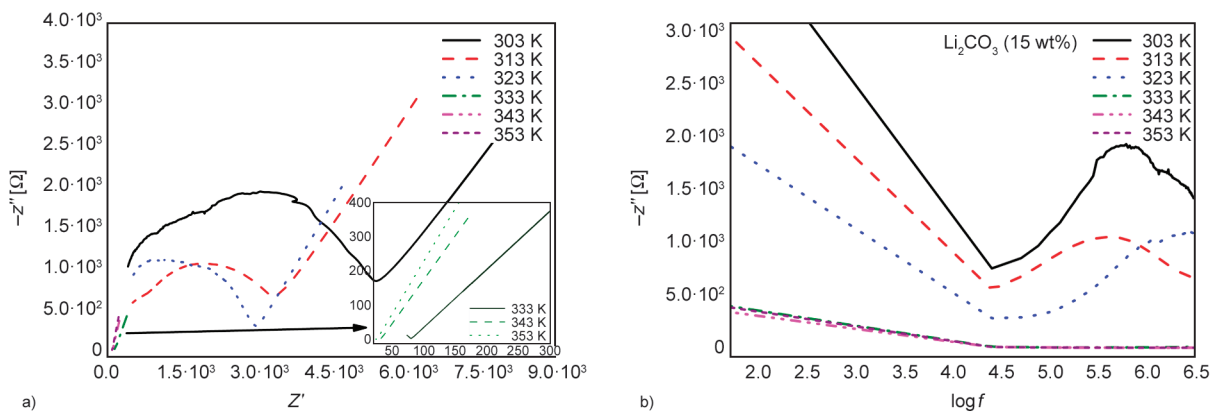


**Figure 11.** a) Cole–Cole plot, and b) imaginary part of impedance ( $Z''$ ) versus  $\log f$ , of Li–salt (15 wt%) doped PVA–CS blend electrolyte for different temperatures.

electrolyte system falls to a very small value at high temperatures. The decrease in resistance at high temperatures is related to the concept that, as temperature increases, the polymer backbone chain becomes more flexible, which promotes the segmental motion of polymer chain segments within the blend electrolyte system and increases the disassociation of salt within the polymer matrix [27, 28]. So that the ionic mobility increases with temperature, hence the enhancement of ionic conductivity in doped polymer blends.

The logical reason for the increase of conductivity in doped polymer blend electrolytes compared to a single polymer-based SPBE system is that the polymer blend electrolytes have more capacity for salt disassociation within the blend matrix. Since more disassociation of salt within the polymer blend matrix facilitates maximum ionic movement, hence conductivity enhances [22]. Figure 11b shows the relaxation peak of mobile charge carriers for different temperatures. The relaxation peaks are observed for

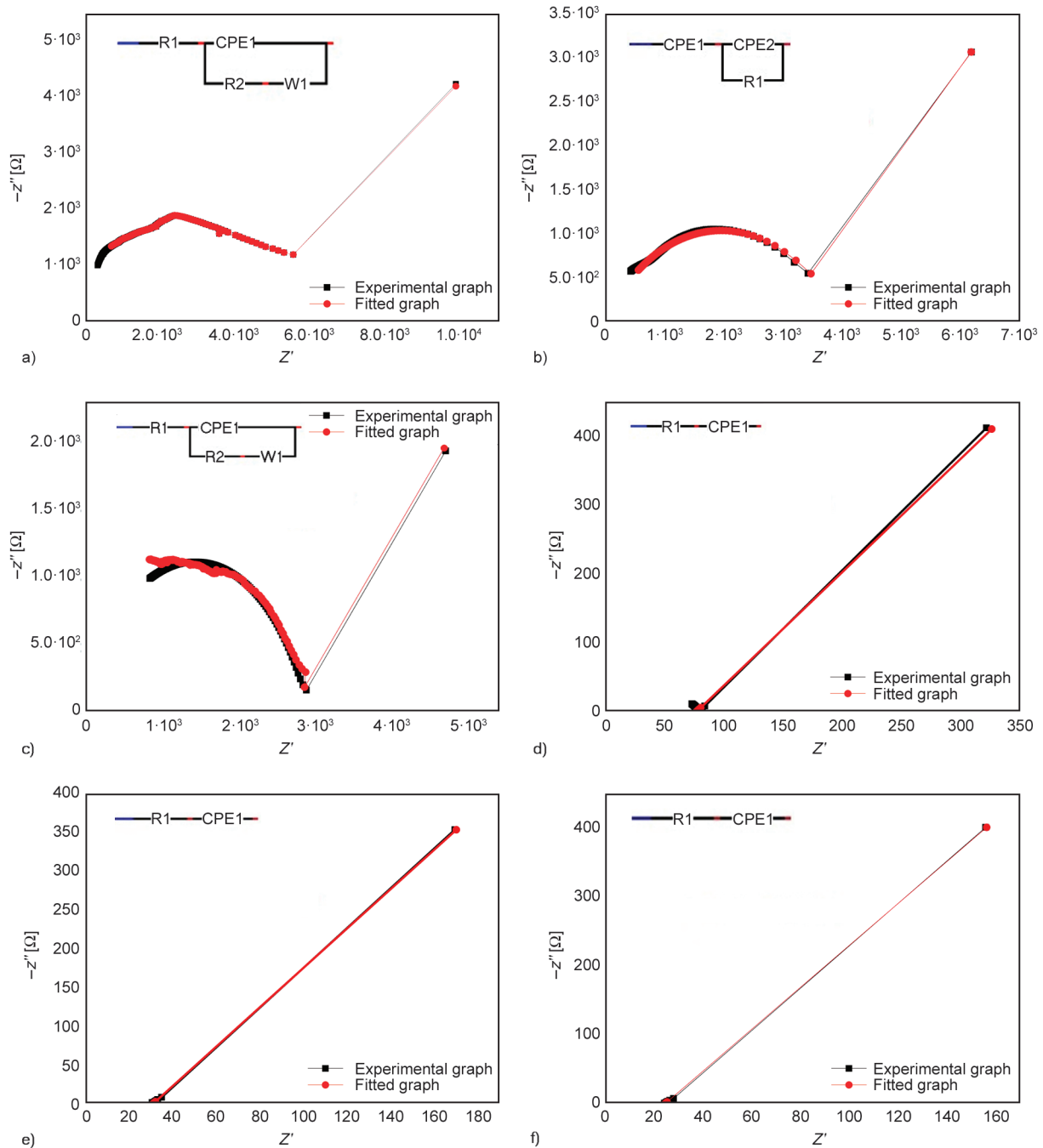
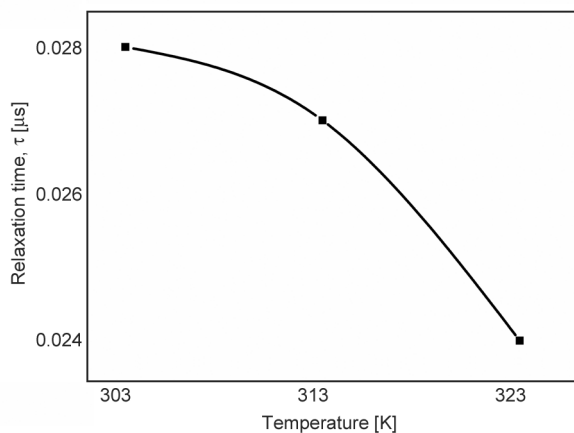


Figure 12. Fitted graph of  $\text{Li}_2\text{CO}_3$  (15 wt%) for different temperatures, a) 303 K, b) 313 K, c) 323 K, d) 333 K, e) 343 K, and f) 353 K.



**Figure 13.** Variation of relaxation time of Li-salt (15 wt%) doped PVA-CS polymer blend electrolyte for different temperatures.

high-conducting polymer blend electrolytes exhibiting enhancement in conductivity at different temperatures. Whereas at low temperatures, the relaxation peaks are appeared because of immobile charge carriers and for high temperatures, the relaxation peaks are observed due to the formation of defects caused by the temperature. Figure 12 exhibits the Cole-Cole plot of experimental and the equivalent circuit-fitted data using electrochemical impedance spectroscopy (EIS spectrum analyzer) of the high conducting ( $\text{Li}_2\text{CO}_3$ , 15 wt%) polymer blend electrolyte film for different temperatures. From the Figure 12 it is clearly observed that the fitted impedance data is in good agreement with the experimental impedance data of the prepared polymer electrolyte film. Figure 13 shows the variation of the relaxation time of ions with respect to temperature; here, it is observed that the  $\tau$  value decreased with an increase in temperature.

### 3.7. Electrical properties

The ionic conductivity in SPEs depends on the mobility and concentration of the charge carriers. By using the measured dielectric parameters, the ac-conductivity of the polymer blend and  $\text{Li}_2\text{CO}_3$  doped polymer electrolyte films are calculated using the Equation (8):

$$\sigma_{ac} = 2\pi f \epsilon_0 \epsilon_r \tan \delta \quad (8)$$

where  $f$  is the applied frequency,  $\epsilon_0$  the permittivity in free space,  $\epsilon_r$  the dielectric constant, and  $\tan \delta$  is the dielectric loss [18]. The frequency-dependent ionic conductivity of pure and  $\text{Li}_2\text{CO}_3$  doped polymer blend electrolytes are depicted in Figure 14.

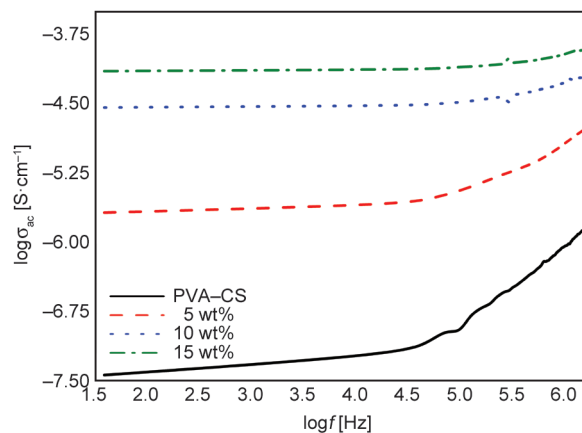


**Figure 14.** Variation of  $\log \sigma_{ac}$  with the frequency of PVA-CS and Li-salt doped polymer blend.

From Figure 14 it is observed that the conductivity of pure polymer blend is relatively low, and it enhances with an increase of frequency. The increase of conductivity is attributed to the fact that when an alternating field is applied across the electrodes, the flexibility of bonds increases, in turn, makes the polymer chains flexible. As a result, a significant increase in the mobility of ions within the electrolytes is expected, which leads to an increase in ionic conductivity and is apparently observed at higher frequency regions. From Figure 14 it is observed that two distinct regions are observed over the measured frequency range. One is the low-frequency plateau region that tends to approach dc-conductivity at zero frequency, and the other is the high-frequency dispersion region which is attributed to ac-conductivity [29]. The conductivity is relatively poor at the plateau region which is due to the electrode polarization; here, the mobility of ions is hindered because of the accumulation of mobile charge carriers at the electrode/electrolyte interface. Whereas as the frequency increases, the bonds present in the polymer blend matrix rotate along with the frequency, which facilitates the segmental motion of polymer chains. As a result of this, the ions are adequately energized to move from one conducting site to another, which leads to the enhancement of conductivity at higher frequency regions. The ionic conductivity also enhances with an increase of dopant concentration which is attributed to the fact that the interaction between functional groups of dopant and the polymer blend creates the void between the nearest localized states, resulting in the lowering of the potential barrier within them. As a result, more and more ionic transfer took place between these localized states [30],

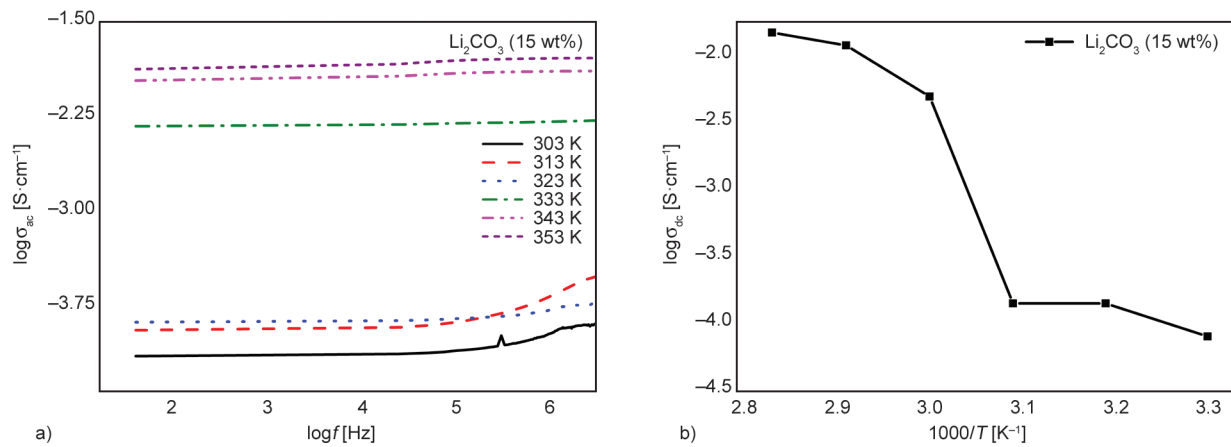


**Figure 15.** a)  $\log \sigma_{ac}$ -conductivity vs.  $\log f$ , b)  $\log \sigma_{dc}$  vs.  $1000/T$  of high conducting polymer blend electrolyte film (Li<sub>2</sub>CO<sub>3</sub>, 15 wt%) for different temperatures.

and hence the enhancement of ionic conductivity is observed in polymer blend electrolytes. The maximum ionic conductivity obtained is  $7.70 \cdot 10^{-5} \text{ S} \cdot \text{cm}^{-1}$  (15 wt%, Li<sub>2</sub>CO<sub>3</sub>).

The highest conducting polymer blend electrolyte is studied with different temperatures as a function of frequency, which is depicted in Figure 15a. The variation of ionic conductivity with frequency follows Jonscher’s universal power law (Equation (9)):

$$\sigma_{ac} = \sigma_{dc} + A\omega^s \quad (9)$$

where  $\sigma_{dc}$  is the DC conductivity is obtained by extrapolating the low-frequency region to the y-axis ( $\log \sigma_{ac}$ ),  $A$  is the pre-exponential factor, and  $s$  the frequency exponent factor ranging from 0 to 1. From Figure 15 it is observed that the conductivity increases with an increase in temperature as well as frequency. The increase in ionic conductivity with temperature is interpreted in terms of the hopping mechanism, polymer chain segmental motion, and local structural relaxation [22, 31]. As temperature increases, the complex sites within the electrolyte system increase, enabling ions to jump from one conducting site to another. Hence the conductivity increases with temperature, and the highest dc-conductivity is observed at 353 K, *i.e.*  $\sigma = 1.42 \cdot 10^{-2} \text{ S} \cdot \text{cm}^{-1}$ . Figure 15b shows the Arrhenius plot (dc-conductivity vs. temperature inverse) of Li<sub>2</sub>CO<sub>3</sub> (15 wt%) doped PVA–CS polymer blend electrolyte system. After 303 K, the observed sudden increase in conductivity is attributed to the transition of the polymer crystalline/semicrystalline phase to the amorphous phase upon doping [32]. As a result, ionic motion (an interchain hopping mechanism) takes place in the doped electrolyte

system; thus, the highest dc-conductivity is observed at 353 K.

### 3.8. Transport properties

The transference numbers corresponding to the ionic ( $t_{ion}$ ) and electronic ( $t_{ele}$ ) transport for Li<sub>2</sub>CO<sub>3</sub> (15 wt%) doped polymer blend electrolyte film has been investigated using Wagner’s polarization technique. According to the method, the highest conducting polymer blend electrolyte was sandwiched between two silver electrodes under the fixed dc-voltage of 1 V and the corresponding dc polarization current was measured as a function of time for the 15% Li<sub>2</sub>CO<sub>3</sub> doped PVA–CS polymer. Figure 16 shows the observed variation of polarization current with time. From this figure, it can be seen that the initial large current  $I_i$  is the contribution of both ions as well as electrons. Then as time proceeds, the current decreases and reaches a steady state after a few

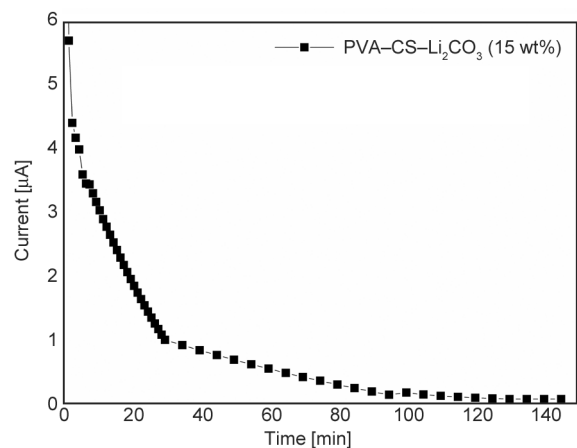


**Figure 16.** Variation of polarization current with time for Li<sub>2</sub>CO<sub>3</sub> doped PVA–CS polymer blends composite film.

minutes of polarization, and at the steady state, the current conduction is due to electrons alone  $I_f$ .

The ion transport number is said to be the ratio of any particle/ion transference number to total conductivity, and for electronic transference, the number is the ratio of electron/hole transference number to total conductivity. The corresponding ionic ( $t_+$ ) and electronic ( $t_-$ ) transference numbers are calculated using Equations (10) and (11):

$$t_+ = \frac{I_i - I_f}{I_i} \quad (10)$$

$$t_- = \frac{I_f}{I_i} \quad (11)$$

where  $I_i$  is the initial current and  $I_f$  is the final current. The observed total ion transference number in  $\text{Li}_2\text{CO}_3$  (15 wt%) doped polymer blend composite film is 0.95, and the ions transfer number is 0.05; this shows the ions play a major role in the conduction mechanism within the blend electrolyte, compared to electron's contribution for conduction. From the observed results, it is concluded that the ions are the majority charge carriers in  $\text{Li}_2\text{CO}_3$  doped polymer blend composite. Hence this kind of blend electrolyte film is suitable for the fabrication of energy storage device applications [32, 33].

### 3.9. Diffusion coefficient

To understand the ionic mobility, the total ionic mobility in the SPE system can be divided into cationic and anionic mobility. It is difficult to determine the exact mobility of charge carriers in the polymer electrolyte system because most of them are bounded to ion pairs. These can be estimated by using the following equations, the diffusion coefficient and mobility of ions in polymer electrolyte are calculated using (Equations (12) and (13)):

$$D = \frac{kT\sigma}{ne^2} \quad (12)$$

$$\mu = \frac{\sigma}{ne} \quad (13)$$

where  $k$  is the Boltzmann constant,  $T$  the temperature,  $\sigma$  the ionic conductivity,  $n$  is the number molecules present [ $\text{cm}^{-3}$ ], and  $e$  is the charge of an electron. The diffusion coefficients ( $D_+$  and  $D_-$ ), cationic ( $\mu_+$ ), and anionic ( $\mu_-$ ) mobility for PVA–CS+ $\text{Li}_2\text{CO}_3$  polymer electrolyte system is determined using equations described in the literature [34] and are listed in Table 5. From Table 5, it is observed that the cationic mobility and diffusion coefficients are high compared to that of anions. From these results, it affirms that the ionic conductivity is strongly influenced by cationic motion and the diffusion coefficient of cations within the electrolyte system [32, 35]. Hence the ionic conduction in  $\text{Li}_2\text{CO}_3$  doped polymer blend electrolyte is mainly due to cations. The increase in mobile charge carriers within the electrolyte films causes increases in the ionic conductivity of the electrolyte films.

### 4. Conclusions

In this study, the pure and Li–salt doped polymer blend composites are prepared by the solution cast method. From FTIR studies, the inter/intra-molecular interaction between  $\text{Li}_2\text{CO}_3$  and PVA–CS takes place due to the collegial effect of hydrogen bonds in polymer blend and  $\text{Li}_2\text{CO}_3$ , and forms charge transfer complexes within the electrolyte films. XRD studies confirm the structural modifications that take place after doping  $\text{Li}_2\text{CO}_3$ , and it is clearly shown that the crystallinity in composites is gradually increased compared to a pristine polymer blend. The SEM images shows the formation of clusters at higher  $\text{Li}_2\text{CO}_3$  (10 and 15 wt%) concentrations, which increases the surface roughness of the blend. In TGA studies, the increase in mass loss percentage with temperature confirms the increased thermal stability of the PVA–CS polymer blend due to doping. From the impedance analysis, it is confirmed that the mobility of charge carriers increases, and the relaxation time of mobile charge carriers decreases with  $\text{Li}_2\text{CO}_3$  concentration. The ac–conductivity study revealed that the conductivity of the blend increases with the doping level; the highest conductivity is achieved for 15 wt% of  $\text{Li}_2\text{CO}_3$  concentration. The

**Table 5.** Transference number, ionic mobility, and diffusion coefficient of 15 wt%  $\text{Li}_2\text{CO}_3$  doped PVA–CS polymer electrolyte.

Weight ratio	$t_+$	$t_-$	$\mu_+$ [ $\text{cm}^2 \cdot \text{V}^{-1} \cdot \text{s}^{-1}$ ]	$\mu_-$ [ $\text{cm}^2 \cdot \text{V}^{-1} \cdot \text{s}^{-1}$ ]	$D_+$ [ $\text{cm}^2 \cdot \text{s}^{-1}$ ]	$D_-$ [ $\text{cm}^2 \cdot \text{s}^{-1}$ ]
$\text{Li}_2\text{CO}_3$ (15 wt%)	0.96	0.04	$7.164 \cdot 10^{-7}$	$0.253 \cdot 10^{-7}$	$1.426 \cdot 10^{-9}$	$0.023 \cdot 10^{-9}$

transport properties reveal that the ionic transference number is more than the electronic transference number within the blended composite.

### Acknowledgements

The authors are thankful to PURSE laboratory, Microtron center, and University Science Instrumentation Center (USIC), Mangalore University for providing UV–Visible spectroscopy, Fourier transforms infrared spectroscopy (FTIR), Thermo gravimetric analysis (TGA), and scanning electron microscopy (SEM), and impedance analyzer. The authors are also thankful to the innovation center MIT, Manipal for providing an X-ray diffractometer (XRD).

### References

- [1] Zheng H., Du Y., Yu J., Huang R., Zhang L.: Preparation and characterization of chitosan/poly(vinyl alcohol) blend fibers. *Journal of Applied Polymer Science*, **80**, 2558–2565 (2001).  
<https://doi.org/10.1002/app.1365>
- [2] Salman Y. A. K., Abdullah O. Gh., Hanna R. R., Aziz S. B.: Conductivity and electrical properties of chitosan – methylcellulose blend biopolymer electrolyte incorporated with lithium tetrafluoroborate. *International Journal of Electrochemical Science*, **13**, 3185–3199 (2018).  
<https://doi.org/10.20964/2018.04.25>
- [3] Shukur M. F., Ithnin R., Illias H. A., Kadir M. F. Z.: Proton conducting polymer electrolyte based on plasticized chitosan–PEO blend and application in electrochemical devices. *Optical Materials*, **35**, 1834–1841 (2013).  
<https://doi.org/10.1016/j.optmat.2013.03.004>
- [4] de Souza Costa–Junior E., Pereira M. M., Mansur H. S.: Properties and biocompatibility of chitosan films modified by blending with PVA and chemically cross-linked. *Journal of Materials Science: Materials in Medicine*, **20**, 553–561 (2009).  
<https://doi.org/10.1007/s10856-008-3627-7>
- [5] Yusof Y. M., Illias H. A., Kadir M. F. Z.: Incorporation of NH<sub>4</sub>Br in PVA–chitosan blend–based polymer electrolyte and its effect on the conductivity and other electrical properties. *Ionics*, **20**, 1235–1245 (2014).  
<https://doi.org/10.1007/s11581-014-1096-1>
- [6] Islam A., Imran Z., Yasin T., Gull N., Khan S. M., Shafiq M., Sabir A., Munawar M. A., Raza M. H., Jamil T.: An investigation of AC impedance and dielectric spectroscopic properties of conducting chitosan–silane cross-linked–poly (vinyl alcohol) blended films. *Materials Research*, **18**, 1256–1263 (2015).  
<https://doi.org/10.1590/1516-1439.043715>
- [7] Bhajantri R. F., Ravindrachary V., Poojary B., Ismayil., Harisha A., Crasta V.: Studies on fluorescent PVA + PVP + MPDMAPP composite films. *Polymer Engineering and Science*, **49**, 903–909 (2009).  
<https://doi.org/10.1002/pen.21341>
- [8] Sagar R. N., Ravindrachary V., Guruswamy B., Hegde S., Mahanthesh B. K., Ku-mari R. P.: Effect of TiO<sub>2</sub> nanoparticles doping on structural and electrical properties of PVA: NaBr polymer electrolyte. *AIP Conference Proceedings*, **1953**, 030216 (2018).  
<https://doi.org/10.1063/1.5032551>
- [9] Xu G., Xu G., Shi T.: Grafting of chitosan Schiff base on graphene oxide and its characterization. *Fullerenes, Nanotubes and Carbon Nanostructures*, **24**, 749–756 (2016).  
<https://doi.org/10.1080/1536383X.2016.1226285>
- [10] Buraidah M. H., Teo L. P., Majid S. R., Arof A. K.: Ionic conductivity by correlated barrier hopping in NH<sub>4</sub>I doped chitosan solid electrolyte. *Physica B*, **404**, 1373–1379 (2009).  
<https://doi.org/10.1016/j.physb.2008.12.027>
- [11] Khiar A. S. A., Puteh R., Arof A. K.: Characterizations of chitosan-ammonium triflate (NH<sub>4</sub>CF<sub>3</sub>SO<sub>3</sub>) complexes by FTIR and impedance spectroscopy. *Physica Status Solidi*, **203**, 534–543 (2006).  
<https://doi.org/10.1002/pssa.200521016>
- [12] Ismayil., Ravindrachry V., Bhajantri R. F., Praveena S. D., Poojari B., Dutta D., Pujari P. K.: Optical and microstructural studies on electron irradiated PMMA: A positron annihilation study. *Polymer Degradation and Stability*, **95**, 1083–1091 (2010).  
<https://doi.org/10.1016/j.polymdegradstab.2010.02.031>
- [13] Thripathi S., Mehrotra G. K., Dutta P. K.: Preparation and physicochemical evaluation of chitosan/poly(vinyl alcohol)/pectin ternary film for food-packaging applications. *Carbohydrate Polymers*, **79**, 711–716 (2010).  
<https://doi.org/10.1016/j.carbpol.2009.09.029>
- [14] Aziz S. B., Abdullah R. M., Rasheed M. A., Ahmed H. M.: Role of ion dissociation on DC conductivity and silver nanoparticle formation in PVA:AgNt based polymer electrolytes: Deep insights to ion transport mechanism. *Polymers*, **9**, 338 (2017).  
<https://doi.org/10.3390/polym9080338>
- [15] Al-Gunaid M. Q. A., Saeed A. M. N., Subramani N. K., Madhukar B. S., Siddaramaiah: Optical parameters, electrical permittivity and *I–V* characteristics of PVA/Cs<sub>2</sub>CuO<sub>2</sub> nanocomposite films for opto-electronic applications. *Journal of Materials Science: Materials in Electronics*, **28**, 8074–8086 (2017).  
<https://doi.org/10.1007/s10854-017-6513-6>
- [16] Han D., Yan L., Chen W., Li W.: Preparation of chitosan/graphene oxide composite film with enhanced mechanical strength in the wet state. *Carbohydrate Polymers*, **83**, 653–658 (2011).  
<https://doi.org/10.1016/j.carbpol.2010.08.038>
- [17] Ali H., Tiama T. M., Ismail A. M.: New and efficient NiO/chitosan/polyvinyl alcohol nanocomposites as antibacterial and dye adsorptive films. *International Journal of Biological Macromolecules*, **186**, 278–288 (2021).  
<https://doi.org/10.1016/j.ijbiomac.2021.07.055>

- [18] Hegde S., Ravindrachary V., Praveena S. D., Guruswamy B., Sagar R. N.: Optical and dielectric properties of Li<sup>+</sup> ion conducting solid polymer electrolyte. *Indian Journal of Advances in Chemical Science*, **6**, 83–87 (2018).  
<https://doi.org/10.22607/IJACS.2018.602004>
- [19] Aziz S. B., Hamsan M. H., Nofal M. M., Karim W. O., Brevik I., Brza M. A., Abdulwahid R. T., Al-Zangana S., Kadir M. F. Z.: Structural, impedance and electrochemical characteristics of electrical double layer capacitor devices based on chitosan: Dextran biopolymer blend electrolytes. *Polymers*, **12**, 1411 (2020).  
<https://doi.org/10.3390/polym12061411>
- [20] Praveena S. D., Ravindrachary V., Bhajantri R. F., Ismayil: Dopant-induced microstructural, optical, and electrical properties of TiO<sub>2</sub>/PVA composite. *Polymer Composites*, **37**, 987–997 (2016).  
<https://doi.org/10.1002/pc.23258>
- [21] Yahia I. S., Mohammed M. I., Nawar A. M.: Multifunction applications of TiO<sub>2</sub>/poly(vinyl alcohol) nanocomposites for laser attenuation applications. *Physica B: Condensed Matter*, **556**, 48–60 (2019).  
<https://doi.org/10.1016/j.physb.2018.12.031>
- [22] Hegde S., Ravindrachary V., Praveena S. D., Ismayil, Guruswamy B., Sagar R. N.: Microstructural, dielectric, and transport properties of proton-conducting solid polymer electrolyte for battery applications. *Ionics*, **26**, 2379–2394 (2020).  
<https://doi.org/10.1007/s11581-019-03383-w>
- [23] Yang J.-M., Wang S.-A.: Preparation of graphene-based poly(vinyl alcohol)/chitosan nanocomposites membrane for alkaline solid electrolytes membrane. *Journal of Membrane Science*, **477**, 49–57 (2015).  
<https://doi.org/10.1016/j.memsci.2014.12.028>
- [24] Abdelaziz M.: Cerium (III) doping effects on optical and thermal properties of PVA films. *Physica B: Condensed Matter*, **406**, 1300–1307 (2011).  
<https://doi.org/10.1016/j.physb.2011.01.021>
- [25] Kathayat K., Panigrahi A., Pandey A., Kar S.: Characterization of electrical behavior of Ba<sub>5</sub>HoTi<sub>3</sub>V<sub>7</sub>O<sub>30</sub> ceramic using impedance analysis. *Materials Sciences and Applications*, **3**, 390–397 (2012).  
<https://doi.org/10.4236/msa.2012.36056>
- [26] Al-Gunaid M. Q. A., Saeed A. M. N., Siddaramaiah: Effects of the electrolyte content on the electrical permittivity, thermal stability, and optical dispersion of poly(vinyl alcohol)–cesium copper oxide–lithium perchlorate nanocomposite solid-polymer electrolytes. *Journal of Applied Polymer Science*, **135**, 45852 (2017).  
<https://doi.org/10.1002/app.45852>
- [27] Shukur M. F., Ithin R., Kadir M. F. Z.: Electrical properties of proton conducting solid biopolymer electrolytes based on starch–chitosan blend. *Ionics*, **20**, 977–999 (2014).  
<https://doi.org/10.1007/s11581-013-1033-8>
- [28] Prajapati G. K., Roshan R., Gupta P. N.: Effect of plasticizer on ionic transport and dielectric properties of PVA–H<sub>3</sub>PO<sub>4</sub> proton conducting polymeric electrolytes. *Journal of Physics and Chemistry of Solids*, **71**, 1717–1723 (2010).  
<https://doi.org/10.1016/j.jpics.2010.08.023>
- [29] Dhayal V., Hashmi S. Z., Kumar U., Choudhary B. L., Kuznetsov A. E., Dalela S., Kumar S., Kaya S., Dolia S. N., Alvi P. A.: Spectroscopic studies, molecular structure optimization and investigation of structural and electrical properties of novel and biodegradable chitosan–GO polymer nanocomposites. *Journal of Material Science*, **55**, 14829–14847 (2020).  
<https://doi.org/10.1007/s10853-020-05093-5>
- [30] Mahendia S., Goyal P. K., Tomar A. K., Chahal R. P., Kumar S.: Study of dielectric behavior and charge conduction mechanism of poly(vinyl alcohol) (PVA)-copper (Cu) and gold (Au) nanocomposites as a bio-resorbable material for organic electronics. *Journal of Electronic Materials*, **45**, 5418–5426 (2016).  
<https://doi.org/10.1007/s11664-016-4677-0>
- [31] Aziz S. B., Abdullah O. Gh., Hussein S. A., Ahmed H. M.: Effect of PVA blending on structural and ion transport properties of CS:AgNt-based polymer electrolyte membrane. *Polymers*, **9**, 622 (2017).  
<https://doi.org/10.3390/polym9110622>
- [32] Sagar R. N., Ravindrachary V., Hegde S., Guruswamy B.: Transport and diffusion properties in PEO–BaCl<sub>2</sub> polymer electrolytes for battery applications. *IOP Conference Series: Journal of Physics*, **1172**, 012078 (2019).  
<https://doi.org/10.1088/1742-6596/1172/1/012078>
- [33] Shukur M. F., Kadir M. F. Z.: Hydrogen ion conducting starch–chitosan blend based electrolyte for application in electrochemical devices. *Electrochimica Acta*, **158**, 152–165 (2015).  
<https://doi.org/10.1016/j.electacta.2015.01.167>
- [34] Francis K. M. G., Subramanian S., Shunmugavel K., Naranappa V., Pandian S. S. M., Nadar S. C.: Lithium ion–conducting blend polymer electrolyte based on PVA–PAN doped with lithium nitrate. *Polymer–Plastics Technology and Engineering*, **55**, 25–35 (2016).  
<https://doi.org/10.1080/03602559.2015.1050523>
- [35] Leena Chandra M. V., Karthikeyan S., Selvasekarapandian S., Vinoth Pandi D., Monisha S., Arulmozhi Packiaseeli S.: Characterization of high ionic conducting PVAc–PMMA blend–based polymer electrolyte for electrochemical applications. *Ionics*, **22**, 2409–2420 (2016).  
<https://doi.org/10.1007/s11581-016-1763-5>

Research article

# Spent coffee grounds utilization for green ultraviolet filter and nanocomposite fabrication

Ha Ngoc Giang<sup>1\*</sup>, Chanh Cong Tran<sup>2</sup>, Tuan Nguyen Anh Huynh<sup>2</sup>, Phuong Thi Minh Doan<sup>1</sup>

<sup>1</sup>Faculty of Chemical Technology, Ho Chi Minh City University of Industry and Trade, 140 Le Trong Tan Street, Tay Thanh Ward, Tan Phu District, Ho Chi Minh City, Viet Nam

<sup>2</sup>Faculty of Chemical and Food Technology, Ho Chi Minh City University of Technology and Education, 1 Vo Van Ngan Street, Linh Chieu Ward, Thu Duc City, Ho Chi Minh City, Viet Nam

Received 3 March 2023; accepted in revised form 12 May 2023

**Abstract.** Spent coffee grounds (SCGs), the main by-product in the coffee industry, were proposed as a starting material to fabricate both ultraviolet (UV) shielding material and nanocomposite based on polyvinyl alcohol (PVA). The extract using low SCGs concentration (0.25 wt%) contains a significant amount of UV-absorbing substances. The UV shielding film from 5 wt% PVA solution and SCGs extract (1 g SCGs/200 ml water) could shield most of the radiation in UV-B and UV-C regions and maintain 63% transmittance at 550 nm. The SCGs after washing were ball milled and the ultrasonic liquid processor was applied to synthesize SCGs nanoparticle. The effects of ultrasonic amplitude and hexadecyltrimethylammonium bromide (CTAB) on the particle's hydrodynamic diameter were investigated. The particle's size of 148 nm was obtained with 50% ultrasonic amplitude. Fourier-transformed infrared spectroscopy (FTIR) results confirmed the presence of hydroxyl groups (–OH) on the SCGs-based nanoparticle's surface. The tensile strength of PVA-SCGs nanocomposite was significantly improved. However, the presence of CTAB in the nano solution could not show a better tensile result. The organic compounds contained in the SCGs extract and even in the nano SCGs solution could enhance thermal oxidation stability for both UV shielding films and nanocomposites.

**Keywords:** *nanomaterials, polymer composites, reinforcements, spent coffee grounds, UV filter*

## 1. Introduction

Coffee has become one of the most popular beverages in many countries and massive waste including spent coffee grounds (SCGs) has been generated by the industry [1, 2]. Because of their low economic value, SCGs are often discarded as waste and it might affect human health and the environment [3]. The SCGs composition is highly varied because of different brewing methods and types of coffee. The main SCGs' components include carbohydrates, lignin, lipids, and protein [4–6]. Even after brewing, many bioactive phenolic compounds were found in SCGs [7–9]. These findings have made the popular waste material from the coffee industry become a

potential source of natural antioxidant compounds. In a recent study, many products from SCGs could be utilized by extracting in water and hydrothermal liquefaction [10]. Many substances including polyphenol, polysaccharide, ketone, acid, ester *etc.* could be detected. Therefore, SCGs were considered as a bioresource that can be utilized for many applications. With high nutrient content, SCGs have been applied as a bio-fertilizer in agriculture [11, 12]. Properties of caffeine and other components from coffee could be applied in sunscreens [13–15] or solar cells [16]. Polyvinyl alcohol (PVA), a water-soluble polymer, was widely used in many applications because of its biocompatibility [17, 18]. Therefore, a

\*Corresponding author, e-mail: [hagn@hufi.edu.vn](mailto:hagn@hufi.edu.vn)

© BME-PT

combination of PVA and UV-absorbing substances in instant coffee had been proposed to form an environmentally friendly material that could shield lights in the UV region [19]. The fabricated films showed good transparency and thermal stability. The components of caffeine, chlorogenic acid, and melanoidin were assigned for the high performance of the PVA-based UV shielding films.

On the other hand, approximately 50 wt% of the SCGs were cellulose and hemicellulose [5]. Therefore, with the high demand for bio-degradable composite, many studies attempted to recycle SCGs as a bio-filler in plastic [20–22]. In the study by Catado *et al.* [23], the properties of pectin filled with SCGs were investigated to apply as food packaging materials. Although the hydrophobization and the reduction of water uptake were achieved, the mechanical properties were reduced with the addition of SCGs. SCGs also contain a significant amount of oil (more than 15%) [24, 25]. The oil extracted from SCGs could be utilized for bio-diesel production [26]. From another viewpoint, oil remaining in SCGs might affect the mechanical properties of the composite. SCGs after oil extraction could improve the mechanical and thermal properties of the formed composites [27, 28]. Leow *et al.* [29] also reported the enhancement in Young's modulus of epoxy resin by adding SCGs or oil-extracted SCGs. However, the tensile strength was significantly decreased because of poor interfacial compatibility between the hydrophilic SCGs-based fillers and the hydrophobic epoxy matrix. Although SCGs have been utilized as green fillers in many studies, less research reported nanomaterial from SCGs. In the nanotechnology field, the use of SCGs as a reducing agent to prepare silver or gold nanoparticles has been investigated [30–32]. In another study, lipid was removed from roasted coffee beans using *n*-hexane, and the components that remained in the solid residue were utilized to synthesize cellulose nanofibers (CNF) [33]. The coffee beans based-CNF was then applied to fabricate composites with PVA. Although the interaction of CNF and PVA had been discussed, the mechanical property of the composite was not reported. In other approaches, carbon dots could be synthesized from coffee bean shells [34] or SCGs [35]. Lee *et al.* [36] reported particles prepared directly from SCGs with the ability to improve the tensile strength of PVA-based composite. There was no oil-extraction step needed and the popular ball mill technique was

applied to reduce the size of SCGs particles. However, the rather large average size of 240 nm and broad size distribution was obtained.

To the best of our knowledge, there is no report of the ability to fabricate stable SCGs nanoparticles under ultrasonic irradiation. Besides, the preparation of the SCGs particles included the washing steps to remove the water-soluble substances which might be still valuable in many cases. A simple approach and methodology to further utilize all SCGs components are still developing. In this study, green nanoparticles and nanocomposites based on SCGs formed with the assistance of an ultrasonic liquid processor shall be presented. Instead of instant coffee, the ability to reuse the extract from SCGs that were discarded during the washing step in the previous article [36] as green UV filters shall be confirmed and discussed.

## 2. Experimental section

### 2.1. Materials

PVA (hydrolysis degree: 85-90%, viscosity: 20.5–24.5 mPa·s) was purchased from Shanghai Aladdin Bio-Chem Technology Co. Ltd (China). Hexadecyltrimethylammonium bromide (CTAB) ( $\geq 98\%$ ) was the product of Sigma-Aldrich (Merck, USA). SCGs were collected from a local coffee shop. The caffeine standard was obtained from the Institute of Drug Quality Control – Ho Chi Minh City (IDQC-HCMC) (Viet Nam). The chlorogenic acid standard was supplied by Acros Organics (Thermo Scientific, United Kingdom).

### 2.2. Methods

The fabrication methods were summarized in Figure 1 which includes the preparation of UV shielding films and PVA-based nanocomposites.

#### *Preparation of UV shielding films*

The collected SCGs were washed with cold distilled water to remove dust and impurity. The product was dried in the oven (80 °C) for 24 h. The dried SCGs were weighed ( $x$  [g] from 0.1 to 30 g) and put into an Erlenmeyer flask containing 200 ml of double distilled water. The mixture was boiled and stirred for 10 min. Then, the obtained mixture was filtered, and the solution was placed into centrifuge tubes. The centrifugation at 5000 rpm for 10 min was applied. The aqueous SCGs extract was collected and directly used for the next step. PVA powder was weighed and added to the extract. For the UV shielding film fabrication,

R1  
R2  
R3  
R4  
R5  
R6  
R7  
R8  
R9  
R10  
R11  
R12  
R13  
R14  
R15  
R16  
R17  
  
R18  
R19  
R20  
R21  
R22  
R23  
R24  
R25  
R26  
R27  
R28  
R29  
R30  
  
R31  
R32  
R33  
R34  
  
R35  
R36  
R37  
R38  
R39  
R40  
R41  
R42  
R43  
R44  
R45  
R46  
R47

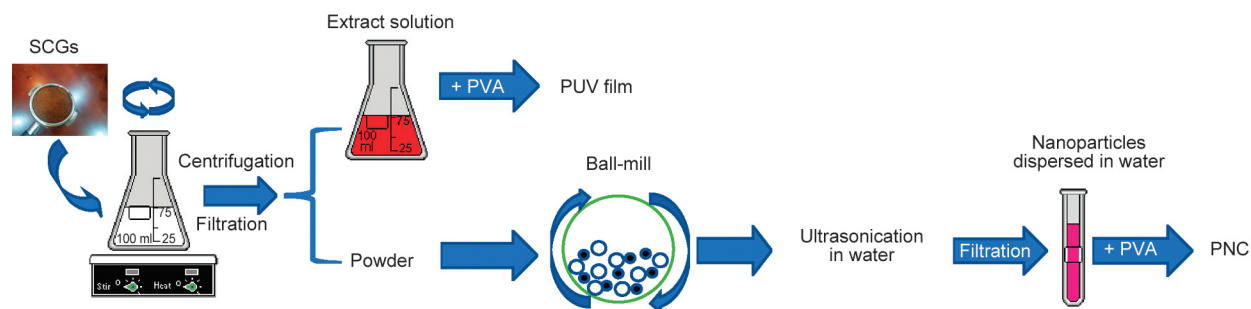


**Figure 1.** Fabrication scheme for UV shielding and nanocomposite samples.

the PVA concentration was fixed at 5 wt% which is similar to the previous report [19] for comparison. The mixture was stirred at room temperature until a clear, homogeneous solution was obtained. The polymeric solution was poured into a Teflon petri dish. The solvent was gradually evaporated at 40 °C to form PVA-based UV shielding (PUV) films. The samples were marked as PUV- $x$ , where  $x$  is the mass [g] of SCGs used in 200 ml H<sub>2</sub>O in the extraction step.

#### *Preparation of nanoparticle solution and PVA-based nanocomposite*

The remaining solid obtained after aqueous extraction from the above procedure was further washed with boiled distilled water until there was no change in the solution color. This step was conducted to remove water-soluble substances that remained in the extracted SCGs. The solid after washing was again dried in the oven (80 °C) for 24 h to obtain a dry powder. The powder was put into a cylindrical ceramic ball mill (speed: 225 rpm) for 40 min. Then, the fine powder was mixed with double distilled water (concentration: 1 wt%). The samples with CTAB were prepared in a similar method. Instead of water, the CTAB solutions (concentration: 60 or 250 mg/100 ml H<sub>2</sub>O) were mixed with the ground SCGs before moving to the next step.

The mixtures in a 50 ml centrifuge tube were placed into an ultrasonic liquid processor (Net power output: 500 Watt, frequency: 20 kHz, vibra-Cell VC505, Sonics & Materials, Inc., USA). A standard probe equipped with a replaceable tip (diameter: 13 mm, amplitude set at 100%: 126 μm) was used. The preset sonication amplitude parameter varied at 30, 50, and 70%. The sonicated mixture was filtered using a qualitative filter paper (Grade 101, Pore size: 20–25 μm, Hangzhou Special Paper Industry Co., Ltd., China) or a glass fiber filter (GF/A, pore size: 1.6 μm, diameter: 47 mm, Whatman, United Kingdom) to obtain

an aqueous solution contained nanoparticles. PVA was added into the SCGs nano-solutions to form homogenous mixtures with varied polymer concentrations (3, 5, 8, or 10 wt%). The PVA-nano SCGs solutions were dried in a silicone mold in ambient conditions to form PVA-based nanocomposite (PNC) films. The nanocomposite samples were named PNC- $y$ , where  $y$  is the PVA concentration in the nano-solution.

### **2.3. Characterization**

UV-Visible spectroscopy was applied to measure the absorbance of the SCGs extract and characterize the transmission of the PUV films. The spectra were obtained using a double-beam spectrophotometer (V730, Jasco, Japan). The scanning mode was applied, and the spectra were achieved in the wavelength region of 250 to 700 nm.

To determine the particle size, the dynamic light scattering (DLS) technique was applied using the equipment of Zetasizer Pro (Malvern, United Kingdom). The backscatter system (detector angle of 173°) and the measuring temperature of 25 °C were set. The sample was equilibrated for 60 s before conducting the measurement. The zeta potential values were determined using the same equipment with disposable folded capillary cells. Each sample was measured three times and an average value was calculated. In addition, a transmission electron microscope (TEM) (JEM 1010, JEOL, Japan) was also applied to directly observe the SCGs-based nanoparticles.

Fourier transform infrared (FTIR) measurement was conducted using the equipment of FTIR-8400s (Shimadzu, Japan). The samples were mixed with KBr powder (Nacalai Tesque, Kyoto, Japan) (approximately 0.1 wt%) and put into a stainless steel mold (diameter: 1.5 cm). The pressure was applied using a manual hydraulic press to form KBr pellets. The FTIR transmission mode was carried out from 4000 to 400 cm<sup>-1</sup> wavenumber.

Thermogravimetric analyzer (TGA) (TGA 55, TA Instruments Co., USA) was performed from room temperature to 700 °C (heating rate: 10 °C·min<sup>-1</sup>). To confirm the thermal oxidative stability of the samples, oxygen purge gas was applied (balance/sample flow rate: 40/25 ml/min).

Mechanical properties were evaluated using a tensile testing machine (FS3000, Testometric, United Kingdom). The experiment was conducted with similar conditions compared to the published research [36]. The film samples were cut into rectangular shapes (15×50 mm). Thickness was measured using a digital micrometer. The tensile test was carried out with a speed of 5 mm·min<sup>-1</sup> to obtain the stress-strain curve. The maximum stress and elongation values in the curve were detected.

The homogeneity of the polymer nanocomposite was monitored using an optical microscope (B-293, Optika, Italy). The microscope was equipped with 10× and 40× objective lenses. The magnified images of the samples were captured by a CMOS camera and exported using Optika Proview software.

### 3. Results and discussion

Figure 2 showed the UV-Visible absorbance spectrum of the extract obtained from 0.5 g SCGs in 200 ml H<sub>2</sub>O. As can be seen, the spectrum contained two main peaks at 278.8 and 322.8 nm. Compared to the pure substances (caffeine and chlorogenic acid) which are usually presented in coffee extract, the peak at 322.8 nm might be originally from chlorogenic acid. However, compared to caffeine's spectrum (peak is at 272.4 nm), the detected peak in the

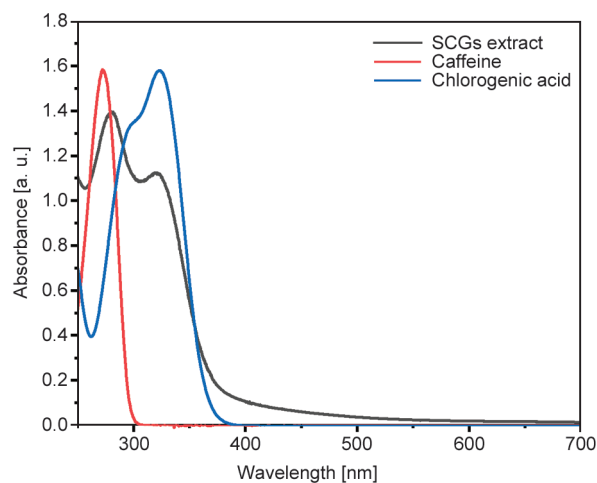


**Figure 2.** UV-Visible absorption spectra (250 to 700 nm) of SCGs extract (0.5 g/200 ml H<sub>2</sub>O), caffeine, and chlorogenic acid solution (30 ppm).

extract (278.8 nm) was slightly shifted to a higher wavelength region. This phenomenon might be due to the interference of the other UV-absorbing substances (chlorogenic acid and melanoidin) in the extract [37, 38]. The UV-Visible absorbance spectrum of the SCGs extract was identical to the reported result using instant coffee [19]. In Figure 2 results, although the extraction was conducted with approximately 0.25 wt% SCGs aqueous mixture for only 10 min, the absorbance values of all detected peaks were higher than 1. Therefore, it could be concluded that the extract from SCGs might contain a significant amount of similar organic compounds presented in the instant coffee solution. It is worth noting that the extraction procedure is rather simple, and the process is similar to the washing step in the previous study [36]. It might open a new approach to utilizing the waste product which is cheaper than the original instant coffee. In the next experiment, the SCGs extract was mixed with PVA to confirm the UV-shielding capability of the formed films.

The transmittance values and the images of PVA films mixed with different types of SCGs extracts were summarized in Figure 3. The UV-shielding ability of the film samples might be affected by the thickness of the film sample. Therefore, the values of transmittance divided by the corresponding thicknesses (in micrometer) were also shown in Figure 3b. However, the relative positions of the spectra obtained in Figure 3b are similar to that in Figure 3a. As can be observed, pure PVA film provides the highest transparency. However, PVA also had the worst protection in the region of UV-A, B, and C (the wavelength is less than 400 nm). When the amount of SCGs used for aqueous solution extraction was 5, 10, 20, or 30 g/200 ml H<sub>2</sub>O, the UV region might be completely cut off after passing the PVA-based films. The transparency in the visible region was also reduced accordingly. On the other hand, when only 0.1 or 0.5 g SCGs was used, the transmittance values at the visible wavelengths were improved. However, there was part of UV light that might be allowed to pass through the films. The sample prepared with only 1 g SCGs provided a reasonable transmittance for the visible lights. The transmittance measured at 550 nm is 63% while this value is 84% for the pure PVA film. Few wavelengths in the UV-A region remained slightly transparent. However, more damaging UV radiation from 290 to 350 nm could be mostly shielded. The investigation showed that the extracted solution

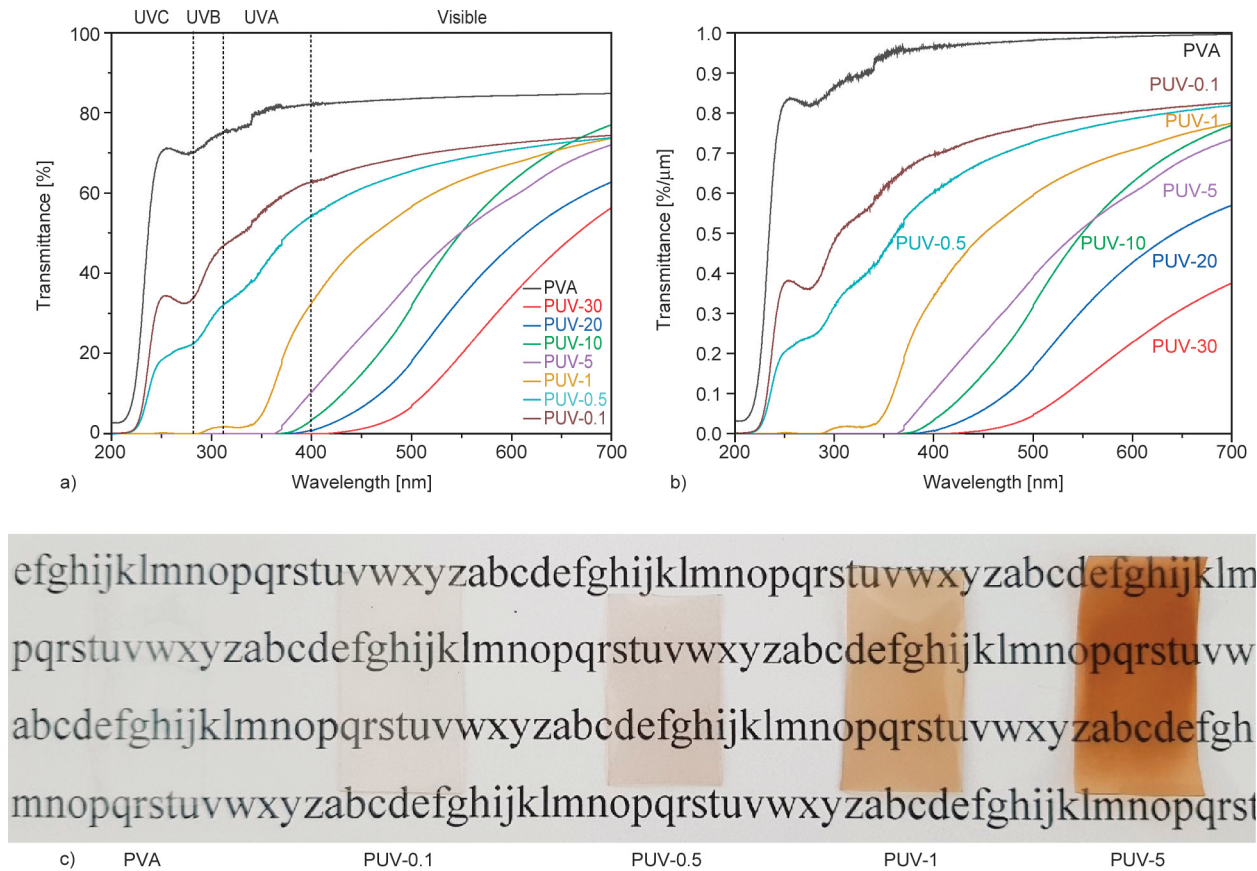


**Figure 3.** a) UV-Visible spectra, b) transmittance values/film's thicknesses spectra, and c) images of PVA film and PVA-based films mixed with various SCGs extractions.

obtained from only 1 g SCGs/200 ml H<sub>2</sub>O (0.5 wt%) could provide a similar UV-shielding effect to the use of 1 wt% of instant coffee reported by the other group [19].

The SCGs after aqueous extraction was further utilized to synthesize nano-fillers. The washed SCGs were ball-milled before forming nanoparticles under the ultrasonic force in an aqueous solution. Ultrasonic

amplitude was varied, and the DLS particle size results of the obtained nanoparticle were summarized in Figure 4 and Table 1. In this investigation, although the conventional filter paper was applied in the filtration step, the average particle size of less than 300 nm still could be achieved. As can be seen, when the amplitude was increased, the smaller Z-average values might be obtained (Table 1). In all cases, although

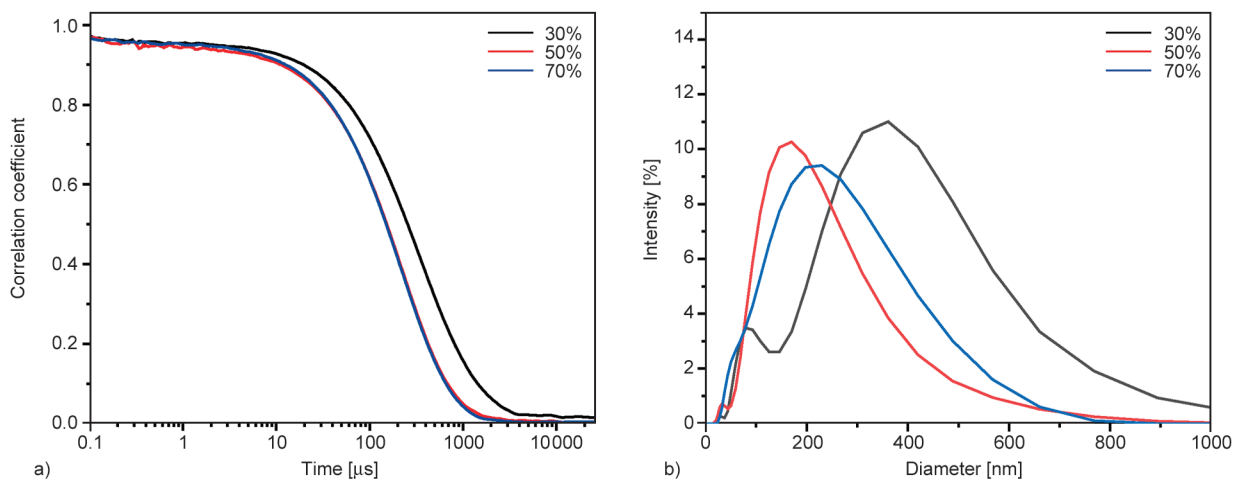


**Figure 4.** a) Plots of the correlation coefficient as a function of time and b) intensity size distribution spectra of SCGs nanoparticle solutions fabricated using qualitative filter papers and various ultrasonic amplitudes.

**Table 1.** DLS results of SCGs nanoparticle solutions using qualitative filter papers and various ultrasonic amplitudes.

Amplitude [%]	30	50	70
Z-Average [nm]	242.6±12.5	154.3±1.0	152.3±0.9
Polydispersity index, PI	0.532±0.071	0.333±0.028	0.291±0.002
Peak mean (Intensity distribution) [nm]	386.9±91.7	171.2±25.8	208.3±18.6

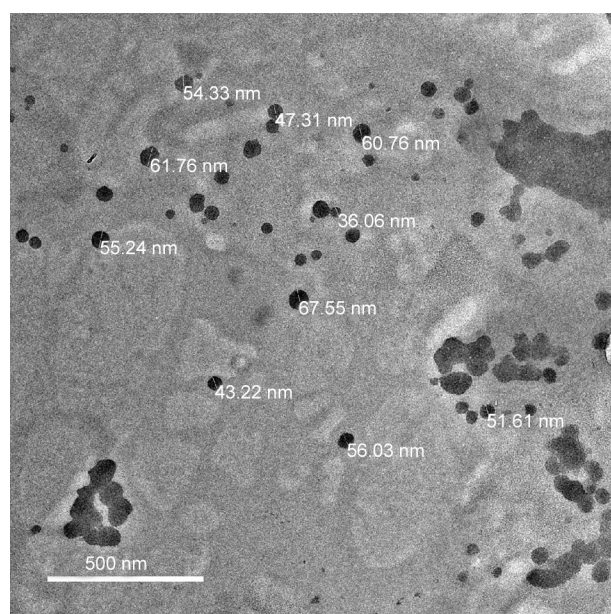
the polydispersity index (PI) values were not large, there were other small peaks that appeared in the DLS intensity distribution which indicated two types of the particle system. It is worth noting that the SCGs components after washing might be mainly carbohydrates. Cellulose, hemicellulose, and lignin which are varied in molecular weight in SCGs might be the main reason for the polydispersity of the nano solutions. The amplitude represents the distance of the ultrasonic tip vibrating from the equilibrium position. Because the SCGs concentration dispersed in water was fixed, the increase in amplitude was directly proportional to the ultrasonic energy used to break down the milled SCGs into smaller particles. Therefore, there was a significant difference between the results obtained from 30 and 50% amplitude. The size distribution was also shifted to a smaller size region. When the amplitude was up to 70%, although the intensity signal of the smaller particle system was slightly increased, the distribution was also stretched to the larger particle area. However, the autocorrelation curves and Z-average values were nearly

unchanged. In addition, the solution temperature quickly increased, and it is difficult to control. Therefore, the amplitude of 50% was applied for the next investigation.

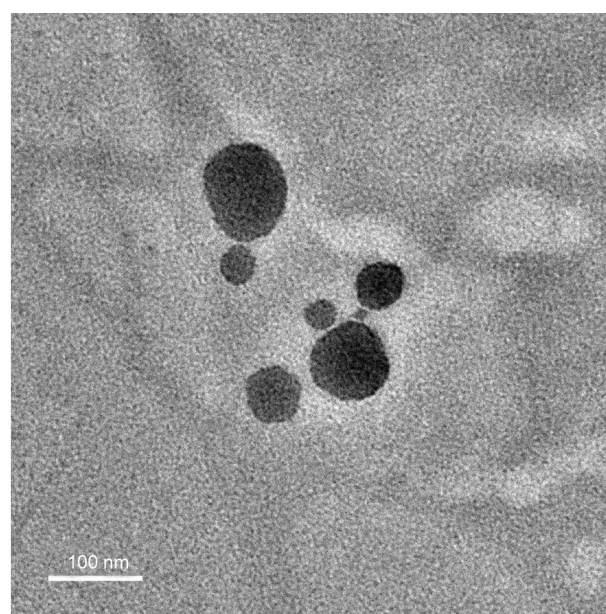
Instead of the qualitative filter paper, the glass fiber filter with a smaller pore size was used to confirm the ability to further reduce the particle size. The DLS results were shown in Table 2. As can be seen, the particle size was slightly improved by applying the glass fiber filter. Figure 5 showed the TEM images of the SCGs particles prepared without using CTAB. As can be seen, this is another evidence that the nanoparticles could be successfully fabricated from SCGs with the assistance of ultrasonication. Although small particles (<100 nm) could be observed, many large particles and aggregations were also detected. The TEM images were in agreement with the polydispersed distribution obtained in the DLS results. Because of the ability to stabilize the nanoparticle, CTAB has been widely applied in nanomaterials research [39–41]. Therefore, in this study, the nanoparticle formed under the presence of CTAB was investigated and the size values were also

**Table 2.** DLS results of SCGs nanoparticle solutions using glass fiber filters and various CTAB concentrations.

CTAB [mg/100 ml]	0	60	250
Z-average [nm]	148.4±0.7	308.9±3.0	190.7±3.5
Polydispersity index, PI	0.214±0.002	0.308±0.008	0.255±0.016
Peak mean (Intensity distribution) [nm]	179.1±15.9	480.8±158.7	208.3±18.6



a)



b)

**Figure 5.** TEM images of SCGs-based nanoparticle sample without CTAB at a magnification of a) 10000× and b) 30000×.

shown in Table 2. The larger particle size was obtained with 60 mg/100 ml CTAB. By increasing to 250 mg/100 ml, although the particle size could be reduced to 190 nm, the result still is higher than that of the sample formed without CTAB (148 nm). This phenomenon might be due to the capping effect of CTAB on the formed nanoparticles [42]. The CTAB structure contains a hydrophilic headgroup (quaternary amine) and a hydrophobic tail (alkyl chain). The SCGs-based nanoparticle with the hydrophilic surface could be covered by CTAB molecules via the charged headgroups. The second layer might be formed by the interaction of hydrophobic alkyl chains among the CTAB molecules. As a result, the CTAB bilayer left the positive headgroups exposed to the solution. Therefore, the hydrodynamic diameter detected by the DLS technique might be increased. This explanation was reconfirmed by considering the particle surface's charge. The zeta potential was  $-17.7 \pm 1.6$  mV while this value was positive ( $25.3 \pm 0.4$  mV) by adding CTAB to the solution. The average particle size obtained by applying the current

protocol is significantly smaller than the previous report (240 nm) [36]. Without removing the solvent, the nanoparticles dispersed in water were directly used for the next steps of nanocomposite fabrication to limit the ability of aggregation.

The nanoparticles prepared using glass filter paper were added into the PVA matrix to confirm the ability to improve the mechanical properties. The tensile results for the samples fabricated from the nano solution with and without CTAB (250 mg/100 ml H<sub>2</sub>O) were shown in Figure 6. Firstly, the film samples were fabricated using 5 and 3 wt% of PVA (PNC-5 or 3 and PNC-5-CTAB or 3-CTAB) and the tensile results were compared. As can be seen, when the SCGs particles prepared with CTAB were mixed with PVA, the tendency of reducing tensile strength (TS) was obtained. The mechanical enhancement could not be observed in all samples with the presence of CTAB. The component of SCGs might contain fatty acids which are difficult to remove during the washing step with pure water. However, these components might leak to the formed nano solution

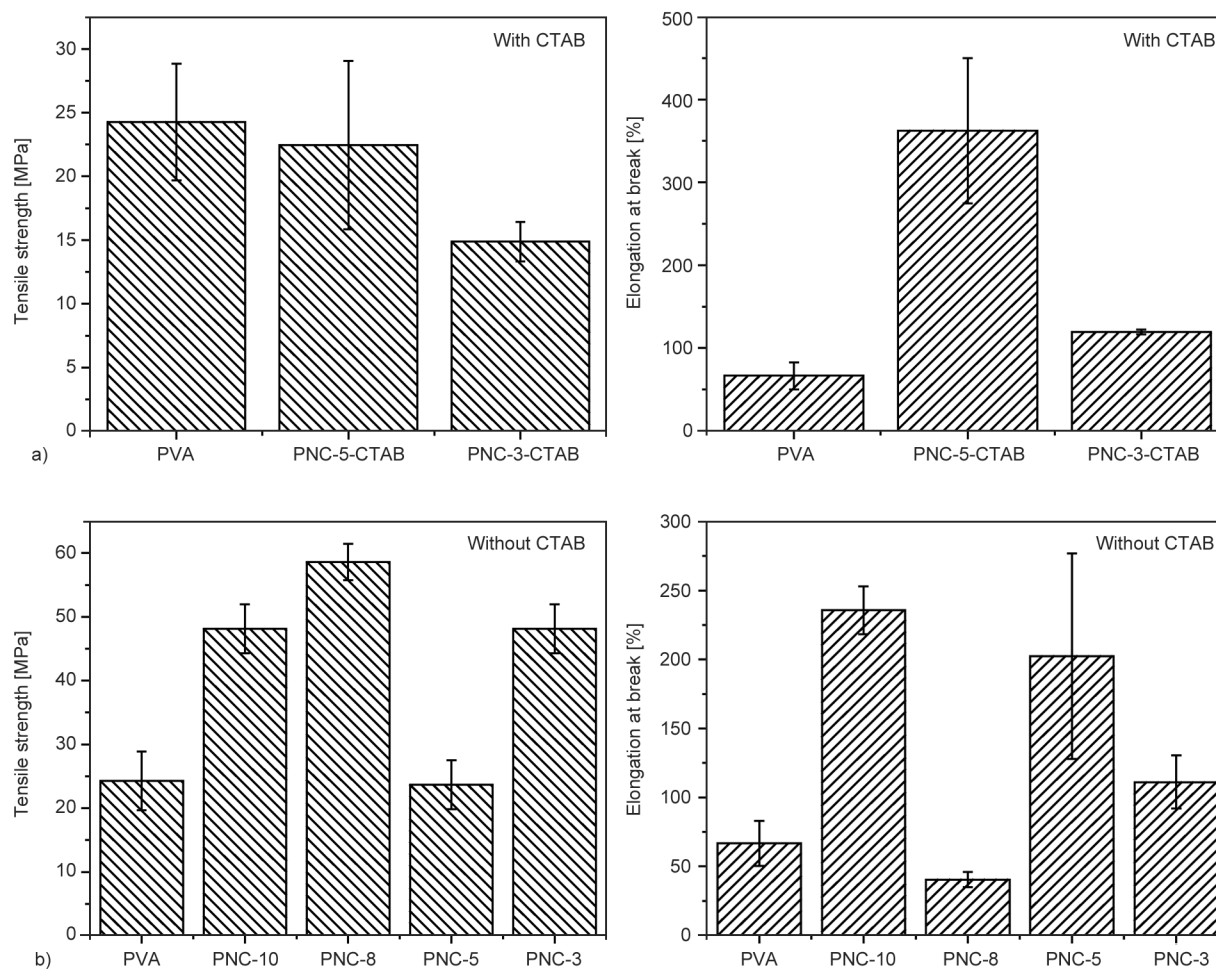
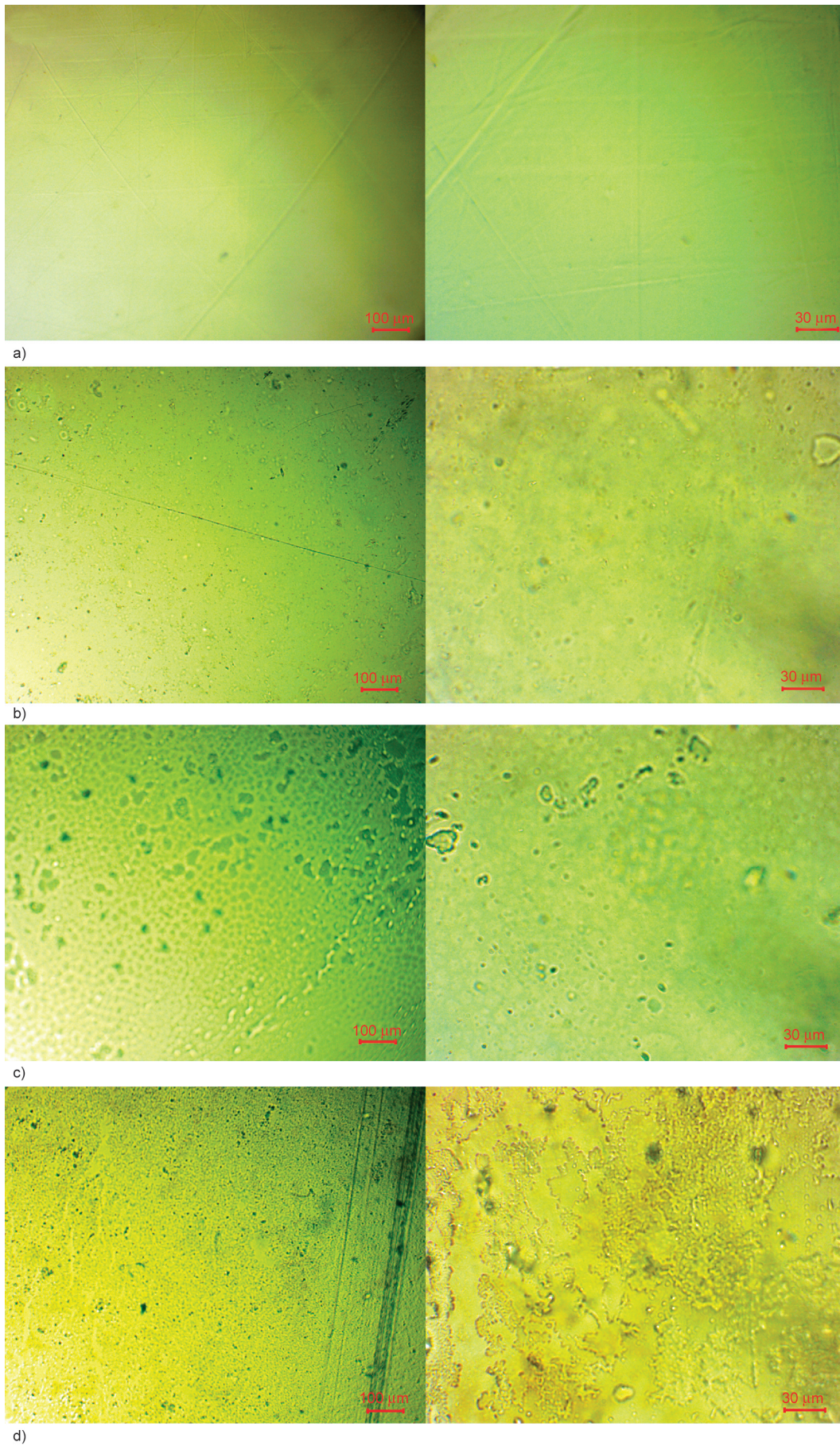


Figure 6. Tensile result for PVA-based nanocomposites from SCGs: a) with CTAB; b) without CTAB.

with the presence of a surface-active reagent of CTAB. These long alkyl chain components might act as a plasticizer in the PVA matrix and reduce the mechanical properties. In addition, the nanoparticles covered by CTAB molecules might not be compatible with the PVA matrix. Therefore, the study was focused on the samples without using CTAB. On the other hand, when SCGs nanoparticles prepared without CTAB were added, TS was significantly improved. The highest TS value (~58 MPa) achieved with 8 wt% of PVA (PNC-8) was more than two times higher than that of the original PVA film (~24 MPa). The same SCGs nano solution was used in all cases while the PVA concentration was decreased. After evaporating water to form nanocomposite, the film samples with less PVA had a higher nanoparticle concentration. When the PVA concentration was 5 wt%, the number of SCGs nanoparticles contained in the composite was high enough to cause some aggregation (Figure 7c). This might be the main reason for the reduction of the mechanical properties. Although the sample of PNC-3 still showed a high TS value, the aggregation of nanoparticles because of high concentration could not be ensured as can be observed in Figure 7d. In addition, the TS value could not be further improved compared to the PNC-8 sample. A smaller nanoparticle concentration with higher mechanical properties was preferred. Interestingly, the PNC-10 sample with the smallest amount of nanoparticles showed an improvement in both TS and elongation at break values.

The effect of SCGs nanoparticles on the stress-strain curves was shown in Figure 8. All samples showed the first linear increase of stress followed by yielding and plastic deformation. Compared to PVA, the elastic region was significantly expanded to a higher stress region in the samples with nanoparticles addition (except the PNC-5 sample). These samples also performed a slight decrease of stress after yielding which is the typical necking in the tensile test. This phenomenon is because of the formation of localized domains in which the polymer chains were re-oriented to a fibrous structure. The nanoparticle occupied in the spaces between the polymer chains might assist the unfolding process. Therefore, the PNC-10 sample with a low nanoparticle concentration could possess good performance in both TS and elongation properties. However, in the PNC-8 with more nano-SCGs, the interaction of filler and polymer chains was dominated. As a result, the increase of TS

and decrease of elongation were obtained. To further confirm the compatibility of PVA molecules and SCGs nanoparticles, FTIR measurement was performed, and the results were summarized in Figure 9. The nanoparticle was prepared via two steps of mechanical treatment including ball milling and ultrasonic radiation. The FTIR spectra shown in Figure 9a could reveal the changing of functional groups with each step. The obtained results of SCGs were similar to the previous publication [29]. The peaks at 2923 and 2853  $\text{cm}^{-1}$  assigned as asymmetric and symmetric C–H vibrations appeared in all SCGs samples. The peak at 1745  $\text{cm}^{-1}$  belonging to C=O bond stretching was also detected in all types of SCGs. The C=O signal might come from various antioxidant substances contained in the SCGs such as caffeine, chlorogenic acid, or fatty acids. Although the signal of this functional group became weaker in the nanoparticle FTIR spectrum, the existence of C=O might still indicate a small amount of the bio-active components remained. In the 4000–3200  $\text{cm}^{-1}$  region, peaks could not be detected clearly in the SCGs after washing with boiled water. However, some small peaks in this region belonging to O–H or N–H bond stretching appeared in the SCGs sample after the ball milling process. This result indicated that the washing process had removed most of the water-soluble substances from the SCGs' surface. However, after milling, the raw SCGs were broken down into smaller pieces and these functional groups trapped inside might be again detectable. Interestingly, the nanoparticle showed a large peak at 3429  $\text{cm}^{-1}$ . In this study, water was used as a dispersed environment and only particles with the polar groups can be stabilized in the medium. Therefore, SCGs-based nanoparticle surfaces might be covered by –OH groups. This might be one of the advantages of the current fabrication method. Because of the presence of polar groups, the synthesized nanoparticle might be dispersed better in the matrix of PVA which also possesses many hydroxyl groups in the side chain. Figure 9b showed the spectrum of PVA in which the FTIR peaks were also detected at similar wavenumbers compared to the previous study [43]. As can be observed, the PNC-8 sample's FTIR spectrum contained the main peaks originating from its components. However, in the case of the nanocomposite, the large peak that appeared in the 4000–3200 region was shifted to a lower wavenumber comparing the similar peaks of nanoparticle and PVA. This phenomenon might be



**Figure 7.** Optical microscope images of PNC at 10× and 40× objective lenses: a) PNC-10, b) PNC-8, c) PNC-5, and d) PNC-3.

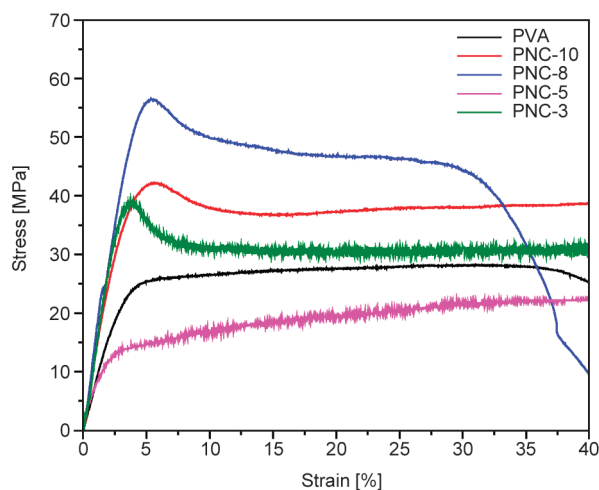


**Figure 8.** Stress-strain curve of PVA-based nanocomposite with SCGs.

an indicator of good compatibility between the nanofiller and the matrix.

Thermal properties in the oxygen atmosphere could reveal the capability against oxidative degradation of the fabricated film samples. The TGA results were summarized in Figure 10. As can be observed, the first loss of weight occurred continuously from room temperature until reaching 150 °C was assigned to the evaporation of water that remained in the film samples. The main and significant weight loss was activated when the temperature reached 200 °C. This large decrease in the TGA signal was because of thermal degradation and decomposition of PVA and organic substances in the matrix. Three types of samples (PVA, PUV, and PNC) showed similar TGA transitions. To remove the interference of water desorption signals, the TGA data were normalized with a value at 170 °C, and the results were shown in Figure 10b. As can be seen, although the difference is small, the PUV sample still clearly showed a better

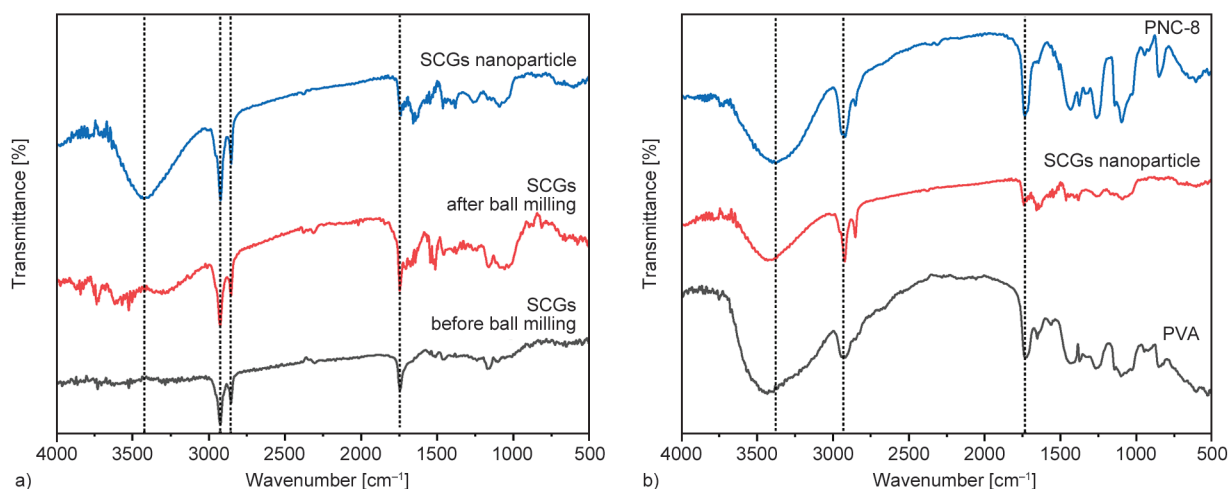


**Figure 9.** FTIR spectra of a) SCGs samples before and after the mechanical treatments; b) PNC-8 sample in comparison to SCGs nanoparticle and PVA.

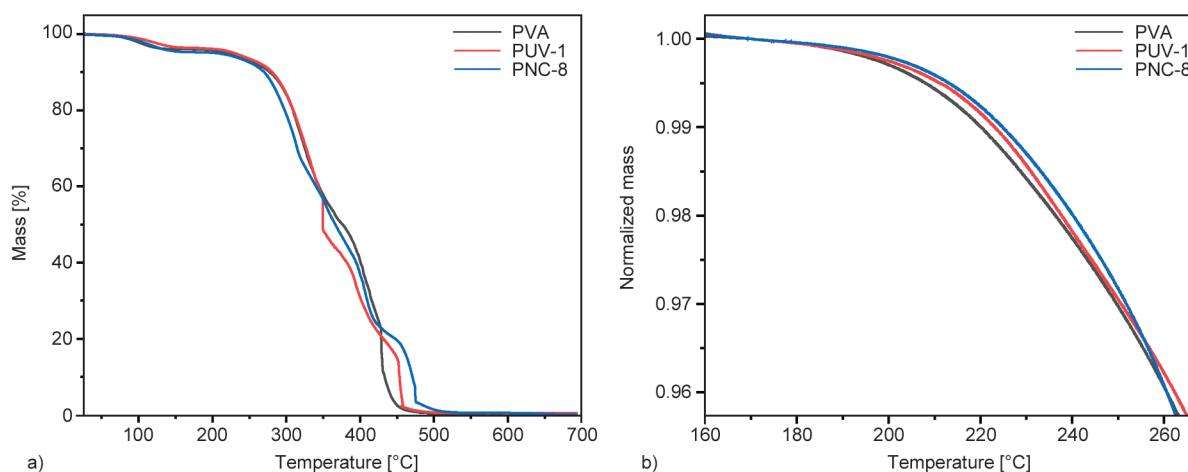


**Figure 10.** TGA results for PVA, PUV-1, and PNC-8: a) plotted from room temperature to 700 °C; b) plotted as normalized value with weight loss at 170 °C from 160 to 265 °C.

thermal-oxidative degradation. This result is in agreement with the previous report [19]. Interestingly, the weight loss signal for the PNC sample also occurred more slowly than that of the original PVA. The nanoparticle prepared in this current study might contain not only carbohydrate particles but also some amount of antioxidant remaining (caffeine or chlorogenic acid). Therefore, the PVA-based composite reinforced by the nanofiller from SCGs could possess both strong mechanical properties and resistance to thermal-oxidative degradation.

#### 4. Conclusions

A green approach of the utilization of both extract solution and the remaining carbohydrate from SCGs respectively for UV filters and nanofillers was confirmed. Although a low concentration of SCGs (~0.25 wt%) was extracted in boiled water for a short time (10 min), the extract contained a significant amount of UV-absorbing substances such as caffeine, chlorogenic acid, and melanoidin. UV shielding materials could be fabricated successfully from 5 wt% PVA solution and the SCGs extracts. The PUV-1 showed complete shielding in the UV-C and most of the UV-B regions while the 63% transparency at 550 nm was maintained. By applying 50% ultrasonic amplitude and filtrating through glass fiber filters, the nano-SCGs solution with an average particle diameter of 148 nm could be obtained. A new and strong FTIR peak that appeared at 3429 cm<sup>-1</sup> could confirm the existence of the OH groups on the surface of nanoparticles. Owing to the strong interaction between the polar groups, the compatibility between the PVA matrix and nano SCGs fillers could be improved. TS value of the nanocomposite fabricated from PVA and nano SCGs particles was significantly higher (more than two times) than that of the original PVA film. The addition of CTAB could change the value of zeta potential from minus to positive value. However, the samples fabricated with CTAB could not yield a better result in nanoparticle size and nanocomposite's mechanical properties. The presence of antioxidant compounds remaining in the nano solution might be the main reason for the enhancement in thermal oxidative properties for both PVA-based UV shielding material and nanocomposite.

#### Acknowledgements

The authors would like to thank MSc Le Thi Kim Anh and MSc Truong Thi Phuong Dung for providing laboratory assistant services.

#### References

- [1] Murthy P. S., Madhava Naidu M.: Sustainable management of coffee industry by-products and value addition – A review. *Resources, Conservation and Recycling*, **66**, 45–58 (2012).  
<https://doi.org/10.1016/j.resconrec.2012.06.005>
- [2] Esquivel P., Jiménez V. M.: Functional properties of coffee and coffee by-products. *Food Research International*, **46**, 488–495 (2012).  
<https://doi.org/10.1016/j.foodres.2011.05.028>
- [3] Fernandes A. S., Mello F. V. C., Thode Filho S., Carpes R. M., Honório J. G., Marques M. R. C., Felzenszwalb I., Ferraz E. R. A.: Impacts of discarded coffee waste on human and environmental health. *Ecotoxicology and Environmental Safety*, **141**, 30–36 (2017).  
<https://doi.org/10.1016/j.ecoenv.2017.03.011>
- [4] Kovalcik A., Obruca S., Marova I.: Valorization of spent coffee grounds: A review. *Food and Bioprocess Processing*, **110**, 104–119 (2018).  
<https://doi.org/10.1016/j.fbp.2018.05.002>
- [5] Ballesteros L. F., Teixeira J. A., Mussatto S. I.: Chemical, functional, and structural properties of spent coffee grounds and coffee silverskin. *Food and Bioprocess Technology*, **7**, 3493–3503 (2014).  
<https://doi.org/10.1007/s11947-014-1349-z>
- [6] McNutt J., He Q.: Spent coffee grounds: A review on current utilization. *Journal of Industrial and Engineering Chemistry*, **71**, 78–88 (2019).  
<https://doi.org/10.1016/j.jiec.2018.11.054>
- [7] Zuurro A., Lavecchia R.: Spent coffee grounds as a valuable source of phenolic compounds and bioenergy. *Journal of Cleaner Production*, **34**, 49–56 (2012).  
<https://doi.org/10.1016/j.jclepro.2011.12.003>
- [8] Pavlović M. D., Buntić A. V., Šiler-Marinković S. S., Dimitrijević-Branković S. I.: Ethanol influenced fast microwave-assisted extraction for natural antioxidants obtaining from spent filter coffee. *Separation and Purification Technology*, **118**, 503–510 (2013).  
<https://doi.org/10.1016/j.seppur.2013.07.035>
- [9] Panusa A., Zuurro A., Lavecchia R., Marrosu G., Petrucci R.: Recovery of natural antioxidants from spent coffee grounds. *Journal of Agricultural and Food Chemistry*, **61**, 4162–4168 (2013).  
<https://doi.org/10.1021/jf4005719>
- [10] Zhang S., Yang J., Wang S., Rupasinghe H. P. V., He Q.: Experimental exploration of processes for deriving multiple products from spent coffee grounds. *Food and Bioprocess Processing*, **128**, 21–29 (2021).  
<https://doi.org/10.1016/j.fbp.2021.04.012>

- [11] Ciesielczuk T., Rosik-Dulewska C., Poluszyńska J., Miłek D., Szewczyk A., Sławińska I.: Acute toxicity of experimental fertilizers made of spent coffee grounds. *Waste and Biomass Valorization*, **9**, 2157–2164 (2018). <https://doi.org/10.1007/s12649-017-9980-3>
- [12] Cervera-Mata A., Navarro-Alarcón M., Delgado G., Pastoriza S., Montilla-Gómez J., Llopis J., Sánchez-González C., Rufián-Henares J. Á.: Spent coffee grounds improve the nutritional value in elements of lettuce (*Lactuca sativa* L.) and are an ecological alternative to inorganic fertilizers. *Food Chemistry*, **282**, 1–8 (2019). <https://doi.org/10.1016/j.foodchem.2018.12.101>
- [13] Rosado C., Tokunaga V. K., Sauce R., de Oliveira C. A., Sarruf F. D., Parise-Filho R., Maurício E., de Almeida T. S., Velasco M. V. R., Baby A. R.: Another reason for using caffeine in dermocosmetics: Sunscreen adjuvant. *Frontiers in Physiology*, **10**, 519 (2019). <https://doi.org/10.3389/fphys.2019.00519>
- [14] Lu Y-P., Lou Y-R., Xie J-G., Peng Q-Y., Zhou S., Lin Y., Shih W. J., Conney A. H.: Caffeine and caffeine sodium benzoate have a sunscreen effect, enhance UVB-induced apoptosis, and inhibit UVB-induced skin carcinogenesis in Skh-1 mice. *Carcinogenesis*, **28**, 199–206 (2007). <https://doi.org/10.1093/carcin/bgl112>
- [15] Marto J., Gouveia L. F., Chiari B. G., Paiva A., Isaac V., Pinto P., Simões P., Almeida A. J., Ribeiro H. M.: The green generation of sunscreens: Using coffee industrial sub-products. *Industrial Crops and Products*, **80**, 93–100 (2016). <https://doi.org/10.1016/j.indcrop.2015.11.033>
- [16] Hu X., Huang H., Hu Y., Lu X., Qin Y.: Novel bio-based composite phase change materials with reduced graphene oxide-functionalized spent coffee grounds for efficient solar-to-thermal energy storage. *Solar Energy Materials and Solar Cells*, **219**, 110790 (2021). <https://doi.org/10.1016/j.solmat.2020.110790>
- [17] Kumar A., Han S. S.: PVA-based hydrogels for tissue engineering: A review. *International Journal of Polymeric Materials and Polymeric Biomaterials*, **66**, 159–182 (2017). <https://doi.org/10.1080/00914037.2016.1190930>
- [18] Kamoun E. A., Kenawy E-R. S., Chen X.: A review on polymeric hydrogel membranes for wound dressing applications: PVA-based hydrogel dressings. *Journal of Advanced Research*, **8**, 217–233 (2017). <https://doi.org/10.1016/j.jare.2017.01.005>
- [19] Lyu Y., Gu X., Mao Y.: Green composite of instant coffee and poly(vinyl alcohol): An excellent transparent UV-shielding material with superior thermal-oxidative stability. *Industrial and Engineering Chemistry Research*, **59**, 8640–8648 (2020). <https://doi.org/10.1021/acs.iecr.0c00413>
- [20] Gaidukova G., Platnieks O., Aunins A., Barkane A., Ingrao C., Gaidukovs S.: Spent coffee waste as a renewable source for the production of sustainable poly(butylene succinate) biocomposites from a circular economy perspective. *RSC Advances*, **11**, 18580–18589 (2021). <https://doi.org/10.1039/D1RA03203H>
- [21] García-García D., Carbonell A., Samper M. D., García-Sanoguera D., Balart R.: Green composites based on polypropylene matrix and hydrophobized spend coffee ground (SCG) powder. *Composites Part B: Engineering*, **78**, 256–265 (2015). <https://doi.org/10.1016/j.compositesb.2015.03.080>
- [22] Wu C-S.: Renewable resource-based green composites of surface-treated spent coffee grounds and polylactide: Characterisation and biodegradability. *Polymer Degradation and Stability*, **121**, 51–59 (2015). <https://doi.org/10.1016/j.polymdegradstab.2015.08.011>
- [23] Cataldo V. A., Cavallaro G., Lazzara G., Milioto S., Parisi F.: Coffee grounds as filler for pectin: Green composites with competitive performances dependent on the UV irradiation. *Carbohydrate Polymers*, **170**, 198–205 (2017). <https://doi.org/10.1016/j.carbpol.2017.04.092>
- [24] Al-Hamamre Z., Foerster S., Hartmann F., Kröger M., Kaltschmitt M.: Oil extracted from spent coffee grounds as a renewable source for fatty acid methyl ester manufacturing. *Fuel*, **96**, 70–76 (2012). <https://doi.org/10.1016/j.fuel.2012.01.023>
- [25] de Melo M. M. R., Barbosa H. M. A., Passos C. P., Silva C. M.: Supercritical fluid extraction of spent coffee grounds: Measurement of extraction curves, oil characterization and economic analysis. *The Journal of Supercritical Fluids*, **86**, 150–159 (2014). <https://doi.org/10.1016/j.supflu.2013.12.016>
- [26] Efthymiopoulos I., Hellier P., Ladommatos N., Kay A., Mills-Lamprey B.: Effect of solvent extraction parameters on the recovery of oil from spent coffee grounds for biofuel production. *Waste and Biomass Valorization*, **10**, 253–264 (2019). <https://doi.org/10.1007/s12649-017-0061-4>
- [27] Tellers J., Willems P., Tjeerdsma B., Sbirrazzuoli N., Guigo N.: Spent coffee grounds as property enhancing filler in a wholly bio-based epoxy resin. *Macromolecular Materials and Engineering*, **306**, 2100323 (2021). <https://doi.org/10.1002/mame.202100323>
- [28] Wu H., Hu W., Zhang Y., Huang L., Zhang J., Tan S., Cai X., Liao X.: Effect of oil extraction on properties of spent coffee ground–plastic composites. *Journal of Materials Science*, **51**, 10205–10214 (2016). <https://doi.org/10.1007/s10853-016-0248-2>
- [29] Leow Y., Yew P. Y. M., Chee P. L., Loh X. J., Kai D.: Recycling of spent coffee grounds for useful extracts and green composites. *RSC Advances*, **11**, 2682–2692 (2021). <https://doi.org/10.1039/D0RA09379C>

- [30] Chien H-W., Kuo C-J., Kao L-H., Lin G-Y., Chen P-Y.: Polysaccharidic spent coffee grounds for silver nanoparticle immobilization as a green and highly efficient biocide. *International Journal of Biological Macromolecules*, **140**, 168–176 (2019).  
<https://doi.org/10.1016/j.ijbiomac.2019.08.131>
- [31] Yust B. G., Rao N. Z., Schwarzmann E. T., Peoples M. H.: Quantification of spent coffee ground extracts by roast and brew method, and their utility in a green synthesis of gold and silver nanoparticles. *Molecules*, **27**, 5124 (2022).  
<https://doi.org/10.3390/molecules27165124>
- [32] Zuorro A., Iannone A., Miglietta S., Lavecchia R.: Green synthesis of silver nanoparticles using spent coffee ground extracts: Process modelling and optimization. *Nanomaterials*, **12**, 2597 (2022).  
<https://doi.org/10.3390/nano12152597>
- [33] Kanai N., Honda T., Yoshihara N., Oyama T., Naito A., Ueda K., Kawamura I.: Structural characterization of cellulose nanofibers isolated from spent coffee grounds and their composite films with poly(vinyl alcohol): A new non-wood source. *Cellulose*, **27**, 5017–5028 (2020).  
<https://doi.org/10.1007/s10570-020-03113-w>
- [34] Zhang X., Wang H., Ma C., Niu N., Chen Z., Liu S., Li J., Li S.: Seeking value from biomass materials: Preparation of coffee bean shell-derived fluorescent carbon dots via molecular aggregation for antioxidation and bioimaging applications. *Materials Chemistry Frontiers*, **2**, 1269–1275 (2018).  
<https://doi.org/10.1039/C8QM00030A>
- [35] Crista D. M. A., el Mragui A., Algarra M., da Silva J. C. G. E., Luque R., da Silva L. P.: Turning spent coffee grounds into sustainable precursors for the fabrication of carbon dots. *Nanomaterials*, **10**, 1209 (2020).  
<https://doi.org/10.3390/nano10061209>
- [36] Lee H. K., Park Y. G., Jeong T., Song Y. S.: Green nanocomposites filled with spent coffee grounds. *Journal of Applied Polymer Science*, **132**, 42043 (2015).  
<https://doi.org/10.1002/app.42043>
- [37] Rufián-Henares J. A., Pastoriza S.: Melanoidins in coffee. in ‘Coffee in health and disease prevention’ (ed.: Preedy V. R.) Academic Press, San Diego, 183–188 (2015).
- [38] Belay A., Ture K., Redi M., Asfaw A.: Measurement of caffeine in coffee beans with UV/vis spectrometer. *Food Chemistry*, **108**, 310–315 (2008).  
<https://doi.org/10.1016/j.foodchem.2007.10.024>
- [39] Singh Z., Singh I.: CTAB surfactant assisted and high pH nano-formulations of copper nanoparticles pose greater cytotoxic and genotoxic effects. *Scientific Reports*, **9**, 5880 (2019).  
<https://doi.org/10.1038/s41598-019-42419-z>
- [40] Elfeky S. A., Mahmoud S. E., Youssef A. F.: Applications of CTAB modified magnetic nanoparticles for removal of chromium (VI) from contaminated water. *Journal of Advanced Research*, **8**, 435–443 (2017).  
<https://doi.org/10.1016/j.jare.2017.06.002>
- [41] Wei M-Z., Deng T-S., Zhang Q., Cheng Z., Li S.: Seed-mediated synthesis of gold nanorods at low concentrations of CTAB. *ACS Omega*, **6**, 9188–9195 (2021).  
<https://doi.org/10.1021/acsomega.1c00510>
- [42] Sui Z. M., Chen X., Wang L. Y., Xu L. M., Zhuang W. C., Chai Y. C., Yang C. J.: Capping effect of CTAB on positively charged Ag nanoparticles. *Physica E: Low-dimensional Systems and Nanostructures*, **33**, 308–314 (2006).  
<https://doi.org/10.1016/j.physe.2006.03.151>
- [43] Mansur H. S., Sadahira C. M., Souza A. N., Mansur A. A. P.: FTIR spectroscopy characterization of poly(vinyl alcohol) hydrogel with different hydrolysis degree and chemically crosslinked with glutaraldehyde. *Materials Science and Engineering: C*, **28**, 539–548 (2008).  
<https://doi.org/10.1016/j.msec.2007.10.088>

Review article

## Polymers are paving their way into defluoridation of water

Vipin Chandra Joshi<sup>1,3</sup>, Saroj Sharma<sup>2,3</sup>, Amit Bhattacharya<sup>2,3\*</sup>

<sup>1</sup>Process Design and Engineering Cell, Council of Scientific & Industrial Research-Central Salt and Marine Chemicals Research Institute (CSIR-CSMCRI), Bhavnagar 364002 Gujarat, India.

<sup>2</sup>Membrane Science and Separation Technology Division, Council of Scientific & Industrial Research-Central Salt and Marine Chemicals Research Institute (CSIR-CSMCRI), Bhavnagar 364002 Gujarat, India.

<sup>3</sup>Academy of Scientific and Innovative Research (AcSIR), Ghaziabad 201002, India

Received 3 February 2023; accepted in revised form 17 May 2023

**Abstract.** There are unequivocal shreds of evidence that polymers touched every sphere of life. They are very versatile and used in many applications depending on the specific intrinsic properties of the materials. Over the last few decades, there has been growing evidence that applying polymer materials in water-purifying has been adopted worldwide. Water fluorine toxicity is challenging us to develop water-purifying polymeric materials. We are presenting the polymeric adsorbent and membrane materials advancement in terms of defluoridation of water.

**Keywords:** polymer membranes, adsorbent, water, defluoridation

### 1. Introduction

The path of polymers began 100 years back. The concept of macromolecule (first coined term) originated from the idea of Herman Staudinger in 1922. Since it began, polymer researchers all over the world have now acquired a larger space. Interestingly, researchers of all disciplines may have taken a step toward polymers. Polymer science is one of the fastest-growing areas and connects many other scientific disciplines. Innovation and ease of productivity are the two most important drivers to shift in the direction of polymers.

Polymers permeate every facet of our day-to-day life and form the very basis of our civilization. Polymers now cover a broader spectrum of efforts and effects. Polymers have marked impressions from nano to macro-size applications. Polymers are at the forefront of new technology in separation science. Separation science addresses separating a part of a mixture/solution and the subsequent removal of impurities for purification purposes. Better understanding

among separation science researchers and easy availability of modern separation science and technology are the key drivers towards including polymers. Separation science and technology are witnessing the shift from conventional to polymer materials. Polymers contribute to material science by providing unique model systems as easily manipulated substances to achieve unique morphologies and properties.

Polymeric materials are widely used as adsorbents, ion exchange, and membranes in separation and purification processes. The applications of polymers show great promise in the areas of water purification. This review deals with natural and synthetic polymers used in adsorption, ion exchange, and membranes to separate fluoride ions. The polymers used in each method are described in terms of their properties, structures, and functions. The design of novel polymers with triggered functions presents new opportunities for development in this arena.

Fluoride ions come into the water because of the interaction of water and the solid aquifer. Groundwater

\*Corresponding author, e-mail: [bhattacharyaamit1@rediffmail.com](mailto:bhattacharyaamit1@rediffmail.com)

© BME-PT

is the primary source of drinking water in many countries [1, 2]. Groundwater is essential compared to other water because it can be drunk directly without treatment, provided it is not contaminated. The groundwater composition depends on the geology of the solid aquifer. Literature reports the fluoride-contaminated hotspots worldwide and the population at risk of its exposure [3–6]. Fluoride ions are in their mineral form on the earth's crust, *viz.* fluorite, biotite, and topaz [7, 8]. The other water fluoride source is industrial waste (*viz.* semiconductor, electroplating, aluminium smelter ceramic, steel, cement, fertilizers, glass etching) [9]. It is considered a vital contaminant in drinking water. Drinking fluoride in water increases the risk of dental and skeletal fluorosis [10–13]. Polymer materials are used in various methods for defluoridation from water. Adsorption, ion exchange, and membrane filtration (pressure and electric potential driven) are efficient methods in this arena.

Owing to the following unique characteristics of polymers, interest among chemists and researchers has increased toward separation science. Some of the features are mentioned below:

- **Unbelievably network:** It provides opportunities for tailoring chemical functionalities. The catenation property of carbon makes the polymers of having a long chain. Because of carbon, atoms are free to rotate in respect of one another, and close coiling or folding takes place. The cohesion forces between the molecules and those of the electronic forces (van der Waals forces, H-bond) join the atoms into chains or other structures. The design of specific surface topologies relates to precise functions.
- **Porosity generation:** Polymer structures can change the porosity generation depending on the variation of solvents/nonsolvents. Thus, it can tune the design as it demands. The property can be engineered into the polymeric system.
- **Charge generation:** There may be an inbuilt or tailored surface charge. The surface functionalization feasibility is there to form charged surface enabling adhered ions/solutes.
- **Feasibility of combining with other polymers/inorganics/organics:** Polymeric materials with synergetic or complementary behaviour between the polymer and the inorganics interacting at the molecular scale. The synergistic combination of multifarious functions by different (polymeric)

materials and self-assembly are also feasible. Polymeric materials with its component and added components ensure structural integrity.

- **Choices of polymers:** There are legions of polymers in the market, and the options are easy as it demands.

## 2. Adsorbent materials

Adsorbent materials can take in another substance. It can also be stated as the condition where ions/compounds can attach. They are related to surface phenomena. The adsorbents are widely used in water purification, *viz.*, removal of contaminants in terms of ions/ molecules. There has been a growth in the use of polymers as adsorbents. Some of the features are mentioned below:

- **Availability of large sorbent:** The sorbent polymer materials are abundant. It may be natural or synthetic.
- **Easy tuning of sorbents:** Polymeric sorbent materials modification is easy as per requirement.
- **Insensitive to toxic substances:** Polymeric material is generally insensitive to toxic ions/substances.
- **Fit into simple operational design:** The polymeric sorbent materials can be fit in any functional arrangement. The use of polymeric materials makes the system economical. Thus, the system with polymer materials is commercially viable. The treatment of pollutants at a high concentration is also feasible.

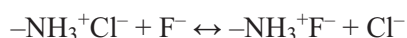
The polymer adsorbent materials are of different categories: biopolymers, synthetic polymers, conducting polymers, and ion exchange resin.

### 3.1. Biopolymers

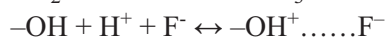
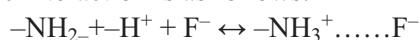
The origin of polymers from bio-resources are termed 'biopolymers'. Plenty of examples (*viz.* chitosan, alginate, carboxy methyl cellulose) of biopolymers acting as adsorbents to the fluoride. Chitosan, the natural biopolymer, has an affinity for negatively charged surfaces. The biodegradable, abundant in nature, the good chelating agent makes it one of the options to prepare low cost and efficiency in defluoridation [14–16]. The homogeneously charged nanoparticles can be incorporated into chitosan. Metal with chitosan *viz.* Fe-chitosan (15.38 mg/g) [17], Al-chitosan (1.7 mg/g) [18], carboxylated chitosan modified ferromagnetic nanoparticles, La<sup>+3</sup> impregnated chitosan/ $\beta$ -cyclodextrin [19] are fluoride scavenging materials. Hydrous mixed metal

oxyhydroxide composites (Fe–Al–Mn@chitosan) make  $F^-$  ions easily accessible to active sites of the porous outer surface. The diffusion of  $F^-$  ions inside the composite matrix made it a better adsorber than fixed Fe–Al–Mn oxyhydroxides [20]. The composite exhibited a maximum adsorption capacity of  $40 \pm 0.5$  mg/g. Al doping chitosan–Fe(III) hydrogel (Al–CS–Fe) showed a high adsorption capacity of 31.16 mg/g [21]. They reported the multiple mechanisms of  $F^-$  adsorption.

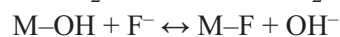
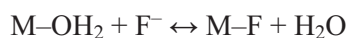
I. Ion exchange between primary amine salt of chitosan and fluoride.



II. In the presence of acid or near the neutralization, the fact of  $-\text{OH}$  and  $-\text{NH}_2$  groups in the metal complex made it positively charged. The electrostatic interaction is as follows:



III. Ligand or ion exchange between metal and fluoride:



Lanthanum has higher affinities for fluoride ions. The combination of gelatin [22], chitosan beads [14, 23] made the composite effective for defluoridation. In this direction, the combination of La(III) with carboxymethyl cellulose (CMC) showed excellent capabilities in defluoridation [24]. The active functionalities formed complexes with metal ions and crosslinking agents [25]. The maximum removal efficiencies of CMC-La and linked-CMC-La (by glutaraldehyde) were 98.85 and 99.31%, respectively, in the case of a fluoride concentration of 40 mg/l. Alginate (SA) and carboxymethyl cellulose (CMC) have a large number of active groups (*viz.* hydroxyl, carboxyl) and have the ability to adsorbents with high removal efficiency [26]. Alginate/carboxymethyl cellulose sodium composite loaded with calcium and aluminium (SA/CMC–Ca–Al) developed the defluoridation abilities. Ca(II) and Al(III) were incorporated into SA/CMC through sodium ion exchange. The maximum adsorption amount for fluoride was 35.98 mg/g at pH 2.0, 298.15 K concentration 100 mg/l. Na-alginate is well-focused for its high dispersion, biocompatibility, relatively low cost, and porous structure. The alginate-based adsorbent had been shaped in different forms. 3D yttrium-based graphene oxide-sodium alginate hydrogel is one of

the forms explored. It is a 3D macroporous structure composed of 2D sheets of graphene oxide with the uniform dispersion of Y(III) onto the gels. The 3D network structure prevented aggregation and facilitated mass transport to the internal system. The inclusion of graphene oxide nanosheets supported the large specific and abundant functional groups *viz.*,  $-\text{COOH}$ ,  $-\text{OH}$ , and epoxy groups. The maximum adsorption capacity of the hydrogel regarding defluoridation was 288.96 mg/g at pH 4.0 [27]. Alginate-based adsorbent by entrapping trimetallic (Fe–La–Ni) oxide into the matrix was helpful in the defluoridation of water. The natural anionic alginate biopolymer is composed of two different monomers (1→4) linked  $\alpha$ -L-guluronate (G) and  $\beta$ -D-mannuronate (M) [28]. The presence of di-tri valent metal ions facilitated the formation of rigid, ordered, and strong structures. It helped to immobilize the nanopowder for the adsorption of ions. The polymeric matrix showed a very high fluoride ion adsorption capacity, *i.e.*, 333 mg/g.

Carboxymethylcellulose (CMC), a biopolymer with a supramolecular structure, possess metal binding sites [29]. It is a linear one with carboxymethyl ( $\text{CH}_2\text{COO}^-$ ) substituent of negative surface charges. It has excellent coordination abilities with metal ions ( $\text{Al}^{3+}$ ,  $\text{Fe}^{3+}$ ). The hydrated state of ions enriched with  $\text{OH}^-$  ions and water molecules can attach  $F^-$  ions. CMC-g-2-acrylamido-2-methyl propane sulfonic acid (AMPS) /Fe/Al composite hydrogel impregnated with activated charcoal [30] was one of the excellent examples in this part. The maximum defluoridation efficiency of metal oxide incorporated was 84.67% at pH 6 at an initial  $F^-$  concentration of 5 mg/l.

Iron-impregnated pectin-g-poly(amidoxime) was based on low-cost natural polymer [31]. The presence of  $-\text{COOH}$  functionalities in the unit of  $\alpha$ -(1→4)-linked-D-galacturonic acid of pectin made it unique for the chelating agent [32]. It possessed metal ion enrichment capabilities and fluoride ions sorption in acidic conditions. The modification through the grafting of poly(amidoxime) and derivatization reactions enhanced the potential of defluoridation. Amidoxime functionalization was tethered pectin-Ca beads to achieve better removal capabilities. The synthesized amidoxime functionalized Ca-pectinate beads were also immobilized with iron to increase their efficiencies. Pectin-g-poly(amidoxime)-Fe complex (Figure 1) showed ~70% adsorption ability at pH 5.0.

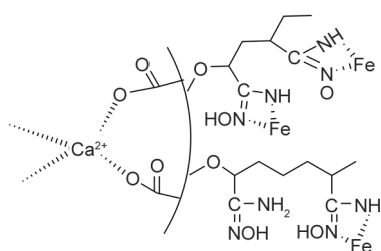


**Figure 1.** Proposed chemical structure of pectin-g-poly(amidoximes)-Fe complex [31].

### 3.2. Synthetic polymers

The polymers generated from the synthetic route are called synthetic polymers. The crosslinked polyvinyl alcohol (PVA)-bimetallic systems *viz.* Ca–Zr–PVA polymer composites were particular adsorbents as the significance of the presence of two metals (Ca/Zr) in terms of selectivity of ions and synergistic effect. The choice of polymer films had a larger surface area. Moreover, a polymer like PVA is always advantageous because of its non-toxic and degradable nature. The fluoride adsorption of the Ca–Zr–PVA polymer composite was 97.14%, compared to pure crosslinked PVA (32%) [33].

Crosslinked PVA gels form due to acetal bridges between the PVA chains. The hydrogels feature their porous network and easy diffusability of ions across the surface. PVA-iron-zirconium hydrogel (PFZH) and PVA-copper-zirconium hydrogel (PCZH) showed promising defluoridation capabilities (100%) [34]. The defluoridation by the systems was pH-independent and least affected by commonly interfering ions ( $\text{HCO}_3^-$ ,  $\text{PO}_4^{3-}$ ,  $\text{Cl}^-$ ,  $\text{NO}_3^-$ ,  $\text{SO}_4^{2-}$ ).

Hydrophilic hyper-crosslinked porous polymer networks, having high surface areas of  $2000 \text{ m}^2/\text{g}$  and robust chemical and thermal stabilities [35, 36], were synthesized from 2,2-biphenol (HHCP1) and bisphenol A (HHCP2) monomers [37]. Ca-loaded networks of the porous polymer resulted in a defluorinating adsorbent. Two monomers had different Ca-loading capacities. Both Ca-loaded networks were effective in defluoridation. Ca-loaded HHCP1 showed the ability of  $(267 \pm 34 \text{ mg/g})$ , whereas HHCP2-Ca had a lower power of  $96.2 \pm 10 \text{ mg/g}$  with faster uptake kinetics.

The adsorbents prepared in the in situ polymerization method were also explored. Crosslinked porous polymeric adsorbent poly(zirconyl methacrylate-*co*-methylmethacrylate) (p(ZrDMA-*co*-MMA)) is one of the examples in this area. Due to its non-toxic nature, zirconium is well-accepted in the polymeric adsorbent field, especially defluoridation. The maximum

fluoride adsorption was found to be 96.54% at neutral pH. The possibility of metal ions leaching was avoided [38]. Crosslinked ZrVAc adsorbents were prepared using zirconyl methacrylate (ZrDMA) and vinyl acetate (VAc), ethylene glycidyl methacrylate (EGDMA), through the suspension polymerization method. The maximum fluoride adsorption capacity was found to be 138 mg/g at pH 7.0 [39]. Gupta *et al.* [40] prepared the polymeric adsorbent based on zirconium dimethacrylate (ZrDMA) and lauryl methacrylate (LMA). The covalently co-ordinated metallic-polymeric moiety brings a stable network. During the adsorption process, it did not leach out any trace elements (Zr,  $\text{F}^-$ ). The crosslinked polymer based on the combination of organometallic vinyl monomers (ZrDMA and AgMA), vinyl monomers (MMA), and (EGDMA) showed the highest adsorption capacities ( $q_{\text{max}}$ ) were obtained as 64 mg/g [41]. The three-dimensional metallopolymer microsphere quaternized poly(zirconyl dimethacrylate-*co*-vinylbenzyl chloride) [ZrVBZ] was reported by Gupta *et al.* [42]. The free radical polymerization in the presence of crosslinker (ethylene glycol dimethacrylate) and porogen (toluene) formed the porous network polymer. The schematic presentation for the polymer synthesis is shown in Figure 2. The maximum adsorption capacity of the polymer for fluoride was 116.5 mg/g. Recently, a similar compound based on poly(zirconyl dimethacrylate-*co*-vinyl imidazole) was also reported. The maximum fluoride adsorption capacity was 109.6 mg/g [43].

Magnetic adsorbents are now familiar in this arena to increase separation efficiency. As fluoride is a hard base with a small size and high, electronegativity magnetic hydrogels have good separation abilities, which were strengthened by lanthanum loading in lanthanum-loaded magnetic cationic hydrogel (MCH-La) [44]. The hydrogels are prepared by crosslinking (3-acrylamidopropyl) trimethylammonium chloride (APTMACl), *N,N*-methylene bisacrylamide (MBA), *N,N,N',N'*-tetramethylethylene-diamine (TEMED) in the presence of  $\gamma\text{-Fe}_2\text{O}_3$ . The maximum fluoride adsorption capacity for MCH-La was 136.78 mg  $\text{F}^-/\text{g}$  at an equilibrium fluoride concentration of 29.3 mg/l and pH 7.0.

Generally, triaryl boron-containing  $\pi$ -conjugated systems are known for their electronic and photophysical properties. But, these systems *viz.* (boron based conjugated microporous polymer) were also explored in defluoridation and  $\text{F}^-$  ion sensors [45]. It was the

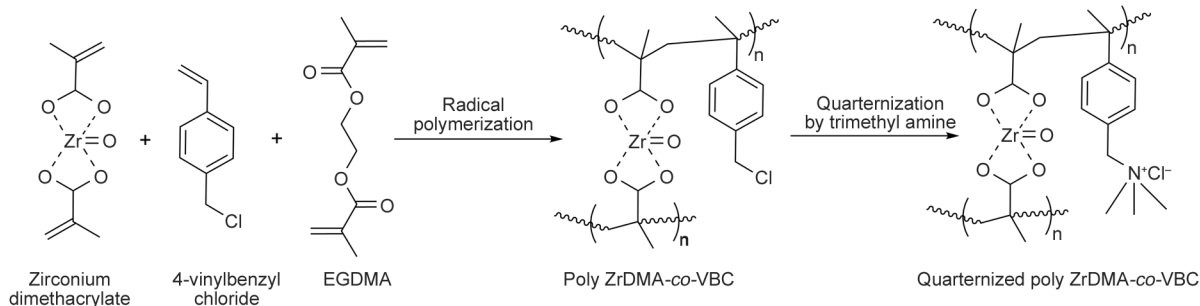


**Figure 2.** Schematic presentation of synthesis of ZrVBZ adsorbent [42].

product of polycondensation of tris(4-bromo-2,6-dimethylphenyl)borane and tris(4-dihydroxyboranylphenyl)amine (TBPA). The conjugated polymer showed an excellent adsorption capacity of up to 24 mg/g at equilibrium fluoride concentrations of 16 mg/l and a temperature of 298 K.

Crosslinked chitosan-polyvinyl alcohol (Ch-PVA) materials were used for defluoridation [46]. The cross-linking materials used were ethylene glycol diglycidyl ether (EGDE) and sodium tripolyphosphate pentabasic (TPP). The presence of epoxy groups bridged the condensation reaction between chitosan and PVA. The ionic crosslinking occurred between TPP and chitosan chains. The maximum fluoride adsorption capacity of the crosslinked material was 12.64 mg/g at pH 7 and 30 °C.

The adsorbent iron-aluminium-cerium tri-metal hydroxide (Fe–Al–Ce) with a polymer latex acrylic-styrene binder coated on the sand by spraying technique. The system showed fluoride adsorption of 3.46 mg/g at pH 7.0 and 50 mg/l fluoride concentration [47]. Polysulfone/ZnCr<sub>3</sub>-NO<sub>3</sub>-layered double hydroxides (PS/ZnCr<sub>3</sub>-NO<sub>3</sub>-LDH) composites were prepared by phase inversion and investigated for defluoridation by Koilraj and Kannan [48].

### 3.3. Conducting polymers

The loss of activities due to agglomeration, low adsorption capacities, reduced selectivity, and difficulty in isolation from an aqueous medium prompted separation researchers to prepare hybrid materials consisting of polymers having large active porous surfaces. In this direction, one of the approaches is adsorbents in conducting polymers domain. Conducting polymers are in conjugation and charge carriers. The charge carriers have gained the freedom to move over the entire chain. It has exchangeable counter ions from the oxidative solution. Thus, it can adsorb the ions on its surface. They exhibit desired

properties like large surface area, chemical stabilities, modifiable surface chemistry, and high affinity for anionic pollutants [49, 50].

The conducting polymer-based materials have four categories, viz. (a) conducting polymer, (b) conducting polymer/adsorbents, (c) conducting polymer/clay minerals, and (d) conducting polymer/inorganic matrices. Hydrous TiO<sub>2</sub>/polypyrrole hybrid nanocomposite showed fluoride's synergistic effect in adsorption capacity. The maximum adsorption capacity gained is 31.93 mg/g [51]. Polypyrrole (PPy)/HSnO (% loading, Pyrrole = 47.41, HSnO = 52.59) exhibited the best defluoridation performance and the maximum adsorption capacity 28.98±0.37 mg/g at 328 K. The hybrid materials possessed good regeneration properties and high desorption efficiency of 95.81% up to three cycles [52]. Fe<sub>3</sub>O<sub>4</sub>/PPy nanohybrid composite showed its excellence in adsorption even after 20 recycles [53]. The adsorption was enhanced in a rotating magnetic field. The maximum removal rate was 78.2% for fluoride (10 mg/l) aqueous solution [54].

The hydrous CeO<sub>2</sub>-Fe<sub>3</sub>O<sub>4</sub> decorated polyaniline fibers gained a maximum capacity was 93.46–117.64 mg/g in a broad pH of 3–10 [55]. Hydrous ZrO<sub>2</sub>-polyaniline (PANI) nanofibers showed the potential of high adsorption capacity towards F<sup>-</sup> ions [49, 56]. Cellulose nanofiber-PANI-templated ferrihydrite nanocomposite, the unique hybrid material, showed an adsorption capacity of 50.80 mg/g [57].

The synergistic effect of polyaniline/alumina (PANI/AlO) and PPy/AlO composite in terms of defluoridation (Figure 3) was reflected in the study of Karthikeyan *et al.* [50]. The maximum amount of adsorption was 6.6 and 8 mg/g for polyaniline/alumina and polypyrrole/alumina, respectively. The removal of fluoride ions by alumina occurs through the formation of an aluminium-fluoro complex, whereas for conducting polymer, it is through ion exchanging of dopant ions.

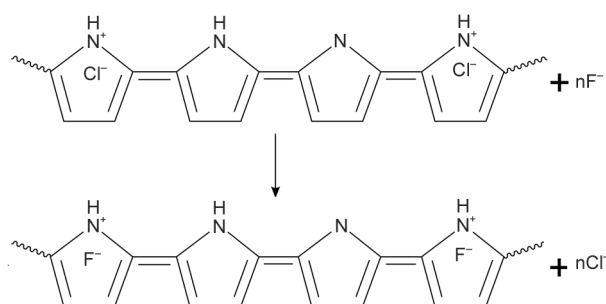


**Figure 3.** Ion exchange phenomena of doped ionizable chloride ions with fluoride ions [50].

Clay-based conducting polymer, polypyrrole-montmorillonite (PPy–MMT) composite, had the potential for defluoridation activities [58]. The maximum adsorption was 5.10 mg/g compared to 2.66 mg/g alone. The physical adsorption and ion exchange mechanistic pathways developed a synergetic approach to fluoride removal. Polypyrrole with attapulgite (magnesium aluminium silicate material) formed a composite showing defluoridation potential from an aqueous solution [59]. The adsorption efficiency was 74.71% at a sorbent dose of 0.18 g.

### 3.4. Ion exchange resin

It is another important class of materials used in this defluoridation arena. The aluminium form of each aminomethyl phosphonic acid-type ion exchanger based on the copolymerization of two monomers (*i.e.*, methyl methacrylate-ethylene glycol dimethacrylate) showed selectivity and excellent capacity for fluoride separation. The uptake was better than that of the commercially available strongly acidic cation exchanger Indion 225 and aminomethyl phosphonic acid-type chelating ion exchanger Duolite ES 467 [60]. Samatya *et al.* [61] prepared the Zr-immobilized resin based on Diolery phosphoric acid (DOLPA) and divinyl benzene (DVB) through surface template polymerization. The preparation was carried out w/o/w an emulsion. PVA was taken as an emulsion

stabilizer. Polystyrene was used as porogen to immobilize more adsorption sites. The schematic illustration of the prepared resin is presented in Figure 4. The removal of fluoride ions using the Zr(IV) complex and phosphate functionality as a recognition site.

Modification by ethylenediamine of synthetic copolymeric resin *viz.* vinylbenzyl chloride/divinylbenzene (VBC/DVB), styrene/divinylbenzene/vinylbenzylchloride (ST/DVB/VBC) and acrylonitrile/divinylbenzene/vinylbenzylchloride (AN/DVB/VB) examined for defluoridation experiment. The resin's mechanistic aspects are presented as follows (Figure 5). AN/DVB/VBC-ED resin possessed higher defluoridation capacity (DC) than ST/DVB/VBC-ED and VBC/DVB-ED resins among all the synthetic resins [62].

Cai *et al.* [63] prepared nanocrystalline Li/Al-based layered hydroxide (LALDH-201) impregnating Li/Al inside a commercial polystyrene anion exchanger D201. The fixed-bed adsorption of LALDH-201 of the Fluoride contaminated groundwater was 4.1 mg/l, ~11 times compared to the anion exchanger D201. A similar study was also carried out using nanosized hydrous zirconium oxide (HZO) within anion exchanger D201. It showed 7–14 times capacity compared to D-201 [64]. ZrO<sub>2</sub> nanoparticles on polymeric anion exchanger resin. Hybrid anion exchange resin was reported by Singh *et al.* [65]. The maximum fluoride uptake capacity of the resin resulted in 12.0 mg/g. Nanosized cerium oxides (NCO) inside a porous polystyrene anion exchanger (PAE) functionalized with positive quaternary amine groups ( $[-N(CH_3)_3^+]$ ) showed the ability for efficient fluoride removal from wastewater [66].

Robshaw *et al.* [67] had shown the defluoridation potential of Purolite<sup>®</sup> S950+ loaded with lanthanum ions [67]. Purolite<sup>®</sup> S950+ commercial resin is a macroporous, weak acid, chelating one. It consisted of a styrene/divinylbenzene main chain with amino

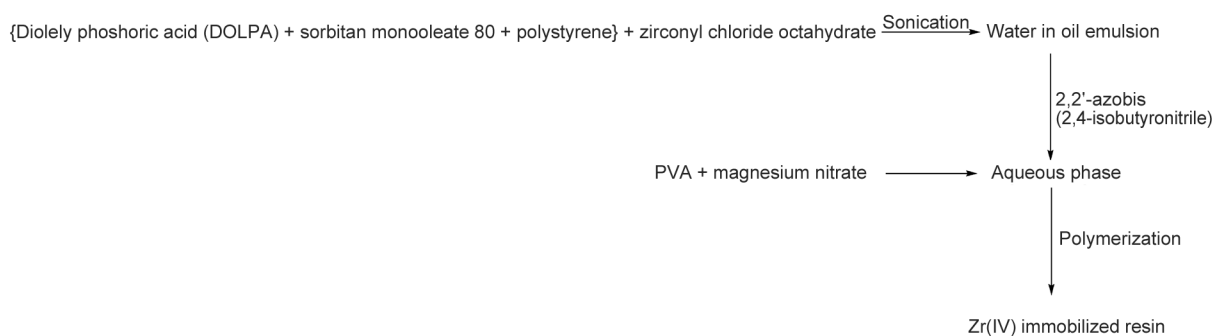
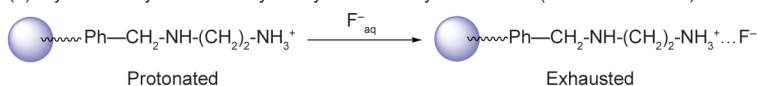


**Figure 4.** Schematic presentation of surface template polymerization with water/oil/water emulsions [61].

(1) Vinylbenzyl chloride/divinylbenzene-ethylenediamine (VBC/DVB-ED) resin



(2) Styrene/divinylbenzene/vinylbenzylchloride-ethylenediamine (ST/DVB/VBC-ED) resin



(3) Acrylonitrile/divinylbenzene/vinylbenzylchloride-ethylenediamine (AN/DVB/VBC-ED) resin

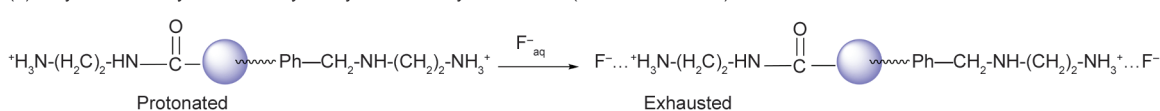


**Figure 5.** Reaction scheme of fluoride sorption onto different resins (VBC/DVB-ED, ST/DVB/VBC-ED, and AN/DVB/VBC-ED) [62].

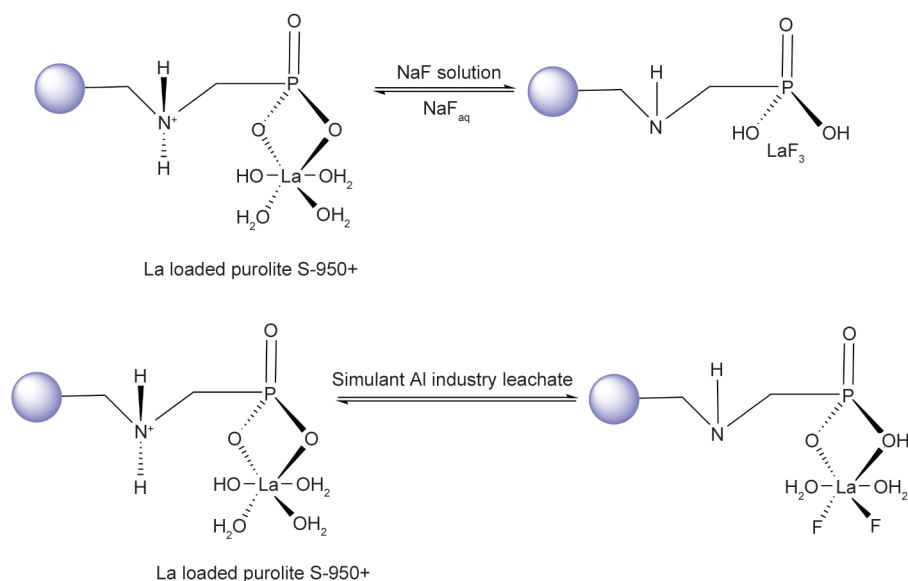


**Figure 6.** Schematic presentation of fluoride adsorption by La-Purolite S 950+ [67].

phosphonic acid functional groups. The La-modified one exhibited a large maximum defluoridation capacity of  $187 \pm 15$  mg/g from the NaF solution and  $126 \pm 10$  mg/g from the leachate. The schematic diagram of the fluoride uptake is represented in Figure 6.

Meenakshi and Viswanathan [68] experimented with Indion FR 10 (IND), crosslinked polystyrene, the chelating resin. The results showed that chelating resin was more selective than an anion-exchange resin for fluoride removal. The mechanistic aspect is in the following figure (Figure 7).

The incorporation of aluminium(hydr)oxide material inside the pores of Purolite A520E (strong-base ion-exchange resin) made it promising for fluoride removal. Purolite A 520E is macroporous polystyrene

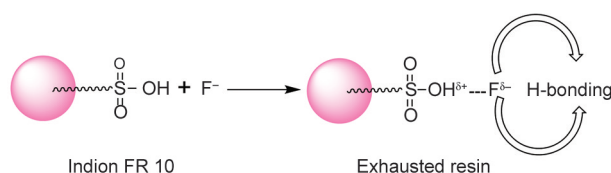


**Figure 7.** Adsorption of fluoride ions by Indion FR 10 resin [68].

crosslinked with divinylbenzene with a quaternary ammonium functional group [69].

The pulverized spent resins were loaded with Zr(IV) ions to develop adsorption sites, which effectively adsorb fluoride ions. The acidic cation exchange resin (MUROMAC MBX8-WH) was polystyrene crosslinked by divinyl benzene and contains sulfonic acid groups [70]. At first, Zr(IV) was adsorbed following the cation exchange reaction. Consequently, the –OH

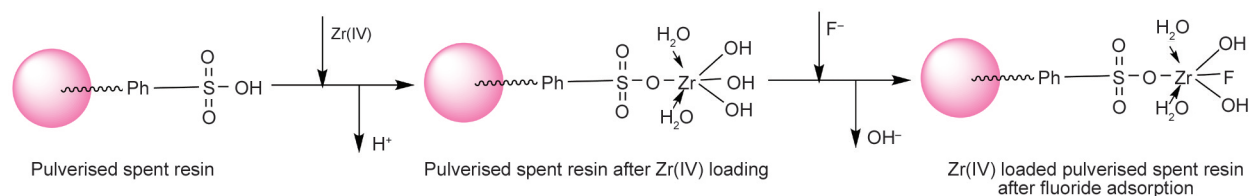


**Figure 8.** Zr(IV) Adsorption mechanism onto spent cation exchange resin powder and that of fluoride ions on the Zr(IV)-loaded spent exchange resin powder [70].

functional group was replaced by fluoride ion respectively (Figure 8).

Amberlite XAD-4TM (styrene-divinyl benzene) had been modified by introducing amino functionality onto the aromatic ring for its application in fluoride remediation [71]. An Al(III)-loaded and Al(OH)<sub>3</sub>-coated chelating resin Lewatit TP 260 (Crosslinked polystyrene, aminomethylphosphonic acid) was prepared. Both the modified forms of the resin showed their abilities to remove F<sup>-</sup>. The maximum adsorption capacity of Al(OH)<sub>3</sub>-coated resin and Al(III)-loaded resin was 0.55 and 0.40 mg/g, respectively [72]. Lanxess TP208 (crosslinked polystyrene with chelating diamino acetate group), a weakly acidic macroporous cation exchange resin exchanged with Al<sup>3+</sup> ions, showed a selective mode of removing fluoride ions [73]. Amberlite IRA400Cl anion resin, polystyrene divinyl benzene copolymer matrix, and chloride as mobile ions showed 76% fluoride removal [74].

#### 4. Membrane materials

There are unequivocal shreds of evidence that membranes are the best water purification solution. The membrane system can be tailor-made per the people's requirements by making it compatible with water sources and demand. The 'fluoride in water' crisis challenges us to develop solutions for a very urgent issue. The membrane sector is vital as a driver of defluoridation techniques and time-to-market development [75–78]. The membranes have unique specialities in separation science as no need of chemicals are needed and have the capabilities to work under a wide pH range. The relevant membrane processes include nanofiltration, reverse osmosis, membrane distillation, and electrodialysis.

The defluoridation activities are mostly fit for nanofiltration as low-pressure RO membranes. Nanofiltration is a separation process positioned between ultrafiltration and reverse osmosis. It replaces conventional methods of water softening with more low pressure than reverse osmosis. The molecular weight

cut off's (MWCO) for the membranes is generally 300 to 1000 Da (diameter in ~1 nm) [79–81]. It showed selectivity in ionic species, with weaker monovalent ions retention than bivalent ions. The process is applicable for total solid retention for salts with low concentrations. The high negative charge of fluoride makes it better retention through the nanofiltration process.

Polymers have flexibility in the preparation of membranes as it inherits the property of pores and charge generation. The breadth of polymers available for membranes has grown in the past few decades. The polymer research echoed this aspect of their behaviours because of its trouble-free processibility, ability to last, and lower price than the other parallel materials. The 'in-built' configurations make it feasible for the separation of ions. Moreover, they are flexible in terms of blending, composite, and surface modification as necessary. Of course, compatibility issues are to be considered. Thin film composite (polymer-based) membranes marked their position in defluoridation.

The composite signifies that different polymers are put together to be useful in applications. In the membrane arena, thin-film composite is a revolutionary technology. It consists of two polymer layers (*i.e.*, support and selective layer). The schematic presentation is as in Figure 9. The significance of the polymer support layer is to bring mechanical strength to sustain higher pressure in its engineering shape. The polymeric support layer was embedded in nonwoven polyester support, which imparted mechanical strength so that

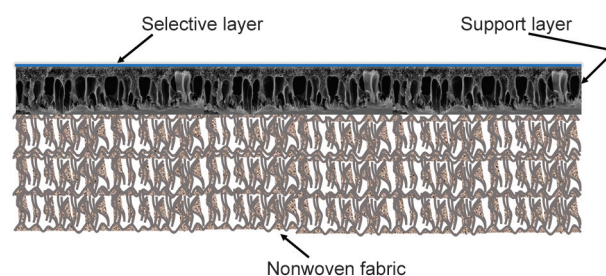


**Figure 9.** Schematic presentation of thin film composite membrane.

the membrane could be artfully worked out in shape and endure higher pressure. The support layer was chosen that fits in phase separation. The wet phase separation technique forms the pores on support layers. It means that diffusive transport of solvent-non-solvent takes place in polymeric matrices. In this regard, a few polymers (*viz.* polysulfone, polyether sulfone, polyvinylidene difluoride) are commonly used. The selective layer controls performance (flux and rejection), whereas the porous support layer is for the sustainability of the selective layer with a minimum resistance in permeate flow. Thus, the composites have specialities, and two important layers can be tuned for different functions.

The selective layer is polyamide considering the importance of  $-\text{CONH}-$  in biological systems. The polyamide formation occurs in situ through an interfacial polymerization reaction between diamines and acids/acid chlorides. The chemistry is represented in Figure 10. It is a straightforward reaction to form a polymer network structure consisting of two/more monomers in different solvents at the interface. The selective layer controls performance (flux and rejection), whereas the porous support layer is for the sustainability of the selective layer with a minimum resistance in permeate flow. Thus, the composite has a speciality, and two important layers can be tuned for different functions. Different amines and acid chlorides are used in interfacial polymerization to form polyamides [82]. Literature reports regarding the various commercial polyamide nanofiltration/low-pressure RO membrane exist. However, the detail of the chemistry of the membrane preparation is not revealed.

Extensive study has been done regarding the use of commercial membranes in defluoridation. As the report mentioned, we intend to unveil the membranes' chemistry and defluoridation potential. BW30 and NF270 (Dow FilmTech™, Minneapolis, MN, USA) are polyamide thin film composite (TFC) membrane. BW30 is a fully aromatic polyamide-based RO membrane, whereas NF270 is a piperazine-based

polyamide NF membrane with semi-aromatic, weakly acidic  $\text{COO}^-$  groups [83]. NF 270 is rather a loose membrane, whereas BW30 is a tight one [84, 85]. The fluoride rejection of NF 270 was lower than BW30. Filmtec NF70-2540 membrane (DOW Chemical, Denmark) having MWCO 180 Da used a thin-film polyamide composite on a polysulfone support designed for tangential filtration [86]. The fluoride rejection was  $>94\%$  for 6 bar pressure. Choi *et al.* [87] experimented with NTR-7250 (polyvinyl alcohol-piperazine based) membrane and compared the performances with NTR-7450 (Nitto Denko) (polysulfone based). NTR-7450 ( $-10$  mV) has a higher surface potential than NTR-7250 ( $-5$  mV at around pH 7). It showed a higher rejection rate than the NTR-7250. The rejection rate of fluoride was  $72\%$  for NTR-7450 whereas for NTR-7250 it was  $70.4\%$  (5 ppm).

The separation of fluoride with the Osmonics spiral module containing the HL 2514 T membrane was carried out. The membrane featured molecular weight cut-off (MWCO) for the organic compounds of about 150 to 300 Da. The module was  $\sim 64$  mm in diameter and 356 mm in length. The HL membrane showed maximum  $>80\%$  fluoride retention [88]. In a different experiment, two commercial polyamide membranes (NF90 and NF400) had different MWCOs, 90 and 400. NF90 rejected all the fluoride ions practically. There was no influence of feed concentration on fluoride, whereas NF400 showed no remarkable performances [89]. Three polyamide nanofiltration membranes (NF70 (Film Tec), DESAL 5DL (Osmonics), and MT 08(PCI)) were used for the defluoridation in natural brackish water from Senegal [90]. The efficiencies of these membranes were closely linked to the nature of the feed solution. The composite membranes were shaped into spiral wounds of a standard size (2540). The rejection rate [%] was 91, 83, and  $90\%$ , respectively, for 5 mg/l, at 8 bar pressure and pH 6 for these membranes [90, 91]. Valentukeviciene *et al.* [91] experimented with polyamide NF270 (piperazine based polyamide)

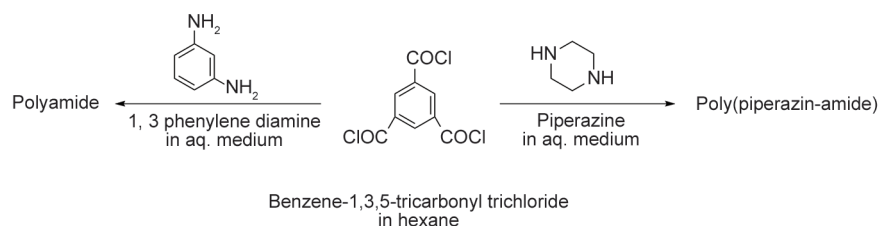


**Figure 10.** Chemistry of selective layer in thin film composite.

and NF90 (aromatic polyamide, Filmtec Dow) membranes. The NF90 can be regarded as a ‘dense’ and the NF270 as a ‘loose’ NF membrane. Both membranes are negatively charged (MWCO of NF90: 200 Da, NF270: 300 D [92]. NF270 represented lower roughness than NF90 [93]. The roughness of the membrane depends on the nature of monomers in interfacial polymerization, support polymers, and preparative conditions. The characteristic features influenced defluoridation performance. NF90 polyamide membrane retained 92% of fluoride ions, whereas NF270 polyamide kept 67%. The permeability results revealed that the NF270 membrane was more productive than the NF90 membrane, as evidenced by Hoinkis *et al.* [92] reported. NF270 could keep the fluoride level below the maximum contaminant level (MCL) (1.5 mg/l) up to 10 mg/l feed concentration. In contrast, the NF90 could keep fluoride permeate concentration below MCL for <20 mg/l feed concentration. Commercial spiral wound RO-SG-2514 (Osmonics) and NF90-2540 (Dow-Filmtec) were used for the defluoridation of water and metal packaging industrial effluent [94]. Both were thin film polyamide composite membranes. The removal efficiency for fluoride was influenced by several parameters: feed concentration, transmembrane pressure, ionic strength, nature of cation associated with fluoride, and pH [95]. NF90-2540 membrane showed maximum rejection (>97.6%), whereas it was 92–97% for RO-SG. Diwara *et al.* [96] experimented with nanofiltration (NF) and low-pressure reverse osmosis (LPRO), both from Dow Chemical, in a membrane filtration plant constructed by Pall Corporation. The NF membrane

resulted in a fluoride retention rate of 63.3–71%, whereas the low-pressure reverse osmosis (LPRO) membrane rejected 97–98.9%. Gedam *et al.* [97] experimented with defluoridation using Filmtec Spiral wound with a composite polyamide membrane module (model no. TW30-1812-75) with an effective area of 0.1054 m<sup>2</sup>, module length of 300 mm and diameter of 40 mm. The spiral-wound membrane module was based on a polyamide membrane with an effective area of 2.5 m<sup>2</sup> (RE 2540, Saehan) [98]. It retained fluoride ions (retention factor >98%). Shen & Schäfer used six commercial membranes (BW30, BW30-LE, NF90, NF270, TFC-SR2 and TFC-SR3) [99]. All these membranes are thin film composite (TFC) membranes with a polyamide-based active layer [100–102]. Some details of the commercial membranes are summarised in Table 1. Chakraborty *et al.* [104] experimented with three thin film polyamide composite nanofiltration membranes (NF-1, NF-2, and NF-20), Sepro Membranes Inc. (USA) for defluoridation. The fluoride rejection [%] was 95, 78, and 86, respectively. The separation performances depended on the difference in characteristics of the membranes. The features depend on the polymers and the membranes’ preparation conditions. Three polyamide nanofiltration thin-film composite (TFC) membranes SR-1 (Koch Fluid System), DS-5-DL (DL) (Osmonics), and DS-51-HL (HL) (Osmonics) were used for the defluoridation performance [105]. The defluoridation performance increased with the higher solution flux and the lower feed concentration. Table 2 depicts the membrane’s physical parameters (pore radius, pure water permeability, and surface electrical potential). The various

**Table 1.** Some details of some commercial membranes.

Membrane	Type	Diamine	Reference
A-15 (Permasep)	Polyamide	1, 3 phenylene diamine	[103]
NF90 (Dow filmtech)	Polyamide	1, 3 phenylene diamine	[102]
NF270 (Dow filmtech)	Poly(piperazine-amide)	Piperazine	
HL (GE Osmonics)	Poly(piperazine-amide)	Piperazine	
DL (GE Osmonics)	Poly(piperazine-amide)	Piperazine	
BW30 (Dow filmtech)	Polyamide	1, 3 phenylene diamine	

**Table 2.** Some parameters of different commercial membranes [105].

Membrane	Pure water permeability, $L_p \cdot 10^9$ [m <sup>3</sup> /(m <sup>2</sup> ·s·kPa)]	Membrane pore radius, $r_p$ [nm]	Membrane electrical potential, $\Psi$ [mV]
SR-1	24.47±0.24	0.70±0.29	35.1±0.27
DS-5-DL (DL)	21.20±0.32	0.58±0.18	35.0±0.63
DS-51-HL (HL)	25.04±0.22	0.41±0.02	53.5±6.83

parameters (*viz.*, the support polymer rejecting polymer layer, reaction conditions) influenced the characteristics.

Researchers [106, 107] experimented with the four RO/NF polyamide membrane systems BW30, LE, NF90, and NF270. The first two were for brackish water, whereas NF90 and NF270 were for nanofiltration applications. NF90 membrane exhibited the best overall performance in water quantity and quality among the four. It was a pilot-scale solar-powered membrane system and employed high-fluoride brackish water in northern Tanzania. Throughout a typical solar day, the NF90 membrane system produced 1582 l of drinking water in permissible fluoride limits, with an average recovery of 27.8% and average specific energy consumption (SEC) of 1.6 kWh/m<sup>3</sup>. Filmtec XLE-440 RO element was used for defluoridation [108]. The composition is unknown. The blending strategies were adopted to make it economical. The RO permeate water with a fluoride concentration of <0.03 mg/l was blended with the artificial groundwater to ensure a fluoride level below 1.3 mg/l in the drinking water.

The exciting study of Saxena *et al.* [109] showed the performance variation of poly(piperazine-amide) coating on different recycled stages of polysulfone (Ps) membranes (I<sup>st</sup> to VIII<sup>th</sup>). The ~15% increase in separation for 10 mg/l fluoride from Memb.-I-Pip to Memb.-VIII-Pip. The maximum separation of fluoride is 84.9% for Memb.-VIII-Pip.

Another attempt had been made to study the consequence of salt in a gelation bath and interfacial polymerization regarding the behaviour of poly(piperazine-amide) TFC membranes to separate fluoride from water. The flux through the polysulfone (Ps) membrane decreased with total dissolved salts (TDS). The increase in salt concentration in the aqueous phase of the interfacial reaction influenced the salt separation abilities of the TFC membranes. The maximum separation of fluoride was ~88% for the prepared membrane in which the salt concentration of the aqueous medium was 5 mg/l in the interfacial polymerization [110].

Apart from the thin film polyamide composite membranes, a few other membranes were experimented with. Iron(III) oxide (Fe<sub>2</sub>O<sub>3</sub>) nanoparticles modified polyethersulfone (PES)/cellulose acetate (CA) blend membranes were one of them [111]. Composite membranes were prepared by incorporating various amounts of Fe<sub>2</sub>O<sub>3</sub> nanoparticles. The defluoridation

potential was confirmed of the Fe<sub>2</sub>O<sub>3</sub> nanoparticles for blended PES/CA membranes. The maximum fluoride removal efficiency of 70.3% was observed for a single run.

The hydrophobic nature of the polymers and polymer membranes played a role in membrane distillation. Plattner *et al.* [112] used commercial polytetrafluoroethylene (PTFE) membrane (General Electric, USA) in membrane distillation (MD). The key feature is the vapour-driven force compared to other pressure-driven technologies in membranes [113]. Direct contact MD produced high-quality water permeate (96–99% F rejection). Coupling with vacuum-enhanced DCMD (VEDCMD), the permeate flux increased by 42%. Hydrophobic polyvinylidene fluoride (PVDF) hollow fiber membranes in membrane distillation [114]. Direct contact membrane distillation (DCMD) is one of the techniques where the hydrophobic membrane directly partitions the feed and the distillate. It was simple, and the condensation occurred inside the membrane module. The maximum permeate flux was 35.6 kg/(m<sup>2</sup>·h).

The ion exchange membranes can remove fluoride ions from water. It shows ion permselectivity and is classified into cation and anion exchange membranes. The positively charged groups are fixed to the anion exchange membrane, and cations are rejected by the positive charge and cannot permeate through anion exchange membranes. This is because anion exchange membranes are only permeable by anions. The electro dialyzer controls selective permeation. The ion exchange membranes have advantages over the ion exchange granules regarding regeneration. The regeneration is not required as it allows ions to permeate by direct current in an electro dialyzer.

The ion exchange membranes are polymer-based. Mostly anion-exchange membranes (*viz.* DSV, AFX, AMX, ACS, AFN, AHA, and SB-6407) had the defluoridation potential [115–117]. AFX anion exchange membrane (polystyrene-divinyl benzene-polyvinyl chloride) was used in a diluted solution [118]. The ion exchange group associated with it was –N(R)<sub>3</sub><sup>+</sup>. It was based on the chemical potential difference between the two compartments partitioned by an ion-exchange polymer. The plasma-modified membranes showed better flux and recovery values compared to pristine membranes. Tor [119] used Neosepta-ACM (anion-exchange membrane) (Tokuyama Soda Co. Ltd.) in the Donnan dialysis

condition. ACM membrane possesses quaternary ammonium as functionality. The membrane was in the chloride ion form. The transport of fluoride ions was maximum at pH 6 of the feed phase and pH 1 of the receiver phase. Durmaz *et al.* [117] experimented with anion exchange membranes used to remove fluoride. The nature of membranes was homogeneous and contained quaternary ammonium bases as ionic groups. They (AFN, AHA, SB-6407) were different from each other in the degree of crosslinking. The fluoride transport order was as follows: AFN>AHA>SB-6407.

Polyvinylidene fluoride (PVDF) blend poly(methyl methacrylate)-*co*-poly(chloromethyl styrene) (PMMA-*co*-PCMSt) membranes prepared through a nonsolvent induced phase separation process (Figure 11). Post-treatment with a tertiary diamine (tetramethyl diamino hexane, TMDAH) of the membranes made it fit for defluoridation. The membrane containing 69.5% w/w copolymer and 30.5% w/w PVDF exhibited excellent fluoride removal efficiency [120].

Membrane capacitive deionization (MCDI) is an advanced technique developed by Lee *et al.* [121]. In the MCDI technique, the counterions (ions with a different charge from the local electrode) are more fully depleted through electrode desorption [122]. Capacitive membrane deionization (MCDI) combined with

a monovalent anion permselective exchange membrane (PSM) was the technique for defluoridation [78]. The MCDI unit cell comprised an acrylic plate, anode electrode, cation exchange membrane (NeocceptaCMX, Tokuyama, Japan), nylon spacer, anion exchange membrane (NeocceptaAMX, Tokuyama, Japan, and SelemionASV, Asahi Glass, Japan), a cathode electrode, and acrylic plate.

Porous membrane composites based on poly(vinylidene fluoride-hexafluoropropylene) (PVDF-HFP) with adsorbents (*viz.* montmorillonite (MMT), zeolites (NaY), bayerite (BAY) and hydroxyapatite (CaHAp)) were prepared by thermally induced phase separation [123]. A maximum fluoride separation of 68% was obtained after 6 filtrations for the CaHAp/P(VDF-HFP) composite membranes.

Cellulose acetate-based mixed matrix membrane (MMM) using mixed metal oxides nanoparticles-polymer composite (Fe-Al-Mn@chitosan) as nanofiller was used in defluoridation [124]. The total fluoride ion rejection (11 096 mg F<sup>-</sup>/m<sup>2</sup>) by the M8 membrane (CA: Fe-Al-Mn@chitosan 92:8) was found to be much higher compared to calculated fluoride rejection, which may be expected through adsorption only (92 mg F/m<sup>2</sup>). The two mechanistic ways proposed were electrostatic repulsion between F<sup>-</sup> and negatively charged MMM surface and the

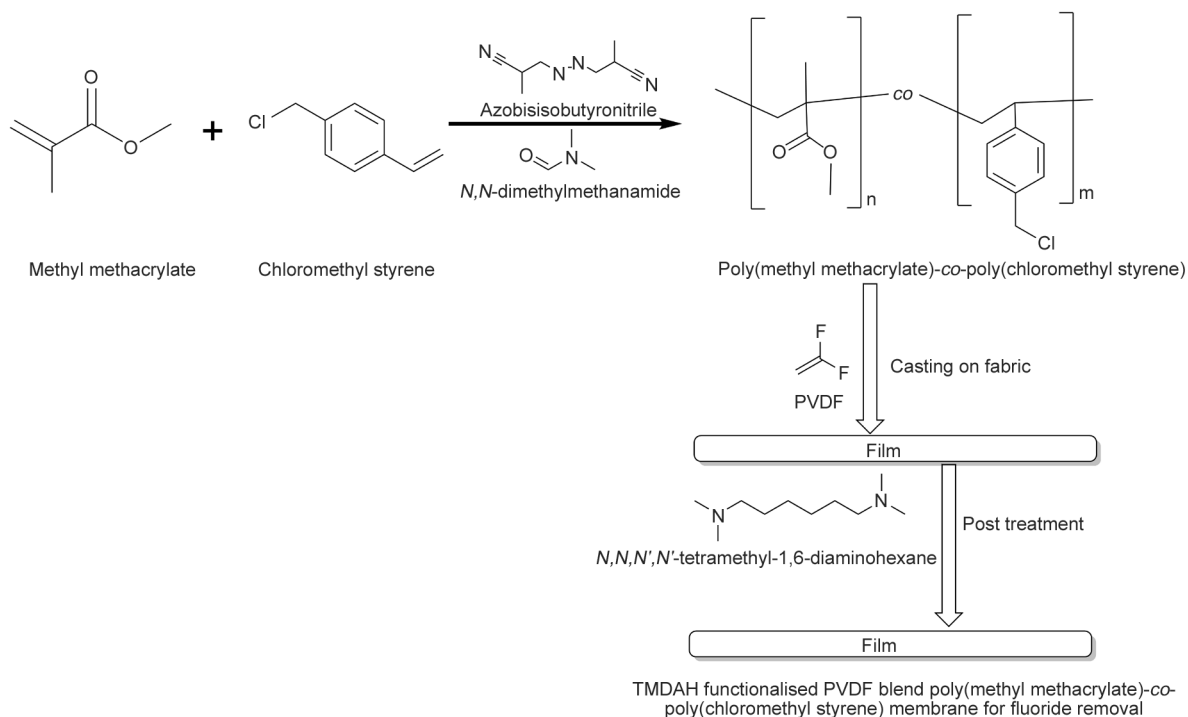


**Figure 11.** Schematic presentation of PMMA-*co*-PCMSt copolymer synthesis and preparation of blend membrane using the nonsolvent induced phase separation and post-treatment with TMDAH [120].

water-swelling nature of chitosan. The swelling nature of chitosan-cellulose acetate pores might create more resistance to water flow.

## 5. Conclusions

The growing global need for water and water treatment has driven the widespread development of Polymeric materials. The researcher's creative power brings forth modified polymers, revealing the possibilities to defluorinate water. The inherent characteristics of polymers made it possible to achieve the requisite properties. The polymeric adsorbent and membrane have paved their way in defluorination. The other direction of polymeric materials is macrocycles (via the crown ether, cyclodextrin, porphyrins) based compounds in which flexible design for specific structures and functions showed many possibilities. It may be promising in the recognition of ions through host-guest chemistry and non-covalent interactions [125, 126]. The stupendous research efforts of polymeric development show people's confidence in the future.

## Acknowledgements

Financial support from the Gujarat Council of Science and Technology (GUJCOST), India, is acknowledged. The manuscript has the CSIR-CSMCR communication number 222/2022.

## References

- [1] Carrard N., Foster T., Willetts J.: Groundwater as a source of drinking water in southeast Asia and the Pacific: A multi-country review of current reliance and resource concerns. *Water*, **11**, 1605 (2019).  
<https://doi.org/10.3390/w11081605>
- [2] Katsanou K., Karapanagioti H. K.: Surface water and groundwater sources for drinking water. in 'Applications of advanced oxidation processes (AOPs) in drinking water treatment' (eds.: Gil A., Galeano L. A., Vicente M. Á.) Springer, Cham, Vol. 67, 1–19 (2017).  
[https://doi.org/10.1007/698\\_2017\\_140](https://doi.org/10.1007/698_2017_140)
- [3] Podgorski J., Berg M.: Global analysis and prediction of fluoride in groundwater. *Nature Communications*, **13**, 4232 (2022).  
<https://doi.org/10.1038/s41467-022-31940-x>
- [4] Jagtap S., Yenkie M. K., Labhsetwar N., Rayalu S.: Fluoride in drinking water and defluorination of water. *Chemical Reviews*, **112**, 2454–2466 (2012).  
<https://doi.org/10.1021/cr2002855>
- [5] Meenakshi, Maheshwari R. C.: Fluoride in drinking water and its removal. *Journal of Hazardous Materials*, **137**, 456–463 (2006).  
<https://doi.org/10.1016/j.jhazmat.2006.02.024>
- [6] Mohapatra M., Anand S., Mishra B. K., Giles D. E., Singh P.: Review of fluoride removal from drinking water. *Journal of Environmental Management*, **91**, 67–77 (2009).  
<https://doi.org/10.1016/j.jenvman.2009.08.015>
- [7] García M. G., Borgnino L.: Fluoride in the context of the environment. in 'Fluorine: Chemistry, analysis, function and effects' (ed.: Preedy V.) Royal Society of Chemistry Publishing, London, 3–21 (2015).
- [8] Sharma S., Bhattacharya A.: Drinking water contamination and treatment techniques. *Applied Water Science*, **7**, 1043–1067 (2017).  
<https://doi.org/10.1007/s13201-016-0455-7>
- [9] Kumar H., Patel M., Mohan D.: Simplified batch and fixed-bed design system for efficient and sustainable fluoride removal from water using slow pyrolyzed okra stem and black gram straw biochars. *ACS Omega*, **4**, 19513–19525 (2019).  
<https://doi.org/10.1021/acsomega.9b00877>
- [10] Adimall N., Li P., Venkatayogi S.: Hydrogeochemical evaluation of groundwater quality for drinking and irrigation purposes and integrated interpretation with water quality index studies. *Environmental Processes*, **5**, 363–383 (2018).  
<https://doi.org/10.1007/s40710-018-0297-4>
- [11] Haritash A. K., Aggarwal A., Soni J., Sharma K., Sapra M., Singh B.: Assessment of fluoride in groundwater and urine, and prevalence of fluorosis among school children in Haryana, India. *Applied Water Science*, **8**, 52 (2018).  
<https://doi.org/10.1007/s13201-018-0691-0>
- [12] Bundschuh J., Maity J. P., Mushtaq S., Vithanage M., Seneweera S., Schneider J., Bhattacharya P., Khan N. I., Hamawand I., Guilherme L. R. G., Reardon-Smith K., Parvez F., Morales-Simfors N., Ghaze S., Pudmenzky C., Kouadio L., Chen C-Y.: Medical geology in the framework of the sustainable development goals. *Science of the Total Environment*, **581–582**, 87–104 (2017).  
<https://doi.org/10.1016/j.scitotenv.2016.11.208>
- [13] Kimambo V., Bhattacharya P., Mtalo F., Mtamba J., Ahmad A.: Fluoride occurrence in groundwater systems at global scale and status of defluorination – State of the art. *Groundwater for Sustainable Development*, **9**, 100223 (2019).  
<https://doi.org/10.1016/j.gsd.2019.100223>
- [14] Bansawal A., Thakre D., Labhsetwar N., Meshram S., Rayalu S.: Fluoride removal using lanthanum incorporated chitosan beads. *Colloids and Surfaces B: Biointerfaces*, **74**, 216–224 (2009).  
<https://doi.org/10.1016/j.colsurfb.2009.07.021>
- [15] Karthikeyan M., Kumar K. K. S., Elango K. P.: Batch sorption studies on the removal of fluoride ions from water using eco-friendly conducting polymer/bio-polymer composites. *Desalination*, **267**, 49–56 (2011).  
<https://doi.org/10.1016/j.desal.2010.09.005>

- [16] Li X., Li Y., Zhang S., Ye Z.: Preparation and characterization of new foam adsorbents of poly(vinyl alcohol)/chitosan composites and their removal for dye and heavy metal from aqueous solution. *Chemical Engineering Journal*, **183**, 88–97 (2012).  
<https://doi.org/10.1016/j.cej.2011.12.025>
- [17] Viswanathan N., Sundaram C. S., Meenakshi S.: Sorption behaviour of fluoride on carboxylated cross-linked chitosan beads. *Colloids and Surfaces B: Biointerfaces*, **68**, 48–54 (2009).  
<https://doi.org/10.1016/j.colsurfb.2008.09.009>
- [18] Swain S. K., Dey R. K., Islam M., Patel R. K., Jha U., Patnaik T., Airolidi C.: Removal of fluoride from aqueous solution using aluminum-impregnated chitosan biopolymer. *Separation Science and Technology*, **44**, 2096–2116 (2009).  
<https://doi.org/10.1080/01496390902881212>
- [19] Preethi J., Meenakshi S.: Fabrication of La<sup>3+</sup> impregnated chitosan/β-cyclodextrin biopolymeric materials for effective utilization of chromate and fluoride adsorption in single systems. *Journal of Chemical and Engineering Data*, **63**, 723–731 (2018).  
<https://doi.org/10.1021/acs.jced.7b00889>
- [20] Chaudhary M., Rawat S., Jain N., Bhatnagar A., Maiti A.: Chitosan-Fe-Al-Mn metal oxyhydroxides composite as highly efficient fluoride scavenger for aqueous medium. *Carbohydrate Polymers*, **216**, 140–148 (2019).  
<https://doi.org/10.1016/j.carbpol.2019.04.028>
- [21] Ma J., Shen Y., Shen C., Wen Y., Liu W.: Al-doping chitosan-Fe(III) hydrogel for the removal of fluoride from aqueous solutions. *Chemical Engineering Journal*, **248**, 98–106 (2014).  
<https://doi.org/10.1016/j.cej.2014.02.098>
- [22] Zhou Y., Yu C., Shan Y.: Adsorption of fluoride from aqueous solution on La<sup>3+</sup>-impregnated cross-linked gelatin. *Separation and Purification Technology*, **36**, 89–94 (2004).  
[https://doi.org/10.1016/S1383-5866\(03\)00167-9](https://doi.org/10.1016/S1383-5866(03)00167-9)
- [23] Thakur N., Kumar S. A., Wagh D. N., Das S., Pandey A. K., Kumar S. D., Reddy A. V. R.: Matrix supported tailored polymer for solid phase extraction of fluoride from variety of aqueous streams. *Journal of Hazardous Materials*, **201–202**, 193–201 (2012).  
<https://doi.org/10.1016/j.jhazmat.2011.11.065>
- [24] Wang J., Lin X., Luo X., Yao W.: Preparation and characterization of the linked lanthanum carboxymethyl-cellulose microsphere adsorbent for removal of fluoride from aqueous solutions. *RSC Advances*, **5**, 59273–59285 (2015).  
<https://doi.org/10.1039/C5RA07024D>
- [25] Viswanathan N., Meenakshi S.: Role of metal ion incorporation in ion exchange resin on the selectivity of fluoride. *Journal of Hazardous Materials*, **162**, 920–930 (2009).  
<https://doi.org/10.1016/j.jhazmat.2008.05.118>
- [26] Wu L., Lin X., Zhou X., Luo X.: Removal of uranium and fluorine from wastewater by double-functional microsphere adsorbent of SA/CMC loaded with calcium and aluminum. *Applied Surface Science*, **384**, 466–479 (2016).  
<https://doi.org/10.1016/j.apsusc.2016.05.056>
- [27] He J., Cui A., Ni F., Deng S., Shen F., Yang G.: A novel 3D yttrium based-graphene oxide-sodium alginate hydrogel for remarkable adsorption of fluoride from water. *Journal of Colloid and Interface Science*, **531**, 37–46 (2018).  
<https://doi.org/10.1016/j.jcis.2018.07.017>
- [28] Sapna, Raghav S., Nair M., Kumar D.: Trimetallic oxide entrapped in alginate polymeric matrix employed for adsorption studies of fluoride. *Surfaces and Interfaces*, **13**, 112–132 (2018).  
<https://doi.org/10.1016/j.surfin.2018.08.005>
- [29] Dogsa I., Tomšič M., Orehek J., Benigar E., Jamnik A., Stopar D.: Amorphous supramolecular structure of carboxymethyl cellulose in aqueous solution at different pH values as determined by rheology, small angle X-ray and light scattering. *Carbohydrate Polymers*, **111**, 492–504 (2014).  
<https://doi.org/10.1016/j.carbpol.2014.04.020>
- [30] Sinha V., Chakma S.: Synthesis and evaluation of CMC-g-AMPS/Fe/Al/AC composite hydrogel and their use in fluoride removal from aqueous solution. *Environmental Technology and Innovation*, **17**, 100620 (2020).  
<https://doi.org/10.1016/j.eti.2020.100620>
- [31] Sharma P., Sen K., Thakur P., Chauhan M., Chauhan K.: Spherically shaped pectin-g-poly(amidoxime)-Fe complex: A promising innovative pathway to tailor a new material in high amidoxime functionalization for fluoride adsorption. *International Journal of Biological Macromolecules*, **140**, 78–90 (2019).  
<https://doi.org/10.1016/j.ijbiomac.2019.08.098>
- [32] Zhu J., Lin X., Wu P., Luo X.: Pectin/Al<sub>2</sub>O<sub>3</sub>-ZrO<sub>2</sub> core/shell bead sorbent for fluoride removal from aqueous solution. *RSC Advances*, **6**, 27738–27749 (2016).  
<https://doi.org/10.1039/C5RA26404A>
- [33] Bhandari R., Janardhana C.: Calcium-zirconium-polyvinyl alcohol polymer composite film as a promising adsorbent for removal of fluoride from aqueous solution. *Desalination and Water Treatment*, **57**, 9437–9443 (2016).  
<https://doi.org/10.1080/19443994.2015.1027961>
- [34] Mani S. K., Bhandari R., Nehra A.: Self-assembled cylindrical Zr(IV), Fe(III) and Cu(II) impregnated polyvinyl alcohol-based hydrogel beads for real-time application in fluoride removal. *Colloids and Surfaces A: Physicochemical and Engineering Aspects*, **610**, 125751 (2021).  
<https://doi.org/10.1016/j.colsurfa.2020.125751>

- [35] Wood C. D., Tan B., Trewin A., Niu H., Bradshaw D., Rosseinsky M. J., Khimyak Y. Z., Campbell N. L., Kirk R., Stöckel E., Cooper A. I.: Hydrogen storage in microporous hypercrosslinked organic polymer networks. *Chemistry of Materials*, **19**, 2034–2048 (2007). <https://doi.org/10.1021/cm070356a>
- [36] Tan L., Tan B.: Hypercrosslinked porous polymer materials: Design, synthesis, and applications. *Chemical Society Reviews*, **46**, 3322–3356 (2017). <https://doi.org/10.1039/C6CS00851H>
- [37] Robshaw T. J., James A. M., Hammond D. B., Reynolds J., Dawson R., Ogden M. D.: Calcium-loaded hydrophilic hypercrosslinked polymers for extremely high defluoridation capacity *via* multiple uptake mechanisms. *Journal of Materials Chemistry A*, **8**, 7130–7144 (2020). <https://doi.org/10.1039/C9TA12285K>
- [38] Khan H., Sharma C. R., Sharma S.: Fabrication of sustainable organometallic polymeric adsorbents for remediation of fluoride from water: A novel approach. *Journal of Water Process Engineering*, **20**, 149–159 (2017). <https://doi.org/10.1016/j.jwpe.2017.10.009>
- [39] Khan H., Gupta A. R., Sharma S.: Organometallic adsorbent for mitigating fluoride from water: An environment-friendly approach. *ChemistrySelect*, **3**, 11765–11774 (2018). <https://doi.org/10.1002/slct.201802406>
- [40] Gupta A. R., Yadav A., Sharma S.: Scavenging fluoride from the aqueous system with porous organometallic three-dimensional architecture: An emerging adsorbent. *Environmental Science and Pollution Research*, **28**, 19166–19178 (2021). <https://doi.org/10.1007/s11356-020-11916-4>
- [41] Gupta A. R., Ranawat B., Singh A., Yadav A., Sharma S.: Zirconium-silver nano organo-bimetallic network for scavenging hazardous ions from water and its antibacterial potentiality: An environment-friendly approach. *Journal of Environmental Chemical Engineering*, **9**, 105356 (2021). <https://doi.org/10.1016/j.jece.2021.105356>
- [42] Gupta A. R., Joshi V. C., Yadav A., Sharma S.: Synchronous removal of arsenic and fluoride from aqueous solution: A facile approach to fabricate novel functional metallopolymer microspheres. *ACS Omega*, **7**, 4879–4891 (2022). <https://doi.org/10.1021/acsomega.1c05456>
- [43] Gupta A. R., Chavda D., Mondal M., Manna M., Sharma S.: Strategic design of advanced sustainable Quaternized poly(zirconyl dimethacrylate-*co*-vinyl imidazole) microsphere as a potential adsorbent for the mitigation of fluoride from aqueous solution. *Journal of Water Process Engineering*, **50**, 103290 (2022). <https://doi.org/10.1016/j.jwpe.2022.103290>
- [44] Dong S., Wang Y.: Characterization and adsorption properties of a lanthanum-loaded magnetic cationic hydrogel composite for fluoride removal. *Water Research*, **88**, 852–860 (2016). <https://doi.org/10.1016/j.watres.2015.11.013>
- [45] Li Z., Li H., Xia H., Ding X., Luo X., Liu X., Mu Y.: Triarylboron-linked conjugated microporous polymers: Sensing and removal of fluoride ions. *Chemistry A European Journal*, **21**, 17355–17362 (2015). <https://doi.org/10.1002/chem.201502241>
- [46] Valdez-Alegria C., Fuentes-Rivas R., Garcia-Rivas J., Arce R. E. Z., de la Luz Jiménez Núñez M., García-Gaitán B.: Synthesis of chitosan-polyvinyl alcohol biopolymers to eliminate fluorides from water. *Biomolecules*, **10**, 156 (2020). <https://doi.org/10.3390/biom10010156>
- [47] Wu H.-X., Wang T.-J., Dou X.-M., Zhao B., Chen L., Jin Y.: Spray coating of adsorbent with polymer latex on sand particles for fluoride removal in drinking water. *Industrial and Engineering Chemistry Research*, **47**, 4697–4702 (2008). <https://doi.org/10.1021/ie800278b>
- [48] Koilraj P., Kannan S.: Aqueous fluoride removal using ZnCr layered double hydroxides and their polymeric composites: Batch and column studies. *Chemical Engineering Journal*, **234**, 406–415 (2013). <https://doi.org/10.1016/j.cej.2013.08.101>
- [49] Parashar K., Ballav N., Debnath S., Pillay K., Maity A.: Hydrous ZrO<sub>2</sub> decorated polyaniline nanofibres: Synthesis, characterization and application as an efficient adsorbent for water defluoridation. *Journal of Colloid and Interface Science*, **508**, 342–358 (2017). <https://doi.org/10.1016/j.jcis.2017.08.044>
- [50] Karthikeyan M., Satheesh Kumar K. K., Elango K. P.: Conducting polymer/alumina composites as viable adsorbents for the removal of fluoride ions from aqueous solution. *Journal of Fluorine Chemistry*, **130**, 894–901 (2009). <https://doi.org/10.1016/j.jfluchem.2009.06.024>
- [51] Parashar K., Ballav N., Debnath S., Pillay K., Maity A.: Hydrous TiO<sub>2</sub>@polypyrrole hybrid nanocomposite as an efficient selective scavenger for the defluoridation of drinking water. *RSC Advances*, **6**, 99482–99495 (2016). <https://doi.org/10.1039/C6RA20151B>
- [52] Parashar K., Ballav N., Debnath S., Pillay K., Maity A.: Rapid and efficient removal of fluoride ions from aqueous solution using a polypyrrole coated hydrous tin oxide nanocomposite. *Journal of Colloid and Interface Science*, **476**, 103–118 (2016). <https://doi.org/10.1016/j.jcis.2016.05.013>
- [53] Wang M., Yan W., Kong W., Wu Z., An X., Wang Z., Hao X., Guan G.: An electroactive and regenerable Fe<sub>3</sub>O<sub>4</sub>@polypyrrole nanocomposite: Fabrication and its defluorination in an electromagnetic coupling system. *Industrial and Engineering Chemistry Research*, **56**, 12738–12744 (2017). <https://doi.org/10.1021/acs.iecr.7b02601>

- [54] Aigbe U. O., Onyancha R. B., Ukhurebor K. E., Obodo K. O.: Removal of fluoride ions using a polypyrrole magnetic nanocomposite influenced by a rotating magnetic field. *RSC Advances*, **10**, 595–609 (2020).  
<https://doi.org/10.1039/C9RA07379E>
- [55] Chigondo M., Paumo H. K., Bhaumik M., Pillay K., Maity A.: Hydrous CeO<sub>2</sub>-Fe<sub>3</sub>O<sub>4</sub> decorated polyaniline fibers nanocomposite for effective defluoridation of drinking water. *Journal of Colloid and Interface Science*, **532**, 500–516 (2018).  
<https://doi.org/10.1016/j.jcis.2018.07.134>
- [56] Wang X., Pan S., Zhang M., Qi J., Sun X., Gu C., Wang L., Li J.: Modified hydrous zirconium oxide/PAN nanofibers for efficient defluoridation from groundwater. *Science of the Total Environment*, **685**, 401–409 (2019).  
<https://doi.org/10.1016/j.scitotenv.2019.05.380>
- [57] Mukherjee S., Ramireddy H., Baidya A., Amala A. K., Sudhakar C., Mondal B., Philip L., Pradeep T.: Nano-cellulose-reinforced organo-inorganic nanocomposite for synergistic and affordable defluoridation of water and an evaluation of its sustainability metrics. *ACS Sustainable Chemistry and Engineering*, **8**, 139–147 (2020).  
<https://doi.org/10.1021/acssuschemeng.9b04822>
- [58] Karthikeyan M., Satheesh Kumar K. K., Elango K. P.: Studies on the defluoridation of water using conducting polymer/montmorillonite composites. *Environmental Technology*, **33**, 733–739 (2012).  
<https://doi.org/10.1080/09593330.2011.592224>
- [59] Chen Y., Li J., Xu H.: Removal of F from water using PPyCl/ATP composites. in 'Proceedings of the 2016 4<sup>th</sup> International Conference on Renewable Energy and Environmental Technology (ICREET 2016), Paris, France' 636–640 (2017).
- [60] Popat K. M., Anand P. S., Dasare B. D.: Selective removal of fluoride ions from water by the aluminium form of the aminomethylphosphonic acid-type ion exchanger. *Reactive Polymers*, **23**, 23–32 (1994).  
[https://doi.org/10.1016/0923-1137\(94\)90107-4](https://doi.org/10.1016/0923-1137(94)90107-4)
- [61] Samatya S., Mizuki H., Ito Y., Kawakita H., Uezu K.: The effect of polystyrene as a porogen on the fluoride ion adsorption of Zr(IV) surface-immobilized resin. *Reactive and Functional Polymers*, **70**, 63–68 (2010).  
<https://doi.org/10.1016/j.reactfunctpolym.2009.10.004>
- [62] Viswanathan N., Prabhu S. M., Meenakshi S.: Development of amine functionalized *co*-polymeric resins for selective fluoride sorption. *Journal of Fluorine Chemistry*, **153**, 143–150 (2013).  
<https://doi.org/10.1016/j.jfluchem.2013.04.002>
- [63] Cai J., Zhang Y., Pan B., Zhang W., Lv L., Zhang Q.: Efficient defluoridation of water using reusable nanocrystalline layered double hydroxides impregnated polystyrene anion exchanger. *Water Research*, **102**, 109–116 (2016).  
<https://doi.org/10.1016/j.watres.2016.06.030>
- [64] Pan B., Xu J., Wu B., Li Z., Liu X.: Enhanced removal of fluoride by polystyrene anion exchanger supported hydrous zirconium oxide nanoparticles. *Environmental Science and Technology*, **47**, 9347–9354 (2013).  
<https://doi.org/10.1021/es401710q>
- [65] Singh S., German M., Chaudhari S., Sengupta A. K.: Fluoride removal from groundwater using zirconium impregnated anion exchange resin. *Journal of Environmental Management*, **263**, 110415 (2020).  
<https://doi.org/10.1016/j.jenvman.2020.110415>
- [66] Dong H., Tang H., Shi X., Yang W., Chen W., Li H., Zhao Y., Zhang Z., Hua M.: Enhanced fluoride removal from water by nanosized cerium oxides impregnated porous polystyrene anion exchanger. *Chemosphere*, **287**, 131932 (2022).  
<https://doi.org/10.1016/j.chemosphere.2021.131932>
- [67] Robshaw T., Tukra S., Hammond D. B., Leggett G. J., Ogden M. D.: Highly efficient fluoride extraction from simulant leachate of spent potlining *via* La-loaded chelating resin. An equilibrium study. *Journal of Hazardous Materials*, **361**, 200–209 (2019).  
<https://doi.org/10.1016/j.jhazmat.2018.07.036>
- [68] Meenakshi S., Viswanathan N.: Identification of selective ion-exchange resin for fluoride sorption. *Journal of Colloid and Interface Science*, **308**, 438–450 (2007).  
<https://doi.org/10.1016/j.jcis.2006.12.032>
- [69] Markovski J., Garcia J., Hristovski K. D., Westerhoff P.: Nano-enabling of strong-base ion-exchange media *via* a room-temperature aluminum (hydr)oxide synthesis method to simultaneously remove nitrate and fluoride. *Science of the Total Environment*, **599–600**, 1848–1855 (2017).  
<https://doi.org/10.1016/j.scitotenv.2017.05.083>
- [70] Paudyal H., Inoue K., Kawakita H., Ohto K., Kamata H., Alam S.: Removal of fluoride by effectively using spent cation exchange resin. *Journal of Material Cycles and Waste Management*, **20**, 975–984 (2018).  
<https://doi.org/10.1007/s10163-017-0659-4>
- [71] Solangi I. B., Memon S., Bhangar M. I.: Removal of fluoride from aqueous environment by modified Amberlite resin. *Journal of Hazardous Materials*, **171**, 815–819 (2009).  
<https://doi.org/10.1016/j.jhazmat.2009.06.072>
- [72] Demirkalp G., Alamut S., Arar Ö., Yüksel Ü., Yüksel M.: Removal of fluoride from water by Al(III)-loaded and Al(OH)<sub>3</sub>-coated chelating resin. *Desalination and Water Treatment*, **57**, 15910–15919 (2015).  
<https://doi.org/10.1080/19443994.2015.1074117>
- [73] Millar G. J., Couperthwaite S. J., Wellner D. B., Macfarlane D. C., Dalzell S. A.: Removal of fluoride ions from solution by chelating resin with imino-diacetate functionality. *Journal of Water Process Engineering*, **20**, 113–122 (2017).  
<https://doi.org/10.1016/j.jwpe.2017.10.004>
- [74] Joshi S., Jana S.: Interaction of aqueous phase fluoride and Amberlite IR400Cl resin: Evaluation of batch process. *Chemical Data Collections*, **32**, 100643 (2021).  
<https://doi.org/10.1016/j.cdc.2020.100643>

- [75] Gangani N., Joshi V. C., Sharma S., Bhattacharya A.: Fluoride contamination in water: Remediation strategies through membranes. *Groundwater for Sustainable Development*, **17**, 100751 (2022).  
<https://doi.org/10.1016/j.gsd.2022.100751>
- [76] Grzegorzec M., Majewska-Nowak K., Ahmed A. E.: Removal of fluoride from multicomponent water solutions with the use of monovalent selective ion-exchange membranes. *Science of the Total Environment*, **722**, 137681 (2020).  
<https://doi.org/10.1016/j.scitotenv.2020.137681>
- [77] Damtie M. M., Woo Y. C., Kim B., Hailemariam R. H., Park K-D., Shon H. K., Park C., Choi J-S.: Removal of fluoride in membrane-based water and wastewater treatment technologies: Performance review. *Journal of Environmental Management*, **251**, 109524 (2019).  
<https://doi.org/10.1016/j.jenvman.2019.109524>
- [78] Pan J., Zheng Y., Ding J., Gao C., van der Bruggen B., Shen J.: Fluoride removal from water by membrane capacitive deionization with a monovalent anion selective membrane. *Industrial and Engineering Chemistry Research*, **57**, 7048–7053 (2018).  
<https://doi.org/10.1021/acs.iecr.8b00929>
- [79] Cadotte J., Forester R., Kim M., Petersen R., Stocker T.: Nanofiltration membranes broaden the use of membrane separation technology. *Desalination*, **70**, 77–88 (1988).  
[https://doi.org/10.1016/0011-9164\(88\)85045-8](https://doi.org/10.1016/0011-9164(88)85045-8)
- [80] Chen S-H., Chang D-J., Liou R-M., Hsu C-S., Lin S-S.: Preparation and separation properties of polyamide nanofiltration membrane. *Journal of Applied Polymer Science*, **83**, 1112–1118 (2002).  
<https://doi.org/10.1002/app.2282>
- [81] Mehiguene K., Garba Y., Taha S., Gondrexon N., Dorange G.: Influence of operating conditions on the retention of copper and cadmium in aqueous solutions by nanofiltration: Experimental results and modelling. *Separation and Purification Technology*, **15**, 181–187 (1999).  
[https://doi.org/10.1016/S1383-5866\(98\)00096-3](https://doi.org/10.1016/S1383-5866(98)00096-3)
- [82] Mehta R., Bhattacharya A.: Diamines as tunable chemicals in thin film composite membrane formation. in 'Advances in chemistry research' (ed.: Taylor J. C.) Nova Science, New York, Vol. 62, 201 (2020).
- [83] Khan M. M. T., Stewart P. S., Moll D. J., Mickols W. E., Nelson S. E., Camper A. K.: Characterization and effect of biofouling on polyamide reverse osmosis and nanofiltration membrane surfaces. *Biofouling*, **27**, 173–183 (2011).  
<https://doi.org/10.1080/08927014.2010.551766>
- [84] Owusu-Agyeman I., Shen J., Schäfer A. I.: Renewable energy powered membrane technology: Impact of pH and ionic strength on fluoride and natural organic matter removal. *Science of the Total Environment*, **621**, 138–147 (2018).  
<https://doi.org/10.1016/j.scitotenv.2017.11.111>
- [85] Owusu-Agyeman I., Reinwald M., Jeihanipour A., Schäfer A. I.: Removal of fluoride and natural organic matter from natural tropical brackish waters by nanofiltration/reverse osmosis with varying water chemistry. *Chemosphere*, **217**, 47–58 (2019).  
<https://doi.org/10.1016/j.chemosphere.2018.10.135>
- [86] Lhassani A., Rumeau M., Benjelloun D., Pontie M.: Selective demineralization of water by nanofiltration application to the defluorination of brackish water. *Water Research*, **35**, 3260–3264 (2001).  
[https://doi.org/10.1016/S0043-1354\(01\)00020-3](https://doi.org/10.1016/S0043-1354(01)00020-3)
- [87] Choi S., Yun Z., Hong S., Ahn K.: The effect of co-existing ions and surface characteristics of nanomembranes on the removal of nitrate and fluoride. *Desalination*, **133**, 53–64 (2001).  
[https://doi.org/10.1016/S0011-9164\(01\)00082-0](https://doi.org/10.1016/S0011-9164(01)00082-0)
- [88] Mnif A., ben Sik Ali M., Hamrouni B.: Effect of some physical and chemical parameters on fluoride removal by nanofiltration. *Ionics*, **16**, 245–253 (2010).  
<https://doi.org/10.1007/s11581-009-0368-7>
- [89] Tahaikt M., el Habbani R., Ait Haddou A., Achary I., Amor Z., Taky M., Alami A., Boughriba A., Hafsi M., Elmidaoui A.: Fluoride removal from groundwater by nanofiltration. *Desalination*, **212**, 46–53 (2007).  
<https://doi.org/10.1016/j.desal.2006.10.003>
- [90] Diawara C. K., Paugam L., Pontié M., Schlumpf J. P., Jaouen P., Quéméneur F.: Influence of chloride, nitrate, and sulphate on the removal of fluoride ions by using nanofiltration membranes. *Separation Science and Technology*, **40**, 3339–3347 (2005).  
<https://doi.org/10.1080/01496390500423706>
- [91] Valentukeviciene M., Zurauskiene R., Boussouga Y. A.: Fluoride removal from groundwater by technological process optimization. *Ecological Chemistry and Engineering S*, **26**, 133–147 (2019).  
<https://doi.org/10.1515/eces-2019-0010>
- [92] Hoinkis J., Valero-Freitag S., Caporgno M. P., Pätzold C.: Removal of nitrate and fluoride by nanofiltration – A comparative study. *Desalination and Water Treatment*, **30**, 278–288 (2011).  
<https://doi.org/10.5004/dwt.2011.2103>
- [93] Chung H-K., Kim W-H., Park J., Cho J., Jeong T-Y., Park P-K.: Application of Langmuir and Freundlich isotherms to predict adsorbate removal efficiency or required amount of adsorbent. *Journal of Industrial and Engineering Chemistry*, **28**, 241–246 (2015).  
<https://doi.org/10.1016/j.jiec.2015.02.021>
- [94] Bejaoui I., Mnif A., Hamrouni B.: Performance of reverse osmosis and nanofiltration in the removal of fluoride from model water and metal packaging industrial effluent. *Separation Science and Technology*, **49**, 1135–1145 (2014).  
<https://doi.org/10.1080/01496395.2013.878956>
- [95] Richards L. A., Vuachère M., Schäfer A. I.: Impact of pH on the removal of fluoride, nitrate and boron by nanofiltration/reverse osmosis. *Desalination*, **261**, 331–337 (2010).  
<https://doi.org/10.1016/j.desal.2010.06.025>

- [96] Diawara C. K., Diop S. N., Diallo M. A., Farcy M., Deratani A.: Performance of nanofiltration (NF) and low pressure reverse osmosis (LPRO) membranes in the removal of fluoride and salinity from brackish drinking water. *Journal of Water Resource and Protection*, **3**, 912–917 (2011).  
<https://doi.org/10.4236/jwarp.2011.312101>
- [97] Gedam V. V., Patil J. L., Kangne S., Sisram R. S., Labhasetwar P.: Performance evaluation of polyamide reverse osmosis membrane for removal of contaminants in ground water collected from Chandrapur district. *Journal of Membrane Science and Technology*, **02**, 1000117 (2012).  
<https://doi.org/10.4172/2155-9589.1000117>
- [98] Ndiaye P. I., Moulin P., Dominguez L., Millet J. C., Charbit F.: Removal of fluoride from electronic industrial effluent by RO membrane separation. *Desalination*, **173**, 25–32 (2005).  
<https://doi.org/10.1016/j.desal.2004.07.042>
- [99] Shen J., Schäfer A. I.: Factors affecting fluoride and natural organic matter (NOM) removal from natural waters in Tanzania by nanofiltration/reverse osmosis. *Science of the Total Environment*, **527–528**, 520–529 (2015).  
<https://doi.org/10.1016/j.scitotenv.2015.04.037>
- [100] Freger V., Gilron J., Belfer S.: TFC polyamide membranes modified by grafting of hydrophilic polymers: An FT-IR/AFM/TEM study. *Journal of Membrane Science*, **209**, 283–292 (2002).  
[https://doi.org/10.1016/S0376-7388\(02\)00356-3](https://doi.org/10.1016/S0376-7388(02)00356-3)
- [101] Pontié M., Dach H., Leparc J., Hafsi M., Lhassani A.: Novel approach combining physico-chemical characterizations and mass transfer modelling of nanofiltration and low pressure reverse osmosis membranes for brackish water desalination intensification. *Desalination*, **221**, 174–191 (2008).  
<https://doi.org/10.1016/j.desal.2007.01.075>
- [102] Tang C. Y., Kwon Y-N., Leckie J. O.: Effect of membrane chemistry and coating layer on physicochemical properties of thin film composite polyamide RO and NF membranes: I. FTIR and XPS characterization of polyamide and coating layer chemistry. *Desalination*, **242**, 149–167 (2009).  
<https://doi.org/10.1016/j.desal.2008.04.003>
- [103] Lee K. P., Arnot T. C., Mattia D.: A review of reverse osmosis membrane materials for desalination – Development to date and future potential. *Journal of Membrane Science*, **370**, 1–22 (2011).  
<https://doi.org/10.1016/j.memsci.2010.12.036>
- [104] Chakraborty S., Roy M., Pal P.: Removal of fluoride from contaminated groundwater by cross flow nanofiltration: Transport modeling and economic evaluation. *Desalination*, **313**, 115–124 (2013).  
<https://doi.org/10.1016/j.desal.2012.12.021>
- [105] Hu K., Dickson J. M.: Nanofiltration membrane performance on fluoride removal from water. *Journal of Membrane Science*, **279**, 529–538 (2006).  
<https://doi.org/10.1016/j.memsci.2005.12.047>
- [106] Shen J., Richards B. S., Schäfer A. I.: Renewable energy powered membrane technology: Case study of St. Dorcas borehole in Tanzania demonstrating fluoride removal via nanofiltration/reverse osmosis. *Separation and Purification Technology*, **170**, 445–452 (2016).  
<https://doi.org/10.1016/j.seppur.2016.06.042>
- [107] Boussouga Y-A., Richards B. S., Schäfer A. I.: Renewable energy powered membrane technology: System resilience under solar irradiance fluctuations during the treatment of fluoride-rich natural waters by different nanofiltration/reverse osmosis membranes. *Journal of Membrane Science*, **617**, 118452 (2021).  
<https://doi.org/10.1016/j.memsci.2020.118452>
- [108] Sehn P.: Fluoride removal with extra low energy reverse osmosis membranes: Three years of large scale field experience in Finland. *Desalination*, **223**, 73–84 (2008).  
<https://doi.org/10.1016/j.desal.2007.02.077>
- [109] Saxena M., Sharma S., Bhattacharya A.: Impacts of recycled polysulfone on the salt separation performance of thin film poly(piperazine-amide) membranes. *Journal of Environmental Chemical Engineering*, **9**, 105869 (2021).  
<https://doi.org/10.1016/j.jece.2021.105869>
- [110] Saxena M., Bhattacharya A.: Innate connection between salts on preparation and separation performance of thin-film poly(piperazinamide) composite membrane. *Materials and Manufacturing Processes*, **37**, 1756–1765 (2022).  
<https://doi.org/10.1080/10426914.2022.2049301>
- [111] Evangeline C., Pragasam V., Rambabu K., Velu S., Monash P., Arthanareeswaran G., Banat F.: Iron oxide modified polyethersulfone/cellulose acetate blend membrane for enhanced defluoridation application. *Desalination and Water Treatment*, **156**, 177–188 (2019).  
<https://doi.org/10.5004/dwt.2018.23174>
- [112] Plattner J., Naidu G., Wintgens T., Vigneswaran S., Kazner C.: Fluoride removal from groundwater using direct contact membrane distillation (DCMD) and vacuum enhanced DCMD (VEDCMD). *Separation and Purification Technology*, **180**, 125–132 (2017).  
<https://doi.org/10.1016/j.seppur.2017.03.003>
- [113] Alkudhiri A., Darwish N., Hilal N.: Membrane distillation: A comprehensive review. *Desalination*, **287**, 2–18 (2012).  
<https://doi.org/10.1016/j.desal.2011.08.027>
- [114] Hou D., Wang J., Zhao C., Wang B., Luan Z., Sun X.: Fluoride removal from brackish groundwater by direct contact membrane distillation. *Journal of Environmental Sciences*, **22**, 1860–1867 (2010).  
[https://doi.org/10.1016/S1001-0742\(09\)60332-6](https://doi.org/10.1016/S1001-0742(09)60332-6)
- [115] Hichour M., Persin F., Molénat J., Sandeaux J., Gavach C.: Fluoride removal from diluted solutions by Donnan dialysis with anion-exchange membranes. *Desalination*, **122**, 53–62 (1999).  
[https://doi.org/10.1016/S0011-9164\(99\)00027-2](https://doi.org/10.1016/S0011-9164(99)00027-2)

- [116] Hichour M., Persin F., Sandeaux J., Gavach C.: Fluoride removal from waters by Donnan dialysis. *Separation and Purification Technology*, **18**, 1–11 (1999).  
[https://doi.org/10.1016/S1383-5866\(99\)00042-8](https://doi.org/10.1016/S1383-5866(99)00042-8)
- [117] Durmaz F., Kara H., Cengeloglu Y., Ersoz M.: Fluoride removal by Donnan dialysis with anion exchange membranes. *Desalination*, **177**, 51–57 (2005).  
<https://doi.org/10.1016/j.desal.2004.11.016>
- [118] Alkan E., Kır E., Oksuz L.: Plasma modification of the anion-exchange membrane and its influence on fluoride removal from water. *Separation and Purification Technology*, **61**, 455–460 (2008).  
<https://doi.org/10.1016/j.seppur.2007.12.012>
- [119] Tor A.: Removal of fluoride from water using anion-exchange membrane under Donnan dialysis condition. *Journal of Hazardous Materials*, **141**, 814–818 (2007).  
<https://doi.org/10.1016/j.jhazmat.2006.07.043>
- [120] Mondal R., Pal S., Bhalani D. V., Bhadja V., Chatterjee U., Jewrajka S. K.: Preparation of polyvinylidene fluoride blend anion exchange membranes *via* non-solvent induced phase inversion for desalination and fluoride removal. *Desalination*, **445**, 85–94 (2018).  
<https://doi.org/10.1016/j.desal.2018.07.032>
- [121] Lee J. B., Park K-K., Eum H-M., Lee C-W.: Desalination of a thermal power plant wastewater by membrane capacitive deionization. *Desalination*, **196**, 125–134 (2006).  
<https://doi.org/10.1016/j.desal.2006.01.011>
- [122] Li H., Zou L.: Ion-exchange membrane capacitive deionization: A new strategy for brackish water desalination. *Desalination*, **275**, 62–66 (2011).  
<https://doi.org/10.1016/j.desal.2011.02.027>
- [123] Nunes-Pereira J., Lima R., Choudhary G., Sharma P. R., Ferdov S., Botelho G., Sharma R. K., Lanceros-Méndez S.: Highly efficient removal of fluoride from aqueous media through polymer composite membranes. *Separation and Purification Technology*, **205**, 1–10 (2018).  
<https://doi.org/10.1016/j.seppur.2018.05.015>
- [124] Chaudhary M., Maiti A.: Fe–Al–Mn@chitosan based metal oxides blended cellulose acetate mixed matrix membrane for fluoride decontamination from water: Removal mechanisms and antibacterial behavior. *Journal of Membrane Science*, **611**, 118372 (2020).  
<https://doi.org/10.1016/j.memsci.2020.118372>
- [125] Chen W., Chen P., Zhang G., Xing G., Feng Y., Yang Y-W., Chen L.: Macrocyclic-derived hierarchical porous organic polymers: Synthesis and applications. *Chemical Society Reviews*, **50**, 11684–11714 (2021).  
<https://doi.org/10.1039/D1CS00545F>
- [126] Skorjanc T., Shetty D., Trabolssi A.: Pollutant removal with organic macrocycle-based covalent organic polymers and frameworks. *Chem*, **7**, 882–918 (2021).  
<https://doi.org/10.1016/J.CHEMPR.2021.01.002>

Research article

# Preparation and properties of transparent poly(aryl ether ketone) films with low dielectric constant

Huijuan Li<sup>1</sup>, Miao Yi<sup>2</sup>, Xin Yin<sup>2</sup>, Wenliang Wu<sup>2</sup>, Shiai Xu<sup>1,3\*</sup> 

<sup>1</sup>School of Materials Science and Engineering, East China University of Science and Technology, 200237 Shanghai, China

<sup>2</sup>Zhejiang Jitai New Materials Co., Ltd, 312369 Shaoxing, China

<sup>3</sup>School of Chemical Engineering, Qinghai University, 810016 Xining, China

Received 23 February 2023; accepted in revised form 19 May 2023

**Abstract.** The objective of this study is to prepare a new poly(aryl ether ketone) (PAEK) with low dielectric constant, high transparency and heat resistance by introducing fluorine atoms and phenolphthalein (PPH) groups into the polymer backbone. The chemical structure of PAEK random copolymers was characterized by Fourier transform infrared spectroscopy (FTIR), proton nuclear magnetic resonance (<sup>1</sup>H-NMR) and X-ray diffraction (XRD), and the molecular weight of PAEK was determined by gel permeation chromatography (GPC). It is found that these random copolymers are soluble in common organic solvents, especially low boiling point solvents, such as CHCl<sub>3</sub>, tetrahydrofuran (THF) and dimethylacetamide (DMAc). Transparent, uniform and flexible films were prepared by casting from DMAc solvent. The PAEK copolymers exhibit high glass transition temperature (163–220 °C by differential scanning calorimetry (DSC) and 168–227 °C by dynamic mechanical analysis (DMA)) and thermal stability with 5% weight loss temperatures of 461–525 °C. The PAEK films show good mechanical properties with tensile strengths of 50–62 MPa. The dielectric constant (*k*) is only 2.31–3.08, and the loss tangent is only 0.003–0.009 at 1 MHz. All films exhibit excellent optical transparency, their UV cutoff wavelength is shorter than 386 nm, and the transmittance at 450 nm is higher than 80%.

**Keywords:** Smart polymers, poly(aryl ether ketone), soluble, low dielectric constant, transparency

## 1. Introduction

Integrated circuits are becoming smaller and more integrated with the rapid development of information and microelectronics technology. However, the miniaturization of circuits brings about an increase in capacitance and resistance, which may cause crosstalk and delay and consequently seriously affect signal transmission. This problem can be effectively improved by reducing the dielectric constant and dielectric loss of the electronic materials [1, 2]. Low dielectric materials should have a low dielectric constant ( $k < 3.0$ , at 1 MHz) and high glass transition temperature ( $T_g > 170$  °C) [3–6]. Traditional transparent materials such as glass have been gradually

replaced by multifunctional polymer materials that are lighter, more flexible and impact resistant, easier to shape, and cheaper. More and more optoelectronic and microelectronic components are made of transparent materials, especially in applications such as display screens, mobile phones, and 5G (5<sup>th</sup> generation mobile networks) mobile device casings [7, 8]. To meet the growing demand of the semiconductor industry and integrated circuit systems, expand the application of poly(aryl ether ketone) (PAEK) in various fields; there is an urgent need to develop transparent PAEK film materials with excellent dielectric properties [9–11]. PAEK is a high-temperature resistant thermoplastic with excellent dielectric properties

\*Corresponding author, e-mail: [saxu@ecust.edu.cn](mailto:saxu@ecust.edu.cn)

© BME-PT

in addition to excellent mechanical properties, heat resistance and chemical corrosion resistance [12, 13]. Polyether ether ketone (PEEK) is one of the most common commercial PAEK materials with a dielectric constant of 3.3 (at 1 MHz) [14–16], which does not meet the requirement of microelectronic applications. Physical or chemical modification is required to improve the optical transparency and reduce the dielectric constant in order to prepare PAEK films with good dielectric properties [17–20].

Traditional PEEK is a semi-crystalline polymer that is only soluble in concentrated sulfuric acid. For this, many approaches have been proposed to improve the solubility of PEEK polymers [21, 22], and novel transparent polymer film materials can be prepared by solvent casting, scraping and spin coating. The resulting transparent films can be easily stretched and cut into different shapes, and thus have wide applications in electronic devices, medical health, weapon, architecture, automobiles, aerospace and food packaging.

The dielectric constant of material is closely related to the polymer structure. According to the Debye equation [23], reducing the number of polarized molecules or the density of polar groups per unit volume is an effective method to prepare low dielectric constant polymers. Since the dielectric constant of air is 1.0, introducing nano-porous materials into the material can reduce the dielectric constant of the composite. However, the presence of nanopores will reduce the mechanical properties of polymer materials and enhance their hygroscopicity through opening pores, leading to deterioration of electrical properties during processing and application. Therefore, it remains challenging to develop low dielectric constant polymer materials [24, 25]. Previous studies have suggested that introducing large-volume side groups [26–28], asymmetric structures [3, 29] or twisted non-coplanar structures [30] can reduce the stacking density of materials and increase the free volume of polymers. The introduction of large-volume side groups contributes to improving the solubility and dielectric properties of the polymer by destructing PAEK molecular structure and hindering the effective stacking of macromolecular chains to increase the space-free volume and reduce the crystallinity of PAEK. The destruction of the PAEK crystalline structure also results in excellent optical transparency, and the rigid structure of large-volume side groups can improve the heat resistance, thermal

stability and tensile strength of polymers [31, 32]. Phenolphthalein (PHPH) monomer contains a cyclic lactone and three bulky non-coplanar distorted benzene rings, which could increase the free volume of the polymer, and reduce the number of polarized groups per unit volume. Ba *et al.* [33] prepared a series of new PAEK copolymers by varying the molar ratio of bisphenol monomers containing pendent rigid adamantyl groups and flexible long side-chains, and these polymers showed low dielectric constants (2.50–2.88 at 1 MHz) and excellent solubility. Due to the strong attraction of electrons outside the nucleus of fluorine atoms and the large interaction between electrons and atomic nucleus, the electron cloud has high density and low polarizability when polarized by the external electric field. Introduction fluorine-containing groups with larger volumes into polymer molecules can reduce the stacking density of the polymer and increase the free volume of the polymer, thereby reducing the dielectric constant of the polymer and improving the transparency. It can also improve the thermal properties of the polymers due to the small atomic size of fluorine element and the high binding energy of C–F bond [34–36]. Liu *et al.* [37] reported the synthesis of novel fluorine-containing PAEK with (3-fluoromethyl) phenyl or (3,5-difluoromethyl) phenyl moieties with low dielectric constants (2.69–2.78 at 1 MHz).

In this study, hexafluorobisphenol A (6F-BPA) and phenolphthalein (PHPH) moieties were introduced into the PAEK backbone through molecular structure design, and a series of novel PAEK transparent films with low dielectric constant, high transparency and heat resistance were obtained by adjusting the ratio of PHPH and 6F-BPA. These novel PAEK films could be used in electronic communications, computers, LED and other fields

## 2. Experimental

### 2.1. Materials

Hexafluorobisphenol A (6F-BPA) was purchased from Meryer Chemical Technology Co., Ltd. (Shanghai, China). Xylene, phenolphthalein (PHPH), 4,4'-difluorobenzophenone (DFBP), *N*-methyl-2-pyrrolidinone (NMP) and sulfolane (TMS) were obtained from Shanghai Aladdin Chemical Reagent (China). The potassium carbonate ( $K_2CO_3$ ) was obtained from Jiangsu Youlide Co., Ltd. *N,N*-dimethylformamide (DMF), *N,N*-dimethylacetamide (DMAc), chloroform ( $CHCl_3$ ) and tetrahydrofuran (THF)

were supplied by Tiantai Fine Chemical Co., Ltd. (China). Commercial PEEK film (PEEK-KF001, 50  $\mu\text{m}$  thick) was purchased from Dongguan Kaifeng Industry Co., Ltd. (China). All chemicals were used as received without further purification.

## 2.2. Synthesis of PAEK random copolymers

A novel PAEK-containing phenolphthalein and trifluoromethyl was synthesized by solution polycondensation [37–39], as shown in Figure 1. The new PAEK copolymers with a PHPH/6F-BPA molar ratio of 100:0, 75:25, 50:50, 25:75 and 0:100 were named as PAEK-1, PAEK-2, PAEK-3, PAEK-4 and PAEK-5, respectively. For instance, the polymerization process of PAEK-2 with a PHPH/6F-BPA molar ratio of 75:25 was as follows. TMS (40 ml), PHPH (2.38 g, 0.0075 mol), 6F-BPA (0.84 g, 0.0025 mol), DFBP (2.18 g, 0.010 mol),  $\text{K}_2\text{CO}_3$  (1.38 g, 0.010 mol) and xylene (20 ml) were mechanically stirred, heated to 135  $^\circ\text{C}$  with a heating jacket, and then reacted at constant temperature for 2 h. After that, the reaction temperature was gradually raised to 170  $^\circ\text{C}$  to remove water from the reaction by azeotropic distillation. After xylene was removed by distillation, the temperature of the system was held at 220  $^\circ\text{C}$  for about 6 h. When the solution viscosity no longer changed significantly, the solution was poured into 500 ml of deionized water. The polymer powder was washed several times with hot distilled

water and methanol, and then dried at 120  $^\circ\text{C}$  for 24 h.

DMAc solvent (10 ml) and purified PAEK particles (1.0 g) were added to a three-necked flask successively and heated slowly to 100  $^\circ\text{C}$  under mechanical agitation. After continuous stirring for 2 h, the uniform PAEK solution was slowly poured onto a preheated clean glass plate in the oven. The solution was put in an atmospheric oven at 80  $^\circ\text{C}$  for 12 h. After that, it was transferred to a vacuum oven at 100  $^\circ\text{C}$  for 24 h. PAEK films were obtained after natural cooling to room temperature, and all films were 50 $\pm$ 0.5  $\mu\text{m}$  thick.

## 2.3. Characterizations

### 2.3.1. Chemical structure analysis

The Fourier transform infrared (FT-IR) spectra of PAEK copolymers were recorded on a Nicolet 6700 FT-IR spectrometer (Thermo Electron, USA) in the range of 4000–400  $\text{cm}^{-1}$  at a resolution of 4  $\text{cm}^{-1}$  over 32 scans at room temperature. KBr pellets were used, and five spectra were averaged. The proton nuclear magnetic resonance ( $^1\text{H-NMR}$ ) spectra were recorded on a Bruker (Billerica, MA, USA) 510 NMR spectrometer (400 MHz) at room temperature (25  $^\circ\text{C}$ ) using deuterated chloroform ( $\text{CDCl}_3$ ) as solvent and tetramethylsilane (TMS) as internal standard. The X-ray diffraction (XRD) patterns were recorded using an Ultima IV X-ray diffractometer

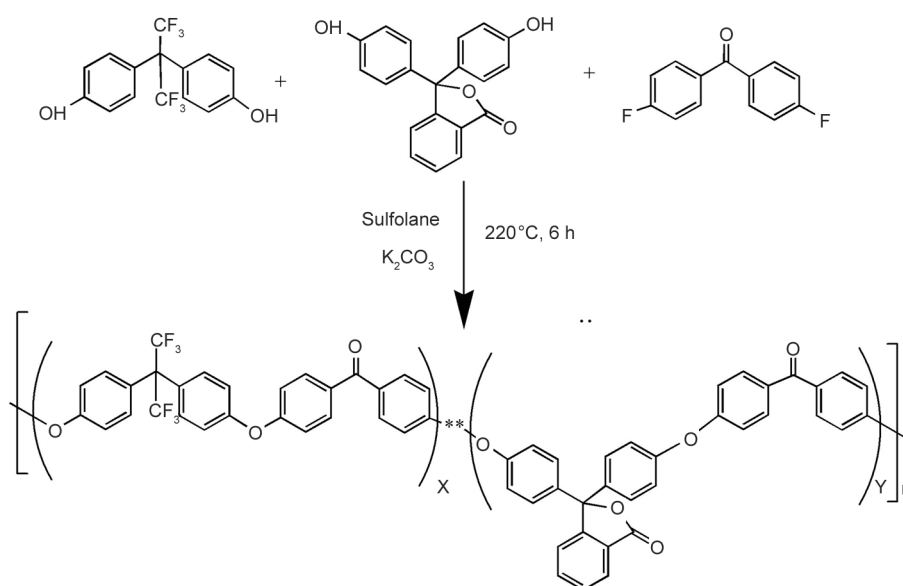


**Figure 1.** The synthetic route of PAEK random copolymers, where X and Y are the mole fractions of 6F-BPA monomer and PHPH in the feed, respectively.

(Rigaku, Japan) at scattering angles ( $2\theta$ ) of  $5\text{--}60^\circ$  with a step of  $4^\circ\cdot\text{min}^{-1}$ .

### 2.3.2. GPC analysis

Gel permeation chromatography (GPC) was performed using PL-GPC 50 (Agilent Technologies Co., Palo Alto, California, USA) instrument with DMF as the eluent and polystyrene as the standard.

### 2.3.3. Solubility analysis

The organic solubility was measured in various organic solvents (10 mg of PAEK powder/1.0 ml of organic solvent) at room temperature ( $25^\circ\text{C}$ ).

### 2.3.4. Thermal analysis

The PAEK copolymers' glass transition temperatures ( $T_g$ ) were measured using a DSC8500 differential scanning calorimeter (DSC) with a scanning rate of  $10^\circ\text{C}\cdot\text{min}^{-1}$  under an  $\text{N}_2$  atmosphere from  $30$  to  $300^\circ\text{C}$ . All PAEK random copolymers were scanned twice for heating and cooling to eliminate the thermal history from  $50$  to  $360^\circ\text{C}$  at a heating rate of  $10^\circ\text{C}\cdot\text{min}^{-1}$  under an  $\text{N}_2$  atmosphere. The glass transition temperature ( $T_g$ ) was recorded at the second heating scan. Thermogravimetric analysis (TGA) was performed on an SDT-Q600 analyzer (TA, USA) under  $\text{N}_2$  atmosphere. Samples were heated from  $30$  to  $800^\circ\text{C}$  at a heating rate of  $10^\circ\text{C}\cdot\text{min}^{-1}$ .

### 2.3.5. Mechanical test

The tensile properties of PAEK films were measured using an MTS E42.503 universal tensile testing machine, where the width of the dumbbell-shaped spline at the narrow part was  $4$  mm, the gauge length was  $20$  mm, the clamp spacing was  $50$  mm, and the

stretching rate was  $10\text{ mm}\cdot\text{min}^{-1}$ . The loss factor curves, storage modulus, and loss modulus at different temperatures were measured with a TA Instruments DMA-Q800 in tensile mode at  $1$  Hz and  $10\ \mu\text{m}$  amplitude with a heating rate of  $3^\circ\text{C}\cdot\text{min}^{-1}$  and temperature scan from  $50$  to  $350^\circ\text{C}$ .

### 2.3.6. Dielectric properties

The dielectric properties of PAEK films were measured using a Concept 40 (Novocontrol GmbH, Germany) broadband dielectric impedance spectrometer at room temperature with frequencies ranging from  $10^3\text{--}10^6$  Hz.

### 2.3.7. Optical properties

The transmittance of PAEK films was recorded on a Yoke 722 (Shanghai Yoke Co. Ltd., Shanghai, China) ultraviolet spectrophotometer in a wavelength range of  $200\text{--}800$  nm.

## 3. Results and discussion

### 3.1. Structure and molecular weight of PAEK copolymers

Figure 2 shows the FTIR spectra of PAEK copolymers with different PHPH/6F-BPA molar ratios. The characteristic absorption bands of carbonyl ( $\text{C}=\text{O}$ ) groups appear near  $1730\text{ cm}^{-1}$ . A sharp characteristic peak appears at  $1769\text{ cm}^{-1}$ , which is assigned to the stretching vibration of the lactone ring ( $\text{O}=\text{C}=\text{O}$ ) of phenolphthalein, and its intensity decreases gradually with the decrease of PHPH content. The strong absorption peaks near  $1598$ ,  $1502$ , and  $1458\text{ cm}^{-1}$  are assigned to the skeleton vibration of the benzene ring on the main chain, while those near  $1240$  and  $1206\text{ cm}^{-1}$  are assigned to the stretching vibration of

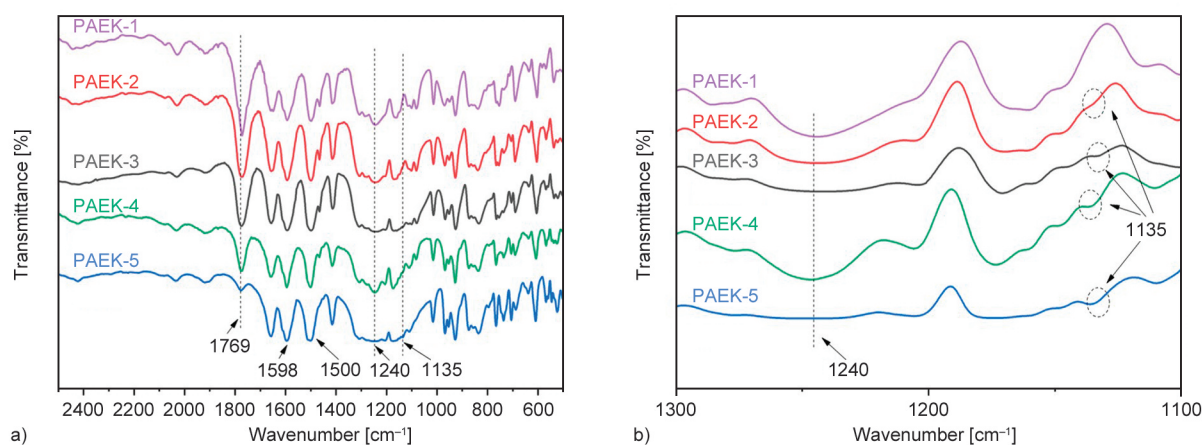


**Figure 2.** FTIR spectra of PAEK copolymers with different PHPH/6F-BPA molar ratios, a) in the wavenumber of  $4000\text{--}400\text{ cm}^{-1}$ , b) in the wavenumber of  $1300\text{--}1100\text{ cm}^{-1}$ .

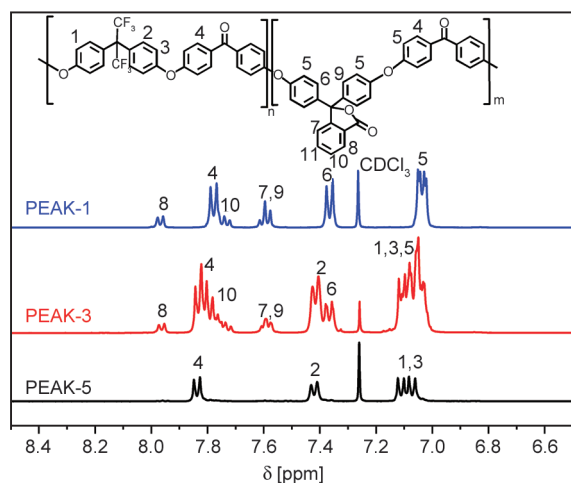


**Figure 3.**  $^1\text{H-NMR}$  spectra of PAEK with different PHPH/6F-BPA molar ratios.

the aryl ether bond (Ar–O–Ar) on the main chain. The absorption band at  $1135\text{ cm}^{-1}$  is the contraction vibration peak of the C–F band, and its intensity is increased with the increase of 6F-BPA content [40]. The structure of PAEK films was confirmed by  $^1\text{H-NMR}$ , as shown in Figure 3. A resonance peak is observed at 7.80 ppm in all PAEK films, which is assigned to the protons of the benzene ring in benzophenone. The two resonance peaks at 7.41 ppm and 7.09 ppm correspond to the protons on the phenyl group of 6F-BPA. PAEK-3 has five resonance peaks at around 7.98, 7.71, 7.61, 7.38, and 7.04 ppm, which are assigned to the protons on the phenyl group from PHPH. Compared to PAEK-1 and PAEK-5, the peak at 7.80 ppm is slightly shifted in PAEK-3, which indicates that PAEK-3 is a random copolymer.

The XRD patterns of the polymers are shown in Figure 4. Although PEEK is a semi-crystalline

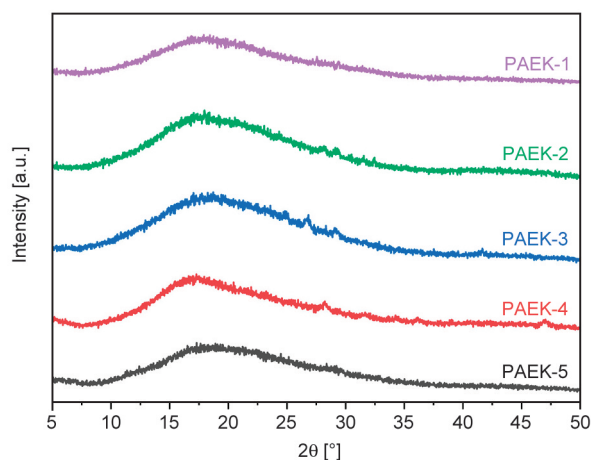


**Figure 4.** XRD spectra of PAEK with different PHPH/6F-BPA molar ratios.

**Table 1.** Molecular weights and distributions of PAEK copolymers.

Samples	PHPH/6F-BPA	$M_n$ [ $10^4\text{ g}\cdot\text{mol}^{-1}$ ]	$M_w$ [ $10^4\text{ g}\cdot\text{mol}^{-1}$ ]	PDI
PAEK-1	100:0	4.59	6.93	1.51
PAEK-2	75:25	4.15	6.77	1.63
PAEK-3	50:50	4.21	6.45	1.53
PAEK-4	25:75	4.02	6.01	1.49
PAEK-5	0:100	4.33	6.41	1.55

polymer [14, 16], no crystalline peaks are observed, indicating that these PAEK films are novel amorphous polymers. The presence of large-volume side groups in PHPH destroys the symmetry of the polymer and increases the free volume. The introduction of the  $-\text{CF}_3$  bond also reduces the tight packing of macromolecular chains and, thus, makes the copolymer become amorphous.

In conclusion, the FTIR,  $^1\text{H-NMR}$ , and XRD results indicate that  $-\text{CF}_3$  and PHPH groups are successfully introduced.

The molecular weights of samples were measured by GPC, as shown in Table 1. The numerical average molecular weights ( $M_n$ ) are higher than  $4\cdot 10^4\text{ g}\cdot\text{mol}^{-1}$ , and the polydispersity index (PDI) values are below 1.7. As the molecular weights of polymers are approximately the same, the comparison of effective physical properties can be made based on molecular structure.

### 3.2. Solubility

The solubility of PAEKs in  $\text{CHCl}_3$ , THF, NMP, DMAc, and DMF is listed in Table 2. All PAEK films can be dissolved in common solvents, and their high solubility is attributed to the introduction of phenolphthalein and trifluoromethyl groups that can

**Table 2.** Solubility of PAEK copolymers.

Samples	NMP	DMAc	$\text{CHCl}_3$	THF	DMF
PAEK-1	+	+	+	+	+
PAEK-2	+	+	+	+	+
PAEK-3	+	+	+	+	+
PAEK-4	+	+	+	+	+
PAEK-5	+	+	+	+	+
PEEK	–	–	–	–	–

NMP: *N*-methylpyrrolidone;  
 DMAc: *N,N*-dimethylacetamide;  
 $\text{CHCl}_3$ : chloroform;  
 THF: tetrahydrofuran;  
 DMF: *N,N*-dimethylformamide;  
 +: soluble at room temperature;  
 –: insoluble.

disturb the tight packing of polymer chains, increase the free volume and decrease the intermolecular force and crystallinity [41].

### 3.3. Thermal properties

The thermal properties of PAEK polymers were examined by DSC (Figure 5) and TGA (Figure 6), and the results are shown in Table 3. The  $T_g$  values of new PAEKs are higher than that of PEEK (143 °C) [14]. As shown in Figure 5, all the DSC curves of PAEKs have a single typical glass transition but no melting peaks, indicating that these copolymers are amorphous. Increasing the proportion of 6F-BPA monomer can decrease the proportion of PHPH monomer and, consequently the  $T_g$  value. At a PHPH/6F-BPA molar ratio of 25:75, the  $T_g$  value of PAEK-3 is 177 °C. This is because PHPH structural unit contains a cyclic lactone carbonyl group (O–C=O) and three bulky non-coplanar distorted benzene rings, which can increase the rotational steric hindrance in the molecular chain and therefore improve the  $T_g$  value [3]. In addition, the  $-CF_3$  group has a large volume, and the aliphatic structure ( $-C-$ ) is not easy to rotate and the fluorine atom would lead to

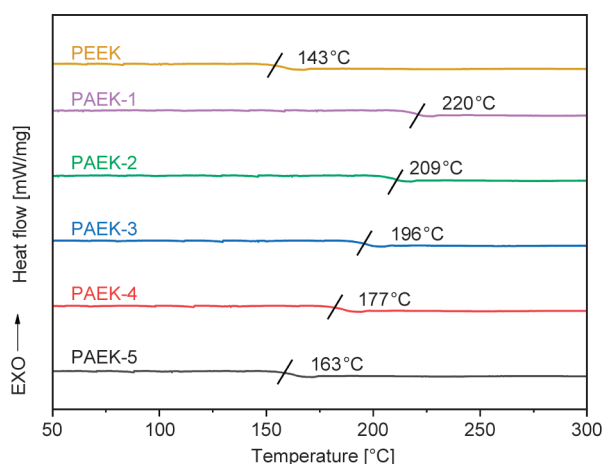


Figure 5. DSC curves of PAEK copolymers.

Table 3. Thermal and mechanical properties of the polymers.

Samples	$T_g^a$ [°C]	$T_g^b$ [°C]	$T_{d5\%}$ [°C]	Tensile strength [MPa]	Tensile modulus [GPa]	Elongation at break [%]
PAEK-1	220	227	461	62±2	1.7±0.1	8.5±0.1
PAEK-2	209	217	486	59±3	1.6±0.2	7.3±0.2
PAEK-3	196	200	504	55±1	1.5±0.1	7.1±0.1
PAEK-4	177	180	516	53±2	1.4±0.1	6.2±0.3
PAEK-5	163	168	525	50±1	1.3±0.3	7.1±0.3
PEEK	148	143	551	96±4	1.9±0.2	150.0±0.2

$T_g^a$ : glass transition temperature measured by DSC at a heating rate of 10 °C·min<sup>-1</sup> under a nitrogen atmosphere;

$T_g^b$ : glass transition temperature measured by DMA at a heating rate of 3 °C·min<sup>-1</sup> under a nitrogen atmosphere;

$T_{d5\%}$ : temperature at 5% weight loss.

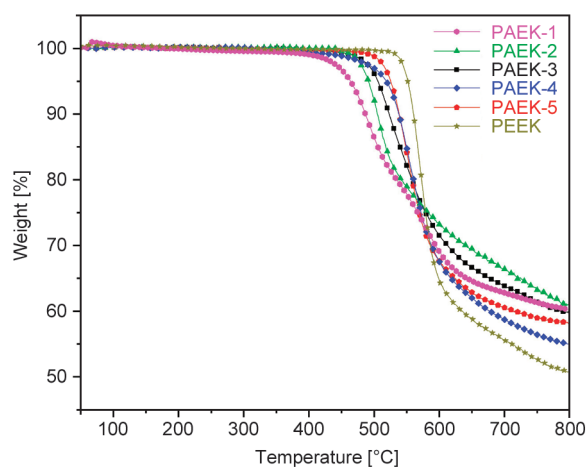


Figure 6. TGA curves of PAEK polymers.

internal plasticization [41]. Therefore, with the increase of 6F-BPA content, the  $T_g$  value of PAEK decreases with increasing 6F-BPA content, but it is still higher than 160 °C.

It is seen from Figure 6 that PAEK copolymers have high thermal stability, where  $T_{d5\%}$  (temperature at 5% weight loss) is higher than 460 °C and  $T_{d10\%}$  (temperature at 10% weight loss) is 470–580 °C. The char yield at 800 °C is 50–63%. The lactone ring shows poor heat resistance, and PAEK-1 starts to decompose at 423 °C. Increasing the 6F-BPA content decreases the lactone ring content of PHPH and consequently increases the decomposition temperature of PAEK [42–44]. In conclusion, the thermal stability of PAEK copolymers increases with the increase of 6F-BPA content, and the polymers have sufficiently high  $T_g$  and excellent thermal stability.

### 3.4. Mechanical properties

Dynamic mechanical and tensile tests were performed to determine the influence of bisphenol content on the mechanical properties of PAEKs. As shown in Table 3, the introduction of large-volume

groups into the main chain of PEEK leads to a decrease in the mechanical properties of the films. Traditional PEEK is a linear, fully aromatic crystalline polymer, and it has high tensile strength and elongation at break due to its rigid benzene ring, flexible ether bonds, and carbonyl groups can enhance the intermolecular force in its molecular chain, as well as its regular molecular segment structure. The introduction of large volume PHPH and lower polarity  $-\text{CF}_3$  groups could disrupt the regular arrangement of PEEK and make the polymer have an amorphous structure. Then the distance between molecular chains is increased and the intermolecular interactions and molecular entanglement are reduced. As a result, the tensile strength is 50–62 MPa, and the tensile modulus is 1.3–1.7 GPa. With the increase of 6F-BPA segments, the rigidity of the molecular chain and the interaction force between molecular chains are reduced. As a result, the mechanical properties of the polymer films are also reduced.

### 3.5. Dynamic thermomechanical properties

The thermal mechanical properties of polymers were detected by dynamic thermomechanical analysis (DMA) (Figure 7), and the results are shown in Table 3. The storage modulus  $E'$  reflects the elastic component of viscoelasticity, and the stiffness of a material. The areas of the storage modulus curve where the values change rapidly correspond to the peaks in the  $\tan \delta$  curve, which represent the glass transition temperature. The polymers' glass transition temperature ( $T_g$ ) increases as the proportion of PHPH group increases. The DMA results are in good agreement with the DSC results. The introduction of large volume groups reduces the regularity of the main

chain and thus leads to a decrease in the initial storage modulus of PAEK films compared to PEEK. With the increase of 6F-BPA content and free volume, the rigidity of molecular chains and intermolecular interactions are reduced, and molecular chain segments are more likely to slide to sliding under external forces. Therefore, the temperature range for the rapid change in film energy storage modulus shifts towards low temperature with the increase of 6F-BPA content.

The plots of  $\tan \delta$  as a function of temperature are presented in Figure 7b. The damping of the material is also the internal friction, representing the ratio of the energy lost by the material during the weekly cycle to the maximum elastic energy storage. The areas in the storage modulus curve where the values change rapidly correspond to the peaks in the  $\tan \delta$  curve and each peak of  $\tan \delta$  corresponds to a specific relaxation process. Each curve exhibits a single and sharp loss peak. These results show that PAEK films have single and outstanding  $T_g$ . It is concluded that PAEK films have excellent thermal mechanical properties.

### 3.6. Dielectric properties

Figures 8a and 8b show the dielectric constant and dielectric loss curves of PAEK films with different 6F-BPA contents at frequencies of  $10^3$ – $10^6$  Hz, respectively. PAEK films and commercial PEEK films are all  $50 \pm 0.5$   $\mu\text{m}$  thick. Figure 8a shows that their dielectric constants are lower than commercial PEEK (3.3 at 1 MHz) and decrease as the test frequency increases. The PAEK with different structures show different dielectric constants, which can be explained by the Debye equation [23] (Equation (1)):

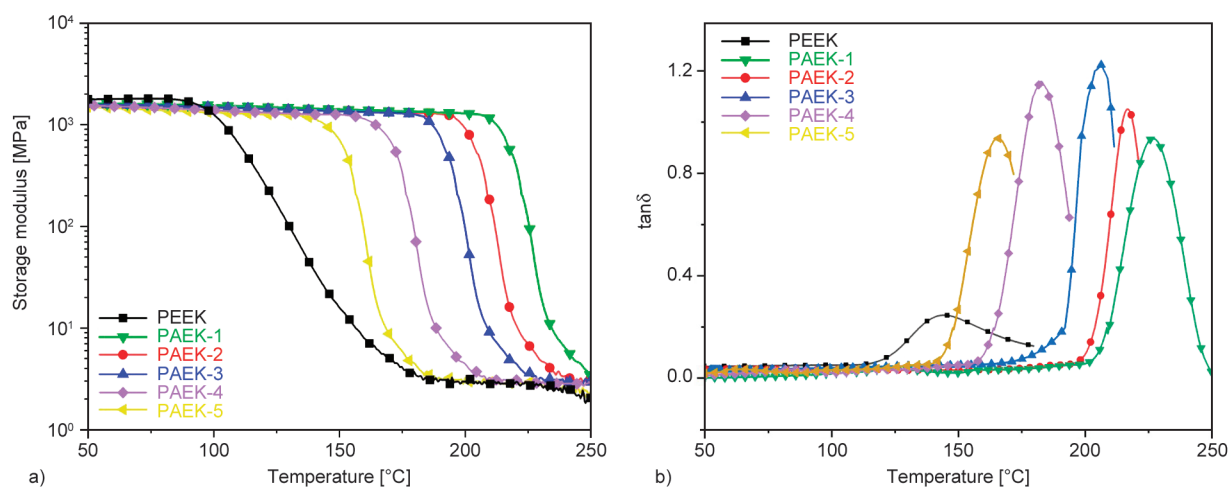
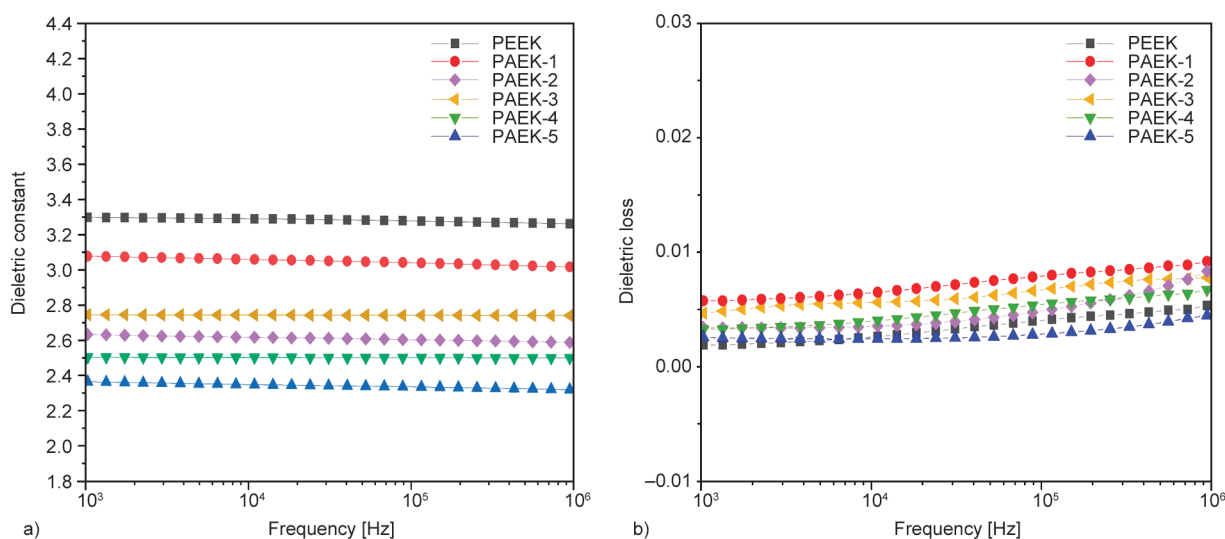


Figure 7. DMA curves of PAEK films: a) storage modulus and b)  $\tan \delta$ .



**Figure 8.** Frequency dependence of a) dielectric constant and b) dielectric loss of PAEK films at room temperature.

$$\frac{\epsilon_r - 1}{\epsilon_r + 2} = \frac{4\pi N}{3} \left( \alpha_e + \alpha_d + \frac{\mu^2}{3k_b T} \right) \quad (1)$$

where  $\epsilon_r$  is the dielectric constant,  $N$  is the number density of dipoles,  $\alpha_e$  is the electric polarization,  $\alpha_d$  is the distortion polarization,  $\mu$  is the orientation polarization related to the dipole moment,  $k_b$  is the Boltzmann constant, and  $T$  is the temperature.

The introduction of large-volume structures with poor regularity can reduce the regularity and the stacking density of the polymer chain and consequently reduce the molar volume of the polymer and  $N$ . The large volume  $-CF_3$  group has a C–F bond with low polarizability and large bond energy, making it difficult for the polymer to polarize and thus leading to reduction of  $\alpha_e$  [41]. Therefore, the dielectric constant of PAEK films at 1 MHz decreases

from 3.08 to 2.31 with the increase of the 6F-BPA content in the bisphenol system. Figure 8b reveals that PAEK films exhibit relatively low dielectric loss. The dielectric loss increases with the increase of frequency because the molecular movement can not follow up the variety of frequencies of the applied electric field [45]. At present, the dielectric constant of standard polyimide (PI) films used in the field of electronics and electrical appliances is about 3.2–3.6 (1 MHz), indicating that PAEK itself has a relatively low dielectric constant compared to PI. Compared to traditional PEEK, these novel PAEK films have lower dielectric constant and dielectric loss and better comprehensive performance.

The properties of previously reported PAEKs are summarized in Table 4. Low dielectric constant materials are needed in electronics and electrical appliances,

**Table 4.** Properties of PAEK polymers and copolymers.

Samples	$T_g^a$ [°C]	$T_{d5\%}$ [°C]	Tensile strength [MPa]	Tensile modulus [GPa]	Dielectric constant at 1 MHz	Reference
PEEK-PFN-2	124	580.3	–	–	3.20	[46]
PAEKs	148–160	>527	95.2–104.0	2.68–3.06	2.75–2.95	[27]
APAEKs	–	530	65–70	1.6–2.0	2.6–2.7	[47]
DDSQ-PEEK	136	396	–	–	1.95	[48]
PNAEK	229 <sup>b</sup>	450	72.47	1.32	2.78	[49]
FPNAEK	225 <sup>b</sup>	443	76.58	1.39	2.49	[49]
AdRES-PEEK	181–250	460–492	41.3–48.3	2.07–3.82	2.69–2.95	[26]
AdNp-PEEK	205–278	480–508	55–89.5	1.95–2.15	2.67–2.92	[26]
NPEEK	167–194	472–545	62.8–104.1	1.5–3.18	2.57–2.99	[50]
iPrPEKC	186	455	95	2.73	2.81	[51]
iPrBPFL-x	209–232	439–478	82–95	1.84–1.86	2.67–2.79	[51]
PHPH/6F-BPA-PAEK	177–220	486–516	53–59	1.4–1.6	2.45–2.70	This work

$T_g^a$ : glass transition temperature measured by DSC except for PNAEK and FPNAEK;

$T_g^b$ : glass transition temperature measured by DMA;

–: not measured.

which helps to improve signal transmission speed and reduce signal delay and signal loss. Excellent heat resistance is also required to withstand the heat generated by the environment and devices. The new PAEK films prepared in this work have high heat resistance ( $T_g > 170^\circ\text{C}$ ) and thermal stability ( $T_{d5\%} > 480^\circ\text{C}$ ), as well as low dielectric constant (2.45–2.70, 1 MHz). Polymer thin film materials with good heat resistance and low dielectric constant can replace traditional inorganic ceramic materials for interlayer dielectric (ILD) and intermetallic dielectric (IMD) in advanced chips.

### 3.7. Optical properties

Figure 9 shows the images of commercial PEEK film and PAEK films. It is seen that PAEK films have better transparency than commercial PEEK film. PAEK-1 and PAEK-2 films are slightly yellow, and they become colorless as more fluorine is introduced. Figure 10 shows the UV-vis spectra of PAEK films of  $50\pm 0.5\ \mu\text{m}$  in the 200–800 nm wavelength range. The cutoff wavelength of PAEK films is 320–386 nm, and the higher the proportion of 6F-BPA in the bisphenol system, the smaller the cutoff wavelength of the polymer film and the higher the optical transmittance. The visible light transmittance of PAEK films at 450 nm can reach 80% or above, which is much higher than that of commercial PEEK. The introduction of  $-\text{CF}_3$  group improves the transparency of PAEK films. This is mainly because the introduction of strong electronegative fluorine atoms causes damage to the conjugation and planar structure of PAEK molecular chain and hinders the conjugation of molecules, and therefore, the maximum absorption peak wavelength of visible light of the polymer shifts to the short wave direction and the transparency of the polymer is improved. Thus, it can be used as potential optoelectronic materials in display screens, mobile phones, and 5G mobile device casings [52–54].

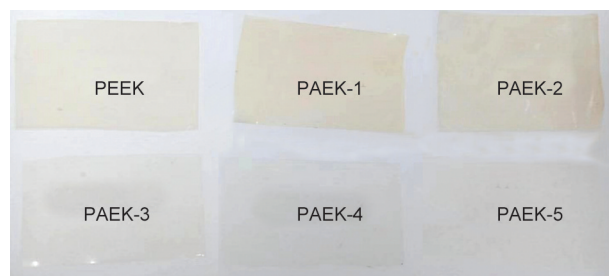


Figure 9. Images of commercial PEEK film and PAEK films.

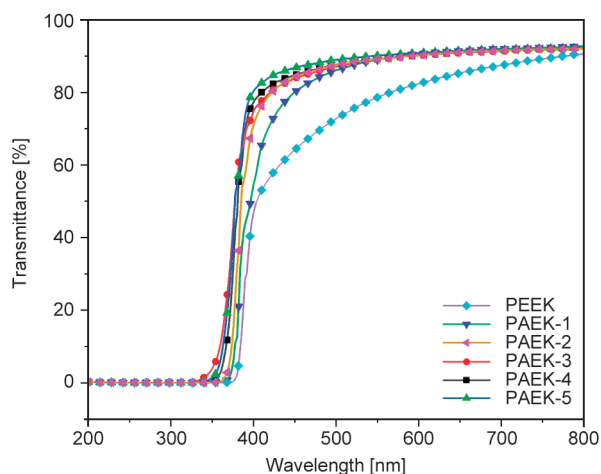


Figure 10. UV-vis spectra of PAEK films.

### 4. Conclusions

In this study, new PAEK copolymers containing  $-\text{CF}_3$  and phenolphthalein groups have been successfully synthesized based on molecular design. These PAEK copolymers are amorphous and exhibit excellent film-forming ability. Compared to commercial PEEK, they exhibit good solubility in common organic solvents. With the increase of 6F-BPA content in the bisphenol system, the mechanical strength of the polymer film is decreased, and the thermal stability of the polymers, transparency and dielectric properties of the films are increased. When the mole fraction of 6F-BPA is 50%,  $T_g$  is  $196^\circ\text{C}$  and  $T_{d5\%}$  is  $504^\circ\text{C}$  under a nitrogen atmosphere. The tensile strength of PAEK-3 film is 55 MPa, and the dielectric constant at 1 MHz is 2.60. The dielectric loss is 0.006. The visible light transmittance at 450 nm is 80%. The properties of copolymers differ depending on the proportion of copolymerization units. This study provides insights into the preparation of PAEK films with low dielectric constant, high optical transparency, good mechanical properties, and high thermal stability and expands the application of PAEK materials to microelectronics, optical waveguides, and display devices.

### Acknowledgements

This research was financially supported by Zhejiang Jitai New Materials Co., Ltd.

### References

- [1] Morgen M., Zhao J.-H., Hu C., Cho T., Ho P. S., Todd E.: Low dielectric constant materials for advanced interconnects. JOM, 51, 37–40 (1999). <https://doi.org/10.1007/s11837-999-0158-8>

- [2] Zhi X. X., Zhang Y., Zhang X. M., Wang H. L., Wu L., An Y. C., Wei X. Y., Liu J. G.: Preparation and properties of semi-alicyclic colorless polyimide films and light-colored sheets with low dielectric features for potential applications in optoelectronic integrated circuits. *Express Polymer Letters*, **15**, 1051–1062 (2021). <https://doi.org/10.3144/expresspolymlett.2021.85>
- [3] Wang Y., Sun J., Jin K., Wang J., Yuan C., Tong J., Diao S., He F., Fang Q.: Benzocyclobutene resin with fluorene backbone: A novel thermosetting material with high thermostability and low dielectric constant. *RSC Advances*, **4**, 39884–39888 (2014). <https://doi.org/10.1039/C4RA05898D>
- [4] Cao T., Wang L., Lin G., An Y., Liu X., Huang Y.: Cross-linked porous polyarylene ether nitrile films with ultralow dielectric constant and superior mechanical properties. *Polymer*, **259**, 125361 (2022). <https://doi.org/10.1016/j.polymer.2022.125361>
- [5] You Y., Liu S., Tu L., Wang Y., Zhan C., Du X., Wei R., Liu X.: Controllable fabrication of poly(arylene ether nitrile) dielectrics for thermal-resistant film capacitors. *Macromolecules*, **52**, 5850–5859 (2019). <https://doi.org/10.1021/acs.macromol.9b00799>
- [6] Homma T.: Low dielectric constant materials and methods for interlayer dielectric films in ultralarge-scale integrated circuit multilevel interconnections. *Materials Science and Engineering R: Reports*, **23**, 243–285 (1998). [https://doi.org/10.1016/S0927-796X\(98\)00012-6](https://doi.org/10.1016/S0927-796X(98)00012-6)
- [7] Cheng K., Yang M-H., Chiu W. W. W., Huang C-Y., Chang J., Ying T-F., Yang Y.: Ink-jet printing, self-assembled polyelectrolytes, and electroless plating: Low cost fabrication of circuits on a flexible substrate at room temperature. *Macromolecular Rapid Communications*, **26**, 247–264 (2005). <https://doi.org/10.1002/marc.200400462>
- [8] Logothetidis S.: Flexible organic electronic devices: Materials, process and applications. *Materials Science and Engineering: B*, **152**, 96–104 (2008). <https://doi.org/10.1016/j.mseb.2008.06.009>
- [9] Dang Z-M., Yuan J-K., Yao S-H., Liao R-J.: Flexible nanodielectric materials with high permittivity for power energy storage. *Advanced Materials*, **25**, 6334–6365 (2013). <https://doi.org/10.1002/adma.201301752>
- [10] Yao S-H., Yuan J-K., Zhou T., Dang Z-M., Bai J.: Stretch-modulated carbon nanotube alignment in ferroelectric polymer composites: Characterization of the orientation state and its influence on the dielectric properties. *The Journal of Physical Chemistry C*, **115**, 20011–20017 (2011). <https://doi.org/10.1021/jp205444x>
- [11] Dang Z-M., Yuan J-K., Zha J-W., Zhou T., Li S-T., Hu G-H.: Fundamentals, processes and applications of high-permittivity polymer–matrix composites. *Progress in Materials Science*, **57**, 660–723 (2012). <https://doi.org/10.1016/j.pmatsci.2011.08.001>
- [12] Zhang Z-Y., Sheng S-R., Zhang X-L., Pan Y., Liu X-L.: New poly(aryl ether ketone)s containing 2,6-diphenylpyridyl units and diphenylphosphinophenyl pendant groups. *High Performance Polymers*, **32**, 753–760 (2020). <https://doi.org/10.1177/0954008319901148>
- [13] Hergenrother P. M., Jensen B. J., Havens S. J.: Poly(arylene ethers). *Polymer*, **29**, 358–369 (1988). [https://doi.org/10.1016/0032-3861\(88\)90347-3](https://doi.org/10.1016/0032-3861(88)90347-3)
- [14] Attwood T. E., Dawson P. C., Freeman J. L., Hoy L. R. J., Rose J. B., Staniland P. A.: Synthesis and properties of polyaryletherketones. *Polymer*, **22**, 1096–1103 (1981). [https://doi.org/10.1016/0032-3861\(81\)90299-8](https://doi.org/10.1016/0032-3861(81)90299-8)
- [15] Rao V. L.: Polyether ketones. *Journal of Macromolecular Science Part C*, **35**, 661–712 (1995). <https://doi.org/10.1080/15321799508021753>
- [16] Giants T. W.: Crystallinity and dielectric properties of PEEK, poly(ether ether ketone). *IEEE Transactions on Dielectrics and Electrical Insulation*, **1**, 991–999 (1994). <https://doi.org/10.1109/94.368664>
- [17] da Silva Burgal J., Peeva L. G., Kumbharkar S., Livingston A.: Organic solvent resistant poly(ether-ether-ketone) nanofiltration membranes. *Journal of Membrane Science*, **479**, 105–116 (2015). <https://doi.org/10.1016/j.memsci.2014.12.035>
- [18] Garcia-Gonzalez D., Rusinek A., Jankowiak T., Arias A.: Mechanical impact behavior of polyether–ether–ketone (PEEK). *Composite Structures*, **124**, 88–99 (2015). <https://doi.org/10.1016/j.compstruct.2014.12.061>
- [19] Lu T., Wen J., Qian S., Cao H., Ning C., Pan X., Jiang X., Liu X., Chu P. K.: Enhanced osteointegration on tantalum-implanted polyetheretherketone surface with bone-like elastic modulus. *Biomaterials*, **51**, 173–183 (2015). <https://doi.org/10.1016/j.biomaterials.2015.02.018>
- [20] Chen Y., Ren F., Dai J. G., Li D., Luo S.: Poly(ether ether ketone)s containing benzene pendant in the molecular chain: Synthesis, characterization and optical properties. *High Performance Polymers*, **33**, 546–553 (2020). <https://doi.org/10.1177/0954008320974074>
- [21] Sheng S-R., Liu X-L., Tong Y-F., Chen L., Wen H-L., Song C-S.: Synthesis and characterization of novel organosoluble methyl substituted poly(aryl ether ketone)s containing sulfone linkage. *Journal of the Chinese Chemical Society*, **52**, 943–946 (2005). <https://doi.org/10.1002/jccs.200500131>
- [22] Wen H., Wang P., Cheng S., Yan T., Cai M.: Synthesis and characterization of novel organosoluble poly(aryl ether ketone)s and poly(aryl ether ketone sulfone)s containing 1,4-naphthylene units. *High Performance Polymers*, **27**, 705–713 (2014). <https://doi.org/10.1177/0954008314557707>
- [23] Kohl P. A.: Low–dielectric constant insulators for future integrated circuits and packages. *Annual Review of Chemical and Biomolecular Engineering*, **2**, 379–401 (2011). <https://doi.org/10.1146/annurev-chembioeng-061010-114137>

- [24] Wang Q., Pu Z., Zheng X., Tian Y., Li X., Zhong J.: Preparation and physical properties of intrinsic low- $\kappa$  polyarylene ether nitrile with enhanced thermo-stability. *Journal of Polymer Research*, **27**, 328 (2020).  
<https://doi.org/10.1007/s10965-020-02311-1>
- [25] Wang L., Liu X., Liu C., Zhou X., Liu C., Cheng M., Wei R., Liu X.: Ultralow dielectric constant polyarylene ether nitrile foam with excellent mechanical properties. *Chemical Engineering Journal*, **384**, 123231 (2020).  
<https://doi.org/10.1016/j.cej.2019.123231>
- [26] Wang G., Geng Z., Zhu X., Zhang S., Liu X.: Synthesis and characterization of soluble low- $\kappa$  poly(aryl ether ketone) copolymers with pendent adamantyl groups. *High Performance Polymers*, **22**, 779–798 (2010).  
<https://doi.org/10.1177/0954008309358926>
- [27] Xie J., Peng W-Y., Li G., Jiang J-M.: Synthesis and characterization of poly(aryl ether ketone)s with fluorinated phenyl in the side chain. *Polymer Bulletin*, **67**, 45–56 (2011).  
<https://doi.org/10.1007/s00289-010-0357-z>
- [28] Liu L., Wang G., Yan T., Cai M.: Synthesis and properties of novel copolymers of poly(ether ketone ketone) and poly(ether sulfone ether ketone ketone) containing 1,4-naphthylene moieties. *High Performance Polymers*, **30**, 172–180 (2017).  
<https://doi.org/10.1177/0954008316685412>
- [29] Eckstorff F., Zhu Y., Maurer R., Müller T. E., Scholz S., Lercher J. A.: Materials with tunable low- $\kappa$  dielectric constant derived from functionalized octahedral silsesquioxanes and spherosilicates. *Polymer*, **52**, 2492–2498 (2011).  
<https://doi.org/10.1016/j.polymer.2011.01.050>
- [30] Liu J., Chen G., Guo J., Mushtaq N., Fang X.: Synthesis of high performance phenolphthalein-based cardo poly(ether ketone imide)s *via* aromatic nucleophilic substitution polymerization. *Polymer*, **70**, 30–37 (2015).  
<https://doi.org/10.1016/j.polymer.2015.05.058>
- [31] Liu B., Hu W., Chen C., Jiang Z., Zhang W., Wu Z., Matsumoto T.: Soluble aromatic poly(ether ketone)s with a pendant 3,5-difluoromethylphenyl group. *Polymer*, **45**, 3241–3247 (2004).  
<https://doi.org/10.1016/j.polymer.2004.03.015>
- [32] Guan X., Nie H., Wang H., Zhao J., Wang Z., Zhou G., Gu Q.: High-performance soluble copolyarylate based on phenolphthalein: Synthesis, characterization and properties. *Polymer International*, **68**, 1729–1738 (2019).  
<https://doi.org/10.1002/pi.5879>
- [33] Ba J., Geng Z., Mu J.: Soluble low- $\kappa$  poly(aryl ether ketone) copolymers containing pendant adamantyl group and long aliphatic side chains. *Journal of Applied Polymer Science*, **130**, 193–200 (2013).  
<https://doi.org/10.1002/app.39146>
- [34] Dhara M. G., Banerjee S.: Fluorinated high-performance polymers: Poly(arylene ether)s and aromatic polyimides containing trifluoromethyl groups. *Progress in Polymer Science*, **35**, 1022–1077 (2010).  
<https://doi.org/10.1016/j.progpolymsci.2010.04.003>
- [35] Myung B. Y., Ahn C. J., Yoon T. H.: Synthesis and characterization of polyimides from novel 1-(3',5'-bis(trifluoromethyl)benzene) pyromellitic dianhydride (6FPP-MDA). *Polymer*, **45**, 3185–3193 (2004).  
<https://doi.org/10.1016/j.polymer.2004.03.010>
- [36] Niu Y., Zhu X., Liu L., Zhang Y., Wang G., Jiang Z.: Synthesis and characterization of poly(aryl ether ketone) with trifluoromethyl-substituted benzene in the side chain. *Reactive and Functional Polymers*, **66**, 559–566 (2006).  
<https://doi.org/10.1016/j.reactfunctpolym.2005.10.009>
- [37] Liu B., Hu W., Chen C., Jiang Z., Zhang W., Wu Z.: Synthesis and characterization of trifluoromethylated poly(aryl ether ketone)s. *Polymers for Advanced Technologies*, **14**, 221–225 (2003).  
<https://doi.org/10.1002/pat.297>
- [38] Harrison W. L., Wang F., Mechem J. B., Bhanu V. A., Hill M., Kim Y. S., McGrath J. E.: Influence of the bisphenol structure on the direct synthesis of sulfonated poly(arylene ether) copolymers. I. *Journal of Polymer Science Part A: Polymer Chemistry*, **41**, 2264–2276 (2003).  
<https://doi.org/10.1002/pola.10755>
- [39] Chen S., Ren D., Li B., Xu M., Liu X.: Investigation on phenolphthalein and bisphenol af based poly(arylene ether nitrile) copolymers: Preparation, thermal, mechanical and dielectric properties. *Polymer Testing*, **96**, 107091 (2021).  
<https://doi.org/10.1016/j.polymertesting.2021.107091>
- [40] Pattharasiriwong P., Jubsilp C., Mora P., Rimdusit S.: Dielectric and thermal behaviors of fluorine-containing dianhydride-modified polybenzoxazine: A molecular design flexibility. *Journal of Applied Polymer Science*, **134**, 45204 (2017).  
<https://doi.org/10.1002/app.45204>
- [41] Shang C., Zhao X., Li J., Liu J., Huang W.: Poly(aryl ether ketone/sulfone)s containing ortho-methyl and pendant trifluoromethyl-substituted phenyl groups: Synthesis and properties. *High Performance Polymers*, **24**, 692–701 (2012).  
<https://doi.org/10.1177/0954008312449845>
- [42] Luo Y-S., Wang Q-Y., Mao X-C., Sheng S-R.: Synthesis and characterization of new cardo poly(ether amide)s containing 9(10H)-anthrone units. *High Performance Polymers*, **32**, 1001–1009 (2020).  
<https://doi.org/10.1177/0954008320918922>
- [43] Xu R., Li L., Jin X., Hou M., He L., Lu Y., Song C., Wang T.: Thermal crosslinking of a novel membrane derived from phenolphthalein-based cardo poly(arylene ether ketone) to enhance CO<sub>2</sub>/CH<sub>4</sub> separation performance and plasticization resistance. *Journal of Membrane Science*, **586**, 306–317 (2019).  
<https://doi.org/10.1016/j.memsci.2019.05.084>

- [44] Hamciuc C., Lisa G., Hamciuc E., Epure E-L., Tudorachi N.: Thermal behavior study and degradation mechanism by TG/MS/FTIR technique of some poly(aryl ether ether ketone)s. *Journal of Analytical and Applied Pyrolysis*, **150**, 104877 (2020).  
<https://doi.org/10.1016/j.jaap.2020.104877>
- [45] Hu J., Gu A., Liang G., Zhuo D., Yuan L.: Preparation and properties of mesoporous silica/bismaleimide/diallylbisphenol composites with improved thermal stability, mechanical and dielectric properties. *Express Polymer Letters*, **5**, 555–568 (2011).  
<https://doi.org/10.3144/expresspolymlett.2011.54>
- [46] Sun H., Lv Y., Zhang C., Zuo X., Li M., Yue X., Jiang Z.: Materials with low dielectric constant and loss and good thermal properties prepared by introducing perfluorononyl pendant groups onto poly(ether ether ketone). *RSC Advances*, **8**, 7753–7760 (2018).  
<https://doi.org/10.1039/C7RA13600E>
- [47] Jao Q., Li N., Zhang P., Wang S., Zhao Y., Feng C., Lv Y.: Synthesis of novel fluorinated poly(aryl ether ketone)s and their properties. *Polymer Science, Series B*, **63**, 333–340 (2021).  
<https://doi.org/10.1134/s1560090421040059>
- [48] Hao J., Wei Y., Li X., Mu J.: Poly(arylene ether ketone)s with low dielectric constants derived from polyhedral oligomeric silsesquioxane and difluorinated aromatic ketones. *Journal of Applied Polymer Science*, **135**, 46084 (2018).  
<https://doi.org/10.1002/app.46084>
- [49] Zhang Y., Jiang H., Liu J., Zhao C., Na H.: Naphthalene-containing poly(arylene ether ketone) with low dielectric constant. *Journal of Applied Polymer Science*, **135**, 46857 (2018).  
<https://doi.org/10.1002/app.46857>
- [50] Liu X., Xu X., Liu Z.: Synthesis and characterization of novel fluorinated naphthalene-based poly(arylene ether ketone)s with low dielectric constants. *Journal of Materials Science: Materials in Electronics*, **30**, 16369–16375 (2019).  
<https://doi.org/10.1007/s10854-019-02008-2>
- [51] Ling M., Yu K., Wang J., Wang Z., Zhou G.: Design and synthesis of novel phenolphthalein-based poly(aryl ether) resin containing isopropyl groups. *Journal of Materials Research and Technology*, **21**, 153–160 (2022).  
<https://doi.org/10.1016/j.jmrt.2022.09.038>
- [52] Tie W., Zhong Z., Wen P., Lee M-H., Li X-D.: Synthesis and characterization of a novel photocrosslinkable fluorinated poly(arylene ether) for optical waveguide. *Materials Letters*, **63**, 1381–1383 (2009).  
<https://doi.org/10.1016/j.matlet.2009.01.079>
- [53] Yen C-T., Chen W-C., Liaw D-J., Lu H-Y.: Synthesis and properties of new polyimide–silica hybrid films through both intrachain and interchain bonding. *Polymer*, **44**, 7079–7087 (2003).  
<https://doi.org/10.1016/j.polymer.2003.09.004>
- [54] Zhao X., Liu J., Yang H., Fan L., Yang S.: Novel polyfluorinated polyimides derived from  $\alpha,\alpha$ -bis(4-amino-3,5-difluorophenyl)phenylmethane and aromatic dianhydrides: Synthesis and characterization. *European Polymer Journal*, **44**, 808–820 (2008).  
<https://doi.org/10.1016/j.eurpolymj.2007.12.016>

Research article

# Releasing of zinc ions from modified zinc oxide surfaces for improvement chemical crosslinks and antibacterial properties of acrylonitrile butadiene rubber films

Pornsiri Toh-ae<sup>1</sup>, Raymond Lee-Nip<sup>2</sup>, Yeampon Nakaramontri<sup>1\*</sup>

<sup>1</sup>Sustainable Polymer & Innovative Composites Material Research Group, Department of Chemistry, Faculty of Science, King Mongkut's University of Technology Thonburi, Bangkok, Thailand

<sup>2</sup>Global Chemical Co., Ltd. Bangpoo Industrial Estate, Samutprakarn, Thailand

Received 3 April 2023; accepted in revised form 1 June 2023

**Abstract.** Acrylonitrile butadiene rubber (NBR) films filled with zinc oxide (ZnO) were prepared via latex mixing. The ZnO of commercial ZnO ( $ZnO_{WH}$ ), ZnO nanoparticles ( $ZnO_{nap}$ ),  $ZnO_{nap}$ -coated with calcium carbonate ( $ZnO_{nap-C}$ ), and titanium dioxide ( $ZnO_{nap-T}$ ) were investigated, and the mechanical and dynamic mechanical properties, crosslink density, and antibacterial activity of the resultant films were explored. The study found that the particle size and distribution of ZnO in the NBR films played a significant role in enhancing their properties. The incorporation of  $ZnO_{nap}$  resulted in a greater enhancement in the properties of the composite film than the  $ZnO_{WH}$  microparticles, with the greatest enhancement achieved with  $ZnO_{nap-C}$ . Furthermore, the composite films filled with 1 phr of  $ZnO_{nap-C}$  exhibited 99.9% bacterial reduction efficacy against *Staphylococcus aureus* and *Escherichia coli* according to ISO 22196:2011 due to the release of reactive oxygen species and zinc ions across the rubber film layers to the bacterial surfaces. In addition, the bactericidal efficacy on the surface of the composite films was investigated by varying the contact kill times in accordance with ASTM D7907-14. The addition of  $ZnO_{nap-C}$  at 4 phr reduced both bacterial levels by 92.00 and 51.85%, respectively, within 30 min. Hence, this research aims to contribute to developing new medical disinfection products, such as medical gloves and multipurpose rubber sheets.

**Keywords:** rubber, polymer composites, recycling, industrial application, material testing

## 1. Introduction

Acrylonitrile butadiene rubber (NBR), also known as nitrile rubber, is commonly synthesized through the copolymerization of acrylonitrile and butadiene monomers. This synthetic rubber is widely distinguished by its excellent heat stability, abrasion resistance, green strength, and oil resistance; thus, NBR is used in the production of several items, including disposable gloves, gaskets, oil seals, hoses, O-rings, automotive parts, footwear, etc. Notably, the need for NBR gloves has significantly increased since these present no allergenic concerns compared to commercial natural rubber (NR) gloves, though NBR has

lower elasticity [1]. However, as with other commercial rubber applications, NBR displays an inability to kill microorganisms on its surface. Hence, the incorporation of antibacterial agents into the rubber matrix has become necessary to inhibit the growth of microorganisms on the product surface. The bacteria *Staphylococcus aureus*, *Pseudomonas aeruginosa*, *Escherichia coli*, *Klebsiella pneumoniae*, *Serratia marcescens*, *Bacillus cereus*, *enterococci*, *Acinetobacter spp.*, and coagulase-negative staphylococci are frequently reported as causing hospital-associated infections. These microorganisms are responsible for human pathogenic diseases and cause

\*Corresponding author, e-mail: [yeampon.nak@kmutt.ac.th](mailto:yeampon.nak@kmutt.ac.th)

© BME-PT

various infections, such as cholecystitis and cholangitis, peritonitis [2], nosocomial bloodstream infection [3], and respiratory and urinary infections [4]. Hospital-associated infections can be transmitted among people via exposure to contaminated water, food, and objects and physical contact with health-care workers [2]. Therefore, the development of products with microbial inhibitory properties has become a significant area of study.

Antibacterial agents are classified as organic and inorganic substances that can destroy or inhibit the growth of microorganisms by disrupting the bacterial membrane structure, resulting in the loss of cytoplasmic components [5]. The applications of inorganic antibacterial agents based on metal and metal oxide nanoparticles have frequently been investigated. Incorporating chemicals with smaller sizes and larger surface areas into the polymer matrix enhances the bacteria-killing efficiency of rubber films due to the resultant increased reactivity, unique quantum size effect, catalytic activity, and ability to release metal ions [6]. The majority of inorganic nanometals and nanometal oxides, including silver [7], copper [8], zinc oxide (ZnO) [9], titanium dioxide [10], etc., have been intensively studied due to their antimicrobial behaviors.

Among these inorganic agents, ZnO constitutes a multifunctional species due to its unique physical and chemical properties, such as high thermal conductivity, a high refractive index, good photochemical activity, UV blocking, and antimicrobial activity together with easy incorporation into elastic polymers. ZnO is harmless to humans and is currently listed as generally recognized as safe (GRAS) by the United States Food and Drug Administration (FDA). Several mechanisms contribute to the antimicrobial activity of ZnO, including (i) the generation of reactive oxygen species (ROS), such as hydrogen peroxide, hydroxyl radicals ( $\cdot\text{OH}$ ), and superoxide anion radicals ( $\cdot\text{O}_2^-$ ); (ii) the release of  $\text{Zn}^{2+}$  ions; and (iii) electrostatic interactions that cause the oxidation of the bacterial cell membrane and cytoplasm [11]. In addition, ZnO nanoparticles are known to have an inhibitory effect on several pathogens, including Gram-positive and Gram-negative bacteria [12, 13], fungi [14], multiple drug-resistant (MDR) bacteria [15], and viruses [16].

However, ZnO is beneficial not only when used on its own but also when added to various manufactured materials in the plastic, fiber, glass, pigment, ceramic,

and rubber industries. In the last-mentioned industry in particular, ZnO is recognized as an activator in the vulcanization reaction in rubber matrices, which involves chemical crosslinking in unsaturated rubber molecules. In addition, the incorporation of ZnO into the polar NBR might contribute to electrostatic interactions, which lead to ionic crosslinking networks and enhanced mechanical properties [17]. In a study investigating the incorporation of ZnO in NR films via latex processes, modified ZnO, in particular, showed effective disruption of *E. coli* through the formation of ROS and  $\text{Zn}^{2+}$  ions, while less enhancement in the properties of the films was observed in the case of unmodified ZnO due to its low surface area and poor degree of dispersion [18]. This implies that the potential role of ZnO is mainly influenced by the degree of ZnO dispersion, the metric that determines the synergistic effect of the improvement in the mechanical and antibacterial properties of the rubber film. However, due to their specific surface areas, ZnO nanoparticles agglomerate easily, reducing the enhancement of the film properties. Thus, this necessitates the modification of ZnO for the dispersion of ZnO nanoparticles in the latex compound, related to increasing the effective surface area in the targeted object.

Therefore, this research aims to evaluate the incorporation of ZnO into NBR composite films by varying the ZnO loadings from 0–20 phr. Different types of ZnO were investigated, including white seal ZnO ( $\text{ZnO}_{\text{WH}}$ ), ZnO nanoparticles ( $\text{ZnO}_{\text{nap}}$ ),  $\text{ZnO}_{\text{nap}}$ -coated with  $\text{CaCO}_3$  in a 90:10  $\text{ZnO}_{\text{nap}}:\text{CaCO}_3$  weight ratio ( $\text{ZnO}_{\text{nap}}\text{-C}$ ), and  $\text{ZnO}_{\text{nap}}$ -coated with  $\text{TiO}_2$  in a 50:50  $\text{ZnO}_{\text{nap}}:\text{TiO}_2$  weight ratio ( $\text{ZnO}_{\text{nap}}\text{-T}$ ). The reinforcement of the NBR matrix with ZnO particles was evaluated based on its mechanical, crosslinking, and thermomechanical properties. The antibacterial activities of the NBR composite films were investigated using *Escherichia coli* (*E. coli*) and *Staphylococcus aureus* (*S. aureus*) as representatives of Gram-negative and Gram-positive bacteria, respectively. This research further aims to contribute to developing new medical disinfection products, such as gloves and multipurpose rubber sheets.

## 2. Experimental section

### 2.1. Materials

Acrylonitrile butadiene rubber (NBR) latex, with a solid content of 40% and containing 45% acrylonitrile content, was purchased from Norrawat Chemical

R1  
R2  
R3  
R4  
R5  
R6  
R7  
R8  
R9  
R10  
R11  
R12  
R13  
R14  
R15  
R16  
R17  
R18  
R19  
R20  
R21  
R22  
R23  
R24  
R25  
R26  
R27  
R28  
R29  
R30  
R31  
R32  
R33  
R34  
R35  
R36  
R37  
R38  
R39  
R40  
R41  
R42  
R43  
R44  
R45  
R46  
R47  
R48  
R49

Limited Partnership (Samut Sakhon, Thailand). The potassium hydroxide was manufactured by Qingdao Hisea Chem Co. Ltd., (Qingdao, China). In addition, 50% Sulfur, 50% zinc 2-mercaptobenzothiazole (ZMBT), and 50% Lowinox CPL (butylated reaction product of para-cresol and dicyclopentadiene) were purchased from Thanodom Trading Co., Ltd. (Bangkok, Thailand). Various types of ZnO particles used in this work are ZnO white seal grade ( $ZnO_{WH}$ ) together with different types of ZnO nanoparticles ( $ZnO_{nap}$ ), including  $ZnO_{nap}$ -adsorbed calcium carbonate ( $CaCO_3$ ) at  $ZnO_{nap}:CaCO_3$  ratios of 90:10% by weight ( $ZnO_{nap-C}$ ) and ZnO-adsorbed titanium dioxide ( $TiO_2$ ) at  $ZnO_{nap}:TiO_2$  ratios of 50:50 by weight ( $ZnO_{nap-T}$ ). All ZnO were supplied by Global Chemical Co., Ltd. (Samut Prakan, Thailand).

## 2.2. Preparation of NBR composite films

The NBR latex compound was carried out according to the formulation presented in Table 1. The latex compounding processes were initiated by the addition of potassium hydroxide solution, sulfur, ZMBT and CPL into NBR latex using a mechanical stirrer at 200 rpm. The mixing was continuously stirred at room temperature for 24 h to form a homogeneous latex compound. Then, the composite films were prepared by stirring the NBR latex compound for 3 min before filling ZnO and continued stirring for another 5 min. Afterward, the latex composite was poured directly into a glass plate and dried at 50 °C for 24 h in order to obtain the composite film at 0.1 mm of thickness slabs sheet.

## 3. Characterization

### 3.1. Molecular structure of ZnO

#### 3.1.1. Particle size analyzer

The  $ZnO_{WH}$ ,  $ZnO_{nap}$ ,  $ZnO_{nap-C}$  and  $ZnO_{nap-T}$  were dispersed in the deionized water at 1.0 wt%. Particle

size and distribution of ZnO suspension were characterized using a light scattering particle size analyzer (HORIBA, LA600, Kyoto, Japan). The average particle size of materials was then reported.

#### 3.1.2. Transmission electron microscope (TEM)

The morphologies of each ZnO particle were analyzed by a transmission electron microscope (TEM) (Model JEOL, JEM-1400, Tokyo, Japan) that operated with an acceleration voltage of 80 kV. The powder of specimens was dispersed in ethanol before sonicating for at least 30 min. The dispersion was finally dropped on the carbon-coated copper grid until the solvent evaporated completely, and the measurement was then started.

#### 3.1.3. Inductively coupled plasma optical emission spectrometer (ICP-OES)

The qualification of Zn ions was analyzed by an inductively coupled plasma optical emission spectrometer (ICP-OES). The amount of total Zn ions in ZnO particles were prepared by the ZnO powder of 100 µg/ml dispersed in deionized water. The sample was incubated for 6 h before adding 0.5 ml of concentrated nitric acid. The solution was subjected to Zn analysis by an Inductively coupled plasma optical emission spectrometer (ICP-OES) (Optima 8000, Perkin Elmer, Massachusetts, USA). The dissolution of ZnO in an aqueous solution was also studied by filtering the ZnO suspension after incubation before analysis.

## 3.2. Properties of NBR/ZnO composite films

### 3.2.1. Tensile properties

Tensile properties of the NBR composite films were measured using a universal testing machine (Model 3365, Instron® Inc., Massachusetts, USA). The dumbbell shape specimens were prepared according to ISO 37 type 2. The tests were performed at a crosshead speed of 500 mm/min.

### 3.2.2. Crosslink density

The crosslink densities of the composite film were performed using swelling in acetone. The sample with  $10 \times 10 \times 0.1$  mm was weight before immersing it into acetone at room temperature for 7 days according to the ASTM D471-79. The swollen samples were removed from the excess solvent before weighing the sample immediately and drying them in a hot air oven at 60 °C until the constant weight was reached.

**Table 1.** The formulation for the preparation of NBR composite foams filled with different types of ZnO.

Ingredients	Contents [phr]
40% NBR latex	100
10% Potassium hydroxide	1.0
50% Sulfur	2.0
50% ZMBT	1.0
25% $ZnO_{WH}$	0–20
25% $ZnO_{nap}$	
25% $ZnO_{nap-C}$	
25% $ZnO_{nap-T}$	

The crosslink density was calculated using the Flory-Rehner equation [19] (Equation (1)):

$$\nu = \frac{1}{V_s} \frac{\ln(1 - V_r) + V_r + \chi V_r^2}{V_r^{1/3} - \frac{V_r}{2}} \quad (1)$$

where  $\nu$  is the crosslink density [mol/cm<sup>3</sup>],  $V_s$  is the molar volume of acetone,  $V_r$  is the volume fraction of rubber in a swollen network,  $\chi$  is the Flory-Huggins interaction parameter between NBR and acetone, which is 0.351 [19].

### 3.2.3. Dynamic mechanical analysis (DMA)

Dynamic mechanical properties of the composite films were determined using a dynamic mechanical analyzer (Model DMA 1 STARe System, Mettler Toledo, USA). The samples were examined under the tension mode in the temperature region from –80 to 100 °C with a heating rate of 5 °C/min at a frequency of 10 Hz and a force of 0.2 N. The dynamic properties of storage modulus ( $E'$ ) and loss tangent ( $\tan \delta$ ) were determined.

### 3.2.4. Morphologies

Morphological properties and energy dispersive X-ray analysis (EDX) of composites were characterized by scanning electron microscope (SEM) (Thermo Fisher Scientific, Massachusetts, USA) in order to see the dispersion of unmodified and modified ZnO inside the NBR matrix. Also, optical microscopy (OM) (Carl Zeiss Microscopy GmbH, Oberkochen, Germany) was applied to clarify the dispersion, distribution and roughness of the disinfectant films in a wide area.

### 3.2.5. Antibacterial properties

The antibacterial activity of the composite film was investigated against *Staphylococcus aureus* (*S. aureus*) (ATCC 6538P) and *Escherichia coli* (*E. coli*) (ATCC 8739) as representative of Gram-positive and -negative bacteria. The qualitative determination of antibacterial properties was performed by inhibition clear zone testing. The bactericidal efficiency on the film surface was determined according to ISO 22196:2011 and ASTM D7907-14.

In inhibition clear zone testing, A single colony of bacteria was incubated under the aseptic condition in Luria Broth (*LB*) medium (Becton, Dickinson and Company, New Jersey, USA) following incubation at 37 °C for 24 h in an incubator shaker (ES-60C, Hangzhou Miu Instruments Co., Ltd, Zhejiang,

China). Further, the bacterial concentrations in the suspensions were adjusted with *LB* to obtain turbidity of 0.5 McFarland (approximately 10<sup>8</sup> CFU/ml) and spread onto the *LB* agar plate. The composite film with a diameter of 6 mm was sterilized with 70% ethanol (Ajax Chemical Co. Ltd., Samutprakarn, Thailand), then placed on the plate and incubated at 37 °C for 24 h. The antibacterial activity of the composite film was measured by the inhibition zone that was observed surrounding the sample [18].

The quantitative determination of the composite film surface was carried out according to ISO 22196:2011. The colony of bacteria was inoculated and cultivated at 37 °C for 24 h, and the bacterial suspension was adjusted with *LB* to obtain turbidity of 0.5 McFarland. The 400  $\mu$ l of bacterial suspension was added onto the composite film surface (square pieces of 50×50 mm), then covered with 40×40 mm of sterilized polyethylene film to ensure even distribution of the bacterial suspension on the surface of the composite film. The sterilized Petri dishes containing the inoculated specimens were incubated at 35 °C for 24 h. After the incubation time, 10 ml of neutralizer was added to the Petri dish and shaken at 100 rpm. The bacterial suspension was collected and diluted using a ten-fold serial dilution method. The appropriate dilutions were then spread on an *LB* agar plate, which was incubated at 35 °C for 24 h. Bacterial colonies that appeared on the agar plates were counted and calculated as colony-forming units per ml [CFU/ml]. The results were reported as the percentage of bacterial reduction, as given in Equation (2):

$$\text{Reduction of bacteria [\%]} = \frac{A - B}{A} \quad (2)$$

where  $A$  and  $B$  are the average numbers of bacterial colonies containing samples without and with an antibacterial agent, respectively.

The standard testing for ASTM D7907 is the antimicrobial test method for the determination of bactericidal efficacy on the medical examination glove surface, which has contact kill times of 0, 5, 10, 20, and 30 min. The bacteria suspension was prepared with a turbidity of 0.5 McFarland. The 20  $\mu$ l of bacteria solution was dropped onto the 10 cm<sup>2</sup> specimen surface and covered with sterilized polyethylene film. The inoculated specimens were incubated at 35 °C for 0, 5, 10, 20, and 30 min. After the specified time, the test specimen was transferred to a 50 ml

centrifuge tube that contained 10 ml of neutralizer solution. Then, the solution was vortexed for 15 seconds. Serial dilution of the neutralizer was performed. 100  $\mu$ l of each dilution was placed with the plate count agar and incubated at 35 °C for 24 h. The number of colonies in the petri dish agar was counted. The results were reported as the percentage of bacterial reduction, as given in Equation (2).

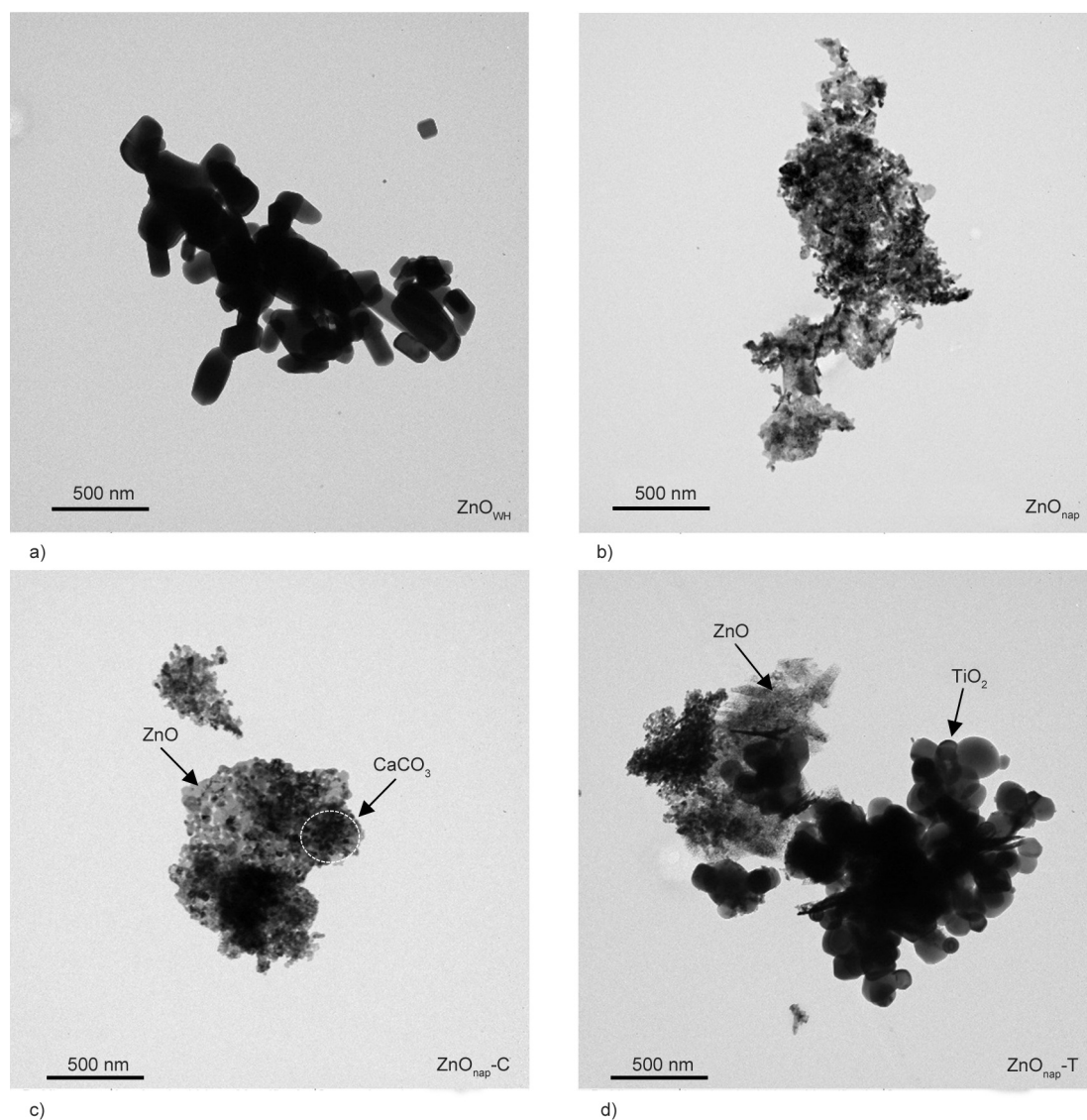
## 4. Results and discussion

### 4.1. Molecular structure of ZnO and modified ZnO

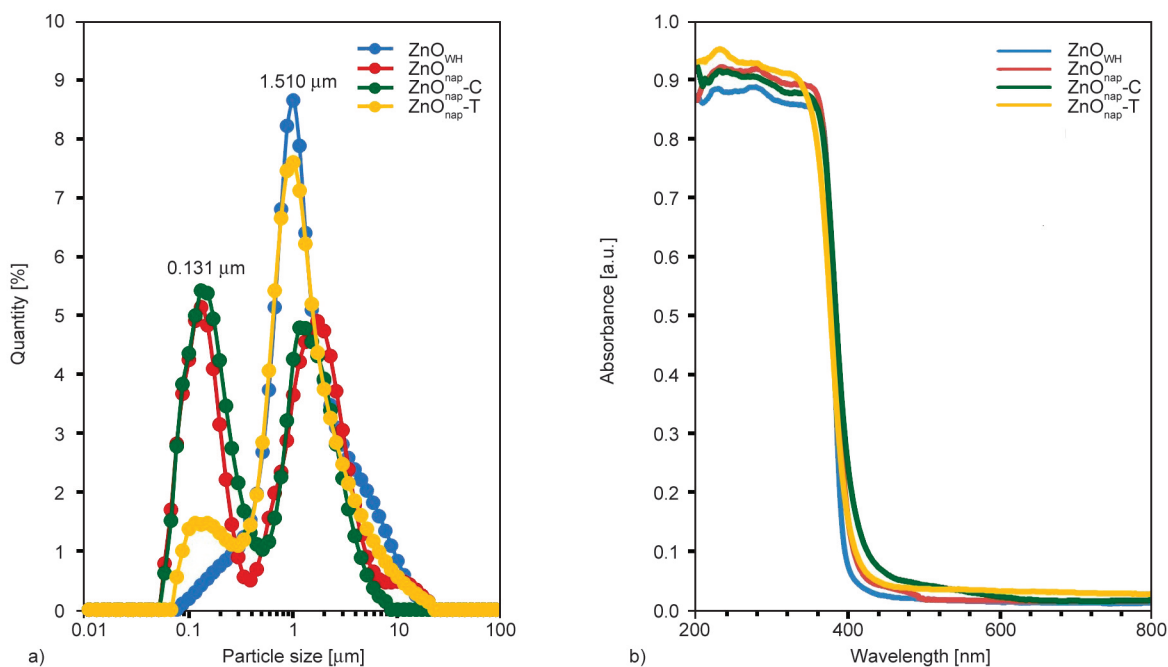
#### Physical appearance

Figure 1 depicts the molecular structures of the different types of ZnO particles, namely, ZnO<sub>WH</sub>, ZnO<sub>nap</sub>, ZnO<sub>nap</sub>-C, and ZnO<sub>nap</sub>-T. One can observe significant differences among the shapes of ZnO<sub>WH</sub> and ZnO<sub>nap</sub>.

Nanorods approximately 3  $\mu$ m in length are noted in ZnO<sub>WH</sub>, while the spherical ZnO<sub>nap</sub> exhibits a particle size of approximately 20 nm. Thus, the smaller particle size of the ZnO<sub>nap</sub> might lead to a larger tendency for agglomeration than the other ZnO particles due to their large specific surface areas. However, in the case of their incorporation into rubber, this can provide the rationale for improving the crosslinking propagation and properties of the rubber composites. In the case of ZnO<sub>nap</sub>-C and ZnO<sub>nap</sub>-T, depicting the modification of ZnO<sub>nap</sub> with CaCO<sub>3</sub> and TiO<sub>2</sub>, respectively, one can observe the formation of smaller and looser ZnO<sub>nap</sub> agglomerates. In addition, the larger size and higher concentration of the ZnO<sub>nap</sub>-T particles indicate stronger agglomeration than in the case of ZnO<sub>nap</sub>-C. The smaller size and lower concentration of ZnO<sub>nap</sub>-C led to the better formation of



**Figure 1.** Physical morphologies of commercial ZnO<sub>WH</sub> together with unmodified (a) and modified ZnO<sub>nap</sub> shown in TEM images. a) ZnO<sub>WH</sub>, b) ZnO<sub>nap</sub>, c) ZnO<sub>nap</sub>-C, d) ZnO<sub>nap</sub>-T.



**Figure 2.** Particle size distribution from particle size analyzer (a) and UV-visible absorbance spectra (b) of commercial ZnO<sub>WH</sub> together with unmodified and modified ZnO<sub>nap</sub>.

the modified chemical. Furthermore, ZnO<sub>nap-C</sub> with a ZnO<sub>nap</sub>:CaCO<sub>3</sub> ratio of 60:40 was also investigated in comparison to a 90:10 ratio, though the former yielded unsuitable properties. Therefore, suitable concentration ratios of ZnO<sub>nap</sub> to CaCO<sub>3</sub> and TiO<sub>2</sub> were used in the present work.

In addition, corresponding to the TEM images in Figure 1, the particle sizes of the ZnO types, measured with a particle size analyzer, are indicated in Figure 2a. As expected, the ZnO<sub>nap</sub> and ZnO<sub>nap-C</sub>, using CaCO<sub>3</sub> to yield a modified core-shell filler, had the smallest particle sizes – approximately 0.1 μm – while the ZnO<sub>WH</sub> and ZnO<sub>nap-T</sub> particles were approximately 1.5 μm in size. Further, Figure 2b depicts UV-visible absorbance spectra of the unmodified and modified ZnO particles to assess their absorption in the UV and visible regions. All four types of ZnO exhibit strong UV absorption in the range of 200–400 nm, and the ZnO<sub>WH</sub> microparticles show lower absorption in the visible light region. Regarding the ZnO nanoparticles, ZnO<sub>nap-C</sub> exhibits a spectral shift toward the longer wavelength region, which induces electron movement after exposure to UV and visible light. This is a factor that affects the activation of the photocatalytic reaction for producing ROS on the rubber surface, which plays an important role in bacterial disruption.

ZnO particles are known to partially dissolve in aqueous solutions, releasing Zn<sup>2+</sup> ions, which may

have an impact on antibacterial activity. The total and dissolved Zn<sup>2+</sup> ion concentrations in aqueous solution were obtained from inductively coupled plasma optical emission spectroscopy (ICP-OES), as presented in Table 2. ZnO<sub>nap-T</sub> shows the lowest total Zn<sup>2+</sup> ion concentration compared with the other ZnO types due to differences in the percentage of ZnO in the particles: ZnO<sub>nap-T</sub> consists of 50.2% ZnO, while ZnO<sub>WH</sub>, ZnO<sub>nap</sub>, and ZnO<sub>nap-C</sub> contain approximately 99.5, 97.8, and 91.4% ZnO, respectively. ZnO<sub>nap-C</sub> shows the highest concentration of dissolved Zn<sup>2+</sup> ions, indicating that the modification of ZnO reduces the agglomeration of ZnO nanoparticles and enhances their dissolution. An increase in the Zn<sup>2+</sup> concentration is principally responsible for enhanced zinc ion levels that activate chemical cross-linking and induce cytotoxicity in the disruption of bacterial cell membranes based on photocatalytic processes [20].

**Table 2.** Zinc ion contents of ZnO<sub>WH</sub> together with unmodified and modified ZnO<sub>nap</sub> received from coupled plasma optical emission spectroscopy (ICP-OES).

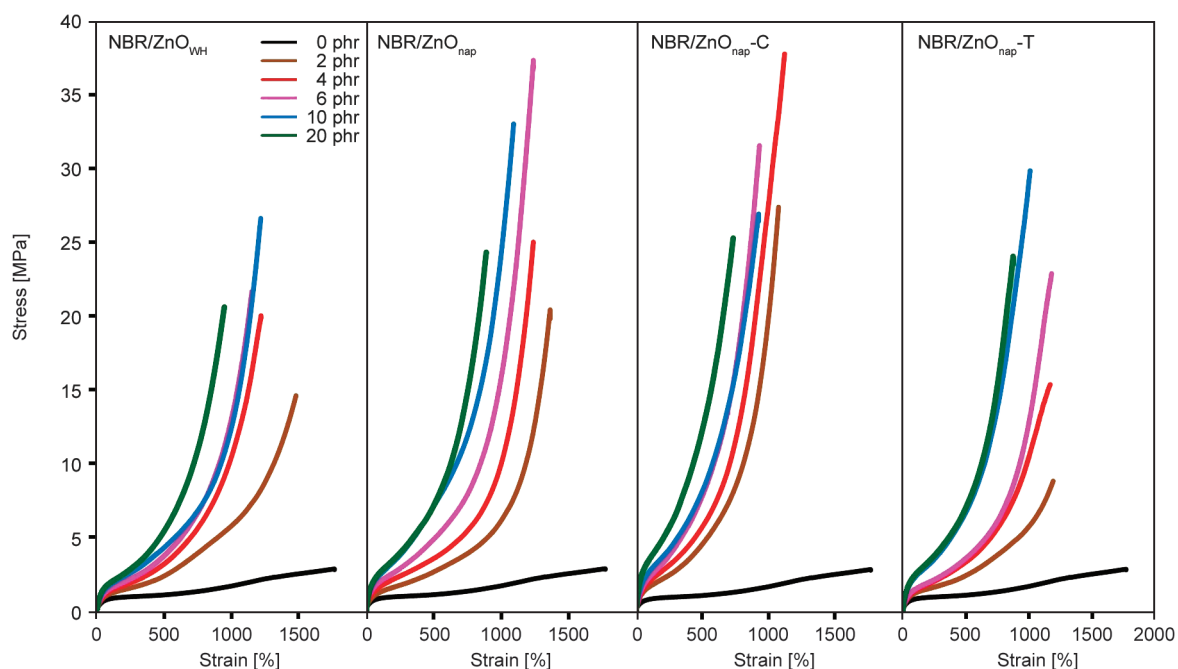
ZnO types	Zn ion contents [mg/l]	
	Total Zn	Soluble Zn
ZnO <sub>WH</sub>	21.49±0.13	0.37±0.00
ZnO <sub>nap</sub>	20.22±0.26	0.22±0.00
ZnO <sub>nap-C</sub>	21.96±0.03	3.90±0.05
ZnO <sub>nap-T</sub>	12.46±0.14	0.30±0.00

## 4.2. Properties of NBR/ZnO composite films

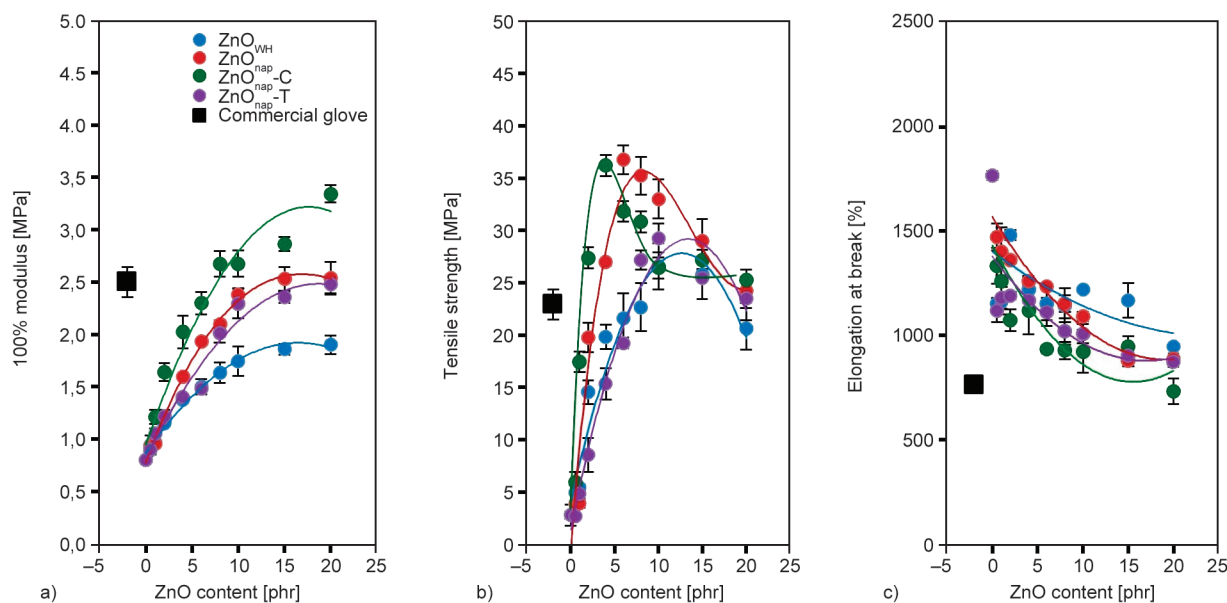
### 4.2.1. Mechanical properties

Figure 3 shows the stress–strain curves of the NBR composite films filled with different types and concentrations of ZnO, including the commercial ZnO ( $\text{ZnO}_{\text{WH}}$ ) and the unmodified and modified  $\text{ZnO}_{\text{nap}}$  species. In addition, the mechanical properties, in terms of the moduli, tensile strength, and elongation at break, of each film are comparatively presented in Figure 4; sharp increases in the curves, particularly after 300% strain, are related to strain-induced crystallization (SIC) behavior, which is known to occur in NR [21]. Although NBR has a lower molecular weight and a shorter molecular main chain than NR, the existing  $\text{C}\equiv\text{N}$  bonds in NBR lead to strong physical intermolecular forces among the NBR chains, especially during the stretching of the samples. Chemical crosslinking among NBR molecules relating to sulfur crosslinking processes also forms the rationale behind the restriction of the failure of NBR films during their stretching/extension in tensile testing. As expected, the degree of chemical crosslinking existing in the films strongly correlates to the activation reaction between the ZnO and the accelerator, which is the main chemical for propagating linkages between the main chains in the rubber. Thus, considering Figure 3, the stress–strain curves indicate two different SIC behaviors for ZnO loadings higher and lower than 2 phr. SIC is not

identified for 0, 0.5, and 1 phr of  $\text{ZnO}_{\text{WH}}$ ,  $\text{ZnO}_{\text{nap}}$ , and  $\text{ZnO}_{\text{nap-T}}$ , which might be due to the poor dispersion of the ZnO species in the NBR matrix, leading to a lower potential for activating crosslinking within the film. With a low crosslink density, external forces can easily break the NBR films due to the films' low resistance to breakages. On the other hand, in the case of  $\text{ZnO}_{\text{nap-C}}$ , a strong increase in the stress–strain curve is indicated after extension up to at least 300% strain; this is due to the better dispersion ability of  $\text{ZnO}_{\text{nap-C}}$ , exhibiting better formation within the filler than  $\text{ZnO}_{\text{nap-T}}$ . Considering the NBR composite films with ZnO concentrations above 2 phr, strong SIC behavior can be observed for all the ZnO types. This implies that all the films display good resistance to breakage during extension at different optimal loadings within the NBR matrix. The results of the tensile properties obtained from the stress–strain curves are shown in Figure 4. Regarding the 100% modulus and tensile strength, greater efficiency in chemical crosslink propagation induces a strong increase in the modulus of the composite films. The modification of  $\text{ZnO}_{\text{nap}}$  with  $\text{CaCO}_3$  effectively improves the dispersion and distribution of  $\text{ZnO}_{\text{nap-C}}$  throughout the NBR matrix (Figures 4a and 4b). The activation of crosslinking is enhanced with the increasing degree of ZnO dispersion, with the optimal modulus achieved at approximately 10 phr for all ZnO types. Thus, the increase in the modulus



**Figure 3.** Stress-strain curves of NBR composite films filled with commercial  $\text{ZnO}_{\text{WH}}$  together with unmodified and modified  $\text{ZnO}_{\text{nap}}$ .



**Figure 4.** Tensile properties in terms of 100% moduli (a), tensile strengths (b) and elongation at breaks (c) of NBR composites films filled with commercial ZnO<sub>WH</sub> together with unmodified and modified ZnO<sub>nap</sub>.

leads to the composite films’ resistance to failure. The optimal ZnO concentration for ZnO<sub>nap</sub> and ZnO<sub>nap</sub>-C occurs at 4 phr before decreasing sharply with loadings above 4 phr. The unmodified ZnO<sub>nap</sub> and ZnO<sub>nap</sub>-T show lower tensile strength at the same level as that of commercial NBR gloves, particularly in the range of 6–20 phr. However, the lowest elongation value of the NBR film filled with ZnO<sub>nap</sub>-C is still higher than that of commercial gloves; as expected, due to the film’s strong resistance to failure, a larger force was applied, and, therefore, the film withstood breakage during stretching (Figure 4c). It should be noted that the commercial glove might utilize a different formulation and chemical concentration compared to the proposed composites.

Considering the activation of chemical crosslinking via the addition of ZnO<sub>WH</sub>, ZnO<sub>nap</sub>, and modified ZnO<sub>nap</sub>, the chemical crosslink density ( $\nu$ ) was estimated based on the Flory–Rehner equation using the swelling method, as depicted in Figure 5. One can observe that  $\nu$  has a good correlation with the obtained tensile properties of the NBR films. The optimal value of  $\nu$  for ZnO<sub>WH</sub>, ZnO<sub>nap</sub>, and ZnO<sub>nap</sub>-T occurs at a loading of 4 phr, while the optimal concentration of ZnO<sub>nap</sub>-C for activating molecular chain crosslinking between the NBR molecules falls in the range from 4–10 phr. Considering the degree of crosslinking, one can note that the use of ZnO<sub>nap</sub>-C leads to a significantly higher  $\nu$  value than the other ZnO types. It supports the hypothesis of the activation of the

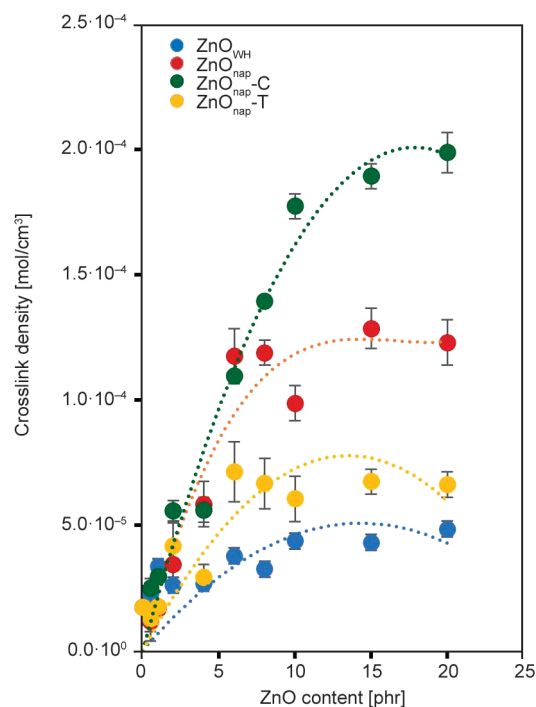


**Figure 5.** Crosslink density of NBR composites films filled with commercial ZnO<sub>WH</sub> together with unmodified and modified ZnO<sub>nap</sub>.

vulcanization reaction within the NBR matrix using CaCO<sub>3</sub>-coated ZnO<sub>nap</sub> at the ZnO<sub>nap</sub>:CaCO<sub>3</sub> wt% ratio of 90:10. One can conclude that the modification of ZnO<sub>nap</sub> to ZnO<sub>nap</sub>-C leads to excellent performance in activating NBR crosslinking, which explains the improvement in the mechanical properties of NBR relating to the proper dispersion and distribution of ZnO<sub>nap</sub>-C throughout the NBR matrix. For

more details, Figure 6 displays the proposed chemical crosslinks among NBR molecules through sulfur curing using ZnO as the activator and filler. Step A, formations of ZnO and sulfur atoms together with the accelerated complex origination based on the reaction of ZnO and accelerator are initiated as seen in (A1) and (A2) of Figure 6, respectively [22]. At this step, reaction formation was activated by heating during chemical crosslinking propagation, so-called vulcanization processes, and therefore reaction efficiency depends on surface areas and degrees of dispersion of ZnO particles which can react to sulfur and also accelerator relating Zn ions releasing mechanism. In Step B, the chemical reaction to the NBR

chains had innovated, and the rubber-bound pendant groups were formed correlating the inserting  $-S_x-O^*$  into the main rubber chains at the allylic carbon position in butadiene unit (B1) [22]. In parallel, the zinc-nitrile complex formation is fabricated among Zn ions and Zn compounds to the  $-CN$  functional groups in the acrylonitrile unit (B2) of Figure 6 [23]. Zn ions play an important role in this step, and therefore, it was the reason for the high mechanical properties in NBR/ZnO<sub>nap</sub>-C films since the ZnO<sub>nap</sub>-C had strongly released Zn ions regarding finding in ICP-OES. Since the zinc-nitrile complex is concerned, the active sulphurating agent formed during the vulcanization reaction might be further involved

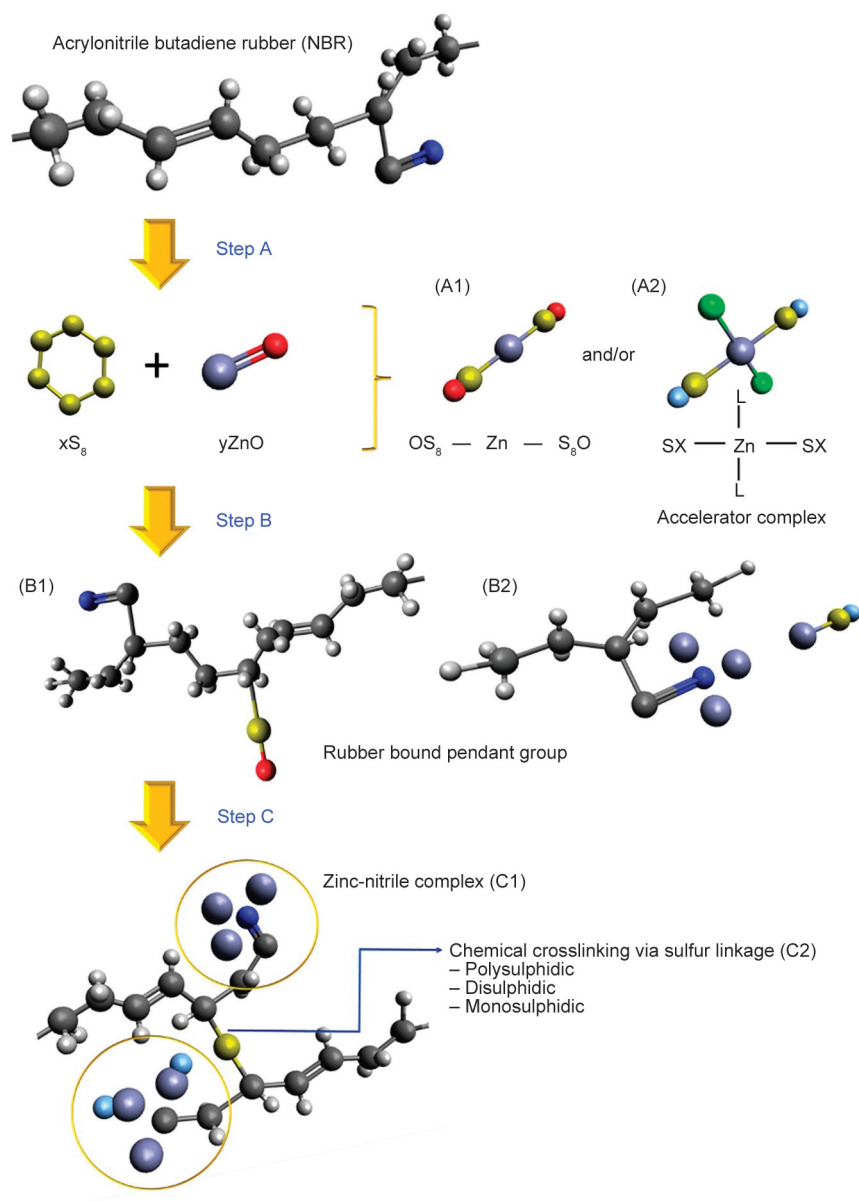


**Figure 6.** Proposed mechanism of chemical crosslinking and Zn ions interaction inside the NBR films filled with ZnO and sulfur. Here, the black, gray, blue, purple, yellow, red, green and light blue atoms refer to carbon, hydrogen, nitrogen, zinc, sulfur, oxygen, ligand and X atoms, respectively.

in the reaction with the nitrile group of NBR to form a zinc-nitrile complex. As a ligand, this donates the electron pair to the zinc present in the complex structure and accelerates the entire process [23]. Therefore, in Step C, the (B2) is still existed as the (C2), while the (B1) can propagate into (C1), relating the formation of sulfur bonding among the NBR molecules by means of poly-, di- and mono-sulphidic crosslinks [22, 23].

#### 4.2.2. Mooney-Rivlin model

The reinforcement efficiency of each ZnO type regarding the NBR composite film matrix can be explained by the arrangement of the NBR molecular chains during extension by fitting the Mooney–Rivlin model to the stress–strain data in Figure 3 using Equation (3) [24]:

$$\sigma^*(\lambda) = \frac{\sigma(\lambda)}{\lambda - \lambda^{-2}} = 2(C_1 + C_2\lambda^{-1}) \quad (3)$$

where  $\sigma^*(\lambda)$  is the reduced engineering stress;  $\sigma(\lambda)$  is the engineering stress; and  $C_1$  and  $C_2$  are the characteristic constants of network chains, determined from the intercept and the slope of the curves, respectively. The extension ratio,  $\lambda$ , is given by  $\lambda = 1 + \varepsilon$ , where  $\varepsilon$  is the engineering strain. Based on the relationship of the calculated reduced stress,  $\sigma^*(\lambda)$ , as a function of the inverse of the extension ratio

( $1/\lambda$ ), the chemical interactions of the films – the chemical crosslinking among the NBR molecular chains [25, 26] – are represented in Figure 7a, as compared to the physical interactions in Figure 7b. The obtained  $C_1$  values are related to the y-intercept of the linear fit to the plot of  $\sigma^*(\lambda)$  versus  $1/\lambda$ , and  $C_2$ , determined from the slope of the fit, is related to the physical interactions (molecular chain entanglement and physical absorption). From the incorporation of the investigated ZnO types, the  $C_2$  values were higher than those of  $C_1$ . This clarifies that most of the NBR molecules have good interactions with the filler surface through physical chain entanglement based on their intermolecular chain attraction. The  $C_2$  value increases upon the addition of 4 phr of ZnO<sub>nap</sub>-C, which correlates well with the increased 100% modulus and tensile strength of the film. This implies that the proper addition of ZnO<sub>nap</sub>-C leads to better dispersion within the film and enhances the degree of reinforcement provided by the filler to the rubber matrix. In addition, considering the  $C_1$ , it is clearly seen that the NBR/ZnO<sub>nap</sub>-C showed the highest chemical interaction inside the films relative to others. It affirms the role of Zn ions releasing from the ZnO particles relating to the chemical crosslinking mechanism proposed in Figure 6. This strong crosslinking among the NBR molecules results in the formation of smooth surfaces on the NBR film, as

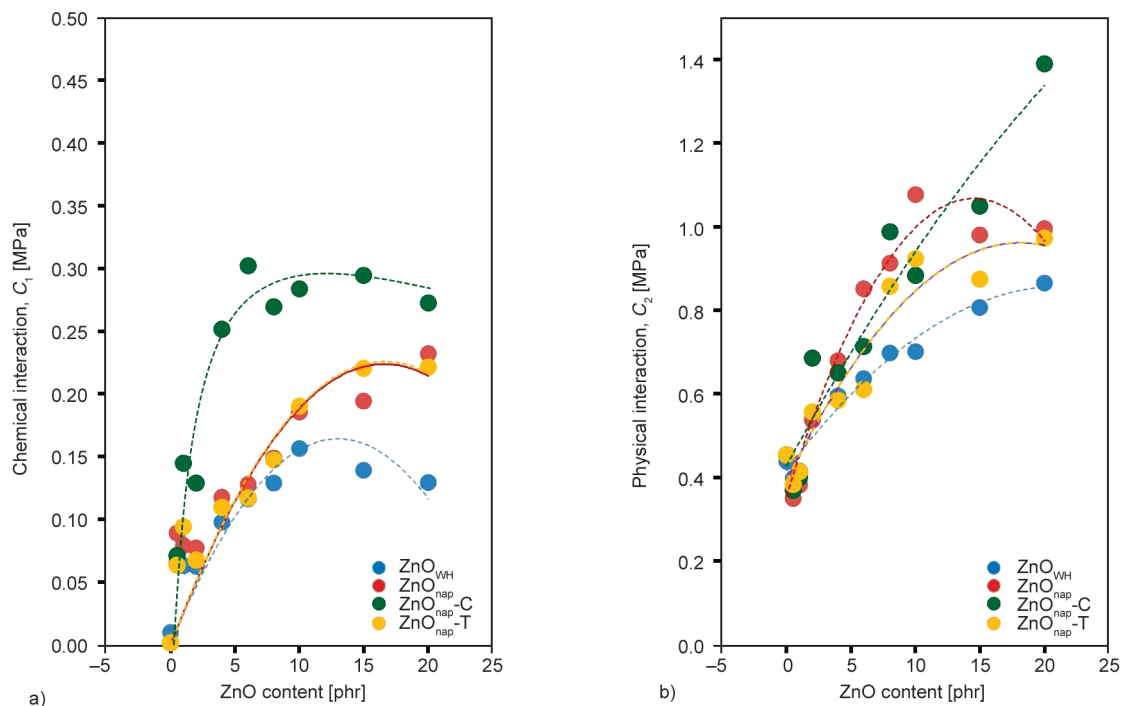
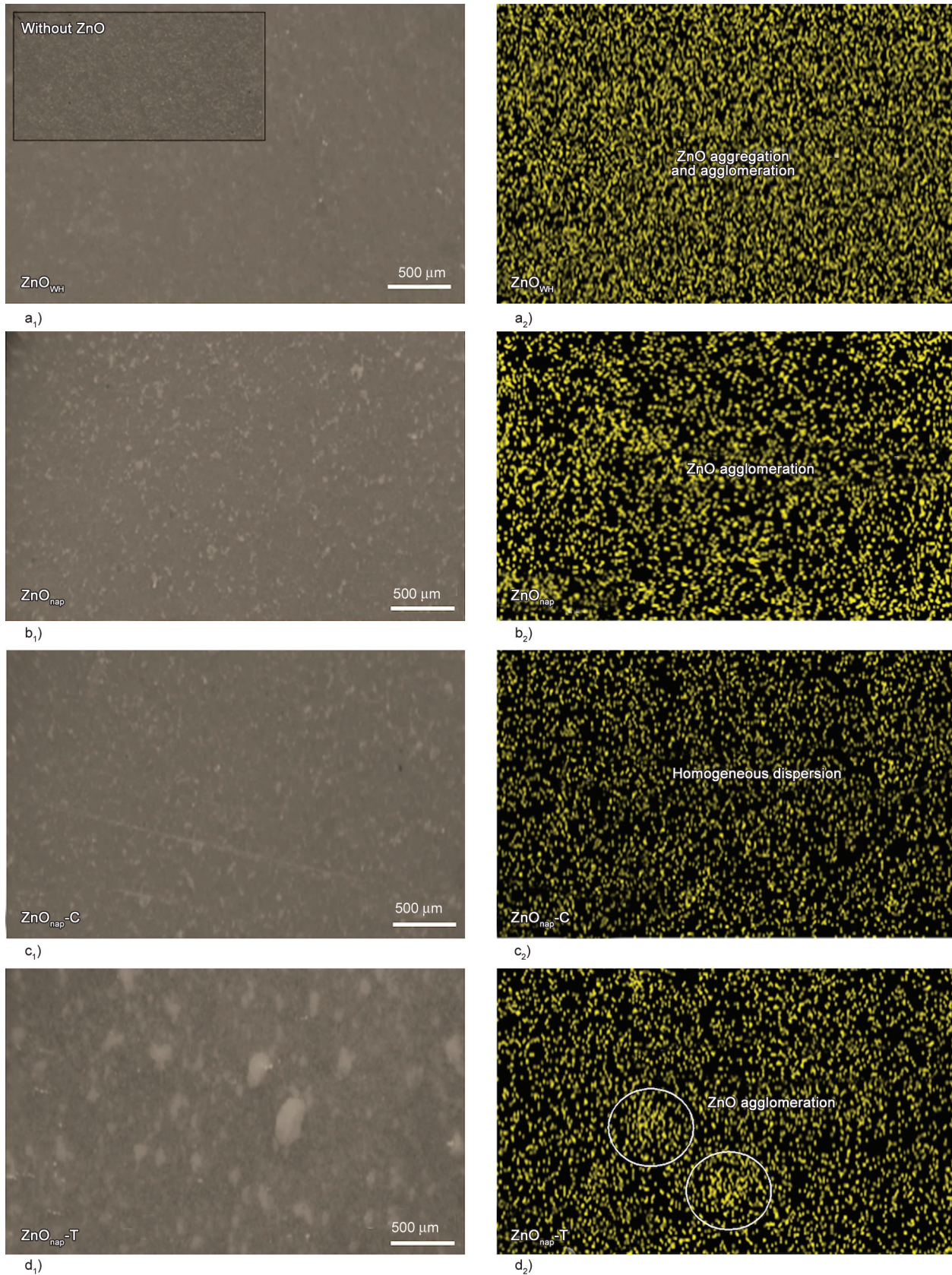


Figure 7. Chemical interaction (a) and physical interaction (b) of the NBR composites films filled with commercial ZnO<sub>WH</sub> together with unmodified and modified ZnO<sub>nap</sub>, calculated through the Mooney-Rivlin equation.

illustrated in the OM images presented in Figure 8. The smoothest surface is observed in the NBR com-

posite films filled with ZnO<sub>nap</sub>-C, while the other composites exhibit significant filler agglomeration



**Figure 8.** Morphologies observed of the OM of the NBR composite films filled with commercial ZnO<sub>WH</sub> together with unmodified and modified ZnO<sub>nap</sub>. a<sub>1</sub>), a<sub>2</sub>) ZnO<sub>WH</sub>, b<sub>1</sub>), b<sub>2</sub>) ZnO<sub>nap</sub>, c<sub>1</sub>), c<sub>2</sub>) ZnO<sub>nap</sub>-C, d<sub>1</sub>), d<sub>2</sub>) ZnO<sub>nap</sub>-T.

and rougher surfaces. The SEM-EDX images demonstrate the agglomeration of ZnO, ZnO<sub>nap</sub>, and modified ZnO<sub>nap</sub>, highlighting the effective dispersion and distribution of ZnO<sub>nap</sub>-C within the NBR matrix, as depicted in Figure 8.

#### 4.2.3. Dynamic mechanical analysis

Not only the mechanical but also the dynamic mechanical properties of the NBR films need to be determined with regard to the elasticity at different temperatures. Figure 9 plots the storage modulus ( $\epsilon'$ ) and loss tangent ( $\tan \delta$ ) as a function of temperature, which ranges from  $-80$  to  $100$  °C. In addition, Table 3 summarizes the glass transition temperature ( $T_g$ ) and  $\tan \delta$  in terms of the maximum value ( $\tan \delta_{\max}$ ) and the values at  $0$  °C ( $\tan \delta_0$ ) and  $60$  °C ( $\tan \delta_{60}$ ). The highest value of  $\epsilon'$  was obtained for the pure NBR, which shows a slightly higher  $\epsilon'$  than the NBR films filled with ZnO<sub>nap</sub>-C and ZnO<sub>nap</sub>. This might be due to the strong chain entanglement of the polar NBR chains, which effectively retards the physical chain deformation at low strain levels. This reasonably leads to obtaining the lowest  $T_g$  and highest  $\tan \delta_{\max}$  for the unfilled NBR film, with both values referring to the elasticity of the film. The NBR/ZnO<sub>nap</sub>-C composite shows the lowest  $T_g$  and highest  $\tan \delta_{\max}$  values from among the filled NBR composites since it contains the highest crosslink density. The temperature that needs to be applied for the film to transition from a glassy to a rubbery state is, therefore, very low, and  $\epsilon'$  changes significantly, leading to a high

$\tan \delta_{\max}$ . On the other hand, the NBR films filled with ZnO<sub>nap</sub> and ZnO<sub>nap</sub>-T show increased  $T_g$  and decreased  $\tan \delta_{\max}$  values relative to those of the NBR/ZnO<sub>nap</sub>-C composite, with the NBR/ZnO<sub>WH</sub> film yielding a considerably higher  $T_g$  value, significantly above  $0$  °C, and the lowest  $\tan \delta_{\max}$ . This implies that the addition of modified ZnO<sub>nap</sub>, in particular, ZnO<sub>nap</sub>-C, improves the elasticity of the NBR film to a greater extent than the other ZnO types by imparting a superior crosslink density and enhanced mechanical properties to the film.

The performance of the NBR films over the investigated temperature range can be interpreted through the  $\tan \delta$  values at  $0$  and  $60$  °C. One can note that a lower  $\tan \delta_{60}$  value is needed, relating to the requirement of high elasticity when handling the films in high-temperature conditions. In contrast, a higher  $\tan \delta_0$  is required due to the hardening of the films in low-temperature conditions. Table 3 shows that NBR/ZnO<sub>nap</sub>-C yields the lowest  $\tan \delta_{60}$ , which is related to the chemical crosslink density and elasticity

**Table 3.** Glass transition temperature ( $T_g$ ) and Tan delta ( $\tan \delta$ ) of NBR composite films filled with different types ZnO at 4 phr.

ZnO types	$T_g$ [°C]	$\tan \delta_{\max}$	$\tan \delta$ at 0 °C	$\tan \delta$ at 60 °C
NBR	-8.50	0.726	0.582	0.188
NBR/ZnO <sub>WH</sub>	3.33	0.300	0.297	0.215
NBR/ ZnO <sub>nap</sub>	-4.33	0.357	0.335	0.087
NBR/ ZnO <sub>nap</sub> -C	-5.83	0.497	0.448	0.078
NBR/ ZnO <sub>nap</sub> -T	-2.67	0.302	0.298	0.152

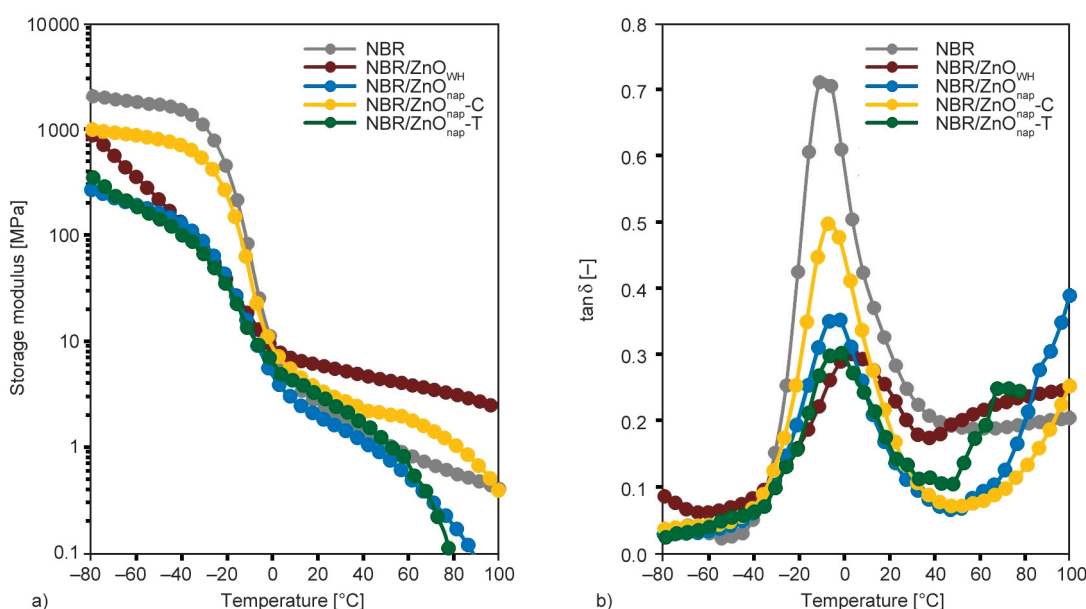


**Figure 9.** Storage modulus (a) and  $\tan \delta$  (b) of NBR composites films filled with commercial ZnO<sub>WH</sub> together with unmodified and modified ZnO<sub>nap</sub> at 4 phr.

of the films. On the other hand, the NBR/ZnO<sub>WH</sub> composite yields the highest  $\tan \delta_{60}$  value due to its significantly high  $T_g$  and low ZnO<sub>WH</sub> surface area for reacting with the film during crosslink propagation. In addition, it was observed that the NBR/ZnO<sub>WH</sub> composite exhibited the highest value of  $\epsilon'$  at temperatures above approximately 30 °C. This indicates that the elasticity effectively decreased beyond room temperature under dynamically low strain. This phenomenon could be attributed to the embedding of rubber molecules within aggregate and agglomerate structures, known as occluded rubber. The presence of numerous particulate aggregations in Figure 8 suggests the existence of extensive areas of occluded rubber in the NBR/ZnO<sub>WH</sub> composite, which helps counteract crosslinked rubber deformation during low-strain application [27, 28]. Regarding  $\tan \delta_0$ , although the pure NBR shows the highest value, its combination with ZnO<sub>nap-C</sub> yields the highest value relative to the other film composites. Therefore, considering the tensile properties and elasticity of the films, the incorporation of ZnO<sub>nap-C</sub> significantly improved the film properties due to the filler's large surface area and good dispersion within the NBR matrix.

#### 4.2.4. Antibacterial properties of NBR composite films

The incorporation of modified ZnO into NBR composite films significantly impacted the films' mechanical and dynamic mechanical properties based on particle size, dispersion considerations and ability for generating chemical crosslinking inside the films. In addition, given that ZnO displays excellent antibacterial performance, the composite films filled with modified ZnO (ZnO<sub>nap-C</sub>) were evaluated in comparison with those containing commercial ZnO (ZnO<sub>WH</sub>) for their antibacterial activity through qualitative and quantitative measurements. The qualitative determination was carried out using the Zone of Inhibition test, and the bactericidal efficiency on the film surface was assessed according to the ISO 22196:2011 and ASTM D7907-14 methods. This antibacterial ability can be originated following the photocatalytic processes onto ZnO particles. The *S. aureus* (ATCC 6538P) and *E. coli* (ATCC 8739) strains, which have been recognized as hospital-associated infections, were studied as representatives of Gram-positive and Gram-negative bacteria, respectively [29]; Figure 10 displays the results of the

Zone of Inhibition tests conducted on the NBR composite films, and the observed diameters of the zones of inhibition (clear zones) are given in Table 4. The clear zones, where there is no growth of bacteria, are notably visible in testing the composite films against *S. aureus*. The composite film filled with ZnO<sub>nap-C</sub> displays a larger inhibition zone than the one with ZnO<sub>WH</sub>, as shown in Table 4. One can observe the formation of the clear zones after the addition of 2 phr ZnO<sub>WH</sub> and ZnO<sub>nap-C</sub>, as shown in Figure 10. In addition, one should note that ZnO loadings over 10 phr are impractical due to the flocculation of the ZnO particles during the process. On the other hand, clear zones in testing the composite films against *E. coli* are not observed, implying that the composite films might have a greater bacterial killing ability against *S. aureus* than *E. coli*.

The ISO 22196:2011 method was used to prove the presence of antibacterial activity on the film surface in direct contact with the bacteria. The colony-forming units were counted to evaluate the antibacterial activity of the NBR composites after 24 h of incubation and assess the bacterial reduction efficacy, as shown in Figure 11. The results indicate that the composite films are effective against both bacterial types, with a bacterial reduction efficacy of 99.9% at a loading of at least 1 phr for ZnO<sub>nap-C</sub> and above 2 phr for ZnO<sub>WH</sub>. Thus, these results demonstrate the antibacterial ability of composite films incorporating nano-sized ZnO particles with small sizes and high specific surface areas, which are more effective in inhibiting bacterial growth than equivalent amounts of conventional ZnO. ZnO is recognized as a semiconductor material that has sufficient band gap energy to absorb photons for producing radical active species. The presence of ZnO in NBR composite films produces ROS, such as hydroxyl ( $\cdot\text{OH}$ ), superoxide ( $\cdot\text{O}_2^-$ ), and peroxy ( $\text{HOO}\cdot$ ) radicals and hydrogen peroxide ( $\text{H}_2\text{O}_2$ ), which are released onto the ZnO surface via a photocatalytic process and play an important role in antibacterial mechanisms [30], as can be seen in the proposed model of Figure 12. In Figure 12a, upon exposure to light, electrons are excited from the valence to the conduction band, producing electron-hole pairs ( $e_{cb}^-$ ,  $h_{vb}^+$ ). The  $h_{vb}^+$  is formed in the valence band and oxidizes water or moisture to form  $\cdot\text{OH}$ , while the  $e_{cb}^-$  in the conduction band reduces oxygen to produce  $\cdot\text{O}_2^-$ , which reacts further with  $\text{H}^+$  to form  $\text{HOO}\cdot$  and  $\text{H}_2\text{O}_2$  and is finally reduced to  $\cdot\text{OH}$ . Among the ROS,  $\cdot\text{OH}$  and

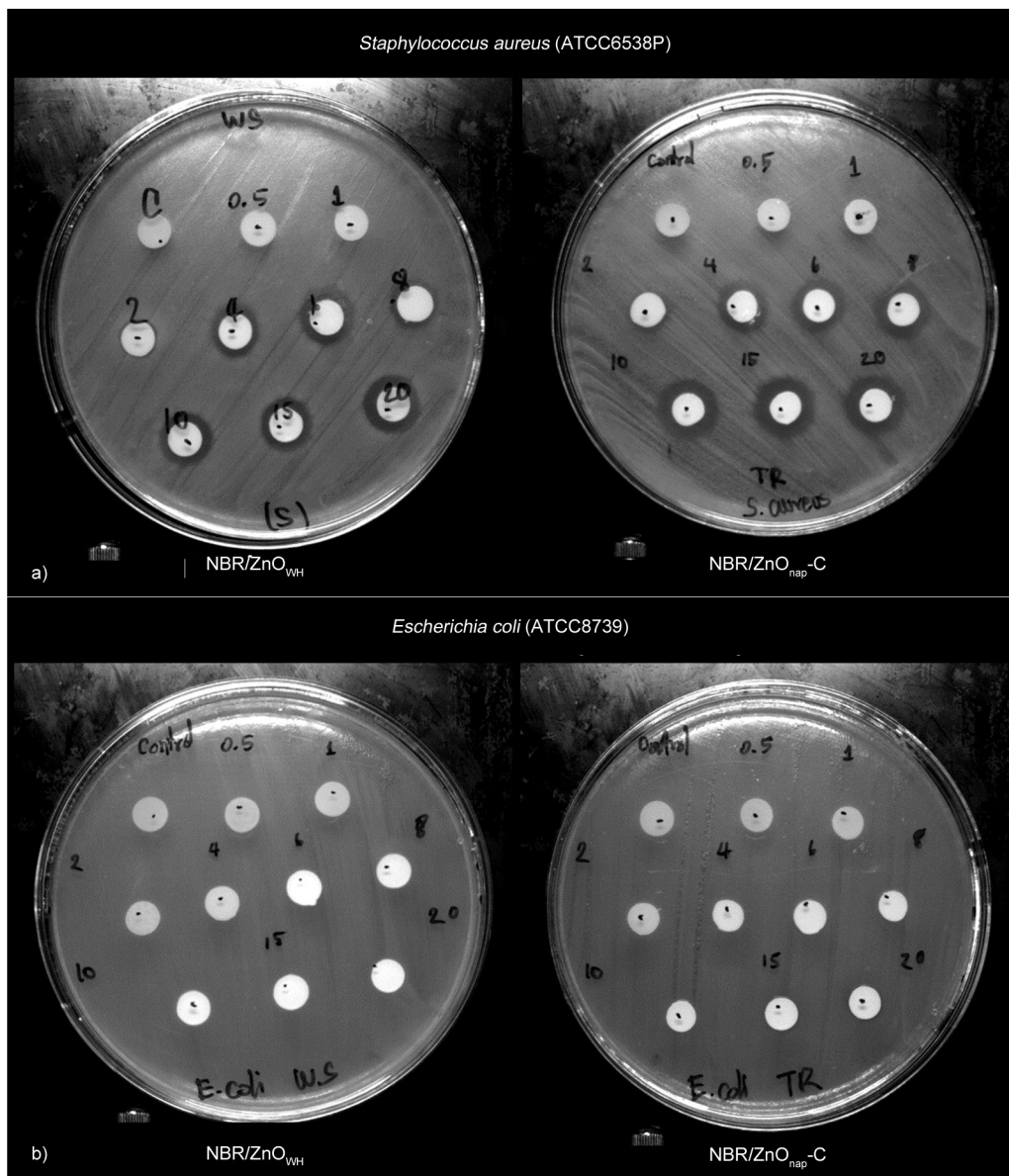


**Figure 10.** Agar disc diffusion of antibacterial against gram-positive *Staphylococcus aureus* (a) and gram-negative *Escherichia coli* (b) of NBR/ZnO<sub>WH</sub> and NBR/ZnO<sub>nap-C</sub> with varying ZnO loading at 0–20 phr.

**Table 4.** Diameter of inhibition clear zone of the NBR composite films filled with ZnO<sub>WH</sub> and ZnO<sub>nap-C</sub>.

ZnO loading [phr]	Inhibition clear zone [mm]			
	<i>Staphylococcus aureus</i>		<i>Escherichia coli</i>	
	NBR/ZnO <sub>WH</sub>	NBR/ZnO <sub>nap-C</sub>	NBR/ZnO <sub>WH</sub>	NBR/ZnO <sub>nap-C</sub>
0.0	0.00	0.00	0.00	0.00
0.5	0.00	0.00	0.00	0.00
1.0	0.00	0.00	0.00	0.00
2.0	1.08±0.57	0.70±0.71	0.00	0.00
4.0	3.64±0.48	3.15±0.72	0.00	0.00
6.0	4.10±0.76	3.75±0.62	0.00	0.00
8.0	3.12±0.55	4.43±0.47	0.00	0.00
10.0	4.56±0.44	5.76±0.36	0.00	0.00
15.0	4.48±0.41	5.59±0.80	0.00	0.00
20.0	5.25±0.87	5.77±0.56	0.00	0.00

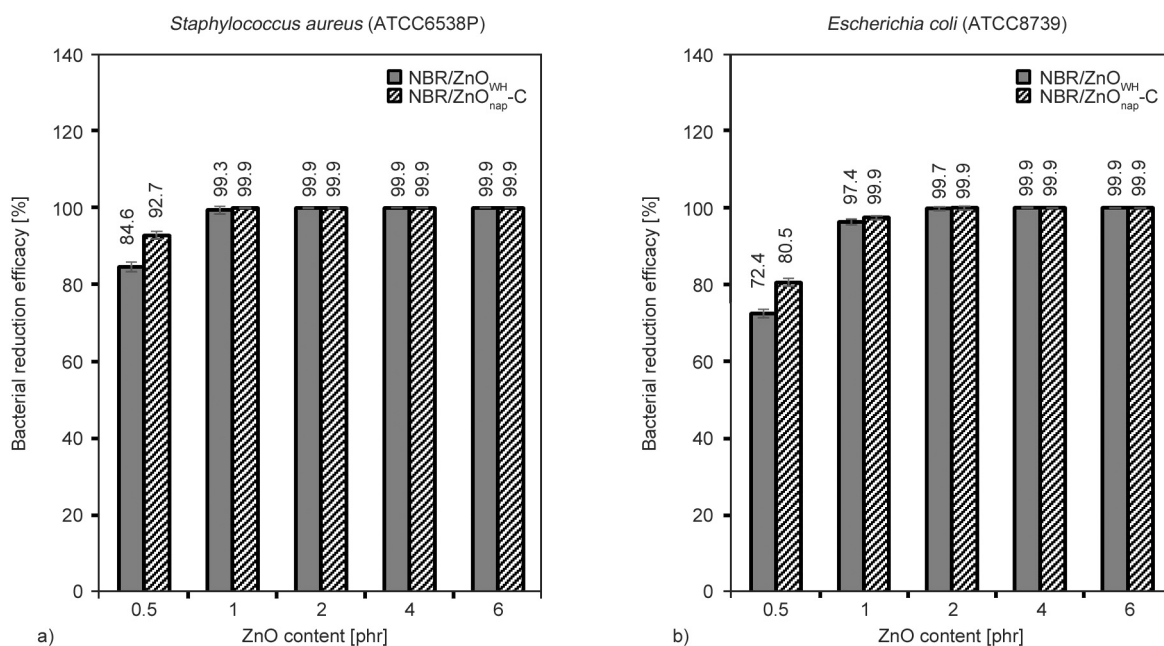


**Figure 11.** Bacterial reduction efficacy against Gram-positive *Staphylococcus aureus* (a) and Gram-negative *Escherichia coli* (b) of NBR films filled ZnO<sub>WH</sub> and ZnO<sub>nap-C</sub> with varying ZnO loading at 0.5–6.0 phr.

H<sub>2</sub>O<sub>2</sub> are recognized as highly reactive species that play a crucial role in antibacterial activity by penetrating the outer membrane of cells, oxidizing the membrane lipids, enzymes, and proteins and causing deoxyribonucleic acid (DNA) damage [31–33]. Finally, intracellular components become damaged, leading to cell death. The release of Zn<sup>2+</sup> ions through the rubber layer is another factor that plays a role in bacterial inactivation. The solubilized Zn<sup>2+</sup> ions reach the outer cell wall and penetrate the cell membrane, reacting with the DNA within the bacterial cells by impeding transportation along with amino acid processing and by disrupting the enzyme system, which leads to bacterial cell death [33] (Figure 12c). In addition, the formation of ROS and the release of Zn<sup>2+</sup> ions are influenced by the ZnO particle size. ZnO nanoparticles with smaller particle sizes and higher specific surface areas are more efficient in producing ROS and Zn<sup>2+</sup> ions [30], which is related to Figure 2 and Table 2. The incorporation of ZnO<sub>nap-C</sub> nanoparticles at 0.5 phr leads to a greater reduction in both bacterial types than the ZnO<sub>WH</sub> microparticles. However, the release of both Zn<sup>2+</sup> and ROS is also related to the ion's movement across the bound rubber to the film surfaces for attacking bacteria. In Figure 12b, it is seen that the ion attraction of zinc-nitrile complexes is the key potential factor for the movement of the existing ions. It is hypothesized that, after the photocatalytic processes, Zn<sup>2+</sup> had connected closely to the ROS<sup>-</sup> which easily moved into NBR through ion-ion

intermolecular forces at the CN in the nitrile unit. This carried both ions to the films' surfaces and met with bacteria and microorganisms relatively.

The bactericidal efficacy on the surface of the NBR composite films against *S. aureus* and *E. coli*, with varying contact kill times of 0, 5, 10, 20, and 30 min, was determined according to the ASTM D7907-14 method, as shown in Figure 13. Bacterial reduction occurs after a contact time of 0 min, as measured by the number of colonies on the composite surface after dropping a bacterial suspension onto the material, covering it with a sterilized polyethylene film for 15 s, and subsequently removing it with a neutralizer solution. This indicates that an antibacterial reaction of ZnO is immediately triggered to kill microorganisms on the composite surface. The results after a contact time of 30 min reveal that the incorporation of ZnO<sub>nap-C</sub> at 4 phr in the composite films leads to 92.00 and 51.85% bacterial reduction efficacy against *S. aureus* and *E. coli*, respectively. Furthermore, ZnO shows greater antibacterial activity against *S. aureus* than the *E. coli*, bacterium, as shown in Figure 13, respectively, due to differences in the structure, chemical composition, and polarity of the bacterial cell membranes. The Gram-negative *E. coli* has a larger negative charge than the Gram-positive *S. aureus* because of its additional lipopolysaccharide layer with a negative potential [34], as depicted in Figure 14; this leads to a lower concentration of negatively charged free radicals, such as superoxide

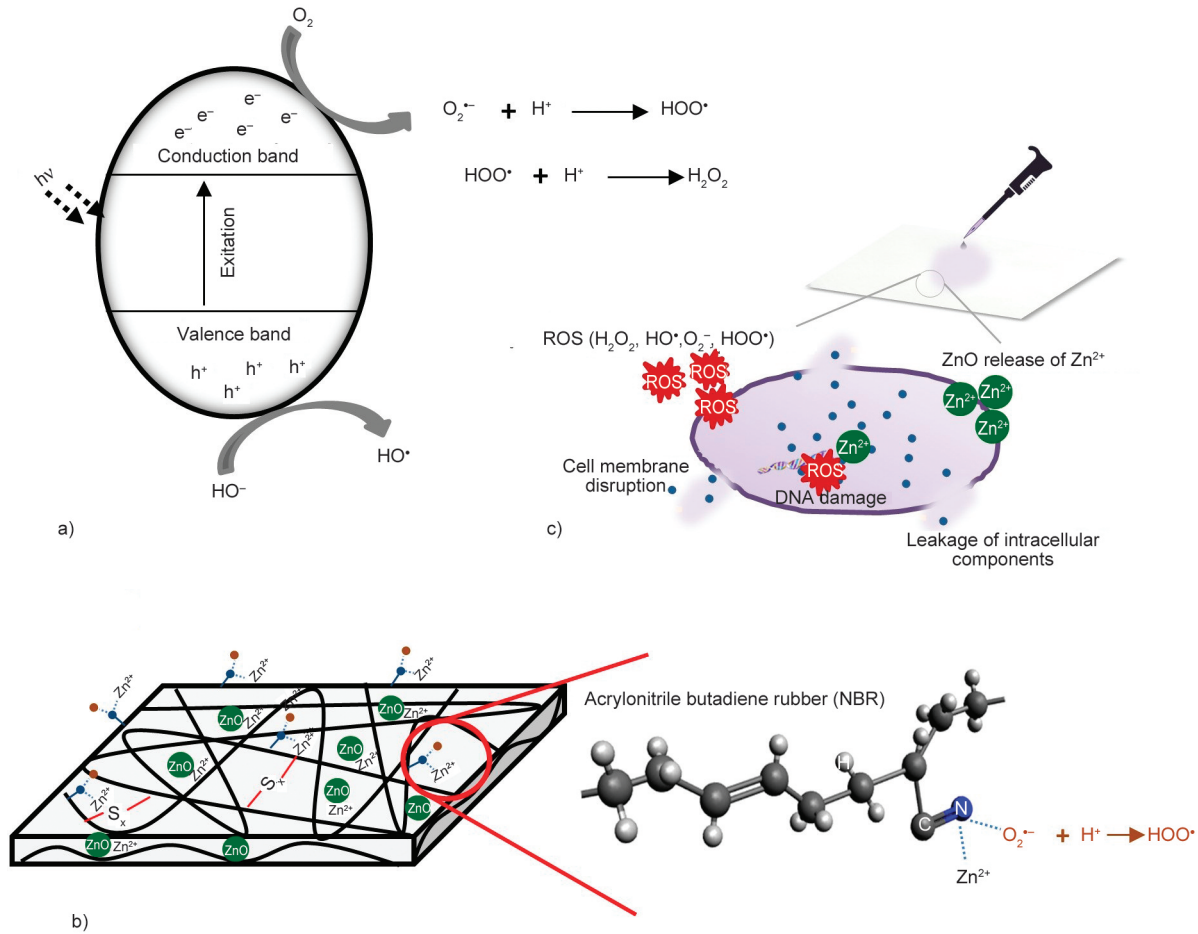


Figure 12. Proposed model of photocatalytic of ZnO particles (a), releasing mechanism for  $Zn^{2+}$  and  $ROS^-$  to the NBR film surface (b) and bacteria disruption from  $Zn^{2+}$  and  $ROS^-$  (c).

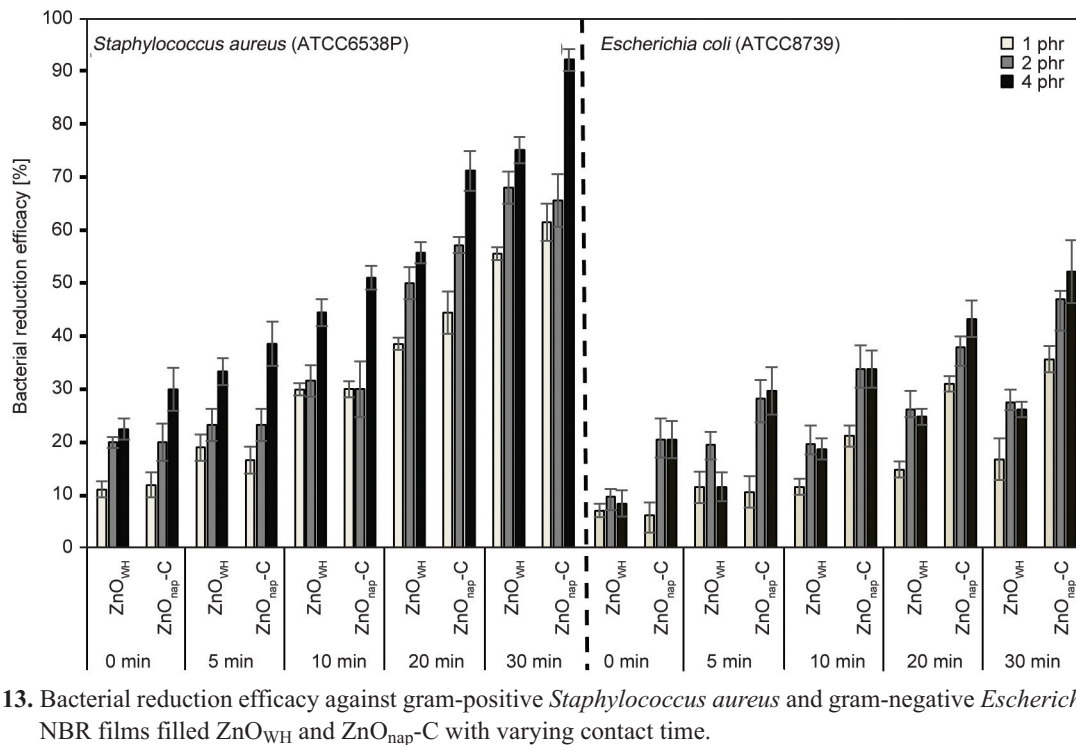


Figure 13. Bacterial reduction efficacy against gram-positive *Staphylococcus aureus* and gram-negative *Escherichia coli* of NBR films filled ZnO<sub>WH</sub> and ZnO<sub>nap-C</sub> with varying contact time.

anions, and peroxide ions penetrating the *E. coli* bacterial cell wall. In addition, *E. coli* has two cell membranes, including inner and outer ones, as shown in Figure 14, while *S. aureus* has one. The outer membrane of Gram-negative bacteria is covered with lipopolysaccharides, which act as a permeability barrier and protect the cells from potentially harmful agents [35]. In comparing the ZnO types, ZnO<sub>nap</sub>-C exhibits a higher percentage of bacterial reduction than ZnO<sub>WH</sub> due to its larger surface area, which leads to a large production of ROS and Zn<sup>2+</sup> ions to damage bacterial cells. In addition, when evaluating the bacterial reduction efficiencies at different concentrations and contact times between rubber and bacteria using ZnO<sub>nap</sub>, a 99.9% reduction was achieved at a ZnO<sub>nap</sub> concentration of 2 phr for both *S. aureus* and *E. coli*. In addition, at a ZnO<sub>nap</sub> concentration of 4 phr, a reduction of 75.5±3.5% for *S. aureus* and 51.0±7.5% for *E. coli* was observed, surpassing the efficiencies of ZnO<sub>WH</sub> and showing slight variation compared to ZnO<sub>nap</sub>-C. This finding aligns with the recent study by Krainoi *et al.* [18], where ZnO<sub>nap</sub> exhibited lower antibacterial efficiency than modified ZnO<sub>nap</sub> due to differences in dispersion and distribution within the rubber matrix. However, while ZnO<sub>nap</sub> demonstrated high bacteria-killing performance, its purity was found to be

equivalent to that of ZnO<sub>WH</sub> at 99.9%, whereas ZnO<sub>nap</sub>-C exhibited a purity of only 90%. This result indicates that nanoparticles present the advantage of possibly reducing the amount of modified ZnO, especially ZnO<sub>nap</sub>-C, in NBR composites while still significantly improving their mechanical and dynamic mechanical properties and antibacterial activity. Therefore, using modified ZnO nanoparticles in NBR composite films presents a good alternative to applying medical disinfection products to prevent the spread of pathogens.

### 5. Conclusions

NBR composite films incorporating different ZnO types, including white seal ZnO (ZnO<sub>WH</sub>), ZnO nanoparticles (ZnO<sub>nap</sub>), CaCO<sub>3</sub>-coated ZnO<sub>nap</sub> (ZnO<sub>nap</sub>-C), and TiO<sub>2</sub>-coated ZnO<sub>nap</sub> (ZnO<sub>nap</sub>-T), were investigated via a latex processing technique. Based on the characteristic structures of the ZnO types, the variations in particle size, band gap energy, and Zn<sup>2+</sup> ion solubility affect the properties of the composite films. The mechanical and dynamic mechanical properties, crosslink density, and antibacterial activity of the composite films were considered; the results indicated that the ZnO particle size and distribution play an important role in improving the crosslink density and mechanical characteristics. The composite

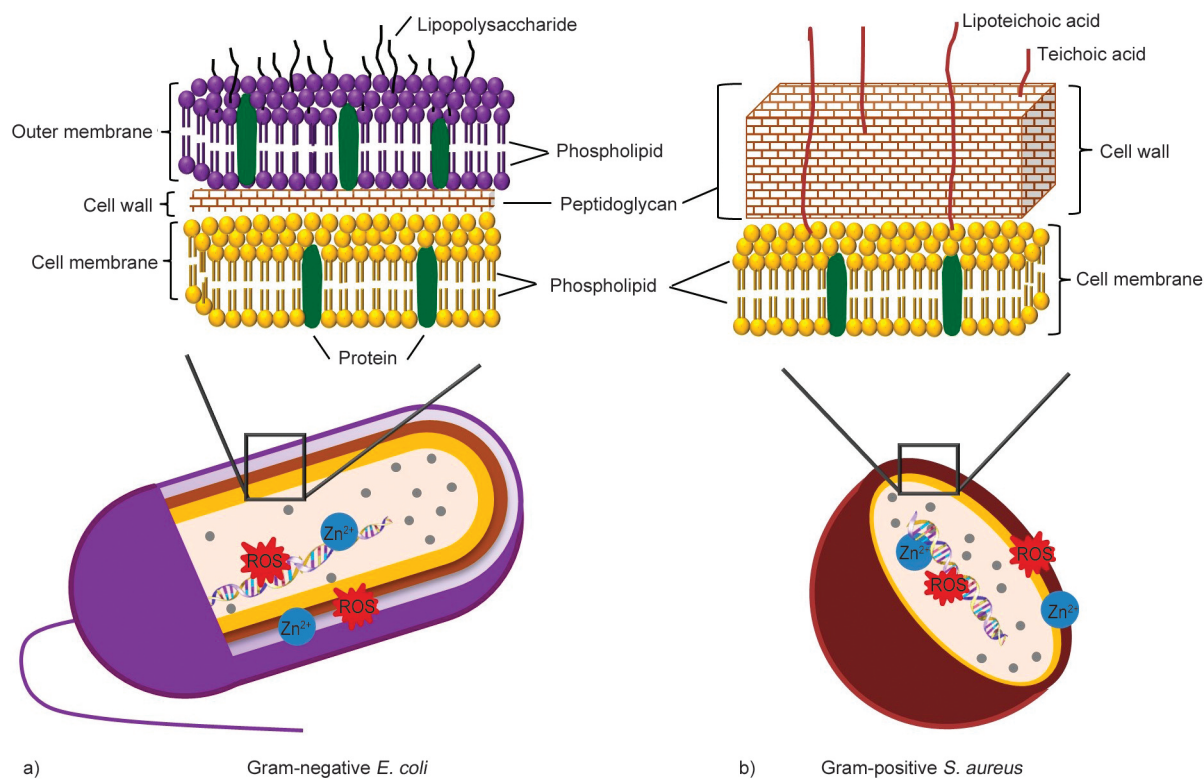


Figure 14. Proposed model of antibacterial mechanisms of ZnO to Gram-negative *E. coli* (a) and Gram-positive *S. aureus* (b).

filled with ZnO<sub>nap</sub>-C activated chemical crosslinking, which was in good agreement with the increased tensile modulus, Mooney–Rivlin plot, and dynamic mechanical results for this composite. In contrast, the incorporation of ZnO<sub>nap</sub> and ZnO<sub>nap</sub>-T gave rise to less enhanced properties in the composites due to the presence of significant ZnO agglomeration. In addition, the low specific surface area of the ZnO<sub>WH</sub> microparticles in their reaction with the NBR molecules during crosslinking led to the least favorable composite properties. The antibacterial activity of the composite films was evaluated through qualitative and quantitative determinations using *S. aureus* and *E. coli* as representatives of hospital-associated infections. The results indicated that both the NBR composite films with ZnO<sub>WH</sub> and ZnO<sub>nap</sub>-C exhibit an inhibition zone against *S. aureus*, while no such observation was made for *E. coli*. However, antibacterial activity on the composite film surface in direct contact with the bacterial cells, tested according to ISO 22196:2011, was observed against both bacterial types, with 99.9% bacterial reduction efficacy at loadings of 1 phr for ZnO<sub>nap</sub>-C and over 2 phr for ZnO<sub>WH</sub>. Bacterial cell structure disruption was achieved through the formation of ROS radicals and the release of Zn<sup>2+</sup> ions, which can be related to the obtained band gap energy and partial solubility of ZnO to release Zn<sup>2+</sup>. In addition, in accordance with ASTM D7907-14, the bactericidal efficacy on the composite film surfaces at various contact kill times between 0 and 30 min was determined. The addition of ZnO<sub>nap</sub>-C at 4 phr yielded 92.00 and 51.85% bacterial reduction efficacy within 30 min against *S. aureus* and *E. coli*, respectively. The results suggest that the use of nanoparticles could reduce the amount of modified ZnO, particularly ZnO<sub>nap</sub>-C, in NBR composites, which is in good agreement with the measured mechanical, dynamic mechanical, and antibacterial properties of the composites. To prevent the spread of pathogens, the use of modified ZnO nanoparticles in NBR composite films in, for example, gloves and multipurpose rubber films presents a suitable alternative to using medical disinfection products.

### Acknowledgements

The authors gratefully acknowledge the Thailand Science Research and Innovation (TSRI) Basic Research Fund: The fiscal year 2023 under project number FRB660073/0164 was acknowledged.

### References

- [1] Critchley E., Pemberton M. N.: Latex and synthetic rubber glove usage in UK general dental practice: Changing trends. *Heliyon*, **6**, e03889 (2020). <https://doi.org/10.1016/j.heliyon.2020.e03889>
- [2] Bodilsen J., Brouwer M. C., Kjærgaard N., Sirks M. J., van der Ende A., Nielsen H., van de Beek D.: Community-acquired meningitis in adults caused by *Escherichia coli* in Denmark and The Netherlands. *Journal of Infection*, **77**, 25–29 (2018). <https://doi.org/10.1016/j.jinf.2018.05.009>
- [3] Tian L., Sun Z., Zhang Z.: Antimicrobial resistance of pathogens causing nosocomial bloodstream infection in Hubei province, China, from 2014 to 2016: A multicenter retrospective study. *BMC Public Health*, **18**, 1121 (2018). <https://doi.org/10.1186/s12889-018-6013-5>
- [4] Čustović A., Smajlović J., Hadžić S., Ahmetagić S., Tihic N., Hadzagić H.: Epidemiological surveillance of bacterial nosocomial infections in the surgical intensive care unit. *Materia Socio-Medica*, **26**, 7–11 (2014). <https://doi.org/10.5455/msm.2014.26.7-11>
- [5] Sarih N. M., Gwee K., Maher S., Rashid A. A.: Natural rubber (NR) latex films with antimicrobial properties for stethoscope diaphragm covers. *Materials*, **15**, 3433 (2022). <https://doi.org/10.3390/ma15103433>
- [6] Koedrith P., Thasiphu T., Jong W-I., Boonprasert R., Tuitemwong K., Tuitemwong P.: Recent trends in rapid environmental monitoring of pathogens and toxicants: Potential of nanoparticle-based biosensor and applications. *Nanomaterials and Nanodevices*, **2015**, 510982 (2015). <https://doi.org/10.1155/2015/510982>
- [7] Ishida T.: Antibacterial mechanism of Ag<sup>+</sup> ions for bacteriolyses of bacterial cell walls *via* peptidoglycan autolysins, and DNA damages. *MOJ Toxicology*, **4**, 345–350 (2018). <https://doi.org/10.15406/mojt.2018.04.00125>
- [8] Salah I., Parkin I. P., Allan E.: Copper as an antimicrobial agent: Recent advances. *RSC Advances*, **11**, 18179–18186 (2021). <https://doi.org/10.1039/D1RA02149D>
- [9] Sirelkhatim A., Mahmud S., Seeni A., Kaus N. H., Ann L. C., Bakhori S. K., Hasan H., Mohamad D.: Review on zinc oxide nanoparticles: Antibacterial activity and toxicity mechanism. *Nano-Micro Letters*, **7**, 219–242 (2015). <https://doi.org/10.1007/s40820-015-0040-x>
- [10] Kubacka A., Diez M. S., Rojo D., Bargiela R., Ciordia S., Zapico I., Albar J. P., Barbas C., dos Santos V. A. P. M., Fernández-García M., Ferrer M.: Understanding the antimicrobial mechanism of TiO<sub>2</sub>-based nanocomposite films in a pathogenic bacterium. *Scientific Reports*, **4**, 4134 (2014). <https://doi.org/10.1038/srep04134>

- [11] Mendes C. R., Dilarri G., Forsan C. F., de Moraes Ruy Sapata V., Lopes P. R. M., de Moraes P. B., Montagnoli R. N., Ferreira H., Bidoia E. D.: Antibacterial action and target mechanisms of zinc oxide nanoparticles against bacterial pathogens. *Scientific Reports*, **12**, 2658 (2022). <https://doi.org/10.1038/s41598-022-06657-y>
- [12] Rutherford D., Jira J., Kolářová K., Matolínová I., Mičová J., Remeš Z., Rezek B.: Growth inhibition of gram-positive and gram-negative bacteria by zinc oxide hedgehog particles. *International Journal of Nanomedicine*, **16**, 3541–3554 (2021). <https://doi.org/10.2147/IJN.S300428>
- [13] Raj N. B., Pavithra Gowda N. P., Pooja O. S., Purushotham B., Kumar M. R. A., Sukrutha S. K., Ravikumar C. R., Nagaswarupa H. P., Murthy H. C. A., Boppana S. B.: Harnessing ZnO nanoparticles for antimicrobial and photocatalytic activities. *Journal of Photochemistry and Photobiology*, **6**, 100021 (2021). <https://doi.org/10.1016/j.jpap.2021.100021>
- [14] Zabrieski Z., Morrell E., Hortin J., Dimkpa C., McLean J., Britt D., Anderson A.: Pesticidal activity of metal oxide nanoparticles on plant pathogenic isolates of pythium. *Ecotoxicology*, **24**, 1305–1314 (2015). <https://doi.org/10.1007/s10646-015-1505-x>
- [15] Anwar M. A., Aqib A. I., Ashfaq K., Deeba F., Khan M. K., Khan S. R., Muzammil I., Shoaib M., Naseer M. A., Riaz T., Tanveer Q., Sadiq M., Lodhi F. L., Ashraf F.: Antimicrobial resistance modulation of MDR *E. coli* by antibiotic coated ZnO nanoparticles. *Microbial Pathogenesis*, **148**, 104450 (2020). <https://doi.org/10.1016/j.micpath.2020.104450>
- [16] El-Megharbel S. M., Alsawat M., Al-Salmi F. A., Hamza R. Z.: Utilizing of (zinc oxide nano-spray) for disinfection against ‘SARS-CoV-2’ and testing its biological effectiveness on some biochemical parameters during (COVID-19 Pandemic)-ZnO nanoparticles have antiviral activity against (SARS-CoV-2). *Coatings*, **11**, 388 (2021). <https://doi.org/10.3390/coatings11040388>
- [17] Choi S.-S., Kim J.-C., Woo C.-S.: Accelerated thermal aging behaviors of EPDM and NBR vulcanizates. *Bulletin of the Korean Chemical Society*, **27**, 936–938 (2006). <https://doi.org/10.5012/bkcs.2006.27.6.936>
- [18] Krainoi A., Poomputsa K., Kalkornsurapranee E., Johns J., Songtipya L., Nip R., Nakaramontri Y.: Disinfectant natural rubber films filled with modified zinc oxide nanoparticles: Synergetic effect of mechanical and antibacterial properties. *Express Polymer Letters*, **15**, 1081–1100 (2021). <https://doi.org/10.3144/expresspolymlett.2021.87>
- [19] El-Nemr K. F., Radi H., Mousa I. M.: Properties of acrylonitrile butadiene rubber modified with acrylate monomers and oligomers using gamma irradiation. *Egyptian Journal of Radiation Sciences and Applications*, **30**, 145–152 (2017). <https://doi.org/10.21608/ejrsa.2018.1749.1019>
- [20] Deng X., Luan Q., Chen W., Wang Y., Wu M., Zhang H., Jiao Z.: Nanosized zinc oxide particles induce neural stem cell apoptosis. *Nanotechnology*, **20**, 115101 (2009). <https://doi.org/10.1088/0957-4484/20/11/115101>
- [21] Brüning K., Schneider K., Roth S. V., Heinrich G.: Kinetics of strain-induced crystallization in natural rubber studied by WAXD: Dynamic and impact tensile experiments. *Macromolecules*, **45**, 7914–7919 (2012). <https://doi.org/10.1021/ma3011476>
- [22] Passador F. R., Rodolfo A., Pessan L. A.: *In situ* dynamic vulcanization of poly(vinyl chloride)/acrylonitrile-butadiene rubber blends. *Journal of Macromolecular Science: Part B*, **48**, 282–298 (2009). <https://doi.org/10.1080/00222340802679607>
- [23] Hait S., Valentín J. L., Jimenez A. G., Ortega R., Ghosh A. K., Stöckelhuber K. W., Wießner S., Heinrich G., Das A.: Poly(acrylonitrile-co-butadiene) as polymeric cross-linking accelerator for sulphur network formation. *Heliyon*, **6**, e04659 (2020). <https://doi.org/10.1016/j.heliyon.2020.e04659>
- [24] Rivlin R. S., Saunders D. W.: Large elastic deformations of isotropic materials VII. Experiments on the deformation of rubber. *Philosophical Transactions of the Royal Society*, **243**, 251–288 (1951). <https://doi.org/10.1098/rsta.1951.0004>
- [25] Schlögl S., Trutschel M.-L., Chassé W., Riess G., Saalwächter K.: Entanglement effects in elastomers: Macroscopic vs microscopic properties. *Macromolecules*, **47**, 2759–2773 (2014). <https://doi.org/10.1021/ma4026064>
- [26] Saleesung T., Reichert D., Saalwächter K., Sirisinha C.: Correlation of crosslink densities using solid state NMR and conventional techniques in peroxide-crosslinked EPDM rubber. *Polymer*, **56**, 309–317 (2015). <https://doi.org/10.1016/j.polymer.2014.10.057>
- [27] Fröhlich J., Niedermeier W., Luginsland H.-D.: The effect of filler–filler and filler–elastomer interaction on rubber reinforcement. *Composites Part A: Applied Science and Manufacturing*, **36**, 449–460 (2005). <https://doi.org/10.1016/j.compositesa.2004.10.004>
- [28] Omnès B., Thuillier S., Pilvin P., Grohens Y., Gillet S.: Effective properties of carbon black filled natural rubber: Experiments and modeling. *Composites Part A: Applied Science and Manufacturing*, **39**, 1141–1149 (2008). <https://doi.org/10.1016/j.compositesa.2008.04.003>
- [29] Haque M., Sartelli M., McKimm J., Bakar M. A.: Health care-associated infections – An overview. *Infection and Drug Resistance*, **11**, 2321–2333 (2018). <https://doi.org/10.2147/idr.s177247>
- [30] Prasanna V. L., Vijayaraghavan R.: Insight into the mechanism of antibacterial activity of ZnO: Surface defects mediated reactive oxygen species even in the dark. *Langmuir*, **31**, 9155–9162 (2015). <https://doi.org/10.1021/acs.langmuir.5b02266>

- [31] Sawai J., Shoji S., Igarashi H., Hashimoto A., Kokugan T., Shimizu M., Kojima H.: Hydrogen peroxide as an antibacterial factor in zinc oxide powder slurry. *Journal of Fermentation and Bioengineering*, **86**, 521–522 (1998). [https://doi.org/10.1016/S0922-338X\(98\)80165-7](https://doi.org/10.1016/S0922-338X(98)80165-7)
- [32] Bogdan J., Zarzyńska J., Pławińska-Czarnak J.: Comparison of infectious agents susceptibility to photocatalytic effects of nanosized titanium and zinc oxides: A practical approach. *Nanoscale Research Letters*, **10**, 309 (2015). <https://doi.org/10.1186/s11671-015-1023-z>
- [33] Krishnamoorthy R., Athinarayanan J., Periyasamy V. S., Alshuniaber M. A., Alshammari G., Hakeem M. J., Ahmed M. A., Alshatwi A. A.: Antibacterial mechanisms of zinc oxide nanoparticle against bacterial food pathogens resistant to beta-lactam antibiotics. *Molecules*, **27**, 2489 (2022). <https://doi.org/10.3390/molecules27082489>
- [34] Sonohara R., Muramatsu N., Ohshima H., Kondo T.: Difference in surface properties between *Escherichia coli* and *Staphylococcus aureus* as revealed by electrophoretic mobility measurements. *Biophysical Chemistry*, **55**, 273–277 (1995). [https://doi.org/10.1016/0301-4622\(95\)00004-h](https://doi.org/10.1016/0301-4622(95)00004-h)
- [35] Li W-R., Xie X-B., Shi Q-Z., Zeng Y-N., Ou-Yang Y-S., Chen Y-B.: Antibacterial activity and mechanism of silver nanoparticles on *Escherichia coli*. *Applied Microbiology and Biotechnology*, **85**, 1115–1122 (2010). <https://doi.org/10.1007/s00253-009-2159-5>

Research article

# Fine-tuning optimization of poly lactic acid impact strength with variation of plasticizer using simple supervised machine learning methods

Jaka Fajar Fatriansyah<sup>1,2\*</sup>, Elvi Kustiyah<sup>3</sup>, Siti Norasmah Surip<sup>4</sup>, Andreas Federico<sup>1</sup>,  
Agrin Febrian Pradana<sup>1</sup>, Aniek Sri Handayani<sup>5</sup>, Mariatti Jaafar<sup>6</sup>, Donanta Dhaneswara<sup>1,2</sup>

<sup>1</sup>Department of Metallurgical and Materials Engineering, Faculty of Engineering, University of Indonesia, Depok, 16424 Jawa Barat, Indonesia

<sup>2</sup>Advanced Materials Research Center (AMRC), Faculty of Engineering, University of Indonesia, Depok, 16424 Jawa Barat, Indonesia

<sup>3</sup>Department of Chemical Engineering, Universitas Bhayangkara Jakarta Raya, Jl. Raya Perjuangan, Bekasi Utara 17121, West Java, Indonesia

<sup>4</sup>Faculty of Applied Sciences, Universiti Teknologi MARA, 40450 Shah Alam, Selangor, Malaysia

<sup>5</sup>Department of Chemical Engineering, Institut Teknologi Indonesia, Jl. Raya Puspitok Serpong 15314, South Tangerang, Indonesia

<sup>6</sup>School of Materials and Mineral Resources Engineering, Universiti Sains Malaysia, Engineering Campus, 14300 Nibong Tebal, Seberang Perai Selatan, Penang, Malaysia

Received 5 April 2023; accepted in revised form 6 June 2023

**Abstract.** The use of machine learning to fine-tune the properties of materials is a remarkable achievement in the 21<sup>st</sup> century. Three machine learning (ML) methods were used to fine-tune and optimize the impact strength of polylactic acid (PLA) with different plasticizers: KNN (K-nearest neighbors), SVR (Support Vector Regression), and ANN (artificial neural networks). The results demonstrated that, though ANN reached a higher  $R^2$  score of 0.901 than the other two ML methods, KNN, with an  $R^2$  score of 0.839, showed more stability than ANN. Based on the current research, KNN is recommended for experimentalists to fine-tune the impact strength of variational plasticizers. The experiment study case with polyethylene glycol 1000 (PEG1000) and octyl epoxy stearate (OES) plasticizer showed good agreement and prediction with experiments. It even showed the fine-tuned impact strength as a function of plasticizer content results, which cannot be achieved by only experiments.

**Keywords:** biodegradable polymers, mechanical properties, modelling and simulation

## 1. Introduction

Poly(lactic acid) (PLA) is a biopolymer material that has a high potential to be developed due to particular properties such as degradability, biocompatibility, good processability, and relatively good mechanical properties in comparison to other biopolymers [1–3]. The increasing attention to climate change and global warming makes PLA an alternative material in the

plastics industry [4]. However, despite its advantages in comparison to petroleum-based polymers, PLA is relatively brittle, stiff, and has low impact strength [5]. These deficiencies make the use of PLA limited to short-term or merely disposable products [6]. The insufficient impact strength of PLA limits its application to broader uses, such as electronic device housing and so on [7]. The use of plasticizers is one

\*Corresponding author, e-mail: [jakafajar@ui.ac.id](mailto:jakafajar@ui.ac.id)

© BME-PT

of the methods to modify PLA's impact strength [8]. However, owing to the wide variety of plasticizer types, it is challenging to select appropriate plasticizers to obtain the specific values of impact strength and optimize them. The trial-and-error experiments require a lot of costs and time, thus rendering these methods ineffective.

The use of machine learning (ML) to guide plastics engineers to find new types of materials is increasingly common, for example, Kim *et al.* [9] used a genetic algorithm (GA) in tandem with ML to design polymer with specific glass transition temperature and high bandgap. The advantage of using GA with ML is that they require less number of hyperparameters than other generative models. In addition, there have been many efforts to optimize specific properties of polymers and polymer composites, such as dielectric properties using kernel ridge regression (KRR) [10] and the least absolute shrinkage and selection operator (LASSO) method [11], glass temperature using active learning [12], gas permeabilities using gaussian process regression [13], mechanical properties using artificial neural networks (ANN) [14] and convolutional neural networks (CNN) [15], and to design smart, self-sensing fiber reinforced plastics using ANN [16]. However, most of these efforts described are too complicated to be useful for ordinary users, and some require large databases for example ANN. Lukasiak *et al.* [17] employed KNN to recognize a pattern of polymeric materials. Tapkin *et al.* [18] used a simple machine-learning method of K-nearest neighbors (KNN) and support vector machine (SVM) to classify Bitumen Images and use them for polypropylene concentration prediction. Costa *et al.* [19] and Gajarska *et al.* [20] used KNN to classify of polymer e-waste and twenty polymers respectively by means of laser-induced breakdown spectroscopy (LIBS). However, KNN and SVM were largely used in classification or pattern recognition.

In this paper, the impact strength of plasticized PLA is predicted and optimized using simple machine learning methods: support vector regression (SVR),

KNN, and ANN with a relatively small database. The reason for using these methods is that they are simple and can be used even by beginner industrial users. The use of SVR and KNN is for representative simple supervised ML models, while ANN is for complex ones. ANN is one of the most common methods in the deep learning regime, albeit still the simplest. The other reason is the limitation of data. It is well known that SVR and KNN are suitable for small sets of data but these methods will easily lead to overfitting. Thus, it needs to be compared with the ANN model which is suitable for a large data set, however according to Feng *et al.* [21] fine-tuned deep neural network (DNN) shows better generalization performance in comparison to simple supervised ML methods.

This study does not use inverse design to select new materials, instead using simple experiments to validate and select specific plasticizer types based on optimized ML methods. The advantage of our approach is that it is simple and can be used by an ordinary user or plastics engineer to optimize their material selection.

## 2. Methods

### 2.1. Dataset characteristics

The prediction of plasticized PLA impact strength involves a dataset containing data from previous experiments with information on the PLA matrix and plasticizer properties. After sorting, cleaning, and trimming the data samples, a total of 54 samples were collected from 11 different previous experiments, which consisted of 14 different types of plasticizers with content in the range of 1 to 30% that were melt-blended with PLA (molecular weight in the range of 86 170 to 207 000 g/mol). The input parameters used for prediction are PLA molecular weight, plasticizer molecular weight, plasticizer density, as well as plasticizer content, and the parameter to be predicted is mechanical impact strength. Statistical information for this dataset is shown in Table 1. Plasticizer content measures the weight ratio of plasticizer to PLA.

**Table 1.** Statistical information of the plasticized PLA dataset.

No.	Features	Mean	Minimum	Maximum	Standard deviation
1.	PLA molecular weight [kg·mol <sup>-1</sup> ]	137.08	86.17	207.00	44.81
2.	Plasticizer molecular weight [kg·mol <sup>-1</sup> ]	0.80	0.16	1.37	0.42
3.	Plasticizer density [g·cm <sup>-3</sup> ]	1.03	0.90	1.30	0.12
4.	Plasticizer content [wt%]	11.00	1.00	30.00	6.87
5.	Impact strength [kJ·m <sup>-2</sup> ]	29.98	4.80	62.90	14.48

## 2.2. Machine learning models

In this paper, we use SVR, KNN, and ANN to predict plasticized PLA impact strength which is programmed using Python programming language version 3.8. SVR and KNN are the classic and simplest shallow ML methods and can be easily understood by plastics engineers and experimentalists. Both methods are on the extreme end of the spectrum of shallow ML methods. SVR requires a minimal number of tuning parameters and can be used properly with careful feature selection, while KNN has a lot of tuning parameters but is also sensitive to outliers. We realize that in polymer science, outlier data exist due to many unknown or hidden experiment settings. The development of the KNN and SVR models is done by using the Scikit-learn Python library. The KNN model involves  $K$  parameters, which describe the number of closest data points to be taken as a representation of the data points to be predicted. The predicted result of the KNN model is the average of the output of the closest data points, as shown in Equation (1):

$$\hat{y}(x) = \frac{1}{k} \sum_{x_i \in N_k(x)} y_i \quad (1)$$

where  $\hat{y}(x)$  is the predicted result,  $k$  denotes the number of closest data points to the input data  $x$ , and  $y_i$  represents the labels of those data points [22]. Euclidean distance was used as the distance calculation metric since it is the default and widely used metric in KNN, as well as generally works great on low-dimensional numeric data compared to other metrics. Euclidean distance calculation can be performed using Equation (2) below:

$$d(p, q) = d(q, p) = \sqrt{\sum_{i=1}^n (q_i - p_i)^2} \quad (2)$$

where  $d(p, q)$  is the Euclidean distance between two points of  $q$  and  $p$ .

The SVR model is built using the radial basis function (RBF) kernel and includes  $C$  and gamma parameters. The kernel is a function that is useful for projecting low-dimensional original data to higher dimensions, as well as converting SVR model computing systems from linear to non-linear and having different mapping capabilities, which can affect the performance of the SVR model. RBF is one of the kernels in SVR that can be used for almost all types of data and involves the gamma parameter, which

describes the magnitude of the influence distance from a data point, thus affecting the degree of curvature of the line or plane defined by the model [23]. The gamma ( $\gamma$ ) value is determined by the RBF kernel free parameter value ( $\sigma$ ), which is expressed through Equation (3) below:

$$\gamma = \frac{1}{2\sigma^2} \quad (3)$$

Unlike the gamma parameter, parameter  $C$  is a penalty factor, which can be used for all types of kernels to balance empirical risk and model confidence level. Parameter  $C$  affects how much deviation the SVR model can tolerate, which is directly correlated with the slack variable ( $\xi$ ) [24], as shown by Equation (4):

$$T = \min: \frac{1}{2} \|w\|^2 + C \sum_{i=1}^n (\xi_i - \xi_i^*) \quad (4)$$

where  $T$  is the SVR goal to minimize the function on the right-hand side of the equation,  $w$  is weight, and is the penalty parameter.

The ANN model is built using the TensorFlow library and involves parameters such as the number of hidden layers and the number of nodes in each layer, epoch, batch size, and learning rate. Epoch describes the model training cycle against all data in the training dataset. The batch size describes the amount of data that will be passed into the ANN model at one time, while the learning rate describes how fast the ANN model learns by determining the weight adjustments to the model based on the gradient loss for each epoch. When it comes to training the model using the data set, each of those models has its own way of interpreting the data, thus resulting in different capabilities and limitations. The advantages and disadvantages of using these models are explained in Table 2. The data set will be fed into each model to see which model can handle the data well based on their superiorities and limitations.

## 2.3. Prediction performance evaluation

The performance of these models in predicting plasticized PLA impact strength was known by calculating the  $R^2$  score, root mean square error ( $RMSE$ ), and relative root mean square error ( $RRMSE$ ). The  $R^2$  score is an evaluation metric that represents the magnitude of the difference between the model's predicted value and the actual value in the dataset, which is calculated based on Equation (5):

**Table 2.** The advantages and disadvantages of KNN, SVR, and ANN models [25–30].

KNN		SVR		ANN	
Advantage	Disadvantage	Advantage	Disadvantage	Advantage	Disadvantage
<ul style="list-style-type: none"> <li>• No training period.</li> <li>• Easy to implement.</li> <li>• Has few parameters to set.</li> <li>• Gives good results even if there is not enough information about the data (few data).</li> </ul>	<ul style="list-style-type: none"> <li>• Does not work well with large data sets and high-dimensionality.</li> <li>• Sensitive to noise and missing data.</li> <li>• To work properly, the features must be expressed in the same scale.</li> </ul>	<ul style="list-style-type: none"> <li>• Generally works well in high-dimensional spaces.</li> <li>• Robust to outliers.</li> <li>• Easy to implement.</li> <li>• Has few parameters to set.</li> </ul>	<ul style="list-style-type: none"> <li>• Not suitable for large data sets.</li> <li>• May be difficult to interpret and understand.</li> <li>• Does not work well when the number of features exceeds the number of training data.</li> </ul>	<ul style="list-style-type: none"> <li>• Can be applied to complex non-linear problems.</li> <li>• Works well with large data sets.</li> <li>• Provides quick predictions after training.</li> </ul>	<ul style="list-style-type: none"> <li>• Has many parameters to set.</li> <li>• Computations are difficult and time-consuming.</li> <li>• Weights and biases are initialized randomly, making the resulting predictions inconsistent.</li> </ul>

$$R^2 = 1 - \frac{\sum_{i=1}^n (\hat{y}_i - y_i)^2}{\sum_{i=1}^n (y_i - \bar{y})^2} \quad (5)$$

where  $n$ ,  $y$ ,  $\bar{y}$ , dan  $\hat{y}_i$  are the sum of the data, the actual value, the average value, and the model’s predicted value, respectively. The  $R^2$  score value is in the range  $-\infty$  to 1, where the level of accuracy will be higher if the value is close to 1 [31]. Meanwhile,  $RMSE$  is an evaluation metric that measures the standard deviation of the prediction error, represented by the square root of the average difference in the model’s predicted value and the actual value, which is calculated using Equation (6) below:

$$RMSE = \sqrt{\frac{1}{n} \sum_{i=1}^n (\hat{y}_i - y_i)^2} \quad (6)$$

The  $RMSE$  value is in the range of 0 to  $+\infty$ , where the level of accuracy will be higher if the value is closer to 0, indicating the closer the distance between the predicted value and the actual value [32].

A dimensionless variant of  $RMSE$  is  $RRMSE$ .  $RRMSE$  is a measure of root mean square error that has been scaled against the actual value and then normalized by the root mean square value.  $RRMSE$  may be used to compare various measurement techniques, whereas  $RMSE$  is constrained by the original measurements’ scale. An increased  $RRMSE$  happens when the predictions turn out to be wrong.  $RRMSE$  expresses the error as a percentage or relative and the value is calculated using Equation (7):

$$RRMSE = \sqrt{\frac{\frac{1}{n} \sum_{i=1}^n (y_i - \hat{y})^2}{\sum_{i=1}^n (y_i)^2}} \quad (7)$$

## 2.4. Experimental design

Validation of the machine learning model prediction results was also carried out through experiments. The same impact resistance experiments as Sungsanit *et al.* [33] and Ferri *et al.* [34] were re-conducted, involving samples in the form of polyethylene glycol (PEG) and octyl epoxy stearate (OES) plasticized PLA. PLA was obtained from Repreper Tech Co., Ltd (Kowloon, Hong Kong) in the form of plastic pellets, PEG1000 (molecular weight of  $1000 \text{ g}\cdot\text{mol}^{-1}$ ) was obtained from Merck (Darmstadt, Germany), and OES (molecular weight of  $408 \text{ g}\cdot\text{mol}^{-1}$ ) was obtained from Traquisa (Barcelona, Spain). Mixing of dried PLA and PEG1000 (with content variations of 5, 10, 15, and 20 wt%) was done in a rheomixer at a temperature of  $190^\circ\text{C}$  and a stirring speed of 30 rpm for 15 minutes, while dried PLA and OES (with content variations of 1, 3, 5, 10, 15 and 20 wt%) were mixed at a temperature of  $180^\circ\text{C}$  and a stirring speed of 60 rpm. The impact resistance testing was carried out at room temperature using the Izod method, according to the ASTM D256 standard specification. The 2.5 millimeters-depth notched specimens with the size of  $64 \times 12.7 \times 3.2 \text{ mm}$  were injection molded and were dried in the vacuum oven overnight prior to testing. The test was performed using a Davenport impact tester with a pendulum hammer of 1.36 J.

## 3. Results and discussions

### 3.1. KNN model performance

Three ML algorithms were used: KNN, SVR, and ANN. The parameters of these algorithms were optimized to obtain the best  $R^2$  score. First, the KNN algorithm was built to do prediction with a variation of the  $K$  parameter which shows the number of nearest neighbors. KNN uses the distance between data

**Table 3.** Effect of variations in  $K$  values on KNN performance.

$K$	$R^2$ score	$RMSE$	$RRMSE$
1	0.839	0.080	15.327
2	0.583	0.129	24.667
3	0.428	0.151	28.890
4	0.319	0.165	31.516
5	0.306	0.167	31.816
6	0.240	0.175	33.313
7	0.158	0.184	35.064
8	-0.019	0.202	38.574
9	-0.166	0.216	41.261
10	-0.294	0.228	43.455

to make classifications or predictions regarding the grouping of an individual data point. Usually, the smaller number of  $K$ , the higher accuracy should be obtained. Here  $K$  was varied from 1 to 10. The results are shown in Table 3. From the table, as  $K$  is increased, the  $R^2$  score decreases.  $RMSE$  sees a similar pattern in which as  $K$  is increased, the  $RMSE$  score is getting worse. It can be understood that a higher value of  $K$ , makes the algorithm less sensitive to the noise. In addition, our dataset is small, and many hidden variables may exist since the mixing of PLA and plasticizer is a complex process. So, Thus, the maximum accuracy should be obtained in a low value of  $K$ , in our case is 1 with an  $R^2$  score of 0.839.

### 3.2. SVR model performance

SVR is an ML algorithm that is built based on the Support Vector Machine (SVM) method but for regression instead of classification. Basically, SVR finds the best fit line for the data points, thus creating a hyperplane that has the maximum number of data points. The varied parameters in SVR are  $C$ , which is a regularization parameter to express tolerance for data point misrepresentation, and gamma, which is a parameter that determines how much curvature there is in a decision boundary. A larger gamma indicates a greater curvature at the boundary, but there is a regression problem in this case. The results of the variation of  $C$  and gamma are given in Table 4. From the table, it was found that the maximum  $R^2$  score is 0.689 with a  $C$  and gamma of 1000 and 0.1, respectively. Considering the complexity of the relationship between features and the target, a larger tolerance is expected. However, the smaller gamma means the regression boundary curvature is not complex.

**Table 4.** Effect of variations in  $C$  and gamma values on SVR performance

$C$	Gamma	$R^2$ Score	$RMSE$	$RRMSE$
0.1	1	0.420	0.264	50.840
1	1	0.576	0.226	43.484
10	1	0.664	0.201	38.677
100	1	0.653	0.204	39.325
1000	1	0.666	0.200	38.594
0.1	0.1	0.093	0.330	63.590
1	0.1	0.464	0.254	48.874
10	0.1	0.546	0.234	44.972
100	0.1	0.671	0.199	38.295
1000	0.1	0.689	0.193	37.229
0.1	0.01	-0.086	0.361	69.558
1	0.01	0.115	0.326	62.803
10	0.01	0.448	0.258	49.620
100	0.01	0.492	0.247	47.559
1000	0.01	0.561	0.230	44.251
0.1	0.001	-0.112	0.366	70.404
1	0.001	-0.085	0.361	69.547
10	0.001	0.117	0.326	62.721
100	0.001	0.444	0.259	49.777
1000	0.001	0.480	0.250	48.122
0.1	0.0001	-0.115	0.366	70.490
1	0.0001	-0.112	0.366	70.400
10	0.0001	-0.085	0.361	69.546
100	0.0001	0.118	0.326	62.713
1000	0.0001	0.444	0.259	49.788

### 3.3. ANN model performance

The ANN algorithm was employed as the third model. After optimization, the following parameters were kept constant: testing set fraction to total data of 0.3, random state of 101, the activation function of ReLU for both input and hidden layers, the activation function of linear for output layer, Adam optimizer, and the mean squared error (MSE) as loss function. Here, the number of hidden layers and the number of nodes were varied to obtain the optimum  $R^2$  score. The results are shown in Table 5. It was found that the optimum  $R^2$  score was obtained with three hidden layers with nodes of 128, 64, and 32 for every hidden layer. Here 1000 epoch was used. Here we found that the number of layers needed is only three, although it is a common conception that the deeper the layer, the more complex the relationship could be captured. However, the number of nodes is quite large, which means the model has a wider network and the complexity of the regression boundary.

**Table 5.** Effect of variations in the number of hidden layers and nodes in each hidden layer on ANN performance.

Number of nodes in the layer of			$R^2$ score	RMSE	RRMSE
1	2	3			
8	–	–	0.507	0.153	26.860
16	–	–	0.705	0.118	20.762
32	–	–	0.560	0.144	25.377
64	–	–	0.580	0.141	24.782
128	–	–	0.690	0.121	21.279
8	8	–	0.494	0.155	27.192
16	16	–	0.641	0.130	22.920
32	32	–	0.660	0.127	22.306
64	64	–	-0.063	0.216	37.705
128	128	–	0.597	0.138	24.284
8	16	–	-0.257	0.165	29.020
8	32	–	0.424	0.165	29.020
8	64	–	0.201	0.187	32.681
8	128	–	0.684	0.118	20.567
16	32	–	0.415	0.160	27.971
16	64	–	0.160	0.192	33.515
16	128	–	0.104	0.198	34.608
32	64	–	0.082	0.201	35.040
32	128	–	0.369	0.166	29.057
64	128	–	-0.760	0.278	48.567
8	8	8	0.138	0.194	33.951
16	16	16	-0.627	0.267	46.650
32	32	32	0.525	0.144	25.195
64	64	64	-0.566	0.262	45.772
128	128	128	-0.276	0.236	41.307
32	32	8	0.529	0.144	25.108
64	64	8	0.165	0.191	33.430
64	64	32	-0.554	0.261	45.590
64	32	16	-0.143	0.224	39.104
64	32	8	-0.245	0.234	40.807
64	32	32	0.395	0.163	28.435
64	8	8	-0.674	0.271	47.325
32	8	8	-0.259	0.235	41.032
128	64	32	0.901	0.068	12.037
128	64	8	-0.171	0.227	39.584
128	32	8	0.433	0.158	27.543

This reflects the complex relationship between features and targets.

**3.4. Summary of optimized model performance and performance stability**

The summary of the optimized  $R^2$  score is given in Figure 1. However, we also conduct tests on the stability of the accuracy. It was found that although ANN gives greater accuracy, the model itself has a wildly fluctuating  $R^2$  score. This may be due to a

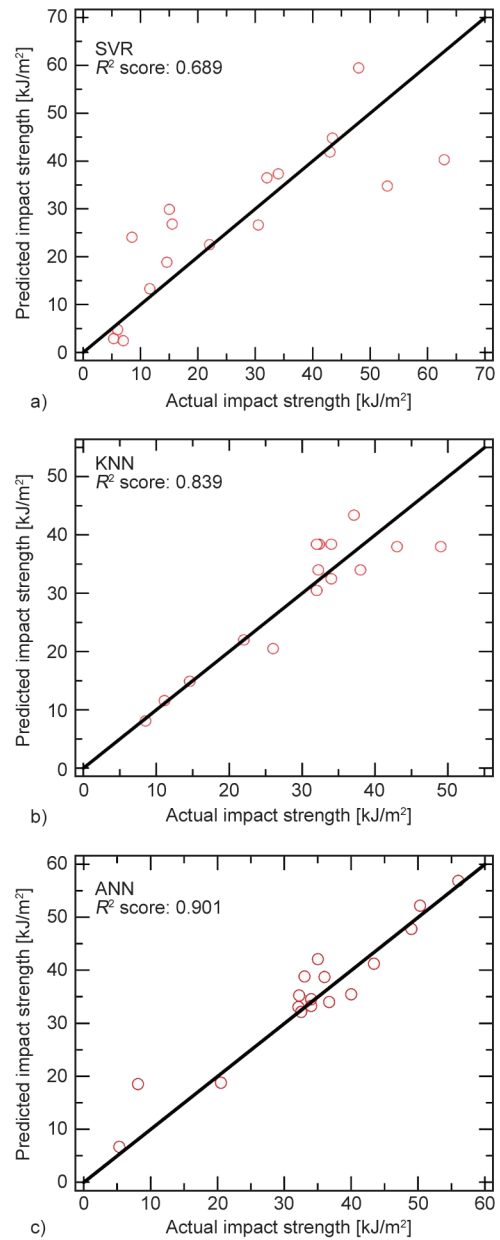


**Figure 1.** Optimized  $R^2$  score plots of a) KNN model, b) SVR model, and c) ANN model.

small quantity of data since ANN needs much larger data points. Thus, we recommend KNN may be used to predict impact strength although the accuracy is smaller than ANN. The accuracy and stability of the results are shown in Figure 2.

**3.5. Correlation coefficients and the feature of importance**

The Pearson correlation coefficient (PCC), or correlation coefficient, measures the linear correlation between features and outputs, which is tabulated in Table 6, and the feature importance measures are presented in Table 7. It should be noted that PCC does not measure nonlinear relationships. According

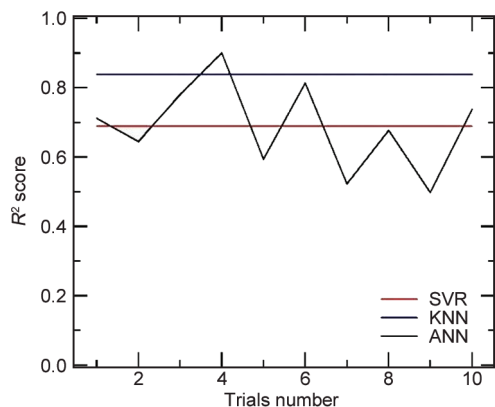


**Figure 2.** Performance ( $R^2$  score) stability of KNN, SVR, and ANN models.

to Table 6, it can be seen that all of the input features are almost independent of each other. It can also be seen that plasticizer density is more correlated to impact strength in comparison to other features, followed by plasticizer molecular weight, PLA molecular weight, and plasticizer to PLA content. This means that it is preferable to change plasticizer density to observe the change in impact strength in comparison to other features. A negative sign of plasticizer density PCC means that as the plasticizer density is increased, the impact strength will likely decrease. Jacobsen and Fritz [8] conducted experiments by adding plasticizer PEG1500, glucose monoesters, and partial fatty acid esters and found that at similar plasticizer contents, the impact resistance of plasticized samples is similar, especially for glucose monoesters and partial fatty acid esters addition. The glucose monoesters and partial fatty acid esters both have similar densities of 1.06 and 1.03, respectively. As pure PLA has no plasticizer, the value of plasticizer density is zero, and according to our model, as we increase plasticizer density, the impact strength decreases, and we found that in our experimental setup, this was true, as pure PLA has higher impact strength (though Jacobsen and Fritz used impact resistance, it can be assumed that impact strength behavior will be somewhat similar). However, the

**Table 6.** Pearson correlation coefficient of plasticized PLA dataset.

	PLA molecular weight	Plasticizer molecular weight	Plasticizer density	Plasticizer content	Impact strength
PLA molecular weight	1	-0.11	0.52	0.15	-0.48
Plasticizer molecular weight	-0.11	1	-0.11	-0.31	0.50
Plasticizer density	0.52	-0.11	1	0.15	-0.58
Plasticizer content	0.15	-0.31	0.15	1	-0.04
Impact strength	-0.48	0.50	-0.58	-0.04	1

**Table 7.** Feature importance of ANN model.

Feature	Feature importance
PLA molecular weight	0.135
Plasticizer molecular weight	0.268
Plasticizer density	0.289
Plasticizer content	0.066

PLA-PEG1500 system cannot be explained by the model, since according to our model it should have a smaller impact strength due to the higher density of the plasticizer in comparison to glucose monoesters and partial fatty acid esters. We suggest that maybe other features affect the impact strength of the PLA-PEG1500 system, and since PCC only measures linear correlation, other effects, such as nonlinearity, could not be captured.

Similar behavior occurs for plasticizer content and PLA molecular weight, which has negative PCC. For plasticizer content, Jacobsen and Fritz [8] also reported that for glucose monoesters and partial fatty acid esters plasticizers with content above 2.5%, the impact resistance decreased as the plasticizer content was increased. Wang *et al.* [35] also reported that the impact strength of printed PLA increased with decreased molecular weight to some extent, which supports our model.

Opposite behavior was observed for the plasticizer molecular weight feature, which has a positive effect on impact strength. Jacobsen and Fritz [8] also reported that the PEG1500-PLA system has higher impact resistance than PLA glucose monoesters and PLA partial fatty acid esters, despite the fact that glucose monoesters and partial fatty acid esters have a lower molecular weight than PEG1500. The results of the feature of importance showed a similar pattern. Plasticizer density, PLA molecular weight, and PLA molecular weight have more importance on the model or prediction side, while plasticizer content does not seem to have strong importance according to the model. It can be understood that when the plasticizer content is changed, the impact strength

does not always increase or decrease, and the effect may be superficially random or not well understood by our model.

### 3.6. Experimental comparison

The experimental comparison was conducted, although the number of samples was small. The model used in this comparison is KNN. The reason is as mentioned in the discussion and results subsection that although the ANN gives more accuracy than KNN, the accuracy values are fluctuating while KNN gives stable yet reliable accuracy. The other reason for using KNN is that, based on the cross-validation that has been conducted, KNN showed a higher  $R^2$  score than SVR and ANN.

The comparison between experiments and predictions is demonstrated in Figure 3. It can be seen that the prediction and the experimental results are close enough for the concentration of PEG1000 and OES to reach 20% concentration. It can be seen that the effect of the addition of plasticizers PEG1000 and OES is complex. Despite the limited number of experimental results, our model can predict the behavior of the impact strength. The advantage of using ML before experiments are that ML can guide experimentalists in finding the most efficient amount of plasticizer to fine-tune the target property. In our case, the experimentalist can fine-tune by varying plasticizer content to obtain maximum impact strength, which in our case study is predicted to be 4 and 5% of the concentration of PEG1000 and OES, respectively.

### 4. Conclusions

Three ML models, KNN, SVR and ANN to predict the impact strength of plasticized PLA have been successfully developed. It was found that ANN has the highest  $R^2$  score of 0.901 in comparison to 0.839 of KNN and 0.689 of SVR. The optimized  $R^2$  score of ANN was obtained at three hidden layers with 128, 64, and 32 nodes, for SVR it was optimized at  $C$  and  $\gamma$  of 1000 and 0.1 respectively, and for KNN at  $K$  of 1. However, the  $R^2$  score stability was found to be fluctuating for ANN, while KNN and SVR shows stable results. Thus, we recommend that KNN can be used as a model instead of ANN, given the small number of experimental data. This may be due to a small number of data since ANN needs much larger data points. PCC analysis revealed that plasticizer density had the highest correlation with impact strength, followed by plasticizer molecular weight, PLA molecular weight, and plasticizer content. This indicates that to some extent, it is preferable to alter plasticizer density in order to examine the effect on impact strength, as opposed to altering other characteristics. Lastly, the experimental comparison was conducted for PLA and PEG1000, and OES as plasticizers. It was found that KNN can predict the complex relationship between plasticizer content and impact strength which can not be easily captured by experiments. We suggest that our approach can be used by experimentalists to conduct the fine-tuning of optimization.

### Acknowledgements

This research is funded by the Directorate of Research and Development, Universitas Indonesia under Hibah PUTI Q2 2023 (Grant No. NKB-818/UN2.RST/HKP.05.00/2023).

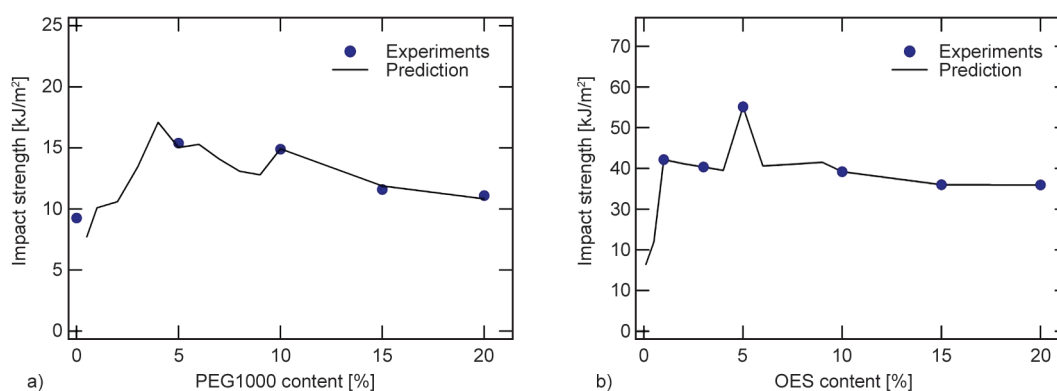


**Figure 3.** The impact strength prediction and the experimental results of a) PEG1000-plasticized PLA and b) OES-plasticized PLA.

## References

- [1] Elsayw M. A., Kim K-H., Park J-W., Deep A.: Hydrolytic degradation of polylactic acid (PLA) and its composites. *Renewable and Sustainable Energy Reviews*, **79**, 1346–1352 (2017).  
<https://doi.org/10.1016/j.rser.2017.05.143>
- [2] Diez-Pascual A. M.: Synthesis and applications of biopolymer composites. *International Journal of Molecular Sciences*, **20**, 2321 (2019).  
<https://doi.org/10.3390/ijms20092321>
- [3] Siakeng R., Jawaid M., Ariffin H., Sapuan S. M., Asim M., Saba N.: Natural fiber reinforced polylactic acid composites: A review. *Polymer Composites*, **40**, 446–463 (2019).  
<https://doi.org/10.1002/pc.24747>
- [4] Jem K. J., Tan B.: The development and challenges of poly(lactic acid) and poly(glycolic acid). *Advanced Industrial and Engineering Polymer Research*, **3**, 60–70 (2020).  
<https://doi.org/10.1016/j.aiepr.2020.01.002>
- [5] Notta-Cuvier D., Odent J., Delille R., Murariu M., Lauro F., Raquez J. M., Bennani B., Dubois P.: Tailoring polylactide (PLA) properties for automotive applications: Effect of addition of designed additives on main mechanical properties. *Polymer Testing*, **36**, 1–9 (2014).  
<https://doi.org/10.1016/j.polymertesting.2014.03.007>
- [6] Agarwal S.: Biodegradable polymers: Present opportunities and challenges in providing a microplastic-free environment. *Macromolecular Chemistry and Physics*, **221**, 2000017 (2020).  
<https://doi.org/10.1002/macp.202000017>
- [7] Bax B., Müssig J.: Impact and tensile properties of PLA/Cordenka and PLA/flax composites. *Composites Science and Technology*, **68**, 1601–1607 (2008).  
<https://doi.org/10.1016/j.compscitech.2008.01.004>
- [8] Jacobsen S., Fritz H. G.: Plasticizing polylactide – The effect of different plasticizers on the mechanical properties. *Polymer Engineering and Science*, **39**, 1303–1310 (1999).  
<https://doi.org/10.1002/pen.11517>
- [9] Kim C., Batra R., Chen L., Tran H., Ramprasad R.: Polymer design using genetic algorithm and machine learning. *Computational Materials Science*, **186**, 110067 (2021).  
<https://doi.org/10.1016/j.commatsci.2020.110067>
- [10] Mannodi-Kanakkithodi A., Chandrasekaran A., Kim C., Huan T. D., Pilania G., Botu V., Ramprasad R.: Scoping the polymer genome: A roadmap for rational polymer dielectrics design and beyond. *Materials Today*, **21**, 785–796 (2018).  
<https://doi.org/10.1016/j.mattod.2017.11.021>
- [11] Chen L., Kim C., Batra R., Lightstone J. P., Wu C., Li Z., Deshmukh A. A., Wang Y., Tran H. D., Vashishta P., Sotzing G. A., Cao Y., Ramprasad R.: Frequency-dependent dielectric constant prediction of polymers using machine learning. *npj Computational Materials*, **6**, 61 (2020).  
<https://doi.org/10.1038/s41524-020-0333-6>
- [12] Kim C., Chandrasekaran A., Jha A., Ramprasad R.: Active-learning and materials design: The example of high glass transition temperature polymers. *MRS Communications*, **9**, 860–866 (2019).  
<https://doi.org/10.1557/mrc.2019.78>
- [13] Zhu G., Kim C., Chandrasekaran A., Everett J. D., Ramprasad R., Lively R. P.: Polymer genome-based prediction of gas permeabilities in polymers. *Journal of Polymer Engineering*, **40**, 451–457 (2020).  
<https://doi.org/10.1515/polyeng-2019-0329>
- [14] Fatriansyah J. F., Surip S. N., Hartoyo F.: Mechanical property prediction of poly(lactic acid) blends using deep neural network. *Evergreen*, **9**, 141–144 (2022).  
<https://doi.org/10.5109/4774229>
- [15] Sun Y., Hanhan I., Sangid M. D., Lin G.: Predicting mechanical properties from microstructure images in fiber-reinforced polymers using convolutional neural networks. *arXiv preprint arXiv:2010.03675* (2020).  
<https://doi.org/10.48550/arXiv.2010.03675>
- [16] Roh H. D., Lee D., Lee I. Y., Park Y-B.: Machine learning aided design of smart, self-sensing fiber-reinforced plastics. *Composites Part C: Open Access*, **6**, 100186 (2021).  
<https://doi.org/10.1016/j.jcomc.2021.100186>
- [17] Lukasiak B. M., Faria R., Zomer S., Brereton R. G., Duncan J. C.: Pattern recognition for the analysis of polymeric materials. *Analyst*, **131**, 73–80 (2006).  
<https://doi.org/10.1039/B510561G>
- [18] Tapkin S., Şengöz B., Şengül G., Topal A., Özçelik E.: Estimation of polypropylene concentration of modified bitumen images by using k-NN and SVM classifiers. *Journal of Computing in Civil Engineering*, **29**, 04014055 (2015).  
[https://doi.org/10.1061/\(ASCE\)CP.1943-5487.0000353](https://doi.org/10.1061/(ASCE)CP.1943-5487.0000353)
- [19] Costa V. C., Aquino F. W. B., Paranhos C. M., Pereira-Filho E. R.: Identification and classification of polymer e-waste using laser-induced breakdown spectroscopy (LIBS) and chemometric tools. *Polymer Testing*, **59**, 390–395 (2017).  
<https://doi.org/10.1016/j.polymertesting.2017.02.017>
- [20] Gajarska Z., Brunnbauer L., Lohninger H., Limbeck A.: Identification of 20 polymer types by means of laser-induced breakdown spectroscopy (LIBS) and chemometrics. *Analytical and Bioanalytical Chemistry*, **413**, 6581–6594 (2021).  
<https://doi.org/10.1007/s00216-021-03622-y>

- [21] Feng S., Zhou H., Dong H.: Using deep neural network with small dataset to predict material defects. *Materials and Design*, **162**, 300–310 (2019).  
<https://doi.org/10.1016/j.matdes.2018.11.060>
- [22] Goyal R., Chandra P., Singh Y.: Suitability of KNN regression in the development of interaction based software fault prediction models. *IERI Procedia*, **6**, 15–21 (2014).  
<https://doi.org/10.1016/j.ieri.2014.03.004>
- [23] Rohmah M. F., Putra I. K. G. D., Hartati R. S., Ardiantoro L.: Comparison four kernels of SVR to predict consumer price index. *Journal of Physics: Conference Series*, **1737**, 012018 (2021).  
<https://doi.org/10.1088/1742-6596/1737/1/012018>
- [24] Rivas-Perea P., Cota-Ruiz J., Chaparro D. G., Venzor J. A. P., Carreón A. Q., Rosiles J. G.: Support vector machines for regression: A succinct review of large-scale and linear programming formulations. *International Journal of Intelligence Science*, **3**, 5–14 (2013).  
<https://doi.org/10.4236/ijis.2013.31002>
- [25] Auria L., Moro R. A.: Support vector machines (SVM) as a technique for solvency analysis. *DIW Berlin Discussion Paper No. 811* (2008).  
<https://doi.org/10.2139/ssrn.1424949>
- [26] Fedorovici L. O., Dragan F.: A comparison between a neural network and a SVM and Zernike moments based blob recognition modules. in '6<sup>th</sup> IEEE International Symposium on Applied Computational Intelligence and Informatics (SACI), Timisoara, Romania' 253–258 (2011).  
<https://doi.org/10.1109/SACI.2011.5873009>
- [27] Yu W. M., Du T., Lim K. B.: Comparison of the support vector machine and relevant vector machine in regression and classification problems. in 'ICARCV 2004 8<sup>th</sup> Control, Automation, Robotics and Vision Conference, Kunming, China' Vol. 2, 1309–1314 (2004).  
<https://doi.org/10.1109/ICARCV.2004.1469035>
- [28] Imandoust S. B., Bolandraftar M.: Application of k-nearest neighbor (KNN) approach for predicting economic events: Theoretical background. *International Journal of Engineering Research and Applications*, **3**, 605–610 (2013).
- [29] Cunningham P., Delany S. J.: K-nearest neighbour classifiers – A tutorial. *ACM Computing Surveys*, **54**, 128 (2021).  
<https://doi.org/10.1145/3459665>
- [30] Ciaburro G., Venkateswaran B.: *Neural networks with R: Smart models using CNN, RNN, deep learning, and artificial intelligence principles*. Packt Publishing, Birmingham (2017).
- [31] Steurer M., Hill R. J., Pfeifer N.: Metrics for evaluating the performance of machine learning based automated valuation models. *Journal of Property Research*, **38**, 99–129 (2021).  
<https://doi.org/10.1080/09599916.2020.1858937>
- [32] Tatachar A. V.: Comparative assessment of regression models based on model evaluation metrics. *International Research Journal of Engineering and Technology*, **8**, 853–860 (2021).
- [33] Sungsanit K., Kao N., Bhattacharya S. N.: Properties of linear poly(lactic acid)/polyethylene glycol blends. *Polymer Engineering and Science*, **52**, 108–116 (2011).  
<https://doi.org/10.1002/pen.22052>
- [34] Ferri J. M., Samper M. D., Garcia-Sanoguera D., Reig M. J., Fenollar O., Balart R.: Plasticizing effect of bio-based epoxidized fatty acid esters on mechanical and thermal properties of poly(lactic acid). *Journal of Materials Science*, **51**, 5356–5366 (2016).  
<https://doi.org/10.1007/s10853-016-9838-2>
- [35] Wang L., Gramlich W. M., Gardner D. J.: Improving the impact strength of poly(lactic acid) (PLA) in fused layer modeling (FLM). *Polymer*, **114**, 242–248 (2017).  
<https://doi.org/10.1016/j.polymer.2017.03.011>

Research article

# Design of biobased non-isocyanate polyurethane (NIPU) foams blown with water and/or ethanol

Vincent Valette, Nasreddine Kébir\* , Fabrice Burel, Laurence Lecamp 

Univ Rouen Normandie, INSA Rouen Normandie, CNRS, PBS UMR 6270, F-76000 Rouen, France

Received 26 April 2023; accepted in revised form 13 June 2023

**Abstract.** A promising process to design non-isocyanate polyurethane (NIPU) foams has been developed. The transurethane polycondensation reaction between fatty biscarbamates, fatty diols, and diamines was used to synthesize a biobased amino-telechelic NIPU oligomer. The prepared oligomer (hard phase) was mixed with an amino-telechelic polydimethylsiloxane (PDMS, soft phase) and then reacted with a biosourced tri-epoxide molecule as crosslinking agent, in the presence of water/ethanol mixtures as physical blowing agents. The crosslinking reaction was followed by Fourier transform infrared spectroscopy (FTIR) and rheometry. The foams can be obtained in less than 2 hours at 95 °C. The prepared foams exhibited cell diameters ranging from 130 to 3090  $\mu\text{m}$ , as well as densities ranging from 55 to 950  $\text{kg/m}^3$ . Their thermal stability thresholds were above 300 °C. They displayed glass transition temperature values ranging from  $-20$  to  $-18$  °C, and low values of the Young modulus ranging from  $2.0 \cdot 10^3$  to  $5.7 \cdot 10^3$  Pa. The hysteresis loss, the recovery time, and the firmness of these foams were dependent on the PDMS content and/or the morphological parameters.

**Keywords:** processing technologies, polymer synthesis, thermosetting resins, NIPU, foam

## 1. Introduction

Polyurethanes (PUs) are a family of versatile and essential polymers that can be found in many application fields such as construction, furniture, bedding, transportation, footwear, and everyday appliances. Polyurethane foams have a significant share of the polyurethane market that is projected to attain 13 million tons in 2024 [1–4].

Commercial PUs foams are usually prepared by reaction of poly-ols with poly-isocyanates. Often,  $\text{CO}_2$  is used as a blowing agent and is produced *in-situ* by the reaction between water and isocyanate [5–7]. A wide range of versatile PU foams can be designed using this straightforward pathway. Nevertheless, isocyanates are toxic chemicals triggering social and health concerns, which have led to a strengthening of the law against them. For instance, PU formulations containing more than 0.1% w/w of residual isocyanate

are forbidden since 2009. To face this worldwide issue, the development of new isocyanate-free processes is of great interest. Today, the literature mentions very few processes for the synthesis of non-isocyanate polyurethane foams (NIPU). These processes are mainly based on the synthesis of a poly(hydroxyurethane) (PHU) matrix from diamine and cyclic carbonates [8–18]. Nevertheless, with one exception, the final foam can only be obtained using high temperatures and/or reaction times, due to the low reactivity of the cyclocarbonate groups.

One technique to design PHU foams is to use physical blowing agents that evaporate during the polymerization process. Solkane, which is a fluorocarbon, was used to prepare PHU foams. The process was performed during 14 h at 80 °C [8]. Supercritical  $\text{CO}_2$  was also used as a blowing agent to prepare PHU foams [9, 10]. Grignard *et al.* [9] conducted the

\*Corresponding author, e-mail: [nasreddine.kebir@insa-rouen.fr](mailto:nasreddine.kebir@insa-rouen.fr)  
© BME-PT

foaming process at 40 °C under 100 or 300 bars for 3 to 24 h, then at 80 °C for 1 min. Mao *et al.* [10] performed the foaming process at 80 °C under pressurization by CO<sub>2</sub> at 150 bar for 6 h.

The second and major technique involves the use of chemical blowing agents. Cornille *et al.* [11] have prepared PHU foams using a self-blowing process. Poly(hydrogenomethylsiloxane) (PHMS) was used as a foaming agent that releases H<sub>2</sub> *in-situ* by the reaction of its SiH groups with a (di-)polyamine during the polymer network formation. The foams were obtained upon heating at 80 °C for 12 h, then at 120 °C for 4 h, respectively. They also succeeded in preparing these foams at room temperature for three days, using a thiourea catalyst [12]. Using the same process, Sternberg and Pilla [13] have prepared carbonated Kraft Lignin, using glycerol carbonate or dimethyl carbonate, and have reacted them with hexamethylenediamine (HMDA) in the presence of PHMS as a blowing agent, and dimethyl sulfoxide (DMSO) to dissolve the lignin part. The foams were obtained at 150 °C after 12 hours.

Clark *et al.* [14] have developed an exotic self-blowing PHU foam through the reaction of polyamine with cyclocarbonated sorbitol. A concomitant side reaction led to release of CO<sub>2</sub> at 100 °C, forming the foam after 20 h of reaction.

Monie *et al.* [15] prepared a self-blowing poly(hydroxyurethane-*co*-hydroxythioether) foam by reacting a cyclocarbonate, a diamine, and a thiol for 4 h at 100 °C. CO<sub>2</sub> was generated *in-situ* as a result of the reaction of the thiol groups with the cyclocarbonates. In another work, they reacted a thiolactone with amine groups to generate the thiols. The prepared foams had several bonds (hydroxyurethanes, thioethers, and amides) [16]. Coste *et al.* [17] used aminolysis of a thiocyclic carbonate to initiate the reaction between the released thiols and cyclic carbonates, resulting in the release of CO<sub>2</sub> and blowing out the PHU matrix. Recently, Bourguignon *et al.* [18] reported a promising process to prepare water-induced self-blown PHU foams. They added water and a catalyst, such as 1,8-diazabicyclo[5.4.0]undec-7-ene (DBU) or KOH, to hydrolyze 5 membered cyclic carbonates in the temperature range of 80–100 °C, for 3–5 hours. This hydrolysis reaction released *in-situ* CO<sub>2</sub> that acted as a blowing agent in PHU formulations composed of a tris(cyclic carbonate) and a diamine. In addition, they showed that by preheating all the components of the formulation separately

for 5 minutes at 100 °C, mixing them and injecting them into a preheated mold (100 °C), they reduced the foaming time from 3 h to 30 min. The resulting foams exhibited properties quite similar to those of their analogues prepared without preheating (3 h), except for a lower density.

The transurethane polycondensation reaction between dialkyl dicarbamates [19–24] and diols, or between dialkyl carbonates and diamines [25–31], is one of the most attractive route to NIPUs. Indeed, compared to PHUs, NIPUs exhibit conventional polyurethane structures. In addition, NIPUs can be made from a large selection of dialkyl dicarbamates or dialkyl dicarbonate molecules, compared to the few commercially available diisocyanate analogues that are precursors of PUs. However, unlike the polyaddition reaction between polyamine and poly(cyclic carbonates), the transurethane polycondensation cannot be used directly to prepare crosslinked NIPU because it is achieved at high temperatures and vacuum to remove the released methanol and to displace the equilibrium. This problem can be circumvented by preparing telechelic NIPU oligomers allowing post-crosslinking via polyaddition reactions under mild conditions [21–32].

Xi *et al.* [25] have prepared NIPU foams by reaction of glucose with dimethylcarbonate (DMC), followed by a reaction with hexamethylene diamine, in the presence of silane as a crosslinking agent. They used NaHCO<sub>3</sub> as a chemical foaming agent that decomposes at high temperature releasing CO<sub>2</sub>. The foaming process took 30 min at 200 °C. These authors prepared similar NIPU foams using maleic acid as foaming initiator and glutaraldehyde as crosslinking agent. The final foams were obtained at room temperature for 5 h, followed by curing at 103 °C for 4 h [25–27]. In another work, they used this same process at room temperature to prepare NIPU foams based on mimosa tannin. The curing of the obtained foams was performed at 70–80 °C overnight [27, 28]. Recently, they prepared self-blowing NIPU foams from tannic acid and citric acid, using a similar procedure [29]. The curing process was performed overnight at 70 °C then at 25 °C for 2 days. Singh and Kaur [30] have prepared similar foams through a reaction between xylose, dimethyl carbonate and hexamethylene diamine, in the presence of citric acid. The foaming/curing process lasted 2 h at 90 °C then 24 h at room temperature. Smith *et al.* [31] have used this methodology to produce foams from tannic

acid, chitosan and DMC, in the presence of glutaraldehyde and other carboxylic acids, *i.e.* malic acid, maleic acid, citric acid and aconitic acid. The final foams were obtained after 72 h at room temperature.

Recently, our team has prepared several biobased amino-terminated NIPU using the transurethane polycondensation between dimethylcarbamates, diols and diamines [32]. Then, they reacted them with a polyepoxide molecule, in the presence of PHMS or its copolymer poly(methylhydroxysiloxane)-*co*-poly(dimethylsiloxane) (PHMS-*co*-PDMS) as blowing agents, to obtain NIPU foams displaying conventional PU structures. The foams were obtained after 30 min of heating at 100 °C (without any preheating) or after 14.5 h at room temperature, which was, as far as we know, the faster process to get NIPU foams [32]. However, this process releases hydrogen, which may limit its use in industry for safety reasons.

In this paper, we propose a solution to this problematic by implementing a green and straightforward process allowing the preparation of biobased NIPU foams from biobased diols and diamines (derived from vegetable oils), dimethyl carbonate (which can be produced from CO<sub>2</sub>), a biobased polyepoxide (derived from glycerol) as a crosslinking agent, an amino terminated PDMS as a soft segment template and surfactant, and water and/or ethanol as a blowing agent. The morphological, thermal and mechanical properties of these materials were investigated.

## 2. Materials

Dimethyl carbonate (DMC, 99%, Sigma Aldrich, France), poly(dimethylsiloxane) bis(3-aminopropyl) terminated (PDMS-A, Sigma Aldrich, France) and 1,5,7-triazabicyclo[4.4.0]dec-5-ene (TBD, 98%, Sigma Aldrich, France). Polyglycerol polyglycidyl ether (DENACOL EX512, Nagase ChemteX, France). Dimer fatty diamide (Priamine<sup>®</sup> 1074, Cargill, France) and dimer fatty diol (Pripol<sup>®</sup> 2033, Cargill, France). All solvents and other reagents were used as received.

## 3. Synthesis

### 3.1. Synthesis of bis-methyl dicarbamate based on Priamine<sup>®</sup> 1074 (BMC)

Priamine<sup>®</sup> 1074 (1 eq.), TBD (0.1 eq.) and DMC (10 eq.) were mixed and stirred for 6 h at 80 °C, in a single-neck round-bottom flask furnished with a magnetic stirrer. The mixture was then cooled down to

room temperature, and then washed with water in diethyl ether. The organic phase was dried over MgSO<sub>4</sub>, which was then removed by filtration. After solvent evaporation, the product was recovered as an orange viscous liquid. <sup>1</sup>H NMR (300 MHz, CDCl<sub>3</sub>) δ [ppm]: 4.64 (broad, 2H; NH), 3.65 (s, 6H; OCH<sub>3</sub>), 3.15 (m, 4H; NHCH<sub>2</sub>), 2.52 to 1 (m, 56H; CH and CH<sub>2</sub>), 0.87 (m, 6H, CH<sub>3</sub>). <sup>13</sup>C NMR (75 MHz, CDCl<sub>3</sub>) δ [ppm]: 157.1 (C=O), 52.0 (OCH<sub>3</sub>), 41.1 (NHCH<sub>2</sub>), 32.0 to 22.8 (CH<sub>2</sub>), 19.8 (CH), 14.2 (CH<sub>3</sub>).

### 3.2. Synthesis of methylcarbamate-terminated NIPU oligomer (NIPU-MC)

Pripol<sup>®</sup> 2033 (6 g, 11.2 mmol), BMC (16.74 g, 25.7 mmol), and TBD (0.16 g, 1.1 mmol) were mixed under a nitrogen stream and stirred for 16 h at 160 °C, in a neat three-neck round-bottom flask furnished with a mechanical stirrer. Then, the medium was placed under vacuum at 0.5 mbar, during 2 h at 160 °C. The product was recovered as an orange viscous oil. <sup>1</sup>H NMR (300 Hz, CDCl<sub>3</sub>) δ [ppm]: 4.66 (broad, 3H; NH), 4.02 (t, 4H; OCH<sub>2</sub>), 3.65 (s, 6H; OCH<sub>3</sub>), 3.14 (m, 8H; NHCH<sub>2</sub>), 2.52 to 1 (m, broad, 173H; CH and CH<sub>2</sub>), 0.85 (m, 6H, CH<sub>3</sub>). <sup>13</sup>C NMR (75 MHz, CDCl<sub>3</sub>) δ [ppm]: 157.1 (C=O), 156.8 (C=O), 64.83 (C–O), 51.9 (OCH<sub>3</sub>), 41.0 (NHCH<sub>2</sub>), 40.9 (NHCH<sub>2</sub>), 37.4 to 22.7 (CH<sub>2</sub>), 19.8 (CH), 14.2 (CH<sub>3</sub>).

### 3.3. Synthesis of amine-terminated NIPU oligomers (NIPU-A)

Priamine<sup>®</sup> 1074 (32.72 g, 60.6 mmol), NIPU-MC (35.79 g, 20.2 mmol.), and TBD (0.28 g, 2.0 mmol) were mixed under a nitrogen stream and stirred for 16 h at 160 °C, in a neat three-neck round-bottom flask furnished with a mechanical stirrer. The medium was then placed under vacuum at 0.5 mbar, during 2 h at 160 °C. The final product was recovered as an orange viscous oil. NIPU-A: <sup>1</sup>H NMR (300 Hz, CDCl<sub>3</sub>) δ [ppm]: 4.68 (broad, 8H; NH), 4.02 (t, 3H; NH(CO)OCH<sub>2</sub>), 3.65 (s, residual; OCH<sub>3</sub>), 3.62 (t, 2H; HOCH<sub>2</sub>), 3.14 (m, 12H; NHCH<sub>2</sub>), 2.6–2 (m, 392H; CH and CH<sub>2</sub>), 0.88 (m, 6H, CH<sub>3</sub>). <sup>13</sup>C NMR (75 MHz, CDCl<sub>3</sub>) δ [ppm]: 163.7 (C=O), 158.9 (C=O), 157.1 (C=O), 156.8 (C=O), 64.8 (C–O), 53.4 (OCH<sub>3</sub>), 42.2 (NHCH<sub>2</sub>), 40.4 (NHCH<sub>2</sub>), 37.4 to 22.8 (CH<sub>2</sub>), 19.8 (CH), 14.2 (CH<sub>3</sub>).

### 3.4. Preparation of NIPU foams

In a polypropylene mould, NIPU-A, DENACOL EX512, PDMS-A and a mixture of water/ethanol

were mechanically blended together at variable molar ratio. Then, the formulation was stirred during 2 min at 2400 rpm using a Speedmixer DAC 150.FVZ.K. A homogenous blend was obtained. The formulation was then placed in an oven at 95 °C during 120 min to produce the final NIPU foam.

## 4. Analysis

### 4.1. Fourier transform infrared spectroscopy (FTIR)

FTIR analysis was achieved with PerkinElmer Spectrum 2000 FTIR (France). This instrument was furnished with a diamond attenuated total reflectance (ATR) device (ATR MK II Golden Gate, Specac, France). Spectra were acquired in the 600 to 4000  $\text{cm}^{-1}$  range, using 10 scans in a nominal resolution of 8  $\text{cm}^{-1}$ .

### 4.2. Nuclear magnetic resonance (NMR)

$^1\text{H}$  NMR and  $^{13}\text{C}$  NMR spectra were acquired with a Bruker 300 Fourier transform spectrometer (France) at 300 and 75 MHz, respectively. The prepared oligomers were analysed in  $\text{CDCl}_3$ , in the presence of tetramethylsilane (TMS) as an internal standard.

### 4.3. Size exclusion chromatography (SEC)

Average molecular weights ( $M_n$  and  $M_w$ ) and dispersity ( $\mathcal{D} = M_w/M_n$ ) of NIPU-MC, NIPU-A, and PDMS-A were evaluated by size exclusion chromatography (SEC). These compounds were dissolved in dichloromethane, filtered (0.45  $\mu\text{m}$ ) and analysed at 25 °C by a Varian PL-GPC50 instrument (France) furnished with two mixed packed columns (PL gel mixed type C). The mobile phase was dichloromethane. Calibration was performed using poly(methyl methacrylate) (PMMA) standards (from 875 to 62 000 g/mol).

### 4.4. Assessment of $M_n$ of NIPU-A and PDMS-A by titration of amine groups

NIPU-A or PDMS-A (1.5 g) was dissolved isopropanol/toluene mixture (25 ml, volume ratio 1/1) at 50 °C. The assay was then performed using a solution of HCl in isopropanol (0.1 mol/l). Bromocresol green was used as a colorimetric indicator. Assuming an average amine functionality of 2.0 for these oligomers, the average molecular weight was calculated using Equation (1):

$$M_n = \frac{2 \cdot m_{\text{oligomer}}}{[\text{HCl}] \cdot V_{\text{eq}}} \quad (1)$$

where  $m_{\text{oligomer}}$  is the weight of oligomer sample,  $[\text{HCl}]$  is the concentration of the HCl titrant solution,  $V_{\text{eq}}$  is the volume at the equivalence (or stoichiometric) point.

### 4.5. Determination of *phr*: stoichiometric parts by weight of curing agent per 100 parts of epoxy resin

The *phr* value was calculated as Equation (2):

$$phr = \frac{AHEW}{EEW} \cdot 100 \quad (2)$$

Amine hydrogen equivalent weight (*AHEW*) was determined as Equation (3):

$$AHEW = \frac{M(\text{amine-terminated oligomer})}{\text{number of active amine hydrogen}} \quad (3)$$

Epoxy equivalent weight (*EEW*) was determined as Equation (4):

$$EEW = \frac{M(\text{epoxy resin})}{\text{number of epoxy function}} \quad (4)$$

### 4.6. Differential scanning calorimetry (DSC)

Differential scanning calorimetry (DSC) analysis was achieved under a nitrogen flow, using a DSC Q2000 instrument (TA Instruments, France) with a heating rate of 10 °C/min, in the range of –50 to 200 °C. The glass transition temperature ( $T_g$ ) was calculated from the second heating cycle using the midpoint method. The area and width of the exothermic peak were used to determine the enthalpy of reaction and the curing range, respectively.

### 4.7. Thermogravimetric analysis (TGA)

Thermo-gravimetric analysis (TGA) was performed under a nitrogen flow, using a TGA Q500 device (TA Instruments, France), with a heating rate of 10 °C/min. The thermal stability of the prepared NIPU foams was estimated through the temperature at 10% of weight loss ( $T_{10\%}$ ).

### 4.8. Dynamic mechanical analysis (DMA)

Dynamic mechanical analysis was achieved with the DMA Q800 (TA Instrument, France). Each sample

was cut into a 10×4 mm cylinder. The mechanical behaviour of the foams was measured with compression clamps in strain ramp mode at room temperature. A preload force of 0.02 N and a strain rate of 2%/min were used, up to 75% of the total foam strain. The resilience was measured in the creep mode at room temperature. The foams were compressed to 50% of their initial thickness with a displacement time of 10 min and a recovery time of 20 min.

#### 4.9. Scanning electron microscopy (SEM)

The prepared NIPU foams were imaged with JEOL scanning electron microscope (JEOL Neoscope JCM-6000, France). Samples were sputter-coated with gold (JFC 1300 Autofine coater: JEOL, France) before imaging. Cross-section morphologies were recorded at 15 kV accelerating voltage, in high vacuum secondary electron mode.

#### 4.10. Rheological study

Rheological analysis was performed on a DHR-2 rheometer (TA Instruments, France) using a parallel plate geometry (ø25 mm), with a geometry gap of 500 µm and a shear rate of 10 s<sup>-1</sup>. Measurements were performed on a temperature range of 30 to 200 °C with a heating rate of 3 °C/min. Viscosity measurements were conducted in the flow temperature ramp mode. The gel point (GP) was assessed using isothermal and temperature ramp tests in oscillatory mode with a frequency of 1 Hz.

#### 4.11. Swelling index (SI)

Each NIPU foam was immersed in 20 ml of CH<sub>2</sub>Cl<sub>2</sub> and stirred for 24 h. Swelling index was calculated as Equation (5):

$$SI = \frac{m_f - m_i}{m_i} \cdot 100 \quad (5)$$

where  $m_f$  is the mass of the sample after 24 h of immersion in CH<sub>2</sub>Cl<sub>2</sub> and  $m_i$  its initial mass.

#### 4.12. Extractible content

Extractible content was calculated as Equation (6):

$$\text{Extractible content} = \frac{m_i - m_r}{m_i} \cdot 100 \quad (6)$$

$m_i$  is the initial mass of the sample,  $m_r$  is the residual mass after extraction in CH<sub>2</sub>Cl<sub>2</sub> for 24 h, followed by drying at 50 °C for 24 h.

#### 4.13. Apparent density

Cylindrical NIPU foams were prepared in a specific mould. The top of the foam which was out of the mould was carefully cut to afford a perfect cylindrical geometry. Apparent density ( $\rho_a$ ) was calculated as Equation (7):

$$\rho_a = \frac{m_i}{\pi \cdot r^2 \cdot h} \quad (7)$$

$m_i$ ,  $r$ , and  $h$  are the initial mass, the radius and the height of the cylindrical foam, respectively.

A digital caliper was used to measure the dimensions of the foams.

### 5. Results and discussion

#### 5.1. Preparation of an amino-telechelic NIPU (NIPU-A)

An amine terminated NIPU oligomer (NIPU-A), based on fatty branched diamines (Priamine<sup>®</sup> 1074) and dialcohols (Pripol<sup>®</sup> 2033), was prepared in three steps in bulk conditions without any purification (Figure 1). In order to limit the chain extension during the polymerization process, an excess higher than 2 in BMC (for preparation of NIPU-MC) and in Priamine<sup>®</sup> (for the preparation of NIPU-A) was used (Figure 1). Consequently, free Priamine<sup>®</sup>, playing the role of reactive diluent, was present in the final liquid product, which exhibited suitable viscosity for the preparation of initial foam mixtures.

The bis-methyl dicarbamate based on Priamine<sup>®</sup> 1074 (BMC) was prepared by the reaction of a large excess of DMC (10 eq) with Priamine<sup>®</sup> 1074, in the presence of TBD as catalyst. The reaction was conducted at 80 °C for 6 h, as previously described [19–24, 32]. The <sup>1</sup>H NMR analysis displayed a total disappearance of the signal of amine groups at 2.65 ppm. The signal of the methyl protons arose at 3.65 ppm. The signal of the methylene groups in the  $\alpha$  position of the methyl carbamate groups was observed at 3.15 ppm. The signal at 4.64 ppm arose from the nitrogen proton of the carbamate groups. The band at 1715 cm<sup>-1</sup> in the FTIR spectrum (Figure 2) corresponds to the H bonded stretching vibration of C=O of the methyl carbamate groups. The bands at 1526 and 3300 cm<sup>-1</sup> correspond to the bending and stretching vibrations of N–H bonds, respectively. The DSC analysis did not show any thermal phenomenon above 80 °C. The TGA analysis showed good thermal stability with  $T_{10\%} > 200$  °C.

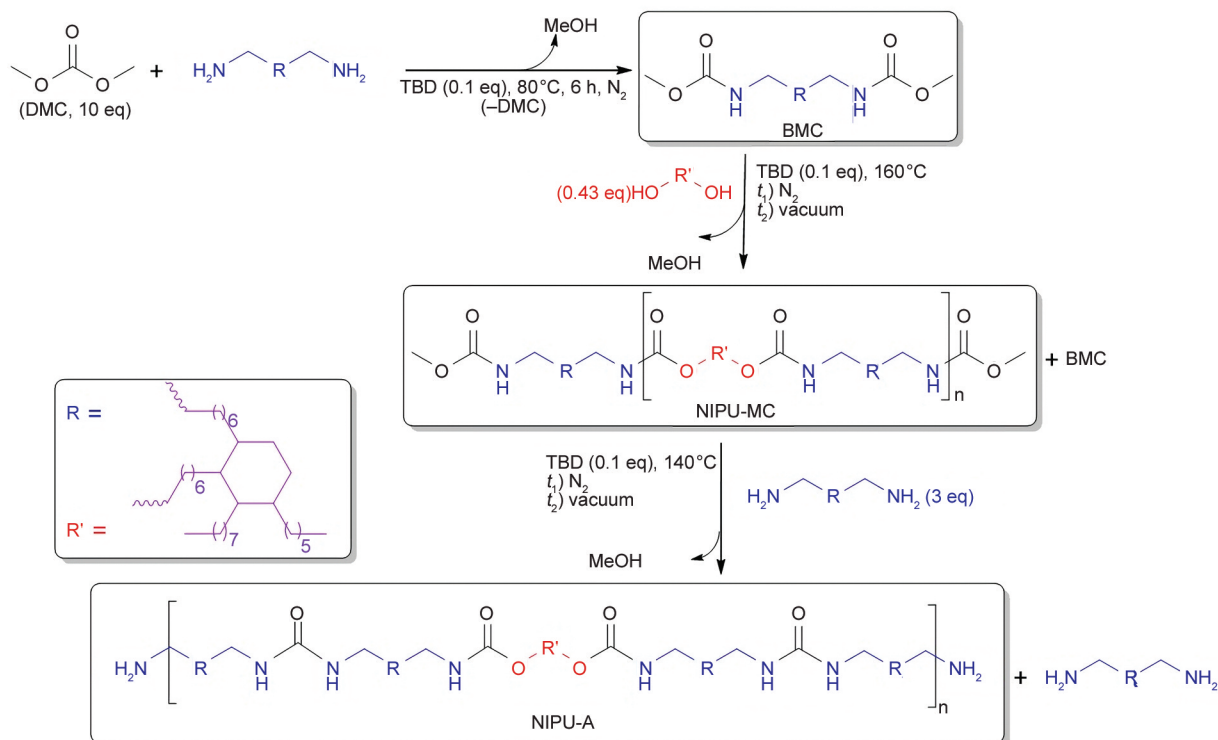


**Figure 1.** Synthesis pathway of the NIPU-A oligomer.

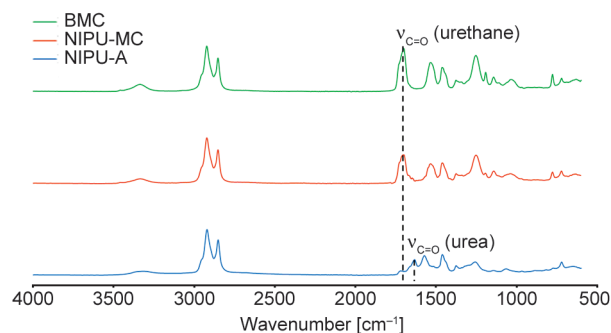


**Figure 2.** FTIR spectra of compounds BMC, NIPU-MC and NIPU-A.

The NIPU oligomer with methylcarbamate chain-ends (NIPU-MC) was prepared by reacting 2.3 eq of BMC with Pripol® 2033 at 160 °C, under a nitrogen flow overnight, and then under vacuum for 2 h, in the presence of TBD, as similarly performed in a previous work [32]. The FTIR spectrum (Figure 2) showed the persistence of the urethane bands. The  $^1\text{H}$  NMR analysis revealed the decrease of the peak of the methyl carbamate groups at 3.65 ppm as well as the absence of a triplet at 3.62 ppm arising from protons in the alpha position to the primary alcohol function. One can also observe the presence of a peak at 4.03 ppm arising from protons in the alpha position to the oxygen of the median urethane function, suggesting that the oligomerization was successful (Figure 3). SEC analysis showed a mixture

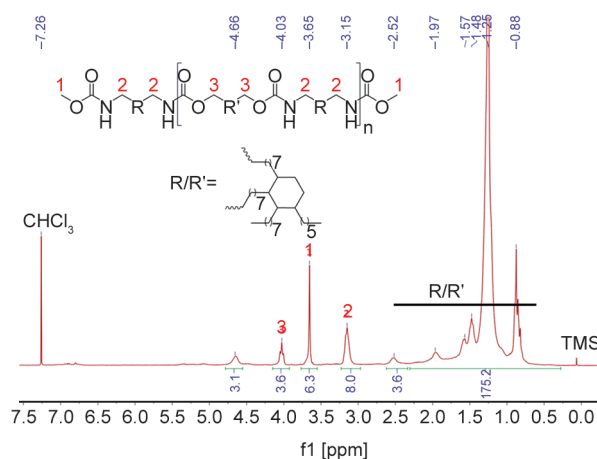


**Figure 3.**  $^1\text{H}$  NMR spectrum in  $\text{CDCl}_3$  of methylcarbamate-terminated NIPU oligomers (NIPU-MC).

of oligomers and BMC (Figure 4). The obtained  $M_n$  value for NIPU-MC was 2520 g/mol with a dispersity of 2.8 (Table 1).

Finally, the NIPU-MC was reacted with 3 eq of Priamine® 1074 leading to a NIPU oligomer with amine end-groups (NIPU-A), as similarly performed in a previous work [32]. The FTIR spectra of this oligomer (Figure 2) displayed urea bands at  $1630\text{ cm}^{-1}$  ( $\text{C}=\text{O}$  stretching) and  $1575\text{ cm}^{-1}$  ( $\text{N}-\text{H}$  bending), suggesting that the excess of amine groups caused a side transurethane reaction along the chain of the NIPU-A, releasing mono- and/or di-alcohols. This supposition was confirmed by  $^1\text{H}$  NMR analysis



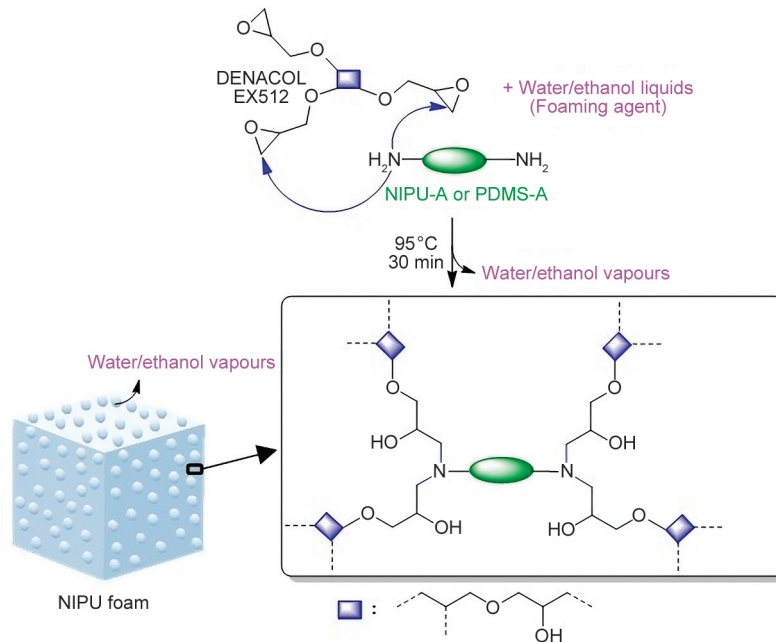


**Figure 6.** The chemical process implemented for the preparation of NIPU foams.

their properties as a function of the nature of the blowing agent and the crosslinking density [32]. Indeed, PDMS-A has no reactive groups along the chain that increase the crosslinking density, and it cannot release hydrogen gas.

The amine and epoxy groups were introduced in the stoichiometric proportions, considering that one amine group can react with two epoxy groups. Therefore, the amine-index of NIPU-A and PDMS-A assessed by titration was used for calculation of  $AHEW$  (Equation (2)) and  $phr$  (Equation (1)) (Table 1).

The average functionality of the starting monomers mixture of 3.4 and the critical conversion at the gel point of 0.58 were calculated using Carothers' equations ( $\bar{f}$ , Equation (9) and  $P_c$ , Equation 10)):

$$\bar{f} = \frac{\sum n_i f_i}{\sum n_i} \quad (9)$$

$$P_c = \frac{2}{\bar{f}} \quad (10)$$

where  $n_i$  is the molar quantity of the monomer  $i$  and  $f_i$  is the functionality of the monomer  $i$  ( $f_i = 4$  for NIPU-A and PDMS-A (since one amine group can react twice) and  $f_i = 3$  for DENACOL EX512).

The crosslinking reaction was first monitored by dynamic rheology, in the absence of foaming agent. The approximative temperature of the gelling point (GP), at a low heating rate of 3 °C/min, was determined as the temperature where  $G'$  (storage modulus) was equal to  $G''$  (loss modulus), *i.e.* at the cross-section

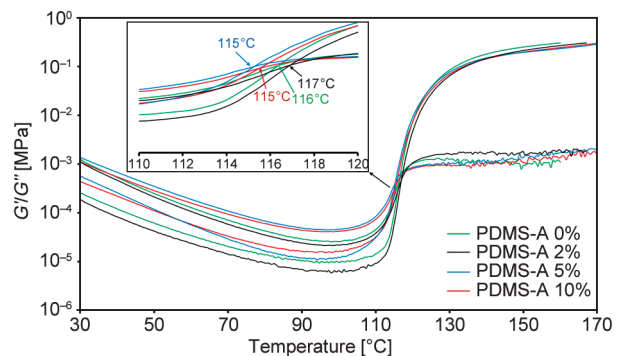


**Figure 7.** Rheological study of NIPU-A/PDMS-A/DENACOL EX512 formulations as a function of temperature, at a heating rate of 3 °C/min.

of the two curves (Figure 7). One can observe that the gelling point temperature was about 116 °C regardless the PDMS-A concentration. However, this temperature is very high and may cause all the foaming agent to evaporate before gelling begins.

Since the boiling temperature of water is 100 °C and the water/ethanol mixture boils at temperatures ranging from 78 °C (azeotropic) to about 95 °C (water-rich mixture), we have tested foaming at close temperatures, *i.e.* 73, 74, 76, 79, 85, 95, 100, 105 and 120 °C. Formulations based on NIPU-A, PDMS-A and a blowing agent (water/ethanol mixtures at several ratios) were heated at the set temperature for 2 h, which is more than enough time for the expansion and evolution of the foam (Table 2). Photos of some prepared NIPU foams are depicted in Figure 8. This preliminary study showed that 95 °C was the best temperature to get foams combining good expansion

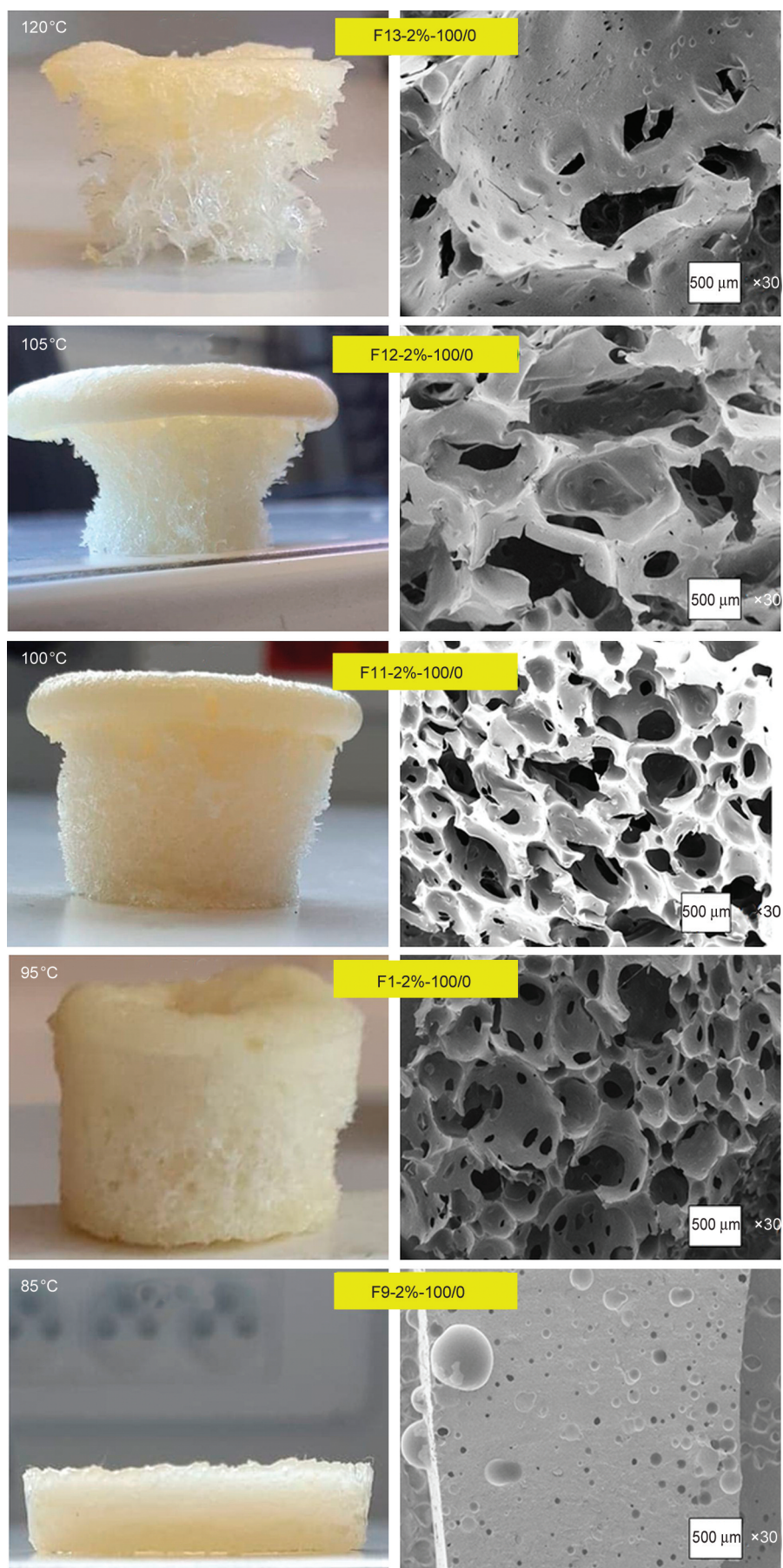


**Figure 8.** Photos (on the left) of NIPU foams based on 2% of PDMS-A and water as foaming agent at different temperatures (F1, F9, F11 to F13) and their corresponding SEM images (on the right).

and apparent mechanical properties. Indeed, at a temperature below or equal to 85 °C, foams could not be obtained, whereas above 95 °C, the blowing agent evaporation was very fast leading to foams presenting macro-cellular morphologies and/or a thick layer of crust, as well as poor mechanical properties.

An isothermal study, in the absence of the blowing agent, was then conducted at 95 and 100 °C to have an idea about the minimal time required to get the gel point (Figures 9 and 10) and to define a universal time for the process. The GP was reached after 194 to 354 s at 95 °C (using formulations with 0 to 10% of PDMS) and after 133 s at 100 °C (using formulation with 2% of PDMS).

In complement to this study, we have performed an isothermal DSC study at the same temperatures (formulations with 2% of PDMS) to evaluate the time required to get the critical conversion of the epoxy-amine system (Figures 11 and 12). The formulations having a high reactivity at 95 and 100 °C, the baseline of the DSC curve couldn't be observed at the beginning. However, the end of the epoxy-amine reaction, attested by the end of energy release, was observed

after about 45 min at 95 °C and after about 30 min at 100 °C, which is well after the gel point and well within the two-hour curing time.

### 5.3. Characterizations of the prepared NIPU foams

The composition and properties of the prepared NIPU foams at the optimal process conditions are depicted in Table 2.

It is noteworthy that the foams were elaborated following three main parameters:

- 1 The molar content of PDMS-A (from 0 to 10%) for a fixed blowing agent composition (H<sub>2</sub>O 100%) and a fixed temperature (95 °C) (Foams: F1, F6, F7 and F8);
- 2 The blowing agent composition (water/ethanol ratios (mol/mol): 100/0, 90/10, 75/25, 50/50, 0/100) for a fixed value of concentration of PDMS-A (2%), a fixed temperature and a fixed total volume of the blowing agent at the liquid state (80 ml) (Foams: F1 to F5; F9 vs. F10);
- 3 The foaming temperature for a fixed formulation (Foams: F1, F9, F11 to F13; F2 vs. F14; F3 vs. F15; F4 vs. F16 and F5 vs. F17).

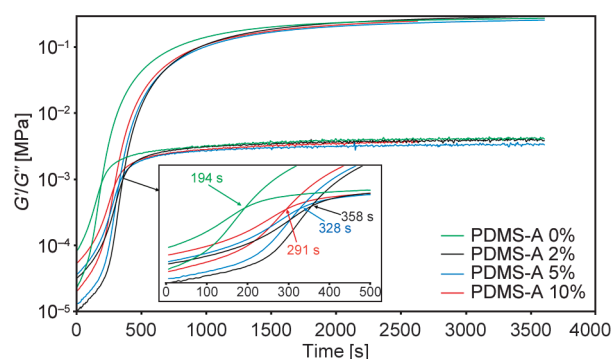


**Figure 9.** Isothermal rheological study at 95 °C of NIPU-A/PDMS-A/DENACOL EX512 formulations as a function of time.

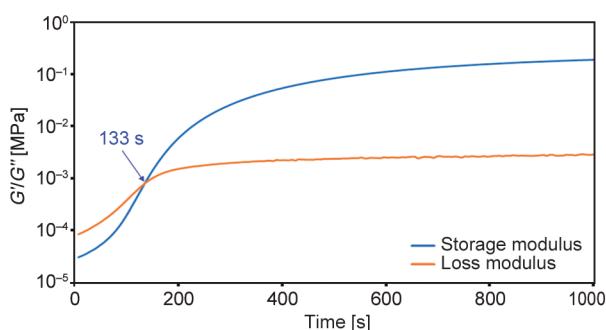


**Figure 10.** Isothermal rheological study at 100 °C of NIPU-A/PDMS-A (2%)/EX512 formulation as a function of time.

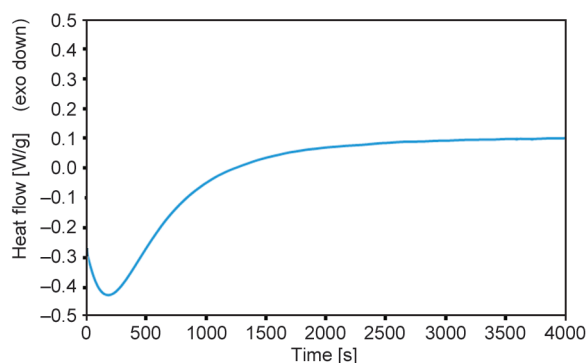


**Figure 11.** Isothermal DSC study at 95 °C of NIPU-A/PDMS-A (2%)/EX512 formulation as a function of time.

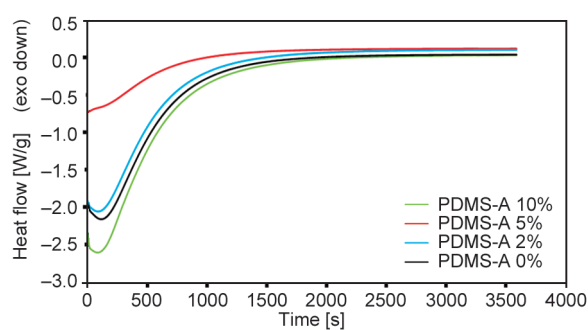


**Figure 12.** Isothermal DSC study at 100 °C of NIPU-A/PDMS-A (0 to 10%)/EX512 formulations as a function of time.

**Table 2.** Composition, apparent density ( $\rho_a$ ), physical and thermal properties of the prepared NIPU foams.

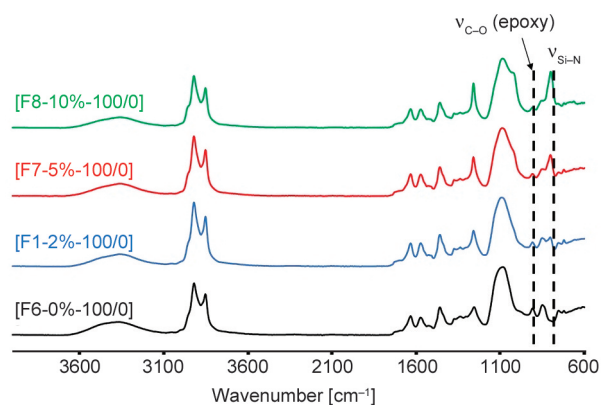
Foams [Fn-p-z] <sup>a</sup>	PDMS-A, p [%]	Water/ethanol, z [mol/mol]	T <sub>foaming</sub> [°C]	$\rho_a$ [kg/m <sup>3</sup> ]	Average cell diameter [ $\mu$ m]	Extractible [wt%]	Swelling index [wt%]
[F1-2%-100/0]	2	100/0	95	190±40	590±270	15±2	1180±410
[F2-2%-90/10]	2	90/10	95	90±4	1540±400	21±2	1350±90
[F3-2%-75/25]	2	75/25	95	115±40	430±150	20±1	1480±210
[F4-2%-50/50]	2	50/50	95	125±20	465±215	19±3	730±130
[F5-2%-0/100]	2	0/100	95	280±25	280±120	13±2	1100±150
[F6-0%-100/0]	0	100/0	95	325±60	600±500	13±1	650±130
[F7-5%-100/0]	5	100/0	95	120±7	400±250	19±5	1500±170
[F8-10%-100/0]	10	100/0	95	160±60	830±300	13±3	1200±130
[F9-2%-100/0]	2	100/0	85	950±60	140±125	9±1	290±10
[F10-2%-75/25]	2	75/25	85	830±20	140±85	14±1	260±9
[F11-2%-100/0]	2	100/0	100	140±6	580±250	23±3	1150±70
[F12-2%-100/0]	2	100/0	105	55±7	3090±880	25±4	1820±160
[F13-2%-100/0]	2	100/0	120	80±17	1240±430	25±2	1400±410
[F14-2%-90/10]	2	90/10	79	670±30	n.a	25±3	260±10
[F15-2%-75/25]	2	75/25	76	880±40	n.a	13±1	280±10
[F16-2%-50/50]	2	50/50	74	790±10	n.a	11±2	290±10
[F17-2%-0/100]	2	0/100	73	910±50	n.a	16±1	300±5
F-commercial PU [12]	–	–	RT	100	600±250	8	980
F-NIPU reference [32]	–	–	100	170±40	360±220	18±2	840±110

<sup>a</sup>F: means foam, n: is the number of the prepared foam, p: is the percentage of PDMS-A, z: is the water/ethanol ratio.

The properties of the prepared NIPU were compared to those of a selected commercial conventional PU foam recently described in the literature [12]. They were also compared to a NIPU foam previously prepared from the same NIPU-A and DENACOL EX512 in the presence of PHMS as a crosslinking and *in-situ* hydrogen-releasing chemical blowing agent [32].

FTIR analysis of the prepared foams exhibited a small residual band of the epoxide group at 830 cm<sup>-1</sup> (Figure 13). The urethane/urea ratio was similar to that of the NIPU-A precursor.

Scanning electron microscopy (SEM) was used to analyse the morphologies of the prepared foams.

**Figure 13.** FTIR spectra of some prepared foams.

Some images are depicted in Figure 14. All the prepared foams exhibited open cells. Foams prepared above 95 °C presented heterogeneous macro-cellular morphologies with cell size above 1 mm and standard deviation ranging from 430 to 880  $\mu$ m (Table 2). Surprisingly, the foam F2-2%-90/10 prepared at 95 °C also exhibited a macro-cellular morphology (1540±400  $\mu$ m). The non-expanded materials prepared at 85 °C exhibited little cells with low size of about 140  $\mu$ m. All the other foams prepared at 95 °C displayed micro-cellular morphologies with cell sizes ranging from 280±120 to 830±300  $\mu$ m. The foams prepared with 50 to 100% of ethanol exhibited the lowest cell sizes. Furthermore, it seems that the amount of PDMS-A in the formulation has not a significant impact on the cell size values, considering the standard deviations. Furthermore, one can observe that these values are in the range of the F-commercial PU (600±250  $\mu$ m) [12] and the F-NIPU reference (360±220  $\mu$ m) [32].

Foams prepared at temperatures above 100 °C as well as the foam F2-2%-90/10 prepared at 95 °C exhibited the lowest density values (55 to 90 kg/m<sup>3</sup>), which is in consistency with their macro-cellular morphologies and cell size values (Table 2). According to the literature [11] these foams can be considered as low-density flexible foams. As expected, the non-expanded

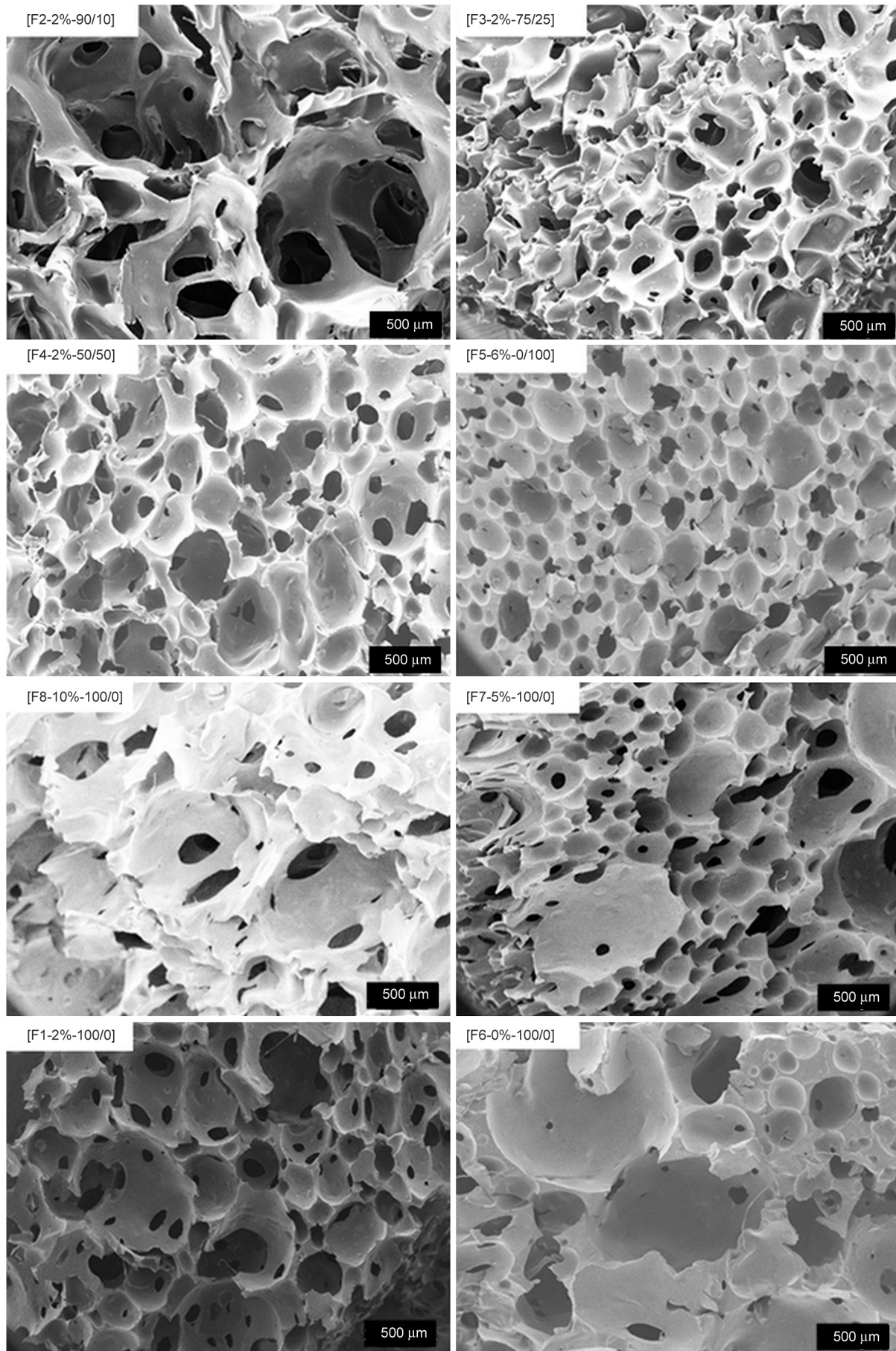


Figure 14. SEM images of the prepared foams, as a function of the H<sub>2</sub>O/Ethanol ratio ( $z$ ) and the PDMS content ( $p$ ).

material prepared at 73 to 85 °C displayed the highest apparent density ( $670\pm 30$  to  $950\pm 60$  kg/m<sup>3</sup>). All the other foams exhibited apparent density values between  $115\pm 40$  and  $325\pm 60$  kg/m<sup>3</sup>, consistent with their corresponding average values of cell size. These foams can be considered as high-density flexible foams [11]. These values are also consistent with those of PHU foams (190 to 300 kg/m<sup>3</sup>), described recently in the literature [11, 12]. They were also in the range of the F-commercial PU (100 kg/m<sup>3</sup>) [12] and F-NIPU reference ( $170\pm 40$  kg/m<sup>3</sup>) [32].

The crosslinking densities of the prepared foams were estimated through their swelling and extractible percentages in dichloromethane (Table 2). Because of their affinity with dichloromethane and their porous structure, the prepared foams displayed high swelling percentages, ranging from 730 to 1820%. The foam prepared at 105 °C (F12) exhibited the highest value of swelling percentage (1820%) and extractible (25%), suggesting the lowest degree of crosslinking. The foam prepared at 120 °C (F13) also possessed a low crosslinked density since they exhibited 25% of extractible percentage and a relatively high swelling percentage (1400%). The foam prepared at 100 °C (F11) displayed lower crosslinking density than its analogue prepared at 95 °C (F1), with extractible values of 23 vs. 15%, respectively, and close swelling percentages (about 1160%). The non-expanded materials prepared at 73 to 85 °C exhibited the lowest swelling percentages due to their non-alveolar structures (256 to 300%). On the other hand, they displayed similar extractible percentages ranging from 9 to 25%, compared to the other foams. All the foams prepared at 95 °C with 2% of PDMS exhibited good and intermediate crosslinking densities with swelling

percentages ranging from 730 to 1480% and extractible percentages of about 19%. The foam without PDMS-A showed the lowest swelling and extractible percentages (650 and 9%, respectively), whereas the foams based on PDMS-A (2 to 10% of PDMS-A) showed higher values of these two parameters. This can be explained by the higher solubility of the PDMS chains in dichloromethane compared to NIPU-A. Furthermore, the F-commercial PU and the F-NIPU reference exhibited close swelling percentages of 980 and 840%, respectively, compared to the prepared foams. Nevertheless, the commercial foam presented a higher crosslinking degree attested by a lower extractible content (8%). The higher extent of extractables in the case of the prepared foams can be explained by a lower theoretical critical conversion at their gel point (58%) as well as by the residual presence of non-reactive chemical functions in the NIPU-A.

Thus, on the base of the morphological characterizations, we could confirm that 95 °C was the optimal temperature to prepare the foams. The thermomechanical properties were then performed only on foams prepared at this temperature (Table 3).

Differential scanning calorimetry was used to assess the thermal properties of the prepared foams. Typical DSC curves are displayed in Figure 15. The foams exhibited close  $T_g$  values ranging from  $-17$  to  $-20$  °C regardless of their PDMS content (Table 3), which is close to the  $T_g$  value of the F-NIPU reference ( $-16$  °C) [32]. The F commercial PU showed a higher  $T_g$  value of 0 °C [12].

Thermogravimetric analysis was used to evaluate the thermal stability of the prepared foams. Typical TGA curves are presented in Figure 16. The thermal

**Table 3.** Mechanical and thermal properties of the optimal NIPU foams prepared at 95 °C.

Foam [Fn-p-z] <sup>a</sup>	HL <sup>b</sup> [%]	$R_{95\%}$ <sup>b</sup> [s]	$ILD_{25\%}$ <sup>b</sup> [kPa]	Young modulus [ $10^3$ Pa]	$T_g$ [°C]	$T_{10\%}$ [°C]
[F1-2%-100/0]	257±4	7	1.12±0.05	3.7±0.02	-19	314
[F2-2%-90/10]	24±5	9	0.77±0.05	2.0±0.01	-20	311
[F3-2%-75/25]	24±4	19	0.74±0.05	3.0±0.01	-19	305
[F4-2%-50/50]	22±4	9	1.21±0.10	3.0±0.01	-18	316
[F5-2%-0/100]	32±3	9	3.58±0.18	5.7±0.03	-20	322
[F6-0%-100/0]	48±2	7	3.79±0.50	4.0±0.02	-20	325
[F7-5%-100/0]	32±5	23	1.09±0.06	3.3±0.01	-18	308
[F8-10%-100/0]	25±4	7	0.93±0.08	2.1±0.01	-19	320
F-commercial PU [12]	–	35	–	230.00	0	328
NIPU reference [32]	21±1	13	–	20.0±0.20	-16	323

<sup>a</sup>F: means foam, n: is the number of the prepared foam, p: is the percentage of PDMS-A, z: is the water/ethanol ratio.

<sup>b</sup>HL: hysteresis loss;  $R_{95\%}$ : Recovery time to 95% of the initial height of the foam;  $ILD_{25\%}$ : indent load deflection at 25%.

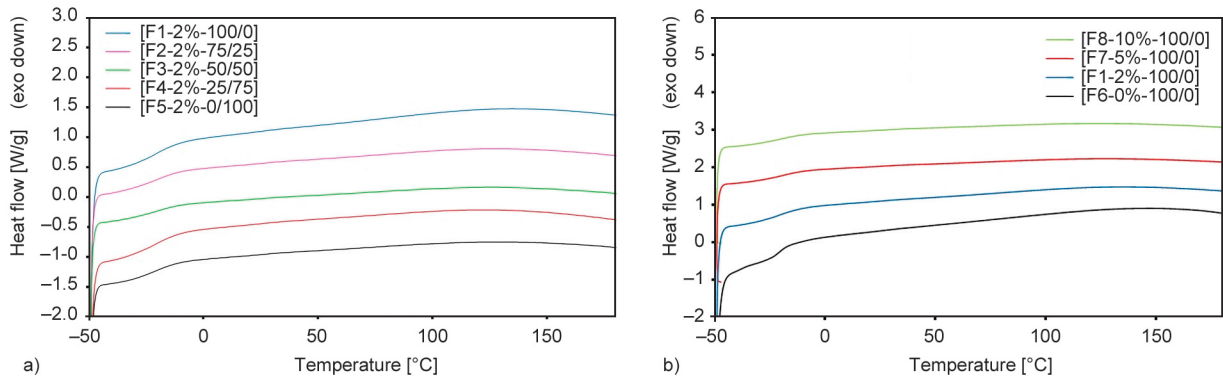


Figure 15. DSC curves of a) F2 to F5 compared to F1 and b) F6 to F8 compared to F1.

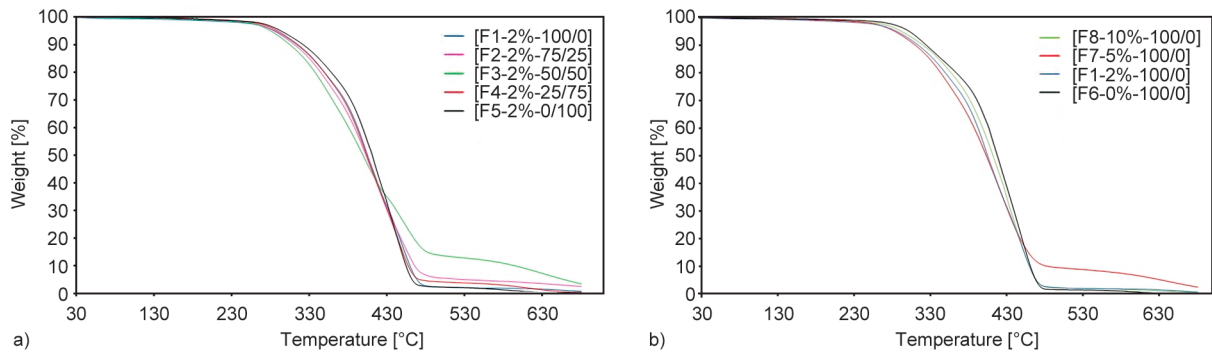


Figure 16. TGA curves of a) F2 to F5 compared to F1 and b) F6 to F8 compared to F1.

temperature at 10% of weight loss ( $T_{10\%}$ ) varied from 305 to 325 °C (Table 3), which is close to the values of the two foams used as references (323 and 328 °C) [12, 32].

Flexible foams can be used in a wide range of applications and their specifications for PU foam can be very different. In this work, we have chosen to use DMA as ultimate tool to characterize the mechanical properties of our foams. Three main mechanical parameters are studied in industrial foam, especially for bedding and seating:

1 Firmness or Indent load deflection ( $ILD$ ), which is evaluated by the force required to compress a foam to 25% of its original height. Commonly used in the mattress foam industry, this parameter

is an indicator of the softness of the foam [32].

The lower the force applied, the softer the foam.

- 2 Hysteresis loss (HL), which is assessed by subtracting the total energy (area under the loading stress-strain DMA curve) and the return energy (area under the recovery curve) divided by the total energy [33]. This parameter indicates the material's ability to absorb energy. Usually, a strain of 75% is employed to assess the hysteresis loss (Figure 17).
- 3 The recovery time to 95% of the initial height of the foam ( $R_{95\%}$ ) is recorded after a starting 50% compression.

The values of these three parameters for foams prepared at the optimal temperature of 95 °C are depicted in Table 3.

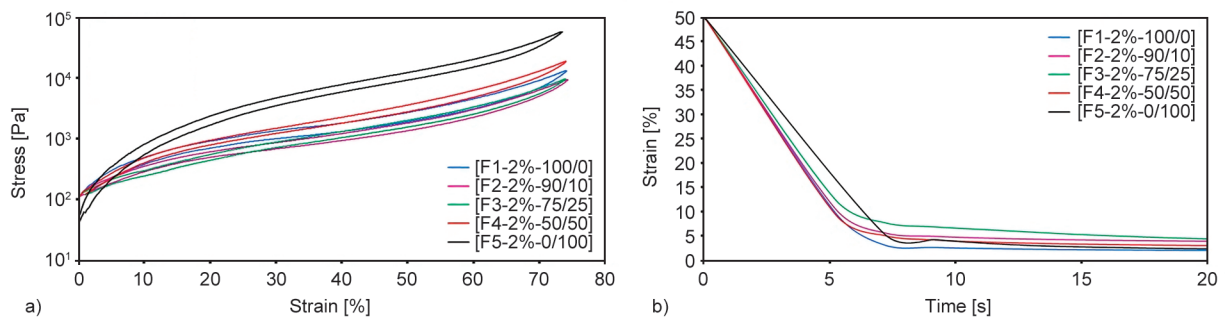


Figure 17. Mechanical properties by DMA of the optimal NIPU foams prepared at 95 °C. a) Stress-strain curves, b) creep mode: 10 min at 50% strain at 35 °C.

However, in the case of foams, there are too many morphological parameters (such as porosity, number of open cells, cell size, wall thickness, bulk density, and degree of crosslinking) that could have an impact on the mechanical properties. It is therefore often difficult to find structure/property relationships easily, except in the case where only one or two parameters are preponderant. In this case, we will note it in the discussion.

Three parts can be distinguished in the DMA stress-strain curves (Figure 17). The first one, between 0 to 10% of strain, is the region of linear elasticity; it is correlated to the deformation required to cause the bending of the foam edges. The plateau zone between 10 and 50–60% deformation is attributed to the collapse of the foam after cell compression. The last part, where the stress is significantly increased over a lower strain, is attributed to the complete compression of the cells (foam densification). Therefore, due to their smaller cell volume, denser foams tend to have a smaller plateau.

The NIPU foams F2, F3, F4 and F8 exhibited HL values varying between 22 and 25%, close to the F-NIPU reference (21%). The foam F6 exhibited an HL value close to 50%. Foams F5 and F7 displayed intermediate HL value of 32%. For probably morphological reasons, the foam F1 exhibited a very high value of HL (257%).

The prepared foams exhibited low  $R_{95\%}$  values ranging from 7 to 23 s (Table 3). The F NIPU reference was in this range (13 s). Foams F3 and F7 exhibited the highest values of  $R_{95\%}$  (19 and 23 s, respectively). This can be correlated to their lowest crosslinking density attested by their highest swelling and extractable percentages.

The prepared foams showed  $ILD_{25\%}$  values ranging from 0.74 to 3.79 kPa (Table 3). It can be observed that this parameter is influenced by the PDMS-A content in the foams. Indeed, the  $ILD_{25\%}$  value decreased from 3.8 kPa to about 1.1 kPa, then to about 0.9 kPa, when the percentage of PDMS-A increased from 0 to 2–5%, then to 10%, respectively. This is probably due to the soft character of the PDMS chain. We can also notice that when the percentage of ethanol in the blowing agent increases from 10–25% to 50%, then to 100%, the  $ILD_{25\%}$  increases from 0.7 to 1.2 kPa, then to 3.6 kPa.

Finally, due to their softness and alveolar microstructures, the prepared NIPU foams showed low values of Young's modulus, ranging from  $2.0 \cdot 10^3$  to

$5.7 \cdot 10^3$  Pa (Table 3). For the same reason, this parameter changed in the same way as  $ILD_{25\%}$  with the percentage of PDMS-A in the foam, *i.e.*, it decreased from  $4.0 \cdot 10^3$  Pa to about  $3.5 \cdot 10^3$  Pa and then to  $2.1 \cdot 10^3$  Pa when the percentage of PDMS-A increased from 0 to 2–5% and then to 10%, respectively. All the prepared foams exhibited lower Young's modulus values than the F-commercial PU ( $230 \cdot 10^3$  Pa) and the reference F-NIPU ( $20 \cdot 10^3$  Pa), which could be explained by the fact that these reference materials lack PDMS-like soft phase. The Young's modulus also changed similarly as  $ILD_{25\%}$  with the ethanol/water ratio in the blowing agent, *i.e.*, it increased from  $2 \cdot 10^3$  to  $3 \cdot 10^3$  Pa and then to  $5.7 \cdot 10^3$  Pa when the percentage of ethanol in the blowing agent increased from 10 to 25–50% and then to 100%, respectively.

## 6. Conclusions

In this work, we have successfully prepared partially biobased flexible NIPU foams from a biobased synthesized amino-terminated NIPU (NIPU-A), a biobased polyepoxide molecule (DENACOL EX512) and an amino-terminated PDMS (PDMS-A), using water/ethanol mixtures as blowing agent. NIPU-A was obtained through the transurethane polycondensation approach from a fatty diamine, a fatty diol and DMC (a CO<sub>2</sub> derivative). DSC and dynamic rheology revealed that the operating conditions to get foams from the different starting formulations were at least 45 min at 95 °C. The obtained optimal foams displayed heterogeneous cell diameters ranging from 400 to 1540 μm and high apparent densities changing from 90 to 320 kg/m<sup>3</sup>. They showed thermal stabilities above 300 °C. They presented negative  $T_g$  values (from –18 to –20 °C) as well as low Young modulus values (from  $2.0 \cdot 10^3$  to  $5.7 \cdot 10^3$  Pa), which is in consistent with their soft physical character. The prepared high-density flexible polyurethane foams exhibited disparate values of hysteresis loss. The recovery time was short and seemed to be mainly impacted by the crosslinking density of these foams. The indent load deflection at 25% as well as the Young modulus were mainly influenced by the PDMS-A content within the foams, which also would explain the differences observed with the F-commercial PU and the F-NIPU reference. Finally, this work highlights the interest of the transurethane polycondensation route to prepare telechelic oligomers, which can be used in the preparation of valuable

NIPU materials. The new process developed in this work can be extended to a variety of chemical structures leading to a variety of foam properties.

## Acknowledgements

The authors gratefully acknowledge the ‘Région Haute-Normandie’ (project PhotoNIPUfoam) for the financial support.

## References

- [1] Dworakowska S., Cornille A., Bogdał D., Boutevin B., Caillol S.: Formulation of bio-based epoxy foams from epoxidized cardanol and vegetable oil amine. *European Journal of Lipid Science and Technology*, **117**, 1893–1902 (2015).  
<https://doi.org/10.1002/ejlt.201500232>
- [2] Kausar A.: Polyurethane composite foams in high-performance applications: A review. *Polymer-Plastics Technology and Engineering*, **57**, 346–369 (2018).  
<https://doi.org/10.1080/03602559.2017.1329433>
- [3] Somarathna H. M. C. C., Raman S. N., Mohotti D., Mutalib A. A., Badri K. H.: The use of polyurethane for structural and infrastructural engineering applications: A state-of-the-art review. *Construction and Building Materials*, **190**, 995–1014 (2018).  
<https://doi.org/10.1016/j.conbuildmat.2018.09.166>
- [4] Ates M., Karadag S., Eker A. A., Eker B.: Polyurethane foam materials and their industrial applications. *Polymer International*, **71**, 1157–1163 (2022).  
<https://doi.org/10.1002/pi.6441>
- [5] Gama N., Ferreira A., Barros-Timmons A.: Polyurethane foams: Past, present, and future. *Materials*, **11**, 1841 (2018).  
<https://doi.org/10.3390/ma11101841>
- [6] Akindoyo J. O., Beg M. D. H., Ghazali S., Islam M. R., Jeyaratnam N., Yuvaraj A. R.: Polyurethane types, synthesis and applications – A review. *RSC Advances*, **6**, 114453–114482 (2016).  
<https://doi.org/10.1039/c6ra14525f>
- [7] Cornille A., Auvergne R., Figovsky O., Boutevin B., Caillol S.: A perspective approach to sustainable routes for non-isocyanate polyurethanes. *European Polymer Journal*, **87**, 535–552 (2017).  
<https://doi.org/10.1016/j.eurpolymj.2016.11.027>
- [8] Blattmann H., Lauth M., Mühlaupt R.: Flexible and bio-based nonisocyanate polyurethane (NIPU) foams. *Macromolecular Materials and Engineering*, **301**, 944–952 (2016).  
<https://doi.org/10.1002/mame.201600141>
- [9] Grignard B., Thomassin J. M., Gennen S., Poussard L., Bonnaud L., Raquez J.-M., Dubois P., Tran M.-P., Park C. B., Jerome C., Detrembleur C.: CO<sub>2</sub>-blown microcellular non-isocyanate polyurethane (NIPU) foams: From bio- and CO<sub>2</sub>-sourced monomers to potentially thermal insulating materials. *Green Chemistry*, **18**, 2206 (2016).  
<https://doi.org/10.1039/c5gc02723c>
- [10] Mao H.-I., Chen C.-W., Yan H.-C., Rwei S.-P.: Synthesis and characteristics of nonisocyanate polyurethane composed of bio-based dimer diamine for supercritical CO<sub>2</sub> foaming applications. *Journal of Applied Polymer Science*, **139**, e52841 (2022).  
<https://doi.org/10.1002/app.52841>
- [11] Cornille A., Dworakowska S., Bogdal D., Boutevin B., Caillol S.: A new way of creating cellular polyurethane materials: NIPU foams. *European Polymer Journal*, **66**, 129–138 (2015).  
<https://doi.org/10.1016/j.eurpolymj.2015.01.034>
- [12] Cornille A., Guillet C., Benyahya S., Negrell C., Boutevin B., Caillol S.: Room temperature flexible isocyanate-free polyurethane foams. *European Polymer Journal*, **84**, 873–888 (2016).  
<https://doi.org/10.1016/j.eurpolymj.2016.05.032>
- [13] Sternberg J., Pilla S.: Materials for the biorefinery: High bio-content, shape memory Kraft lignin-derived non-isocyanate polyurethane foams using a non-toxic protocol. *Green Chemistry*, **22**, 6922–6935 (2020).  
<https://doi.org/10.1039/D0GC01659D>
- [14] Clark J. H., Farmer T. J., Ingram I. D. V., Lie Y., North M.: Renewable self-blowing non-isocyanate polyurethane foams from lysine and sorbitol. *European Journal of Organic Chemistry*, **2018**, 4265–4271 (2018).  
<https://doi.org/10.1002/ejoc.201800665>
- [15] Monie F., Grignard B., Thomassin J.-M., Mereau R., Tassaing T., Jerome C., Detrembleur C.: Chemo- and regioselective additions of nucleophiles to cyclic carbonates for the preparation of self-blowing non-isocyanate polyurethane foams. *Angewandte Chemie*, **132**, 17181–17189 (2020).  
<https://doi.org/10.1002/ange.202006267>
- [16] Monie F., Grignard B., Detrembleur C.: Divergent aminolysis approach for constructing recyclable self-blown nonisocyanate polyurethane foams. *ACS Macro Letters*, **11**, 236–242 (2022).  
<https://doi.org/10.1021/acsmacrolett.1c00793>
- [17] Coste G., Negrell C., Caillol S.: Cascade (dithio)carbonate ring opening reactions for self-blowing polyhydroxythiourethane foams. *Macromolecular Rapid Communication*, **43**, 2100833 (2022).  
<https://doi.org/10.1002/marc.202100833>
- [18] Bourguignon M., Grignard B., Detrembleur C.: Water-induced self-blown non-isocyanate polyurethane foams. *Angewandte Chemie International Edition*, **61**, e202213422 (2022).  
<https://doi.org/10.1002/anie.202213422>
- [19] Duval C., Kébir N., Charvet A., Martin A., Burel F.: Synthesis and properties of renewable nonisocyanate polyurethanes (NIPUs) from dimethylcarbonate. *Journal of Polymer Science Part A Polymer Chemistry*, **53**, 1351–1359 (2015).  
<https://doi.org/10.1002/pola.27568>

- [20] Kébir N., Nouigues S., Moranne P., Burel F.: Non-isocyanate thermoplastic polyurethane elastomers based on poly(ethylene glycol) prepared through the transurethanization approach. *Journal of Applied Polymer Science*, **134**, 44991 (2017).  
<https://doi.org/10.1002/app.44991>
- [21] Boisaubert P., Kébir N., Schuller A. S., Burel F.: Photocrosslinked non-isocyanate polyurethane acrylate (NIPUa) coatings through a transurethane polycondensation approach. *Polymer*, **206**, 122855 (2020).  
<https://doi.org/10.1016/j.polymer.2020.122855>
- [22] Boisaubert P., Kébir N., Schuller A. S., Burel F.: Photocrosslinked coatings from an acrylate terminated non-isocyanate polyurethane (NIPU) and reactive diluent. *European Polymer Journal*, **138**, 109961 (2020).  
<https://doi.org/10.1016/j.eurpolymj.2020.109961>
- [23] Martin A., Lecamp L., Labib H., Aloui F., Kébir N., Burel F.: Synthesis and properties of allyl terminated renewable non-isocyanate polyurethanes (NIPUs) and polyureas (NIPUreas) and study of their photocrosslinking. *European Polymer Journal*, **84**, 828–836 (2016).  
<https://doi.org/10.1016/j.eurpolymj.2016.06.008>
- [24] Boisaubert P., Kébir N., Schuller A.-S., Burel F.: Polyurethane coatings from formulations with low isocyanate content using a transurethane polycondensation route. *Polymer*, **240**, 124522 (2022).  
<https://doi.org/10.1016/J.POLYMER.2022.124522>
- [25] Xi X., Pizzi A., Gerardin C., Du G.: Glucose-biobased non-isocyanate polyurethane rigid foams. *Journal of Renewable Materials*, **7**, 301–312 (2019).  
<https://doi.org/10.32604/jrm.2019.04174>
- [26] Xi X., Pizzi A., Gerardin C., Lei H., Chen X., Amirou S.: Preparation and evaluation of glucose based non-isocyanate polyurethane self-blowing rigid foams. *Polymers*, **11**, 1802 (2019).  
<https://doi.org/10.3390/polym11111802>
- [27] Chen X., Xi X., Pizzi A., Fredon E., Zhou X., Li J., Gerardin C., Du G.: Preparation and characterization of condensed tannin non-isocyanate polyurethane (NIPU) rigid foams by ambient temperature blowing. *Polymers*, **12**, 750 (2020).  
<https://doi.org/10.3390/POLYM12040750>
- [28] Chen X., Li J., Xi X., Pizzi A., Zhou X., Fredon E., Du G., Gerardin C.: Condensed tannin-glucose-based NIPU bio-foams of improved fire retardancy. *Polymer Degradation and Stability*, **175**, 109121 (2020).  
<https://doi.org/10.1016/j.polymdegradstab.2020.109121>
- [29] Azadeh E., Chen X., Pizzi A., Gerardin C., Gerardin P., Essawy H.: Self-blowing non-isocyanate polyurethane foams based on hydrolysable tannins. *Journal of Renewable Materials*, **10**, 3217–3227 (2022).  
<https://doi.org/10.32604/jrm.2022.022740>
- [30] Singh P., Kaur R.: Sustainable xylose-based non-isocyanate polyurethane foams with remarkable fire-retardant properties. *Journal of Polymers and the Environment*, **31**, 743–753 (2023).  
<https://doi.org/10.1007/s10924-022-02638-4>
- [31] Smith D. L., Rodriguez-Melendez D., Cotton S. M., Quan Y., Wang Q., Grunlan J. C.: Non-isocyanate polyurethane bio-foam with inherent heat and fire resistance. *Polymers*, **14**, 5019 (2022).  
<https://doi.org/10.3390/polym14225019>
- [32] Valette V., Kébir N., Tiavarison F. B., Burel F., Lecamp L.: Preparation of flexible biobased non-isocyanate polyurethane (NIPU) foams using the transurethanization approach. *Reactive and Functional Polymers*, **181**, 105416 (2022).  
<https://doi.org/10.1016/J.REACTFUNCTPOLYM.2022.105416>
- [33] Alzoubi M. F., Tanbour E. Y., Al-Waked R.: Compression and hysteresis curves of nonlinear polyurethane foams under different densities, strain rates and different environmental conditions. in ‘Proceedings of the ASME 2011 International Mechanical Engineering Congress and Exposition, Denver, USA’, Vol. **9**, 101–109 (2011).  
<https://doi.org/10.1115/IMECE2011-62290>